The Dissertation Committee for Shihong Chi Certifies that this is the approved version of the following dissertation:

SIMULATION OF WAVE PROPAGATION IN BOREHOLES AND RADIAL PROFILING OF FORMATION ELASTIC PARAMETERS

Committee:

Kenneth E. Gray, Co-Supervisor

Carlos Torres-Verdín, Co-Supervisor

Kamy Sepehrnoori

Tarek M. Habashy

David T. Blackstock

Francis X. Bostick, Jr.

SIMULATION OF WAVE PROPAGATION IN BOREHOLES AND RADIAL PROFILING OF FORMATION ELASTIC PARAMETERS

by

Shihong Chi, B.S., M.S., M.S.

Dissertation

Presented to the Faculty of the Graduate School of
The University of Texas at Austin
in Partial Fulfillment
of the Requirements
for the Degree of

Doctor of Philosophy

The University of Texas at Austin
December 2003

Dedication

With love to my son, my wife, and my parents.

Acknowledgements

I would like to express my gratitude and appreciation for the support of my supervisors, Dr. Carlos Torres-Verdín and Dr. Kenneth E. Gray. Their patience, understanding, constant guidance, and constructive criticism of my research work have made my stay at UT a unique experience. I thank Dr. Torres-Verdín for making my summer internship with Baker Atlas/Inteq possible. Dr. Xiaoming Tang and Dr. Arthur Cheng offered many discussions and support in my research and future career. My gratitude goes to Dr. Kamy Sepehrnoori, Dr. Tarek M. Habashy, Dr. David T. Blackstock, and Dr. Francis X. Bostick, Jr. for giving me their comments and suggestions during their busy schedules. Dr. Youli Quan provided many suggestions and much assistance during the development of the forward modeling algorithm and computer code described in this work. I am also grateful to the sponsors of UT Austin's Research Consortium on Formation Evaluation, Baker Atlas, Halliburton, Schlumberger, Shell International E&P, and Anadarko Petroleum Corporation for their support of this work.

My friends and colleagues have made my stay at Austin interesting and memorable. I thank you all for the friendships. All the people in the group of Formation Evaluation make my daily life interesting and I would like to mention their names here: Alvaro Grijalba-Cuenca, Bovan George, Chaoshun Hu, Emmanuel Toumelin, Guozhong Gao, Hee Jae Lee, Jackline Renno, Jesus Mauricio Salazar, Jianghui Wu, Junsheng Hou, Maika Gambús-Ordaz, Okhtay

Taghizadeh, Olga Magareta Campos, Omar J. Varela, Omer F. Alpak, Subhadeep Chowdhury, Thaimar Ramirez, Yoann Hispa, and Zhan Wu. My other Chinese fellows in the department include: Chunlou Li, Dan Shan, Liying Zhang, Jianguo Zhang, Qichong Li, Qiang Xu, Xingru Wu, Xiuli Gai, and many others. Particularly, my appreciation goes to Jianghui Wu for his help on simulating mud-filtrate invasion and Omer Alpak for his assistance on the inversion algorithm.

To my son Isaac, I thank him for his love and the strength and inspiration I gain from him.

To my wife Aichou, I express my thanks for her love, spiritual support and infinite patience during my study, and pushing me to be the best that I can be. Without her, I simply could not have done it.

SIMULATION OF WAVE PROPAGATION IN BOREHOLES AND RADIAL PROFILING OF FORMATION ELASTIC PARAMETERS

Publication No._____________

Shihong Chi, Ph.D.
The University of Texas at Austin, 2003

Supervisors: Kenneth E. Gray, and Carlos Torres-Verdín

Modern acoustic logging tools measure in-situ elastic wave velocities of rock formations. These velocities provide ground truth for time-depth conversions in seismic exploration. They are also widely used to quantify the mechanical strength of formations for applications such as wellbore stability analysis and sand production prevention. Despite continued improvements in acoustic logging technology and interpretation methods that take advantage of full waveform data, acoustic logs processed with current industry standard methods often remain influenced by formation damage and mud-filtrate invasion.

This dissertation develops an efficient and accurate algorithm for the numerical simulation of wave propagation in fluid-filled boreholes in the presence of complex, near-wellbore damaged zones. The algorithm is based on the generalized reflection and transmission matrices method. Assessment of mud-filtrate invasion effects on borehole acoustic measurements is performed through simulation of time-lapse logging in the presence of complex radial invasion zones. The validity of log corrections performed with the Biot-Gassmann fluid substitution model is assessed by comparing the velocities estimated from array waveform data simulated for homogeneous and radially heterogeneous formations that sustain mud-filtrate invasion.

The proposed inversion algorithm uses array waveform data to estimate radial profiles of formation elastic parameters. These elastic parameters can be used to construct more realistic near-wellbore petrophysical models for applications in seismic exploration, geo-mechanics, and production. Frequency-domain, normalized amplitude and phase information contained in array waveform data are input to the nonlinear Gauss-Newton inversion algorithm. Validation of both numerical simulation and inversion is performed against previously published results based on the Thomson-Haskell method and travel time tomography, respectively. This exercise indicates that the numerical method is stable and efficient for the simulation of wave propagation in boreholes surrounded by complex invasion zones. Additional tests of the inversion algorithm are performed on array waveform data acquired in a low-porosity gas field.

Mud-filtrate invasion effects are not measurable on the estimated P- and S- wave velocities for depths of invasion around 2-3 borehole diameters. Acoustic log corrections performed with the Biot-Gassmann fluid substitution model can only be used for the case of deep invasion. The inversion examples indicate that physically consistent radial profiles of formation density and P- and S-wave velocities can be reconstructed from array waveform data.

Table of Contents

List of Tables

List of Figures

Chapter 1: Introduction

1.1 INTRODUCTION

Acoustic logging data are now being used in many applications in the petroleum industry. In reservoir characterization studies, velocity logs provide key data for time-depth conversions of seismic data. In the area of geomechanics, the velocities are used for estimation of in-situ strength of rock formations. Specific applications include wellbore stability analysis, reservoir stimulation, and sanding prevention during production. Acoustic full waveform logging has become an important means of estimating in-situ formation petrophysical properties. In-situ effective permeability logs are routinely estimated using Stoneley wave data measured from array waveforms. Acoustic porosity logs are an important type of porosity log in the petroleum industry. Bypassed zones in a mature field can be found and fluid movements can be monitored by time-lapse acoustic logging during enhanced oil/gas recovery projects. This latter technique can also be used to quantify changes in the strength of rock formations due to hydrocarbon production and subsequent compaction. Early detection of weakening in the producing formation can prevent sanding, which causes casing erosion, borehole failures and subsequent shutdown of producing wells.

Use of seismic amplitude data in reservoir characterization requires that velocities at well locations be accurate. However, because of formation damage and fluid invasions in near-wellbore regions, measured velocities using acoustic logging are often those of invaded zones, despite the fact that modern acoustic tools are designed to sense past them. If the velocity models are not accurate, the reservoir geometrical images and the petrophysical model and rock moduli for geomechanical applications become inaccurate. In seismic-well tie applications, it is often observed that synthetic seismograms simulated using velocity data from acoustic logs do not satisfactorily match the measured seismograms. Inaccurate velocity estimations are partly due to the industry standard Slowness-Time-Coherence (STC) (Kimball and Marzetta, 1986) method used in processing.

Fluid invasion in the near-wellbore region changes formation fluid saturation in rock formations, and profiles of elastic properties in rocks surrounding a well will change accordingly. Specifically, heavier drilling fluid makes the near-wellbore region exhibit higher P- and lower S-wave velocities. This will in turn influence the characteristics of full waveform measurements in acoustic logging operations. An STC processing sequence gives only P- and S-wave logs affected by the invaded zone from array full waveforms, though abundant information regarding the invaded zone can be contained in full waveforms (Paillet and Cheng, 1991).

In slow formations, wherein the shear wave velocity is slower than the acoustic velocity of the borehole fluid, even full waveform measurements of a monopole acoustic logging do not exhibit the shear wave components. Therefore, the STC processing will yield estimates of shear wave velocity.

Quantitative estimation of minimum source-receiver separation to sense past the damaged zone has been suggested with the use of ray approximation theory (Baker, 1984). However, when velocity changes in the damaged zone are primarily due to mud-filtrate invasion, the radial velocity distributions are different from those caused by stress relief. Forward modeling techniques must be used to investigate invasion effects. These techniques mainly include the Thomson-Haskell method (Tubman, 1984) and the finite difference method (Cheng et al., 1995). The first method is not stable for high frequency problems. Finite difference methods are computationally intensive and hence are not amenable to inversion.

Corrections to velocity logs using fluid-substitution model have been proposed (Walls and Carr, 2001) for cases when discrepancies are found between the synthetic and measured seismograms. Modern acoustic tools commonly use monopole and dipole sources in logging operations. It has been shown that low frequency dipole tools penetrate two to three borehole diameters into the formation (Plona, et al., 2002). High frequency monopole tools penetrate one borehole diameter, sensing only the damaged zone in many situations. When the invasion depth is beyond the depth of investigation of a logging tool, the measured velocities are those of the damaged zone and, subsequently, log corrections become necessary. Such corrections of mud-filtration effects on acoustic logs often require of an assessment of the depth of mud-filtrate invasion and of the selection of a suitable rock physics model, since many other factors such as stress relief and shale swelling often influence the measured velocities as well.

A great deal of information regarding formation properties is borne by full array waveforms in addition to P- and S-wave velocities. Attenuation of Stoneley waves across the receiver array has been successfully used to quantify formation fractures (Tang and Cheng, 1988, Tang et al., 1991, Tang and Cheng, 1996). Methods have also been developed to estimate shear velocities from measured Stoneley wave velocities (Cheng, 1994).

Full waveform inversion was used by Cheng (1989) to determine shear wave velocity in soft formations. This is a very useful approach because direct shear wave logging is expensive and not feasible in old wells. A full waveform inversion of acoustic data can potentially yield radial profiles of elastic properties. This has been a challenging subject, partly because of the lack of knowledge of the source’s mechanical coupling with the borehole and the surrounding formations. Cheng’s (1989) method overcomes the problems of unknown source and receiver coupling with the formation when there is negligible formation damage in the near-wellbore region.

In this dissertation, a detailed assessment of mud-filtrate invasion effects on measured acoustic logs is performed so that to validate log corrections performed with the Biot-Gassmann fluid-substitution model. This work also provides near-wellbore profiles of elastic parameters from amplitude and phase information contained in array full waveforms, filling one of the obvious gaps in full waveform logging. Knowledge of the detailed radial profiles of the elastic parameters in the near-wellbore region will promote better uses of current acoustic logging measurements for seismic imaging, wellbore stability, and production operations. Specifically, assessment of mud-filtrate invasion effects on acoustic logging will provide a basis for performing log corrections with a rock physics model and will offer an opportunity for better seismic-well ties. Radial profiles of near-wellbore elastic parameters will show the impact of formation damage on estimations of formation properties and wellbore stability models, and will extend the application of acoustic full waveform data to the estimation of density. Formation damage information can potentially save millions of dollars by helping to prevent borehole collapsing alone.

An efficient and robust forward modeling tool is necessary for detailed studies on the fluid invasion effects on full waveform logging. Therefore, a new way to model acoustic wave propagation in boreholes is first evaluated using the integral equation method. It is found that a special form of Green's function needs to be introduced in the formulation. A new algorithm is then developed, based on the concept of generalized reflection and transmission matrices, for the numerical simulation of multipole acoustic logging measurements in the presence of cylindrically layered media. The Green's function for a borehole in radially multilayered media is implicitly considered in the formulation. Adoption of normalized Hankel functions and normalizing factors overcomes the numerical instability that exists in the Thomson-Haskell method for high-frequency problems. Using the reflection coefficient of the outward-directed wave in every layer and the transmission coefficient of the incoming wave from the outlying layers, the generalized reflection and transmission matrices are reconstructed for each layer. An efficient recursive scheme is implemented to compute the generalized reflection and transmission matrices. Then, displacement and stress can be computed within any layer or at any layer interface. Discrete wavenumber integrals and Fast Fourier Transforms (FFT) are used to transform the acoustic measurements from the frequency-wavenumber domain to the time-space domain.

To assess mud-filtrate invasion effects on the measured acoustic logs, a reservoir simulator is first used to numerically simulate the radial profiles of mud filtrate and connate fluid for various mud and reservoir types. Then the Biot-Gassmann fluid substitution model is used to calculate the corresponding radial profiles of the elastic parameters. Concentric radial layered formation models are built based upon finely discretized radial profiles of the elastic parameters. Monopole and dipole synthetic waveforms are simulated using the newly developed forward modeling code for homogeneous uninvaded and multilayered formation models. The P- and S-wave velocities are estimated from the full array waveforms using an industry standard STC method. By comparing the velocities for the two formation models, one can thoroughly investigate the mud-filtrate invasion effects.

Full waveforms are sensitive not only to radial profiles of compressional- and shear-wave velocity but also to density. An STC method for acoustic data processing yields at most P- and S-wave velocities for each logging depth. Therefore, STC methods only make use of partial information of full waveform data. However, inversion of full waveform data gives rise to radial distributions of bulk density and compressional- and shear-wave velocities, which can be used to improve the construction and reliability of petrophysical reservoir models.

A nonlinear Gauss-Newton algorithm is used in the dissertation for the estimation of radial profiles of elastic parameters. The array waveforms are first fast-Fourier transformed from the time domain to the frequency domain. A new complex-valued array data set is obtained by normalizing the remaining traces using one of the traces for comparison. Since the normalized spectral ratios do not involve source information, the barrier is eliminated for specific source information in full waveform inversion. The inversion algorithm minimizes the misfit between the measured normalized wavefield and the modeled normalized wavefield in a selected frequency band.

1.2 OBJECTIVE OF THIS DISSERTATION

The ultimate objective of this dissertation is to provide accurate velocity measurements and near-wellbore radial profiles for various applications in the petroleum industry. This goal is achieved by approaching the following three areas: 1) development of an efficient and robust numerical simulation code for wave propagation in boreholes in the presence of radial, complex, invaded zones, 2) assessment of mud-filtration effects on velocity estimates obtained with STC processing of array full waveform logging data, and 3) estimation of radial profiles of elastic formation properties via inversion. The study is focused on how to use more effectively travel time and spectrum information that are available in current array full waveforms logging data.

1.3 OUTLINE OF THIS DISSERTATION

The dissertation is subdivided into six segmental chapters. Chapter 1 introduces the impetus of this dissertation and some of the problems in borehole acoustic logging. It summarizes the efforts that have been made to try to overcome the same problems, outlines the new developments and methodologies to approach these problems. Finally, it states the objectives of research and briefly introduces the organization of this dissertation.

Chapter 2 achieves the first goal of this dissertation, which is to develop an efficient code for simulating wave propagation phenomena in fluid-filled boreholes in the presence of radial complex invasion zones. This chapter derives the integral equation formulation for elastic wave propagation in solid media, describes the approach used to numerically simulate elastic wave scattering phenomena, investigates the challenges of this approach in solving wave propagation problems in fluid-filled boreholes, and recommends an efficient way to achieve the forward modeling task.

Chapter 3 develops a new algorithm for the simulation of multipole acoustic logging measurements in the presence of cylindrically layered media. The algorithm uses the generalized reflection and transmission matrices method, thereby completing the first goal of the dissertation.

Chapter 4 addresses the second goal of the dissertation. A detailed study is undertaken (a) to simulate the radial distribution of saturation of mud filtrate, (b) to assess mud-filtrate invasion effects on borehole acoustic measurements, and (c) to investigate the suitability of log corrections based on the Biot-Gassmann fluid substitution model.

Chapter 5 focuses on radial profiling of elastic parameters in the near-wellbore region using a local optimization technique. This is the last goal of the dissertation. The algorithm uses the complex-domain-frequency spectra of array full waveform data. A normalization process is applied to eliminate the role played by the acoustic source. A study is performed of the election of frequency on the performance of the inversion algorithm. Sensitivity analyses are conducted to study the impact of inaccurate inputs of borehole parameters, normalizing traces, noises, and model flatness on the inversion results.

Chapter 6 summarizes the algorithms used in forward and inversion modeling of array sonic data in the presence of radially complex near-wellbore invasion profiles. Key findings in the dissertation are also itemized and described in some detail. Further developments, tests, and alternative approaches are recommended for approaching the research problems described in Chapter 1.

Chapter 2: Solution of Elastic Scattering Problems with an Integral Equation Formulation

Integral equation formulations are ideal for borehole logging problems in which the acoustic/elastic scatterer remains fixed while a sensing tool is moved continuously along the axis of the borehole. Approximations such as Born and extended Born can be derived and evaluated for efficient simulation of logging measurements. Integral equation formulations are also an ideal quantitative tool to approach the more difficult inverse problem of estimating spatial distributions of elastic properties from full waveform acoustic measurements of wave propagation.

In this chapter, the method of moments (MoM), Born, and extended Born approximations are introduced for solving elastic scattering problems in the frequency domain. The formulations are tested and validated against the benchmark problem of scattering from a circular elastic cylinder. Accordingly, an infinitely long line source is embedded in an elastic, homogeneous, and isotropic background. The axis of symmetry of the infinitely long elastic cylinder is assumed parallel to the strike of the line source. A discussion is presented on the technical problem of selecting a suitable Green's tensor when applying the developed formulations to simulate wave propagation in boreholes.

For spatial variations of density and Lamé constants, the MoM yields accurate displacement as compared to the analytical solution. The Born and extended Born approximations yield results that are comparable to those of the MoM in several of the cases studied, and they can be orders of magnitude faster than the MoM. For the same cases, the extended Born approximation provides more accurate results than those of the Born approximation, and it is more efficient than a rigorous MoM formulation.

The MoM is appropriate for solving small-scale elastic scattering problems with coupled compressional and shear wave propagation. On the other hand, the extended Born approximation remains as fast as the Born approximation and more accurate for elastic scattering problems. A Green's tensor defined for a model with a borehole penetrating radially multilayered rock formation makes it efficient for simulation of wave propagation in fluid-filled boreholes exhibiting mud-filtrate invasion zones.

2.1 INTRODUCTION

Numerical simulation of wave propagation in boreholes provides insight to the effects of borehole environments, formation stress and anisotropy, and logging tools on the measured full waveforms. Time domain finite-difference methods have been proved to be powerful and versatile tools for simulating acoustic measurements under these conditions (Yoon and McMechan, 1992, Cheng et al., 1995, and Liu and Sinha, 2000). To represent the borehole and to model the logging tool with acceptable accuracy, a fine finite-difference grid must be used in space. Furthermore, the finite-difference grid needs to extend far enough in the radial direction into the formation to keep the simulated waveforms from being contaminated by reflected waves at the outer boundary of the grid. These requirements make it difficult for finite-difference methods to investigate elastic wave propagation in the vast volume of surrounding rock formations far from the boreholes. A stretched grid formulation that uses variable grid steps has been developed to overcome this problem (Huang, 2003). Despite all these efforts, finite-difference simulation methods are still time-consuming and are not amenable to approach the more difficult inverse problem of estimating spatial distributions of elastic properties from full waveform acoustic logging measurements.

Integral equation methods have been widely used in simulation of electromagnetic wave propagation in heterogeneous media, (Harrington, 1968). The standard method of moments (Harrington, 1968) for solving scattering problems by integral equation formulations requires large memory storage and expensive computation time for inverting complex full matrices. This has promoted the development of faster algorithms and approximate solutions. In the area of electric logging, Gao (2002) developed a fast and efficient full wave modeling algorithm that made use of the shift-invariant property of the Green's tensor in regular grids and of the multiplication of a Toeplitz matrix by a vector with a Fast Fourier Transform (FFT).

Approximations to integral equation formulations have been developed to overcome the difficulties associated with the MoM. The Born approximation (Born, 1933) is routinely used in solving large-scale electromagnetic (EM) scattering problems in arbitrarily heterogeneous media. Other approximations to integral equation formulations, such as extended Born (Habashy et al., 1993, Torres-Verdín and Habashy, 1994) and Quasi-Linear (Zhadnov and Fang, 1996), have been developed to improve the efficiency of computation in the EM domain. A new approximation making use of the smoothness property of EM scattering current (Gao et al., 2003) has been developed to simulate the EM logging responses in dipping and anisotropic formations. The method is more than 10 times faster than a finite-difference algorithm (Gao, 2003, personal communication).

In acoustic/elastic wave scattering problems, many references can be found that solely address the simulation of acoustic wave propagation (e.g., Shi and Shirahatti, 1996, Xu and Liu, 2001, Hyde, 2003). This type of problem can be solved by borrowing from the techniques developed in EM domain. However, elastic wave propagation in bounded media involves coupled compressional- and shear- waves. In terms of the displacement vector, the integral equation for elastic wave scattering problems involves derivatives of the displacement in the integrand (Ayme-Bellegarda and Habashy, 1992). This makes the solution by way of integral equations extremely challenging.

The central part of this chapter is the formulation and numerical solution of integral equations for elastic wave propagation in a homogeneous, isotropic elastic medium with a cylindrical inclusion. Integral equation formulations are developed in the frequency domain and the corresponding simulations are compared against the analytical solution (detailed in Appendix A) for a benchmark canonical problem. In addition, based on the integral equation formulation, Born and extended Born approximations are derived and evaluated against an accurate MoM solution. Both approximations considerably increase the efficiency and speed of computation of the elastic response. The chapter ends with a discussion on one way to apply the integral equation method for the simulation of wave propagation phenomena in fluid-filled boreholes.

2.2 AN INTEGRAL EQUATION FORMULATION

Consider a Cartesian coordinate frame for which a given location, $\overline{r}$, is expressed in terms of the unit vectors $\hat{x}$, $\hat{y}$, and $\hat{z}$ in the x, y, and z directions, respectively; i.e., $\overline{r} = x\hat{x} + y\hat{y} + z\hat{z}$.

Assume a source consisting of a monochromatic force $\overline{f}$ giving rise to a vector displacement vector $\overline{u}$. In the frequency domain, the equation of motion for the displacement $\overline{u}$ in a linear, elastic, isotropic and inhomogeneous medium is given by a differential wave equation (Ayme-Bellegarda and Habashy, 1992)

$$\omega^2 \rho \overline{u} + (\lambda + 2\mu)\nabla\left(\nabla \cdot \overline{u}\right) - \mu \nabla \times \nabla \times \overline{u} + (\nabla\lambda)\nabla \cdot \overline{u} + (\nabla\mu) \cdot \overline{\overline{S}} = -\overline{f}, \qquad (2.1)$$

where

$$\overline{\overline{S}} = \nabla\overline{u} + \left(\nabla\overline{u}\right)^T ,$$

$$\rho\left(\overline{r}\right) = \rho_b\left(\overline{r}\right) + \delta\rho\left(\overline{r}\right), \tag{2.2}$$

$$\lambda\left(\overline{r}\right) = \lambda_b\left(\overline{r}\right) + \delta\lambda\left(\overline{r}\right), \tag{2.3}$$

and

$$\mu\left(\overline{r}\right) = \mu_b\left(\overline{r}\right) + \delta\mu\left(\overline{r}\right). \tag{2.4}$$

Here, ρ, λ, and μ are the density and Lamé constants of the scatterer, ρ_b, λ_b, and μ_b are the density and Lamé constants of a background medium, $\delta\rho$, $\delta\lambda$, and $\delta\mu$ are the differences between the density and Lamé constants of the scatterer and the background medium, and ω is the angular frequency.

Substitution of equations (2.2) through (2.4) into equation (2.1) gives

$$\begin{aligned}&\omega^2\rho_b\overline{u} + (\lambda_b + 2\mu_b)\nabla\left(\nabla\cdot\overline{u}\right) - \mu_b\nabla\times\nabla\times\overline{u} + (\nabla\lambda_b)\nabla\cdot\overline{u} + (\nabla\mu_b)\cdot\overline{\overline{S}}\\ &= -\overline{f} - \overline{f_s},\end{aligned} \tag{2.5}$$

where

$$\overline{f_s} = \omega^2\delta\rho\overline{u} + (\delta\lambda + 2\delta\mu)\nabla\left(\nabla\cdot\overline{u}\right) - \delta\mu\nabla\times\nabla\times\overline{u} + (\nabla\delta\lambda)\nabla\cdot\overline{u} + (\nabla\delta\mu)\cdot\overline{\overline{S}} . \tag{2.6}$$

In compact form, equation (2.6) can be rewritten as

$$\overline{f_s} = \omega^2\delta\rho\overline{u} + \nabla\left(\delta\lambda\nabla\cdot\overline{u}\right) + \nabla\cdot\left(\delta\mu\overline{\overline{S}}\right). \tag{2.7}$$

To cast equation (2.5) into an integral equation, a Green’s tensor is introduced for a homogeneous, isotropic, unbounded, elastic solid in the form of

$$\overline{\overline{G}}\left(\overline{r},\overline{r_0}\right) = \frac{1}{\omega^2\rho_b}\left[-\nabla\nabla\,\mathrm{g}_C\left(\left|\overline{r}-\overline{r_0}\right|\right) + \left(\kappa_{sb}^2\overline{\overline{I}} + \nabla\nabla\right)\mathrm{g}_S\left(\left|\overline{r}-\overline{r_0}\right|\right)\right], \tag{2.8}$$

where

$$\mathrm{g}_C\left(\left|\bar{r}-\bar{r}_0\right|\right)=\frac{\mathrm{e}^{ik_{cb}\left|\bar{r}-\bar{r}_0\right|}}{4\pi\left|\bar{r}-\bar{r}_0\right|}, \tag{2.9}$$

with $\kappa_{\boldsymbol{cb}}^2=\dfrac{\omega^2\rho_{\boldsymbol{b}}}{\lambda_{\boldsymbol{b}}+2\mu_{\boldsymbol{b}}}$,

and

$$\mathrm{g}_S\left(\left|\bar{r}-\bar{r}_0\right|\right)=\frac{\mathrm{e}^{ik_{sb}\left|\bar{r}-\bar{r}_0\right|}}{4\pi\left|\bar{r}-\bar{r}_0\right|}, \tag{2.10}$$

with $k_{sb}^2=\dfrac{\omega^2\rho_b}{\mu_b}$. Here, k_{cb} and k_{sb} are the compressional and shear wavenumbers of the background medium, respectively, $\overline{\overline{I}}$ is the unity tensor, and $\bar{r}$ and $\bar{r}_0$ are the field and source points, respectively. The functions $g_{\boldsymbol{c}}$ and $g_{\boldsymbol{S}}$ are scalar Green's functions for compressional and shear waves, respectively, when the source is a delta impulse. These functions are solutions of the scalar Helmholtz equations (Kong, 1990)

$$\nabla^2\mathrm{g}_C(\bar{r},\bar{r}_0)+\kappa_{cb}^2\mathrm{g}_C(\bar{r},\bar{r}_0)=-\delta(\bar{r}-\bar{r}_0), \tag{2.11}$$

and

$$\nabla^2\mathrm{g}_S(\bar{r},\bar{r}_0)+\kappa_{sb}^2\mathrm{g}_S(\bar{r},\bar{r}_0)=-\delta(\bar{r}-\bar{r}_0). \tag{2.12}$$

The Green's tensor satisfies the following differential equation

$$\begin{aligned}\omega^2\rho_b\overline{\overline{G}}+(\lambda_b+2\mu_b)\nabla\left(\nabla\cdot\overline{\overline{G}}\right)-\mu_b\nabla\times\nabla\times\overline{\overline{G}}+(\nabla\lambda_b)\nabla\cdot\overline{\overline{G}}+(\nabla\mu_b)\cdot\overline{\overline{\Gamma}}\\=-\overline{\overline{\mathrm{I}}}\delta\left(\bar{r}-\bar{r}_0\right),\end{aligned} \tag{2.13}$$

where

$$\overline{\overline{\Gamma}}=\nabla\overline{\overline{G}}+\left(\overline{\overline{G}}\right)^T,$$

and $\delta\left(\bar{r}-\bar{r}_0\right)$ is the Dirac delta function.

The vector $\overline{u}_b(\overline{r})$ is defined as the displacement in a homogeneous and unbounded background. Starting from equations (2.5) and (2.13) and making use of Green's theorem with the radiation condition imposed at infinity, one reaches an integral representation form (Habashy et al., 1994) for $\overline{u}(\overline{r})$, namely,

$$\overline{u}(\overline{r}) = \overline{u_b}(\overline{r}) + \int_\tau \mathrm{d}\overline{r}_0 \,\overline{\overline{G}}(\overline{r},\overline{r}_0)\cdot \overline{f_s}(\overline{r}_0), \tag{2.14}$$

where τ is the spatial support of the scatterer. Equation (2.14) is a Fredholm integral equation of the second kind. This representation for displacement is valid everywhere in space, inside the scatterer as well as outside.

2.3 INTEGRAL EQUATION FORMULATION FOR SPATIAL VARIATIONS OF DENSITY

In this section, the case in which $\delta\lambda$ and $\delta\mu$ are zero is considered as an example of a solution. In other words, only density contrasts exist between the scatterer and the background medium. For this perturbation case, equation (2.14) for the displacement vector can be simplified to

$$\overline{u}(\overline{r}) = \overline{u_b}(\overline{r}) + \int_\tau \omega^2 \delta\rho \overline{\overline{G}}(\overline{r},\overline{r}_0)\cdot \overline{u}(\overline{r}_0)\, d\overline{r}_0 \,. \tag{2.15}$$

2.3.1 Method of Moments (MoM) Formulation

To solve for the displacement $\overline{u}(\overline{r})$, the scatterer region is first divided into N small cells such that the wavefield internal to each cell can be regarded as constant. By assuming that $\delta\rho$ is also uniform within each cell, equation (2.15) can be rewritten as

$$\overline{u}(\overline{r}) = \overline{u_b}(\overline{r}) + \omega^2 \sum_{i=1}^{N} \delta\rho_i \int_{\tau_i} \mathrm{d}\overline{r}_0 \,\overline{\overline{G}}(\overline{r},\overline{r}_0)\cdot \overline{u}_i(\overline{r}_0) \,. \tag{2.16}$$

Let $\bar{r}_j$ be the center of the j-th cell, and j =1, 2, …, N. By assuming that $\bar{u}_j(\bar{r})$ is constant within each cell [indicating $\bar{u}_j(\bar{r}) = \bar{u}_j(\bar{r}_j)$] and by making use of equation (2.16), the displacement in the j-th cell can be written as

$$\bar{u}_j(\bar{r}_j) = \overline{u_{bj}}(\bar{r}_j) + \omega^2 \sum_{i=1}^{N} \delta\rho_i \left[\int_{\tau_i} \mathrm{d}\bar{r}_0\, \bar{\bar{G}}(\bar{r}_j, \bar{r}_0) \right] \cdot \bar{u}_i(\bar{r}_i), \text{ j=1, 2, …, N.} \tag{2.17}$$

By making use of the Kronecker product notation, equation (2.17) can be expressed as

$$\left[\bar{\bar{I}}\delta_{ij} - \omega^2 \sum_{i=1}^{N} \delta\rho_i \left[\int_{\tau_i} \bar{\bar{G}}(\bar{r}_j, \bar{r}_0) \mathrm{d}\bar{r}_0 \right] \right] \cdot \overline{u_i}(\bar{r}_i) = \bar{u}_{bj}(\bar{r}_j). \tag{2.18}$$

This last equation can be written in compact matrix notation as

$$AX = B, \tag{2.19}$$

where

$$A = \begin{bmatrix} \bar{\bar{I}} - \omega^2 \delta\rho_1 \int_{\tau_1} \bar{\bar{G}}(\bar{r}_1, \bar{r}_0) \mathrm{d}\bar{r}_0 & \cdots & -\omega^2 \delta\rho_N \int_{\tau_N} \bar{\bar{G}}(\bar{r}_1, \bar{r}_0) \mathrm{d}\bar{r}_0 \\ -\omega^2 \delta\rho_1 \int_{\tau_2} \bar{\bar{G}}(\bar{r}_2, \bar{r}_0) \mathrm{d}\bar{r}_0 & \cdots & -\omega^2 \delta\rho_N \int_{\tau_N} \bar{\bar{G}}(\bar{r}_2, \bar{r}_0) \mathrm{d}\bar{r} \\ \cdots & \cdots & \cdots \\ -\omega^2 \delta\rho_1 \int_{\tau_1} \bar{\bar{G}}(\bar{r}_N, \bar{r}_0) \mathrm{d}\bar{r}_0 & \cdots & \bar{\bar{I}} - \omega^2 \delta\rho_N \int_{\tau_N} \bar{\bar{G}}(\bar{r}_N, \bar{r}_0) \mathrm{d}\bar{r}_0 \end{bmatrix},$$

$$X = \begin{bmatrix} \bar{\mathrm{u}}_1(\bar{r}_1) \\ \bar{\mathrm{u}}_2(\bar{r}_2) \\ \cdots \\ \bar{\mathrm{u}}_{\mathrm{N}}(\bar{r}_N) \end{bmatrix}, \text{ and } B = \begin{bmatrix} \bar{\mathrm{u}}_{b1}(\bar{r}_1) \\ \bar{\mathrm{u}}_{b2}(\bar{r}_2) \\ \cdots \\ \bar{\mathrm{u}}_{bN}(\bar{r}_N) \end{bmatrix}.$$

Consider a two-dimensional (2-D) rectangular cell whose sides are parallel to the x, and z directions. For this particular case, the entries of vectors *X* and *B* are given by

$$x_j = \begin{bmatrix} u_{jx} \\ u_{jz} \end{bmatrix}, \text{ and } b_j = \begin{bmatrix} u_{bjx} \\ u_{bjz} \end{bmatrix}.$$

Appendix B provides explicit formulae for the numerical integration of the dyadic Green's tensor for a 2-D rectangular cell. By solving the linear system represented by equation (2.19), a solution is obtained for the displacement vector inside each discretization cell within the scatterer. Subsequently, by making use of equation (2.17), the displacement vector outside the scatterer is computed, where $\bar{r}_j$ is the location of the j-th receiver.

2.3.2 Born Approximation

Many practical applications make use of the Born and Rytov approximations (Habashy et al., 1993). These first-order approximations assume that the scattered fields inside scatterers are negligible compared to the internal elastic background wavefield. The Born approximation is obtained by replacing the total displacement vector inside the integrand on the right hand side of equation (2.15) with the incident field. It is written as

$$\bar{u}(\bar{r}) = \bar{u}_b(\bar{r}) + \int_\tau \omega^2 \delta\rho \overline{\overline{G}}(\bar{r},\bar{r}_0)\cdot\bar{u}_b(\bar{r}_0)\, d\bar{r}_0 \,. \tag{2.20}$$

An explicit form that can be readily used for computation of displacement outside the scatterer can be obtained from equation (2.17).

2.3.3 Extended Born Approximation

The Born approximation is much faster and requires far less memory storage than the MoM. However, it remains accurate only for small perturbations in medium properties. To deal with large density contrasts and scatterer dimensions, iterative schemes, such as iterative Born and iterative distorted Born, have been developed to further refine the Born approximation. In these procedures, the internal wavefield is updated in progressive linear steps (Habashy and Mittra, 1987). A nonlinear elastic scattering approximation under the name of “extended Born approximation” was introduced by Habashy et al. (1994). They derived a source-independent scattering tensor from the spatial density distribution. The scattering tensor operates on the background wavefield to produce the desired approximation to the internal wavefield. For the purpose of clarity, this section provides a detailed derivation of the extended Born approximation specialized for elastic scattering problems. The derivation closely follows that of the extended Born approximation specialized for EM scattering problems (Torres-Verdín and Habashy, 1994).

First consider the approximation to the integral equation for the displacement vector inside the scatterer. The integral equation (2.15) is valid inside the scatterer. By introducing the total displacement into the integrand on the right hand side of equation (2.15), one can write

$$\begin{aligned}\overline{u}(\overline{r}) = \overline{u}_b(\overline{r}) &+ \int_\tau \omega^2 \delta\rho \overline{\overline{G}}(\overline{r},\overline{r}_0)\, d\overline{r}_0 \cdot \overline{u}(\overline{r}) \\ &+ \int_\tau \omega^2 \delta\rho \overline{\overline{G}}(\overline{r},\overline{r}_0)\, d\overline{r}_0 \cdot \left[\overline{u}(\overline{r}_0) - \overline{u}(\overline{r})\right]. \end{aligned} \tag{2.21}$$

Because the contributions of $\overline{u}(\overline{r})$ in the last two terms of equation (2.21) cancel out, equations (2.15) and (2.21) are equivalent. After some algebraic manipulation, equation (2.21) can be expressed as

$$\overline{u}(\overline{r}) = \overline{\overline{\Gamma}}(\overline{r}) \cdot \left[\overline{u}_b(\overline{r}) + \int_\tau \omega^2 \delta\rho \overline{\overline{G}}(\overline{r},\overline{r}_0) \cdot \left[\overline{u}(\overline{r}_0) - \overline{u}(\overline{r})\right] d\overline{r}_0\right], \tag{2.22}$$

with the tensor $\overline{\overline{\Gamma}}(\overline{r})$ given by

$$\overline{\overline{\Gamma}}(\overline{r}) = \left\{\overline{\overline{I}} - \int_\tau d\overline{r}_0 \frac{\delta\rho}{\rho_b}\left[-\nabla\nabla\, \mathrm{g}_C\left(\left|\overline{r} - \overline{r}_0\right|\right) + \left(\kappa_{sb}^2 \overline{\overline{I}} + \nabla\nabla\right) \mathrm{g}_S\left(\left|\overline{r} - \overline{r}_0\right|\right)\right]\right\}^{-1}. \tag{2.23}$$

As $\overline{r}_0$ approaches $\overline{r}$, the difference between $\overline{u}(\overline{r})$ and $\overline{u}(\overline{r}_0)$ becomes zero. Then the integral in equation (2.22) can be dropped even though the Green's tensor $\overline{\overline{G}}(\overline{r},\overline{r}_0)$ is singular at $\overline{r}_0 = \overline{r}$ in 2-D and 3-D media. Therefore, equation (2.15) can be approximated by

$$\overline{u}(\overline{r}) \approx \overline{\overline{\Gamma}}(\overline{r}) \cdot \overline{u}_b(\overline{r}),\ \forall \overline{r} \in \tau . \tag{2.24}$$

and this last expression is called the extended Born approximation. To better understand the assumptions made in deriving the above approximation, the displacement vector is written in a Taylor series expansion about $\overline{r}_0 = \overline{r}$, namely,

$$\overline{u}(\overline{r}_0) = \overline{u}(\overline{r}) + (\overline{r}_0 - \overline{r}) \cdot \nabla \overline{u}(\overline{r}_0 = \overline{r}) + O\left(\left| \overline{r}_0 - \overline{r} \right|^2 \right). \tag{2.25}$$

It becomes evident then that when the gradient or higher-order variations of the displacement vector are small, the approximation to the internal displacement vector will remain accurate.

Substituting equation (2.24) into equation (2.15) yields the nonlinear approximation for the displacement vector outside the support of density variation, namely,

$$\overline{u}(\overline{r}) = \overline{u_b}(\overline{r}) + \int_\tau \omega^2 \delta\rho \overline{\overline{G}}(\overline{r},\overline{r}_0) \cdot \overline{\overline{\Gamma}}(\overline{r}_0) \cdot \overline{u}_b(\overline{r}_0)\, d\overline{r}_0, \forall \overline{r} \notin \tau . \tag{2.26}$$

2.3.4 Benchmark Example

The geometrical configuration of the benchmark problem is shown in Figure 2.1. A dilatational line source excites only compressional waves. The strike of the elastic circular cylinder acting as a scatterer is aligned with the y axis. Because an analytical solution to this problem exists, the example serves as a good benchmark for the validity and accuracy of the MoM and the Born and extended Born approximations. Appendix A provides a derivation of the analytical solution for this scattering problem

For the assumed problem, the background elastic wavefield can be written as

$$\bar{u}_b(\bar{\rho},\bar{\rho}_s)=u_b(\bar{\rho},\bar{\rho}_s)\frac{\bar{\rho}-\bar{\rho}_s}{|\bar{\rho}-\bar{\rho}_s|}, \tag{2.27}$$

where

$$u_b(\bar{\rho},\bar{\rho}_s)=-\frac{i}{4}f_T\frac{k_{cb}^3}{\omega^2}H_1^{(1)}\left(k_{cb}|\bar{\rho}-\bar{\rho}_s|\right), \tag{2.28}$$

$$\bar{\rho}_s=x_s\hat{x}+z_s\hat{z},$$

and

$$\bar{\rho}=x\hat{x}+z\hat{z}.$$

Here, f_T is the strength of the line source, i is the imaginary unit ($\sqrt{-1}$), and $H_1^{(1)}$ is the Hankel function of the first kind and order 1.

The expressions necessary to compute the internal field using the extended Born approximation are given by

$$u_x^{\text{int}}(\bar{\rho},\bar{\rho}_s)\approx u_b(\bar{\rho},\bar{\rho}_s)\left[\frac{x-x_s}{|\bar{\rho}-\bar{\rho}_s|}\Gamma_{xx}(\bar{\rho})+\frac{z-z_s}{|\bar{\rho}-\bar{\rho}_s|}\Gamma_{xz}(\bar{\rho})\right], \tag{2.29}$$

and

$$u_z^{\text{int}}(\bar{\rho},\bar{\rho}_s)\approx u_b(\bar{\rho},\bar{\rho}_s)\left[\frac{x-x_s}{|\bar{\rho}-\bar{\rho}_s|}\Gamma_{xz}(\bar{\rho})+\frac{z-z_s}{|\bar{\rho}-\bar{\rho}_s|}\Gamma_{zz}(\bar{\rho})\right], \tag{2.30}$$

where the superscript “int” indicates internal field,. Γ_{xx}, Γ_{xz}, and Γ_{zz} are the components of the scattering tensor defined by equation (2.23) and their explicit expressions are given by Habashy et al. (1994).

The scattered displacement is then given by

$$\Delta u_x(\overline{\rho}, \overline{\rho}_s) \approx \sum_{i=1}^{N} \frac{\delta\rho_i}{\rho_b} \int_{\tau_i} \left[G_{xx}(\overline{\rho}, \overline{\rho}_0) u_x^{\text{int}}(\overline{\rho}_0, \overline{\rho}_s) + G_{xx}(\overline{\rho}, \overline{\rho}_0) u_z^{\text{int}}(\overline{\rho}_0, \overline{\rho}_s) \right] d\overline{\rho}_0 , \tag{2.31}$$

and

$$\Delta u_z(\overline{\rho}, \overline{\rho}_s) \approx \sum_{i=1}^{N} \frac{\delta\rho_i}{\rho_b} \int_{\tau_i} \left[G_{xz}(\overline{\rho}, \overline{\rho}_0) u_x^{\text{int}}(\overline{\rho}_0, \overline{\rho}_s) + G_{zz}(\overline{\rho}, \overline{\rho}_0) u_z^{\text{int}}(\overline{\rho}_0, \overline{\rho}_s) \right] d\overline{\rho}_0 , \tag{2.32}$$

where N is the number of cells used to discretize the scattering cylinder, and G_{xx}, G_{xz}, and G_{zz} are the three components of the Green's tensor $\overline{\overline{G}}$, given by Habashy et al. (1994).

For the Born approximation, the internal displacement is simply the background field. The scattered displacement can be obtained by replacing the internal field in equations (2.31) and (2.32) with the corresponding expressions for the background field.

As described in Figure 2.1, the radius of the scatterer is 0.15 m, and the number of discritization cells is 10 and 20 in the radial and azimuthal directions, respectively. Figure 2.2 shows that the MoM produces results that coincide with those of the analytical solution. On the other hand, the extended Born approximation yields results close to those of the analytical solution for the real parts in the x and z directions and for the imaginary part in the x direction. For the imaginary part in the z direction, both Born and extended Born approximations yield the same results and remain close to those obtained with the analytical solution.

Figure 2.3 shows that when the scatterer radius is reduced from 0.15 m to 0.05 m, the Born approximation results become much closer to those of the analytical solution. For sources operating at frequencies in the range from 1 kHz to 10 kHz, Figure 2.4 shows that the results of the MoM, the Born and extended Born approximations coincide with those of the analytical solution. Close to 100 kHz, all of the numerical solutions considerably deviate from those of the analytical solution.

It is also well known that the MoM involves the inverting of a full complex matrix and the computational complexity is on the order of O(N^3), where N is the number of cells within the scatterer. On the other hand, the Born and extended Born approximations only involves multiplication of matrices by vectors. The computational complexity of both methods is approximately O(N^2). Therefore, the Born and extended Born approximations are much more efficient than the MoM.

2.4 INTEGRAL EQUATION FORMULATION FOR SPATIAL VARIATIONS OF λ

For the case in which $\delta\lambda$ is not zero within the scatterer, the equation for the vector displacement (2.14) can be rewritten as

$$\bar{u}(\bar{r}) = \bar{u}_b(\bar{r}) + \int_\tau d\bar{r}_0 \bar{\bar{G}}(\bar{r},\bar{r}_0)\cdot\left[\nabla\left(\delta\lambda\nabla\cdot\bar{u}(\bar{r}_0)\right)\right]. \tag{2.33}$$

Notice that in equation (2.33), gradient and divergence operations are with respect to the integral variable $\bar{r}_0$. It then follows that

$$\bar{u}_s(\bar{r}) = \int_\tau d\bar{r}_0 \bar{\bar{G}}(\bar{r},\bar{r}_0)\cdot\left[\nabla_0\left(\delta\lambda\nabla_0\cdot\bar{u}(\bar{r}_0)\right)\right]. \tag{2.34}$$

To simplify equation (2.34) into a form that is more suitable for numerical simulation, a new variable, p, is defined as

$$p(\bar{r}_0) = \delta\lambda\left[\nabla_0\cdot\bar{u}(\bar{r}_0)\right]. \tag{2.35}$$

By making use of the relation

$$\nabla_0\cdot\left(p\bar{\bar{G}}\right) = p\nabla_0\cdot\bar{\bar{G}} + \nabla_0 p\cdot\bar{\bar{G}}, \tag{2.36}$$

as well as the reciprocity theorem of the Green's tensor, namely,

$$\overline{\overline{G}}^T\left(\bar{r},\overline{r_0}\right)=\overline{\overline{G}}\left(\overline{r_0},\bar{r}\right)=\overline{\overline{G}}\left(\bar{r},\overline{r_0}\right), \tag{2.37}$$

equation (2.34) can be written as

$$\begin{aligned}\bar{u}_s\left(\bar{r}\right)&=\int_\tau d\overline{r_0}\,\overline{\overline{G}}\left(\bar{r},\overline{r_0}\right)\cdot\left[\nabla_0 p\left(\overline{r_0}\right)\right]\\ &=\int_\tau d\overline{r_0}\left[\nabla_0 p\left(\overline{r_0}\right)\right]\cdot\overline{\overline{G}}^T\left(\bar{r},\overline{r_0}\right)\\ &=\int_\tau d\overline{r_0}\left[\nabla_0 p\left(\overline{r_0}\right)\right]\cdot\overline{\overline{G}}\left(\bar{r},\overline{r_0}\right)\\ &=\int_\tau d\overline{r_0}\left[\nabla_0\cdot\left(p\left(\overline{r_0}\right)\overline{\overline{G}}\left(\bar{r},\overline{r_0}\right)\right)-p\left(\overline{r_0}\right)\nabla_0\cdot\overline{\overline{G}}\left(\bar{r},\overline{r_0}\right)\right].\end{aligned} \tag{2.38}$$

By recalling Stokes' theorem, one has

$$\begin{aligned}\int_\tau d\overline{r_0}\nabla_0\cdot\left(p\left(\overline{r_0}\right)\overline{\overline{G}}\left(\bar{r},\overline{r_0}\right)\right)&=\int_{\partial\tau}p\left(\overline{r_0}\right)\left[\bar{n}\cdot\overline{\overline{G}}\left(\bar{r},\overline{r_0}\right)\right]dA\\ &=\int_{\partial\tau}\delta\lambda\left(\nabla_0\cdot\bar{u}\right)\left[\bar{n}\cdot\overline{\overline{G}}\left(\bar{r},\overline{r_0}\right)\right]dA,\end{aligned} \tag{2.39}$$

where $\partial\tau$ is the outer surface of the scatterer.

On the surface of the scatterer, by definition (Ayme-Bellegarda and Habashy, 1992) $\delta\lambda=\delta\mu=0$. Consequently,

$$\int_\tau d\overline{r_0}\nabla_0\cdot\left[p\left(\overline{r_0}\right)\overline{\overline{G}}\left(\bar{r},\overline{r_0}\right)\right]=\int_{\partial\tau}\delta\lambda\left(\nabla_0\cdot\bar{u}\right)\left[\bar{n}\cdot\overline{\overline{G}}\left(\bar{r},\overline{r_0}\right)\right]dA=0, \tag{2.40}$$

and

$$\bar{u}_s\left(\bar{r}\right)=-\int_\tau d\overline{r_0}\,\delta\lambda\nabla_0\cdot\overline{\overline{G}}\left(\bar{r},\overline{r_0}\right)\left[\nabla_0\cdot\bar{u}\left(\overline{r_0}\right)\right]. \tag{2.41}$$

By enforcing the relationship $\nabla F\left(r\right)=-\nabla_0 F\left(r\right)$ to equation (2.41), the total displacement can be written as

$$\bar{u}\left(\bar{r}\right)=\bar{u}_b\left(\bar{r}\right)-\int_\tau d\overline{r_0}\,\delta\lambda\nabla_0\cdot\overline{\overline{G}}\left(\bar{r},\overline{r_0}\right)\left[\nabla_0\cdot\bar{u}\left(\overline{r_0}\right)\right]. \tag{2.42}$$

2.4.1 Method of Moments (MoM) Formulation

For the numerical solution of equation (2.42), the scatterer is discretized into small cells, in which the displacement vector is assumed constant within each cell. Explicit formulations are developed in the following section for computing the elastic wavefield.

To compute the displacement vector when only $\delta\lambda$ is not zero, the divergence of the internal displacement inside the scatterer must be computed via equation (2.42). By applying the divergence operator on both sides of the integral wave equation with respect to a field point, $\bar{r}$, one obtains

$$\begin{aligned}\nabla\cdot\bar{u}(\bar{r}) &= \nabla\cdot\bar{u}_b(\bar{r}) - \nabla\cdot\int_\tau \delta\lambda\, d\bar{r}_0 \nabla_0\cdot\bar{\bar{G}}(\bar{r},\bar{r}_0)\left[\nabla_0\cdot\bar{u}(\bar{r}_0)\right] \\ &= \nabla\cdot\bar{u}_b(\bar{r}) - \int_\tau \delta\lambda\, d\bar{r}_0 \left\{\nabla\cdot\nabla_0\cdot\bar{\bar{G}}(\bar{r},\bar{r}_0)\right\}\left[\nabla_0\cdot\bar{u}(\bar{r}_0)\right].\end{aligned} \tag{2.43}$$

Substitution of $\nabla\cdot F(R) = -\nabla_0\cdot F(R)$ into equation (2.43) yields

$$\nabla\cdot\bar{u}(\bar{r}) = \nabla\cdot\bar{u}_b(\bar{r}) + \nabla\cdot\nabla\cdot\int_\tau \delta\lambda\, d\bar{r}_0 \bar{\bar{G}}(\bar{r},\bar{r}_0)\left(\nabla_0\cdot\bar{u}(\bar{r}_0)\right). \tag{2.44}$$

The divergence of the displacement, $\nabla\cdot\bar{u}$, can then be solved using the MoM. Accordingly, the discretized form of equation (2.44) becomes

$$\begin{aligned}\nabla\cdot\bar{u}_j &= \nabla\cdot\bar{u}_{bj} + \sum_{i=1}^{N}\delta\lambda_i \nabla\cdot\nabla\cdot\int_{\tau_i} d\bar{r}_0 \bar{\bar{G}}(\bar{r}_j,\bar{r}_0)\left(\nabla\cdot\bar{u}_i\right) \\ &= \nabla\cdot\bar{u}_{bj} + \sum_{i=1}^{N}\delta\lambda_i\left(\nabla\cdot\bar{q}_{ij}\right)\left(\nabla\cdot\bar{u}_i\right) \qquad ,\end{aligned} \tag{2.45}$$

where

$$\bar{q}_{ij} = \nabla\cdot\int_{\tau_i} d\bar{r}_0 \bar{\bar{G}}(\bar{r}_j,\bar{r}_0), \tag{2.46}$$

and j=1, 2, …N.

Technical details of the formulation for computing the divergence of the background field are given in Appendix C. Analytical formulations for the divergence of the volume integral of the Green's tensor over a circle and for its divergence are given in Appendix D. These expressions can be used to approximate those of a rectangular cell by making use of an equivalent radius (Torres-Verdín and Habashy, 1994).

Equation (2.45) can be rewritten as a linear system of equations

$$\sum_{i=1}^{N}\left(\delta_{ij} - \delta\lambda_i \nabla\cdot\overline{q}_{ij}\right)\left(\nabla\cdot\overline{u}_i\right) = \nabla\cdot\overline{u}_{bj}, \tag{2.47}$$

where j = 1, 2, …N. The solution of this linear system provides the divergence of the displacement, $\nabla\cdot\overline{u}$, within each cell of the scatterer. Subsequently, the displacement vector can be computed using the discretized form of equation (2.42), namely,

$$\overline{u}_j\left(\overline{r}_j\right) = \overline{u}_{bj}\left(\overline{r}_j\right) + \sum_{i=1}^{N}\delta\lambda_i\left(\overline{q}_{ij}\right)\left[\nabla\cdot\overline{u}_i\left(\overline{r}_i\right)\right], \tag{2.48}$$

where $\overline{r}_i$ is the center of the i-th cell, and $\overline{r}_j$ is the location of the j-th receiver.

2.4.2 Born Approximation

Replacing the internal field in equation (2.42) with the background field to yields the Born approximation for the total field, i.e.,

$$\overline{u}\left(\overline{r}\right) = \overline{u}_b\left(\overline{r}\right) - \int_{\tau} d\overline{r}_0\,\delta\lambda\nabla_0\cdot\overline{\overline{G}}\left(\overline{r},\overline{r}_0\right)\left(\nabla_0\cdot\overline{u}_b\left(\overline{r}_0\right)\right). \tag{2.49}$$

For the benchmark problem, substitution of the analytic formulation of the background field in Appendix C and the divergence of the Green's tensor in Appendix D into equation (2.49), yields the Born formulation for the total wavefield in the discretized form, namely,

$$\bar{u} = \bar{u}_b - \frac{\pi f_T k_{cb}^6}{8\omega^2}\sum_{i=1}^{N}\delta\lambda_i \left\{ H_1^{(1)}(k_{cb}R_i)J_1(k_{cb}a_i)\left[H_0^{(1)}(k_{cb}r_{si}) + \frac{H_1^{(1)}(k_{cb}r_{si})}{k_{cb}r_{si}} \right]\right\}\bar{e}_{Ri}, \quad (2.50)$$

where $R_i = \left|\bar{r} - \bar{r}_i\right|$ is the distance between a receiver and the center of the i-th cell, a_i is the equivalent radius of the i-th cell, $r_{si} = \left|\bar{r}_s - \bar{r}_j\right|$ is the distance between the source and the center of the j-th cell, and $\bar{e}_{Ri}$ is the unit vector pointing from the center of the i-th cell to the receiver.

2.4.3 Extended Born Approximation

Similar to the case of density variations, the extended Born approximation can be obtained by rewriting equation (2.43) as

$$\begin{aligned}\nabla\cdot\bar{u}\left(\bar{r}\right) = \nabla\cdot\bar{u}_b\left(\bar{r}\right) - \int_\tau \delta\lambda\, d\bar{r}_0\left[\nabla\cdot\nabla_0\cdot\bar{\bar{G}}\left(\bar{r},\bar{r}_0\right)\right]\left[\nabla\cdot\bar{u}\left(\bar{r}\right)\right] \\ - \int_\tau \delta\lambda\, d\bar{r}_0\left[\nabla\cdot\nabla_0\cdot\bar{\bar{G}}\left(\bar{r},\bar{r}_0\right)\right]\left[\nabla_0\cdot\bar{u}\left(\bar{r}_0\right) - \nabla\cdot\bar{u}\left(\bar{r}\right)\right].\end{aligned} \quad (2.51)$$

After some algebraic manipulations, equation (2.51) can be rewritten as,

$$\nabla\cdot\bar{u}\left(\bar{r}\right) = \bar{\bar{\Pi}}\left(\bar{r}\right)\cdot\left\{\nabla\cdot\bar{u}_b\left(\bar{r}\right) - \int_\tau \delta\lambda\, d\bar{r}_0\left[\nabla\cdot\nabla_0\cdot\bar{\bar{G}}\left(\bar{r},\bar{r}_0\right)\right]\left[\nabla_0\cdot\bar{u}\left(\bar{r}_0\right) - \nabla\cdot\bar{u}\left(\bar{r}\right)\right]\right\},$$

(2.52)

where the tensor $\bar{\bar{\Pi}}\left(\bar{r}\right)$ is given by

$$\bar{\bar{\Pi}}\left(\bar{r}\right) = \left\{\bar{\bar{I}} - \int_\tau \delta\lambda d\bar{r}_0\left[\nabla\cdot\nabla_0\cdot\bar{\bar{G}}\left(\bar{r},\bar{r}_0\right)\right]\right\}^{-1}. \quad (2.53)$$

If the divergence of the internal displacement vector can be accurately approximated by the first term in its Taylor series expansion about $\bar{r}_0 = \bar{r}$, equation (2.52) can be approximated by

$$\nabla\cdot\bar{u}\left(\bar{r}\right) \approx \bar{\bar{\Pi}}\left(\bar{r}\right)\cdot\left[\nabla\cdot\bar{u}_b\left(\bar{r}\right)\right],\ \forall\bar{r}\in\tau. \quad (2.54)$$

The accuracy of this last approximation depends on two assumptions made in the derivation: one is that $\nabla \cdot \nabla \cdot \overline{\overline{G}}(\overline{r}, \overline{r}_0)$ falls off sufficiently fast as $\overline{r}_0$ moves away from $\overline{r}$; the second is that the variations in the divergence of the internal displacement vector $\nabla \cdot \overline{u}(\overline{r})$ from its approximations at $\overline{r}$ are small (Torres-Verdín, Habashy, 1994).

The nonlinear approximation for the displacement vector computed outside the support of the density variations is obtained by substituting equation (2.54) into equation (2.42) , i.e.,

$$\overline{u}(\overline{r}) = \overline{u_b}(\overline{r}) - \int_\tau \delta\lambda \nabla_0 \cdot \overline{\overline{G}}(\overline{r}, \overline{r_0}) \cdot \overline{\overline{\Pi}}(\overline{r_0}) \cdot \nabla_0 \cdot \overline{u}_b(\overline{r_0})\, d\overline{r_0}, \forall \overline{r} \notin \tau . \qquad (2.55)$$

2.4.4 Benchmark Example

Solution of the benchmark problem for only $\delta\lambda$ variations is calculated assuming a 1 kHz source. In the first case, Figure 2.5 shows that the real and imaginary parts of the displacement of the scattered field simulated using the MoM completely overlay with those of the analytical solution. This indicates that the MoM yields accurate results. Using a slightly coarser discretization scheme, Figure 2.6 shows that the Born and extended Born approximations yield acceptable results for the x component of the scattered field and give very good results for the z component.

2.5 INTEGRAL EQUATION FORMULATION FOR SPATIAL VARIATIONS OF DENSITY, λ, AND μ VARIATIONS

2.5.1 Elastodynamic Wave Equations in Indicial Notation

In indicial notation, the Lippman-Schwinger equation (Pike and Sabatier, 2002) for elastic waves scattered by a volume inhomogeneity can be rewritten as

$$u_j\left(\bar{r}\right) = u_{bj}\left(\bar{r}\right) + \int_\tau d\bar{r}_0 \left\{\delta\rho\left(\bar{r}_0\right)\omega^2 u_k\left(\bar{r}_0\right) G_{kj}\left(\bar{r}, \overline{r_0}\right) - \delta\Gamma_{iklm}\left(\bar{r}_0\right)\partial'_l u_m\left(\bar{r}_0\right)\partial'_k G_{ij,k}\left(\bar{r}, \overline{r_0}\right)\right\},$$

(2.56)

where

$$\delta\Gamma_{iklm}\left(\bar{r}\right) = \Gamma_{iklm}\left(\bar{r}\right) - \Gamma^0_{iklm}\,, \tag{2.57}$$

$$\rho\left(\bar{r}\right) = \rho_b + \delta\rho\left(\bar{r}\right), \tag{2.58}$$

u_{bj} and u_{bj} are the jth components of the displacement of the background field and total field, respectively, i, j, k, l, and m are integers ranging from one to three for a 3-D scattering problem.

In general, density ρ and elastic parameters Γ_{iklm} are functions of position, whereas Γ^0_{iklm} and ρ_b are constant.

For an isotropic scatterer, one has

$$\delta\Gamma_{iklm}\left(\bar{r}\right) = \delta\lambda\left(\bar{r}\right)\delta_{ik}\delta_{lm} + \delta\mu\left(\bar{r}\right)\left(\delta_{il}\delta_{km} + \delta_{im}\delta_{lk}\right). \tag{2.59}$$

Substitution of equation (2.59) and the identity $\partial = -\partial'$ into the scattering equation (2.56) yields

$$\begin{aligned}
u_j\left(\bar{r}\right) = {} & u_{bj}\left(\bar{r}\right) + \int_\tau d\bar{r}_0 \left\{\omega^2\delta\rho\left(\bar{r}_0\right)u_k\left(\bar{r}_0\right)G_{kj}\left(\bar{r}, \overline{r_0}\right) + \delta\lambda\left(\bar{r}_0\right)\delta_{ik}\delta_{lm}\partial'_l u_m\left(\bar{r}_0\right)\partial_k G_{ij}\left(\bar{r}, \overline{r_0}\right)\right. \\
& \left. + \delta\mu\left(\bar{r}_0\right)\left(\delta_{il}\delta_{km} + \delta_{im}\delta_{kl}\right)\partial'_l u_m\left(\bar{r}_0\right)\partial_k G_{ij}\left(\bar{r}, \overline{r_0}\right)\right\} \\
= {} & u_{bj}\left(\bar{r}\right) + \int_\tau d\bar{r}_0 \left\{\omega^2\delta\rho\left(\bar{r}_0\right)u_k\left(\bar{r}_0\right)G_{kj}\left(\bar{r}, \overline{r_0}\right) + \delta\lambda\left(\bar{r}_0\right)\partial'_l u_l\left(\bar{r}_0\right)\partial_k G_{kj}\left(\bar{r}, \overline{r_0}\right)\right. \\
& \left. + \delta\mu\left(\bar{r}_0\right)\left(\partial'_i u_k\left(\bar{r}_0\right) + \partial'_k u_i\left(\bar{r}_0\right)\right)\partial_k G_{ij}\left(\bar{r}, \overline{r_0}\right)\right\}.
\end{aligned}$$

(2.60)

2.5.2 Method of Moments (MoM) Formulation

In the following equations, for notational convenience, a comma “,” indicates differentiation with respect to the spatial coordinate following it.

In a 2-D coordinate system in terms of the x and z coordinates, the integral scattering equation (2.60) can be explicitly written as

$$\begin{aligned} u_x = u_{bx} + \int_\tau d\bar{r}_0 \{ & \omega^2 \delta\rho (u_x G_{xx} + u_z G_{zx}) + \delta\lambda (u_{x,x} + u_{z,z})(G_{xx,x} + G_{zx,z}) \\ & + \delta\mu [2u_{x,x} G_{xx,x} + u_{z,x} (G_{xx,z} + G_{zx,x}) + u_{x,z} (G_{xx,z} + G_{zx,x}) + 2u_{z,z} G_{zx,z}]\}, \end{aligned} \tag{2.61}$$

and

$$\begin{aligned} u_z = u_{bz} + \int_\tau d\bar{r}_0 \{ & \omega^2 \delta\rho (u_x G_{xz} + u_z G_{zz}) + \delta\lambda (u_{x,x} + u_{z,z})(G_{xz,x} + G_{zz,z}) \\ & + \delta\mu [2u_{x,x} G_{xz,x} + u_{z,x} (G_{xz,z} + G_{zz,x}) + u_{z,z} (G_{xz,z} + G_{zz,x}) + 2u_{z,z} G_{zz,z}]\}. \end{aligned} \tag{2.62}$$

In order to solve for the derivatives of the internal field, one differentiates equations (2.61) and (2.62)with respect to x and z, to obtain

$$\begin{aligned} u_{x,x} = u_{bx,x} + \int_\tau d\bar{r}_0 \{ & \omega^2 \delta\rho (u_x G_{xx,x} + u_z G_{zx,x}) + \delta\lambda (u_{x,x} + u_{z,z})(G_{xx,xx} + G_{zx,zx}) \\ & + \delta\mu [2u_{x,x} G_{xx,xx} + u_{z,x} (G_{xx,zx} + G_{zx,xx}) + u_{x,z} (G_{xx,zx} + G_{zx,xx}) + 2u_{z,z} G_{zx,zx}]\}, \end{aligned} \tag{2.63}$$

$$\begin{aligned} u_{x,z} = u_{bx,z} + \int_\tau d\bar{r}_0 \{ & \omega^2 \delta\rho (u_x G_{xx,z} + u_z G_{zx,z}) + \delta\lambda (u_{x,x} + u_{z,z})(G_{xx,xz} + G_{zx,zz}) \\ & + \delta\mu [2u_{x,x} G_{xx,xz} + u_{z,x} (G_{xx,zz} + G_{zx,xz}) + u_{x,z} (G_{xx,zz} + G_{zx,xz}) + 2u_{z,z} G_{zx,zz}]\}, \end{aligned} \tag{2.64}$$

$$
\begin{aligned}
u_{z,x} = u_{bz,x} + \int_\tau d\bar{r}_0 \{ & \omega^2 \delta\rho (u_x G_{xz,x} + u_z G_{zz,x}) + \delta\lambda (u_{x,x} + u_{z,z})(G_{xz,xx} + G_{zz,zx}) \\
& + \delta\mu [2u_{x,x} G_{xz,xx} + u_{z,x} (G_{xz,zx} + G_{zz,xx}) + u_{x,z} (G_{xz,zx} + G_{zz,xx}) + 2u_{z,z} G_{zz,zx}]\},
\end{aligned}
\tag{2.65}
$$

and

$$
\begin{aligned}
u_{z,z} = u_{bz,z} + \int_\tau d\bar{r}_0 \{ & \omega^2 \delta\rho (u_x G_{xz,z} + u_z G_{zz,z}) + \delta\lambda (u_{x,x} + u_{z,z})(G_{xz,xz} + G_{zz,zz}) \\
& + \delta\mu [2u_{x,x} G_{xz,xz} + u_{z,x} (G_{xz,zz} + G_{zz,xz}) + u_{x,z} (G_{xz,zz} + G_{zz,xz}) + 2u_{z,z} G_{zz,zz}]\}.
\end{aligned}
\tag{2.66}
$$

It should be noted that when the differentiation with respect to x and z are applied, the displacement and its components inside the integrals remain unaffected as they are solely functions of the field coordinates *x₀* and *z₀*.

To simplify the notation, define

$$
\overline{\overline{\Lambda}} = \int_\tau \overline{\overline{G}}(\bar{r}, \bar{r}_0) d\bar{r}_0 = \begin{bmatrix} g_{xx} & g_{xz} \\ g_{zx} & g_{zz} \end{bmatrix}. \tag{2.67}
$$

For an isotropic medium, using the reciprocity theorem of the Green's tensor,

$$
\overline{\overline{G}}^T (\bar{r}, \bar{r}_0) = \overline{\overline{G}}(\bar{r}_0, \bar{r}) = \overline{\overline{G}}(\bar{r}, \bar{r}_0), \tag{2.68}
$$

one obtains $g_{xz} = g_{zx}$.

Following the standard MoM procedure, one divides the scatterer into N small cells, and assumes the derivatives of the internal field, $\delta\rho$, $\delta\lambda$ and $\delta\mu$ are constant within each cell. Ensuing equations in discretized form are given by

$$
\begin{aligned}
\sum_{j=1}^{N} \Big[& (\delta_{ij} - \omega^2 \delta\rho g_{xx}^{ji}) u_x^j - \omega^2 \delta\rho g_{zx}^{ji} u_z^j - [\delta\lambda (g_{xx,x}^{ji} + g_{zx,z}^{ji}) + 2\delta\mu g_{xx,x}^{ji}] u_{x,x}^j \\
& - \delta\mu (g_{xx,z}^{ji} + g_{zx,x}^{ji}) u_{z,x}^j - \delta\mu (g_{xx,z}^{ji} + g_{zx,x}^{ji}) u_{x,z}^j - [\delta\lambda (g_{xx,x}^{ji} + g_{zx,z}^{ji}) + 2\delta\mu g_{zx,z}^{ji}] u_{z,z}^j \Big] = u_{bx}^i ,
\end{aligned}
\tag{2.69}
$$

$$\begin{aligned}&\sum_{j=1}^{N}\Big[-\omega^2\delta\rho g_{xz}^{ji}u_x^j+\left(\delta_{ij}-\omega^2\delta\rho g_{zz}^{ji}\right)u_z^j-\left[\delta\lambda\left(g_{xz,x}^{ji}+g_{zz,z}^{ji}\right)+2\delta\mu g_{xz,x}^{ji}\right]u_{x,x}^j\\&-\delta\mu\left(g_{xz,z}^{ji}+g_{zz,x}^{ji}\right)u_{z,x}^j-\delta\mu\left(g_{xz,z}^{ji}+g_{zz,x}^{ji}\right)u_{x,z}^j-\left[\delta\lambda\left(g_{xz,x}^{ji}+g_{zz,z}^{ji}\right)+2\delta\mu g_{zz,z}^{ji}\right]u_{z,z}^j\Big]=u_{bz}^i\,,\end{aligned}\tag{2.70}$$

$$\begin{aligned}\sum_{j=1}^{N}\Big[-\omega^2\delta\rho g_{xx,x}^{ji}u_x^j-\omega^2\delta\rho g_{zx,x}^{ji}u_z^j+\left[\delta_{ij}-\delta\lambda\left(g_{xx,xx}^{ji}+g_{zx,zx}^{ji}\right)-2\delta\mu g_{xx,xx}^{ji}\right]u_{x,x}^j&\\-\delta\mu\left(g_{xx,zx}^{ji}+g_{zx,xx}^{ji}\right)u_{x,z}^j-\delta\mu\left(g_{xx,zx}^{ji}+g_{zx,xx}^{ji}\right)u_{z,x}^j&\\-\left[\delta\lambda\left(g_{xx,xx}^{ji}+g_{zx,zx}^{ji}\right)+2\delta\mu g_{zx,zx}^{ji}\right]u_{z,z}^j\Big]=u_{bx,x}^i\ ,&\end{aligned}\tag{2.71}$$

$$\begin{aligned}\sum_{j=1}^{N}\Big[-\omega^2\delta\rho g_{xx,z}^{ji}u_x^j-\omega^2\delta\rho g_{zx,z}^{ji}u_z^j-\left[\delta\lambda\left(g_{xx,xz}^{ji}+g_{zx,zz}^{ji}\right)+2\delta\mu g_{xx,xz}^{ji}\right]u_{x,x}^j&\\+\left[\delta_{ij}-\delta\mu\left(g_{xx,zz}^{ji}+g_{zx,xz}^{ji}\right)\right]u_{x,z}^j-\delta\mu\left(g_{xx,zz}^{ji}+g_{zx,xz}^{ji}\right)u_{z,x}^j&\\-\left[\delta\lambda\left(g_{xx,xz}^{ji}+g_{zx,zz}^{ji}\right)+2\delta\mu g_{zx,zz}^{ji}\right]u_{z,z}^j\Big]=u_{bx,z}^i\,,&\end{aligned}\tag{2.72}$$

$$\begin{aligned}\sum_{j=1}^{N}\Big[-\omega^2\delta\rho g_{xz,x}^{ji}u_x^j-\omega^2\delta\rho g_{zz,x}^{ji}u_z^j-\left[\delta\lambda\left(g_{xz,xx}^{ji}+g_{zz,zx}^{ji}\right)+2\delta\mu g_{xz,xx}^{ji}\right]u_{x,x}^j&\\-\delta\mu\left(g_{xz,zx}^{ji}+g_{zz,xx}^{ji}\right)u_{x,z}^j+\left[\delta_{ij}-\delta\mu\left(g_{xz,zx}^{ji}+g_{zz,xx}^{ji}\right)\right]u_{z,x}^j&\\-\left[\delta\lambda\left(g_{xz,xx}^{ji}+g_{zz,zx}^{ji}\right)+2\delta\mu g_{zz,zx}^{ji}\right]u_{z,z}^j\Big]=u_{bz,x}^i\ ,&\end{aligned}\tag{2.73}$$

and

$$\begin{aligned}\sum_{j=1}^{N}\Big[-\omega^2\delta\rho g_{xz,z}^{ji}u_x^j-\omega^2\delta\rho g_{zz,z}^{ji}u_z^j-\left[\delta\lambda\left(g_{xz,xz}^{ji}+g_{zz,zz}^{ji}\right)+2\delta\mu g_{xz,xz}^{ji}\right]u_{x,x}^j&\\-\delta\mu\left(g_{xz,zz}^{ji}+g_{zz,xz}^{ji}\right)u_{x,z}^j-\delta\mu\left(g_{xz,zz}^{ji}+g_{zz,xz}^{ji}\right)u_{z,x}^j&\\+\left[\delta_{ij}-\delta\lambda\left(g_{xz,xz}^{ji}+g_{zz,zz}^{ji}\right)-2\delta\mu g_{zz,zz}^{ji}\right]u_{z,z}^j\Big]=u_{bz,z}^i\ ,&\end{aligned}\tag{2.74}$$

where j, i=1, 2, …N.

Here, the single superscript is used to indicate the index of a given cell. The double superscript, ji, denotes the contribution of the j-th cell to the i-th cell in the integral of the Green's tensor. It is assumed that the differentiation and the integration are interchangeable since the Green's tensor is continuous in the spatial domain of the scatterer.

Note that in equations (2.72) and (2.73) the coefficients of $u^{j}_{z,x}$ and $u^{j}_{x,z}$ are the same, hence combining them can reduce one set of unknowns. To reduce the number of unknown to be solved, one introduces the variables

$$v = u_{z,x} + u_{x,z}\,, \tag{2.75}$$

and

$$v_b = u_{bz,x} + u_{bx,z}\,. \tag{2.76}$$

Then by adding equations (2.72) and (2.73) and by inserting equations (2.75) and (2.76) into the resulting equation, one obtains

$$\begin{aligned}
&\sum_{j=1}^{N}\Big[-\omega^2\delta\rho\left(g^{ji}_{xx,z}+g^{ji}_{xz,x}\right)u^{j}_{x}-\omega^2\delta\rho\left(g^{ji}_{zx,z}+g^{ji}_{zz,x}\right)u^{j}_{z}\\
&-\left[\delta\lambda\left(g^{ji}_{xx,xz}+g^{ji}_{zx,zz}+g^{ji}_{xz,xx}+g^{ji}_{zz,zx}\right)+2\delta\mu\left(g^{ji}_{xx,xz}+g^{ji}_{xz,xx}\right)\right]u^{j}_{x,x}\\
&+\left[\delta_{ij}-\delta\mu\left(g^{ji}_{xx,zz}+g^{ji}_{zx,xz}+g^{ji}_{xz,zx}+g^{ji}_{zz,xx}\right)\right]v^{j}\\
&-\left[\delta\lambda\left(g^{ji}_{xx,xz}+g^{ji}_{zx,zz}+g^{ji}_{xz,xx}+g^{ji}_{zz,zx}\right)+2\delta\mu\left(g^{ji}_{zx,zz}+^{ji}_{zz,zx}\right)\right]u^{j}_{z,z}\Big]=v^{i}_{b}\,.
\end{aligned} \tag{2.77}$$

By combining $u^{j}_{z,x}$ and $u^{j}_{x,z}$ in equations (2.69) through (2.74), and inserting (2.75) and (2.76) into the resulting equations, one finds

$$\begin{aligned}
&\sum_{j=1}^{N}\Big[\left(\delta_{ij}-\omega^2\delta\rho g^{ji}_{xx}\right)u^{j}_{x}-\omega^2\delta\rho g^{ji}_{zx}u^{j}_{z}-\left[\delta\lambda\left(g^{ji}_{xx,x}+g^{ji}_{zx,z}\right)+2\delta\mu g^{ji}_{xx,x}\right]u^{j}_{x,x}\\
&\qquad-\delta\mu\left(g^{ji}_{xx,z}+g^{ji}_{zx,x}\right)v^{j}-\left[\delta\lambda\left(g^{ji}_{xx,x}+g^{ji}_{zx,z}\right)+2\delta\mu g^{ji}_{zx,z}\right]u^{j}_{z,z}\Big]=u^{i}_{bx}\quad,
\end{aligned} \tag{2.78}$$

$$\begin{aligned}
&\sum_{j=1}^{N}\Big[-\omega^2\delta\rho g^{ji}_{xz}u^{j}_{x}+\left(\delta_{ij}-\omega^2\delta\rho g^{ji}_{zz}\right)u^{j}_{z}-\left[\delta\lambda\left(g^{ji}_{xz,x}+g^{ji}_{zz,z}\right)+2\delta\mu g^{ji}_{xz,x}\right]u^{j}_{x,x}\\
&\qquad-\delta\mu\left(g^{ji}_{xz,z}+g^{ji}_{zz,x}\right)v^{j}-\left[\delta\lambda\left(g^{ji}_{xz,x}+g^{ji}_{zz,z}\right)+2\delta\mu g^{ji}_{zz,z}\right]u^{j}_{z,z}\Big]=u^{i}_{bz}\quad,
\end{aligned} \tag{2.79}$$

$$\begin{aligned}
&\sum_{j=1}^{N}\Big[-\omega^2\delta\rho g^{ji}_{xx,x}u^{j}_{x}-\omega^2\delta\rho g^{ji}_{zx,x}u^{j}_{z}+\left[\delta_{ij}-\delta\lambda\left(g^{ji}_{xx,xx}+g^{ji}_{zx,zx}\right)-2\delta\mu g^{ji}_{xx,xx}\right]u^{j}_{x,x}\\
&\qquad-\delta\mu\left(g^{ji}_{xx,zx}+g^{ji}_{zx,xx}\right)v^{j}-\left[\delta\lambda\left(g^{ji}_{xx,xx}+g^{ji}_{zx,zx}\right)+2\delta\mu g^{ji}_{zx,zx}\right]u^{j}_{z,z}\Big]=u^{i}_{bx,x}\quad,
\end{aligned} \tag{2.80}$$

and

$$\sum_{j=1}^{N}\Big[-\omega^2\delta\rho g^{ji}_{xz,z}u^j_x-\omega^2\delta\rho g^{ji}_{zz,z}u^j_z-\left[\delta\lambda\left(g^{ji}_{xz,xz}+g^{ji}_{zz,zz}\right)+2\delta\mu g^{ji}_{xz,xz}\right]u^j_{x,x}$$
$$-\delta\mu\left(g^{ji}_{xz,zz}+g^{ji}_{zz,xz}\right)v^j+\left[\delta_{ij}-\delta\lambda\left(g^{ji}_{xz,xz}+g^{ji}_{zz,zz}\right)-2\delta\mu g^{ji}_{zz,zz}\right]u^j_{z,z}\Big]=u^i_{bz,z}\,. \qquad (2.81)$$

The above five equations form a linear system of equations with 5N by 5N unknowns. Solving this system yields the internal field and its partial derivative within all of the disretization cells.

The scattered field can be computed using the following expression

$$u^i_{sx}=\sum_{j=1}^{N}\Big\{\omega^2\delta\rho\left(g^{ji}_{xx}u^j_x+g^{ji}_{zx}u^j_z\right)+\delta\lambda\left(g^{ji}_{xx,x}+g^{ji}_{zx,z}\right)\left(u^j_{x,x}+u^j_{z,z}\right)$$
$$+\delta\mu\left[2g^{ji}_{xx,x}u^j_{x,x}+\left(g^{ji}_{xx,z}+g^{ji}_{zx,x}\right)\left(u^j_{z,x}+u^j_{x,z}\right)+2g^{ji}_{zx,z}u^j_{z,z}\right]\Big\}, \qquad (2.82)$$

and

$$u^i_{sz}=\sum_{j=1}^{N}\Big\{\omega^2\delta\rho\left(g^{ji}_{xz}u^j_x+g^{ji}_{zz}u^j_z\right)+\delta\lambda\left(g^{ji}_{xz,x}+g^{ji}_{zz,z}\right)\left(u^j_{x,x}+u^j_{z,z}\right)$$
$$+\delta\mu\left[2g^{ji}_{xz,x}u^j_{x,x}+\left(g^{ji}_{xz,z}+g^{ji}_{zz,x}\right)\left(u^j_{z,x}+u^j_{x,z}\right)+2g^{ji}_{zz,z}u^j_{z,z}\right]\Big\}, \qquad (2.83)$$

where j=1, 2, …N, and i =1, 2, …M. In these last equations, N is the number of cells in the scatterer, and M is the number of receivers.

2.5.3 Born Approximation

To solve the general elastic scattering problem using equation (2.56), one needs to know the total displacement vector inside the scatterer. For many problems, the Born approximation is used to compute the scattered waves. Such an approximation is obtained by replacing the total wavefield in the right-hand of equation (2.56) with the background wavefield. Thus, the Born approximation of the scattering equation is given by

$$u_j\left(\bar{r}\right)=u_{bj}\left(\bar{r}\right)+\int_\tau d\bar{r}_0\left\{\delta\rho\left(\bar{r}_0\right)\omega^2u_{bj}\left(\bar{r}_0\right)G_{kj}\left(\bar{r},\overline{r_0}\right)-\delta\Gamma_{iklm}\left(\bar{r}_0\right)\partial'_l u_{bj}\left(\bar{r}_0\right)\partial'_k G_{ij,k}\left(\bar{r},\overline{r_0}\right)\right\}.$$

(2.84)

2.5.4 Extended Born Formulation

Similar to the cases of spatial variations of density and λ, the extended Born approximation can be obtained by rewriting equation (2.60) as

$$\begin{aligned}
u_j(\bar{r}) &= u_{bj}(\bar{r}) \\
&+\left[\int_\tau d\bar{r}_0 \omega^2 \delta\rho(\bar{r}_0) G_{kj}(\bar{r},\bar{r}_0)\right] u_k(\bar{r}) + \int_\tau d\bar{r}_0 \omega^2 \delta\rho(\bar{r}_0)\left[u_k(\bar{r}_0) - u_k(\bar{r})\right] G_{kj}(\bar{r},\bar{r}_0) \\
&+ \int_\tau d\bar{r}_0 \left[\delta\lambda(\bar{r}_0) G_{kj,k}(\bar{r},\bar{r}_0)\right] u_{l,l}(\bar{r}) + \int_\tau d\bar{r}_0 \delta\lambda(\bar{r}_0)\left[u_{l,l}(\bar{r}_0) - u_{l,l}(\bar{r})\right] G_{kj,k}(\bar{r},\bar{r}_0) \\
&+ (\delta_{il}\delta_{km} + \delta_{im}\delta_{kl}) \int_\tau d\bar{r}_0 \left[\delta\mu(\bar{r}_0) G_{ij,k}(\bar{r},\bar{r}_0)\right] u_{m,l}(\bar{r}) \\
&+ (\delta_{il}\delta_{km} + \delta_{im}\delta_{kl}) \int_\tau d\bar{r}_0 \delta\mu(\bar{r}_0)\left[u_{m,l}(\bar{r}_0) - u_{m,l}(\bar{r})\right] G_{ij,k}(\bar{r},\bar{r}_0) \; .
\end{aligned}$$

(2.85)

If one writes the displacement vector in a Taylor series expansion about $\bar{r}_0 = \bar{r}$, namely,

$$\begin{aligned}
u_j(\bar{r}_0) &= \sum_{n=0}^{\infty} \sum_{i_1+i_2+i_3=n} \frac{1}{i_1! i_2! i_3!} \left(x_1^0 - x_1\right)^{i_1} \left(x_2^0 - x_2\right)^{i_2} \left(x_3^0 - x_3\right)^{i_3} \frac{\partial^n u_j(\bar{r})}{\partial x_1^{i_1} \partial x_2^{i_2} \partial x_3^{i_3}} \\
&= u_j(\bar{r}) + \left(x_k^0 - x_k\right) u_{j,k}(\bar{r}) + \frac{1}{2}\left(x_k^0 - x_k\right)\left(x_l^0 - x_l\right) u_{j,kl}(\bar{r}) + O\left[\left(\bar{r}_0 - \bar{r}\right)\right]^3 \\
&= u_j(\bar{r}) + \left(\bar{r}_0 - \bar{r}\right) \cdot \nabla u_j(\bar{r}) + \frac{1}{2}\left(\bar{r}_0 - \bar{r}\right) \cdot \left[\nabla\nabla u_j(\bar{r})\right] \cdot \left(\bar{r}_0 - \bar{r}\right) + O\left[\left(\bar{r}_0 - \bar{r}\right)\right]^3 ,
\end{aligned} \tag{2.86}$$

it becomes evident that in cases where $\nabla\nabla u_j(\bar{r})$ or higher-order variations of the displacement vector are negligible, one can obtain similar extended Born approximations.

For the partial derivatives of the internal field $u_{j,i}(\bar{r}_0)$ inside the integrand of equation (2.60), one has the following expansion:

$$
\begin{aligned}
u_{j,i}\left(\overline{r_0}\right) &= \sum_{n=0}^{\infty}\sum_{i_1+i_2+i_3=n}\frac{1}{i_1!i_2!i_3!}\left(x_1^0-x_1\right)^{i_1}\left(x_2^0-x_2\right)^{i_2}\left(x_3^0-x_3\right)^{i_3}\frac{\partial^n u_{j,i}\left(\overline{r}\right)}{\partial x_1^{i_1}\partial x_2^{i_2}\partial x_3^{i_3}}\\
&= u_{j,i}\left(\overline{r}\right)+\left(x_k^0-x_k\right)u_{j,ik}\left(\overline{r}\right)+\frac{1}{2}\left(x_k^0-x_k\right)\left(x_l^0-x_l\right)u_{j,ikl}\left(\overline{r}\right)+O\left[\left(\overline{r}_0-\overline{r}\right)\right]^3\\
&= u_{j,i}\left(\overline{r}\right)+\left(\overline{r}_0-\overline{r}\right)\cdot\nabla u_{j,i}\left(\overline{r}\right)+\frac{1}{2}\left(\overline{r}_0-\overline{r}\right)\cdot\left[\nabla\nabla u_{j,i}\left(\overline{r}\right)\right]\cdot\left(\overline{r}_0-\overline{r}\right)+O\left[\left(\overline{r}_0-\overline{r}\right)\right]^3 .
\end{aligned}
\tag{2.87}
$$

A similar conclusion can be drawn for the case of the internal displacement vector $u_j\left(\overline{r_0}\right)$, except that it is now only required that the second-order derivatives be spatially smooth, and that the derivatives of $\overline{\overline{G}}\left(\overline{r},\overline{r}_0\right)$ be a highly peaked function. The accuracy can be improved by considering the first order approximation of the internal displacement vector so that the neglected derivatives of $u_j\left(\overline{r_0}\right)$ are second-order or higher.

Taking into account the definition of the integral of $\overline{\overline{G}}\left(\overline{r},\overline{r}_0\right)$ and by applying the zero-order approximation of the internal displacement vector and its first-order derivatives to equations (2.61) through (2.66) , one obtains the following linear system of equation for each cell:

$$
\begin{aligned}
u_x &= u_{bx}+\omega^2\delta\rho\left(u_x g_{xx}+u_z g_{zx}\right)+\delta\lambda\left(u_{x,x}+u_{z,z}\right)\left(g_{xx,x}+g_{zx,z}\right)\\
&\quad+\delta\mu\left[2u_{x,x}g_{xx,x}+u_{z,x}\left(g_{xx,z}+g_{zx,x}\right)+u_{x,z}\left(g_{xx,z}+g_{zx,x}\right)+2u_{z,z}g_{zx,z}\right],
\end{aligned}
\tag{2.88}
$$

$$
\begin{aligned}
u_z &= u_{bz}+\omega^2\delta\rho\left(u_x g_{xz}+u_z g_{zz}\right)+\delta\lambda\left(u_{x,x}+u_{z,z}\right)\left(g_{xz,x}+g_{zz,z}\right)\\
&\quad+\delta\mu\left[2u_{x,x}g_{xz,x}+u_{z,x}\left(g_{xz,z}+g_{zz,x}\right)+u_{z,z}\left(g_{xz,z}+g_{zz,x}\right)+2u_{z,z}g_{zz,z}\right],
\end{aligned}
\tag{2.89}
$$

$$
\begin{aligned}
u_{x,x} &= u_{bx,x}+\omega^2\delta\rho\left(u_x g_{xx,x}+u_z g_{zx,x}\right)+\delta\lambda\left(u_{x,x}+u_{z,z}\right)\left(g_{xx,xx}+g_{zx,zx}\right)\\
&\quad+\delta\mu\left[2u_{x,x}g_{xx,xx}+u_{z,x}\left(g_{xx,zx}+g_{zx,xx}\right)+u_{x,z}\left(g_{xx,zx}+g_{zx,xx}\right)+2u_{z,z}g_{zx,zx}\right],
\end{aligned}
\tag{2.90}
$$

$$
\begin{aligned}
u_{x,z} &= u_{bx,z}+\omega^2\delta\rho\left(u_x g_{xx,z}+u_z g_{zx,z}\right)+\delta\lambda\left(u_{x,x}+u_{z,z}\right)\left(g_{xx,xz}+g_{zx,zz}\right)\\
&\quad+\delta\mu\left[2u_{x,x}g_{xx,xz}+u_{z,x}\left(g_{xx,zz}+g_{zx,xz}\right)+u_{x,z}\left(g_{xx,zz}+g_{zx,xz}\right)+2u_{z,z}g_{zx,zz}\right],
\end{aligned}
\tag{2.91}
$$

$$
\begin{aligned}
u_{z,x} = {} & u_{bz,x} + \omega^2 \delta\rho\left(u_x g_{xz,x} + u_z g_{zz,x}\right) + \delta\lambda\left(u_{x,x} + u_{z,z}\right)\left(g_{xz,xx} + g_{zz,zx}\right) \\
& + \delta\mu\left[2u_{x,x} g_{xz,xx} + u_{z,x}\left(g_{xz,zx} + g_{zz,xx}\right) + u_{x,z}\left(g_{xz,zx} + g_{zz,xx}\right) + 2u_{z,z} g_{zz,zx}\right], \quad (2.92)
\end{aligned}
$$

and

$$
\begin{aligned}
u_{z,z} = {} & u_{bz,z} + \omega^2 \delta\rho\left(u_x g_{xz,z} + u_z g_{zz,z}\right) + \delta\lambda\left(u_{x,x} + u_{z,z}\right)\left(g_{xz,xz} + g_{zz,zz}\right) \\
& + \delta\mu\left[2u_{x,x} g_{xz,xz} + u_{z,x}\left(g_{xz,zz} + g_{zz,xz}\right) + u_{x,z}\left(g_{xz,zz} + g_{zz,xz}\right) + 2u_{z,z} g_{zz,zz}\right]. \quad (2.93)
\end{aligned}
$$

Solving the linear system embodied by equations (2.88)-(2.93) yields the approximations of the internal displacement vector and its first order derivatives. Subsequently, equations (2.82) and (2.83) can be used to compute the scattered field.

In the MoM and the Born and extended Born approximations, one needs to know the background field and its first order partial derivatives to solve for the scattered field. The corresponding derivations are given in Appendix C. Another important effort is to obtain the integral of the Green's tensor and of its first- and second-order derivatives before computing the scattered field. These derivations are detailed in Appendix D

2.5.5 Benchmark Example

Finally, the numerical simulation at 1 kHz for simultaneous spatial variation in all three elastic parameters is described in Figure 2.7. This figure shows that the real and imaginary parts of the displacement of the scattered field simulated with the MoM are very close to those of the analytical solution. It can also be seen from Figure 2.7 that the extended Born approximation gives a better result for the imaginary part of the z component than the Born approximation.

Figure 2.8 shows that from 100 Hz to 10 kHz, the results of the MoM, Born and extended Born approximations all match those of the analytical solution. Close to 100 kHz, the numerical solutions deviate from the analytical solution. Of course, reducing the cell size will improve the results at the expense of more computation time and memory resources.

A final approximation exercise consists of replacing the stiffness matrix of the MoM by its diagonal elements. The result of this approximation is shown in Figure 2.8. Since the latter result is not better than the Born approximation, such an approximation is not explored any further in this dissertation.

2.6 SUITABILITY OF THE GREEN'S TENSOR FOR ELASTIC OR FLUID MEDIA

In this section, the physics involved in EM and acoustic logging is discussed, and a suitable Green's function is recommended for the numerical simulation of wave propagation in fluid-filled boreholes.

In electric logging problems, both the borehole fluid and the rock formation can be characterized by their dielectric constant and electrical conductivity. The electric and magnetic currents are continuous across interfaces between borehole fluid and rock formation. Therefore, it is appropriate to resort to a single Green's tensor for a homogenous, isotropic, unbounded background medium in order to construct the integral equation formulation for EM scattering.

For acoustic logging applications, however, only compressional waves are supported by fluid-filled boreholes, while the rock formation can support both compressional and shear motions. At the interface between the borehole fluid and rock formation, the tangential stress and displacement are not continuous across the boundary.

Assuming that either the Green's tensor for a fluid or that for an elastic medium can be used to construct an integral equation for wave propagation in the presence of a fluid-solid interface, displacements in both the elastic medium and the fluid can be represented by

$$\bar{u} = \bar{u}_b + \int_\tau d\bar{r}_0 \bar{\bar{G}}\left(\bar{r},\bar{r}_0\right)\cdot\left[\omega^2\delta\rho\bar{u} + \nabla_0\left(\delta\lambda\nabla_0\cdot\bar{u}\right) + \nabla_0\cdot\left(\delta\mu\bar{\bar{S}}\right)\right]. \tag{2.94}$$

The above equation is valid for any location $\bar{r}$, in the fluid and inside the elastic scatterer. If $\bar{r}$ approaches the boundary $\bar{r}_a$ from the fluid and the solid simultaneously, equation (2.94) dictates that the displacement and the ensuing stress become equal at the boundary because of However, this conclusion violates the interface condition that the tangential stress and displacement be discontinuous across a general material boundary. Therefore, neither the Green's tensor for a fluid nor that for an elastic medium can be used to construct an integral equation for wave propagation in fluid-filled boreholes.

The question then remains how to construct an integral equation that can properly address such a scattering problem. One way is to construct a Green's tensor for an inhomogeneous medium, which is formed by a fluid-filled borehole penetrating a homogenous or multilayered rock formation (Lu and Liu, 1995). For multilayered formations, the Green's tensor can be that of a multilayered formation that also include the fluid-filled borehole. In the next chapter, an equivalent form of such a Green's tensor is developed for a radially multilayered formation and used for the simulation of multipole acoustic measurements. The corresponding formulation for the monopole case can be inferred from the work reported by Chen et al. (1996).

2.7 CONCLUSIONS

In this Chapter, the method of moments, the Born and extended Born approximations have been developed to solve full-wave elastic scattering problems assuming spatial variations of elastic parameters. Three cases were considered, namely, only density variations, only Lamé coefficient λ, and simultaneous variations of density and Lamé coefficients, λ and μ. The integral equation formulation makes use of a

Green’s tensor for an isotropic and homogeneous background. A canonical benchmark problem was solved using the method of moments and the Born and extended Born approximations. Simulation results were compared against those of the analytical method.

The method of moments yields accurate results and suggests the validity of the approach. However, both the Born and extended Born approximations are much more efficient than the MoM. For the case in which only density contrasts exist, the simulation errors entailed by both approximations are less than 5%. The accuracy of the approximations significantly decreases when the contrast between the scatterer and the background medium increases or else when the size of the scatterer increases with respect to the local elastic wavelength.

A more appropriate Green’s tensor for simulating wave propagation in fluid-filled boreholes is the one constructed under the assumption of a fluid-filled borehole penetrating a homogeneous or radially multilayered, elastic medium.

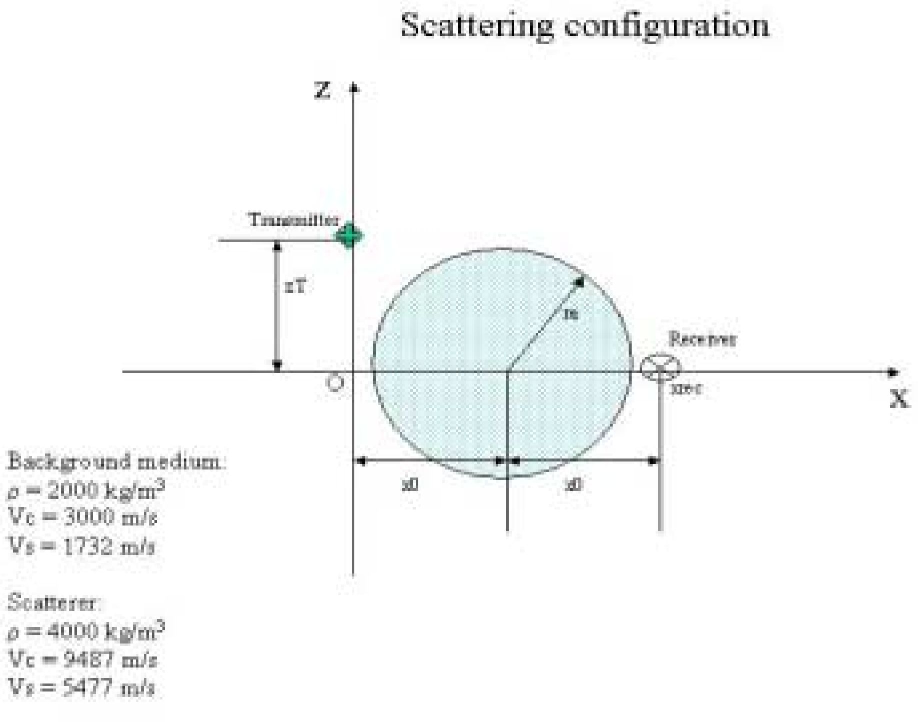

Figure 2.1: Graphical description of the benchmark problem used to assess the efficiency and accuracy of elastic scattering formulations with integral equations. The associated geometrical dimensions are specified in the following figures.

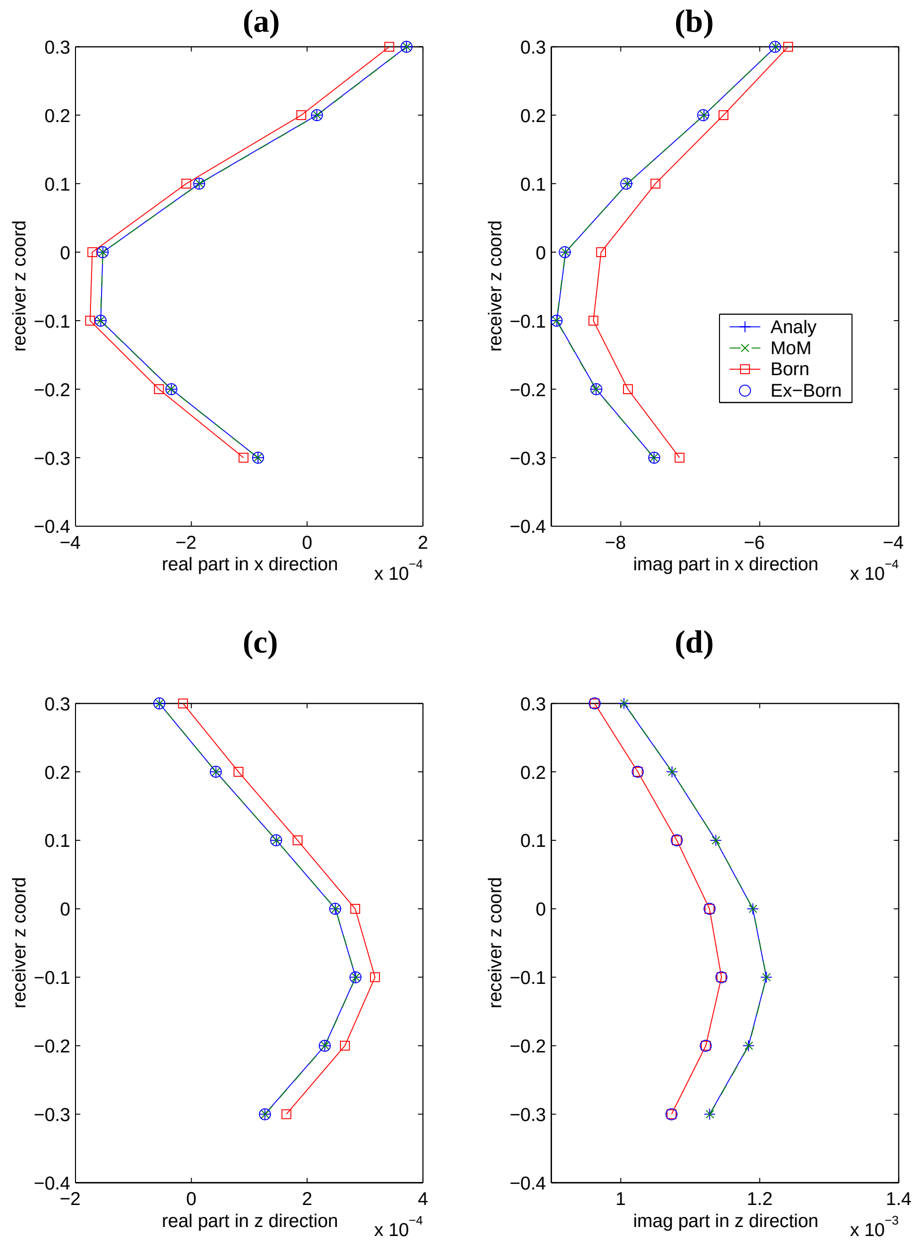

Figure 2.2: Comparison of the real (a) and imaginary (b) parts of the x component and the real (c) and imaginary (d) parts of the z component of the displacement of the scattered waves computed with the analytical solution, MoM, Born approximation, and extended Born approximation for only density variation. The frequency of the source is 500 Hz. The units of the axes of the plots are in meters. The geometrical variables shown in Figure 2.1, x_0, x_{rec}, r_a, and z_T are 0.3 m, 0.6 m, 0.15 m, and 0.3 m, respectively.

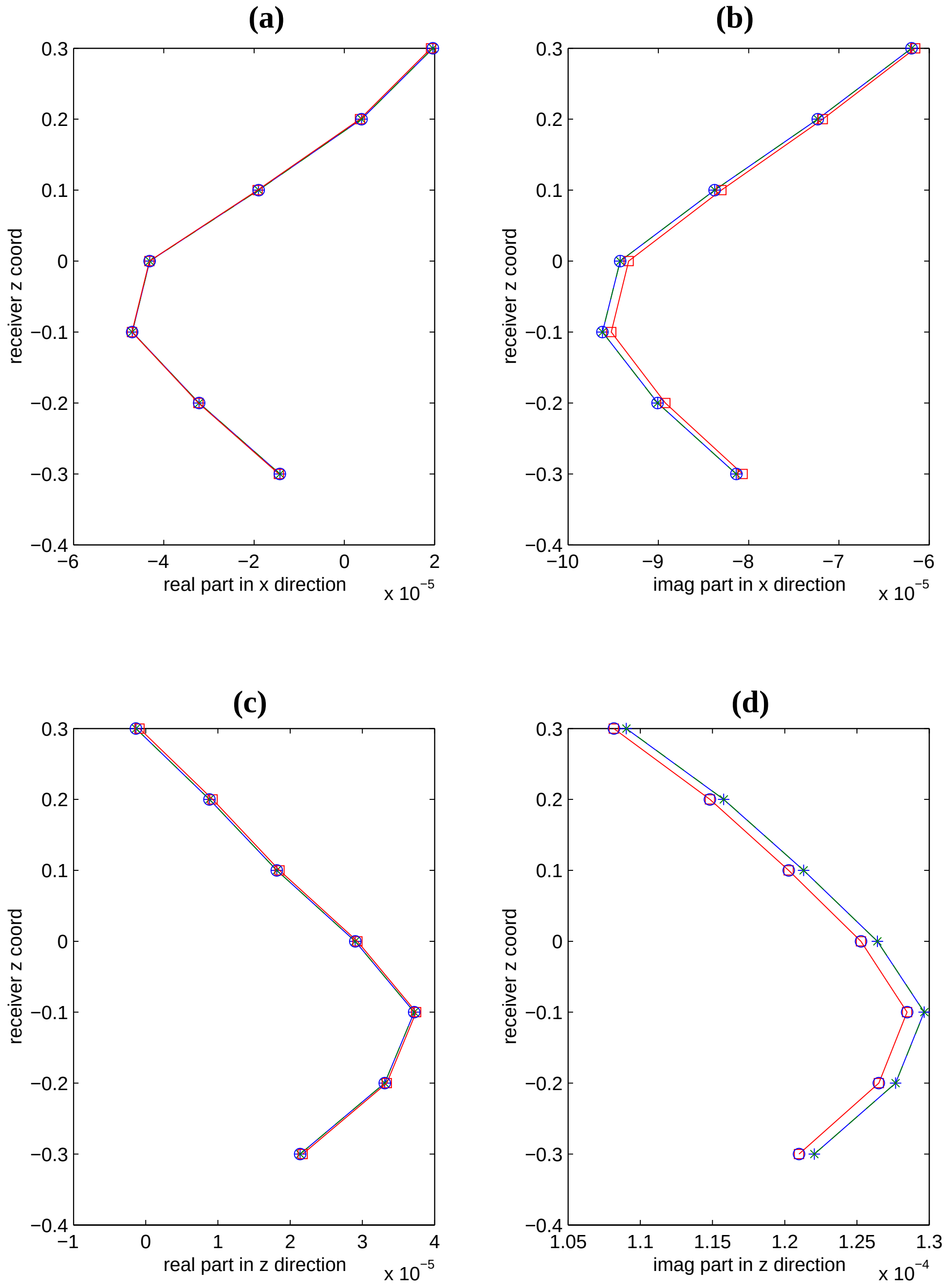

Figure 2.3: Comparison of the real (a) and imaginary (b) parts of the x component and the real (c) and imaginary (d) parts of the z component of the displacement of the scattered waves computed with the analytical solution, MoM, Born approximation, and extended Born approximation for only density variation. The frequency of the source is 500 Hz. The units of the axes are in meters. The same scattering configuration as Figure 2.2 is used except that the radius of scatterer reduces to 0.05 m.

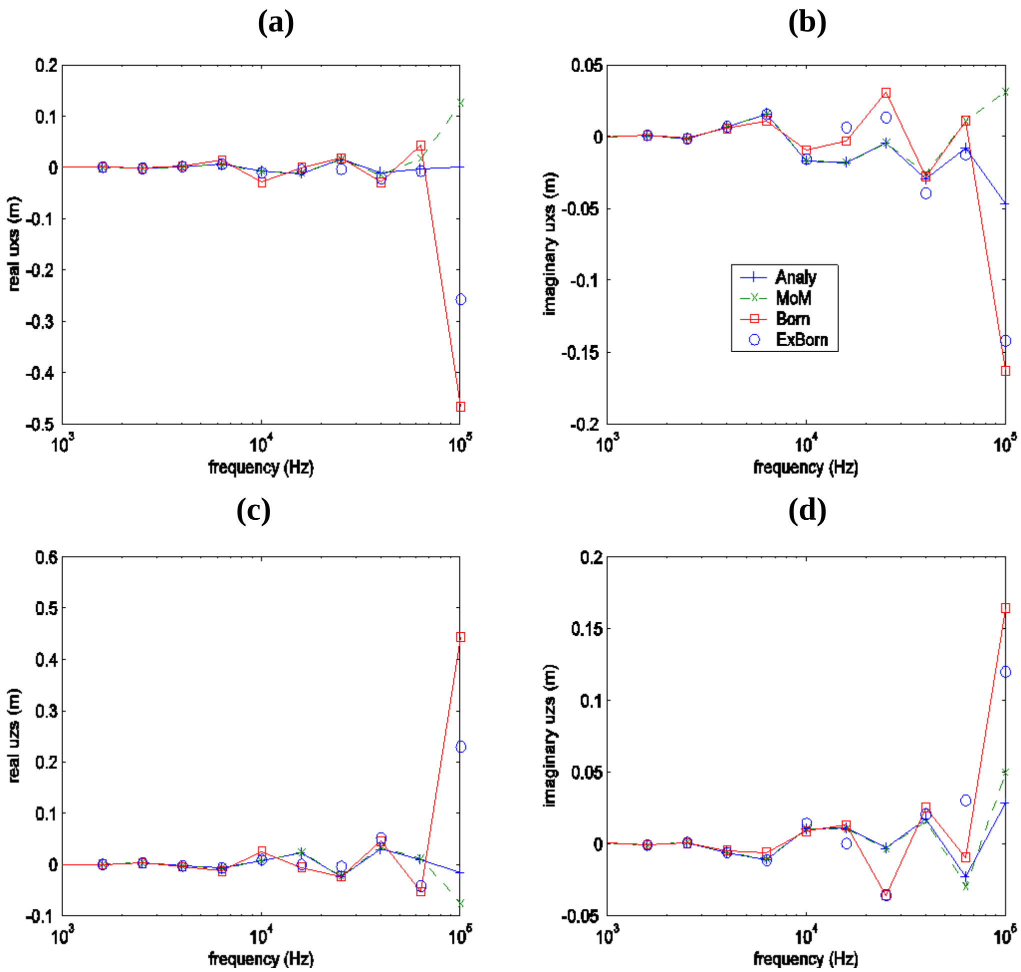

Figure 2.4: Comparison of the real (a) and imaginary (b) parts of the x component and the real (c) and imaginary (d) parts of the z component of the displacement of the scattered wave simulated for model shown in Figure 2.1 for the case of only density variation. The scatterer is divided into 10 and 20 grids in the radial and azimuthal directions, respectively. The frequency of the source ranges from 1 kHz to 100 kHz.

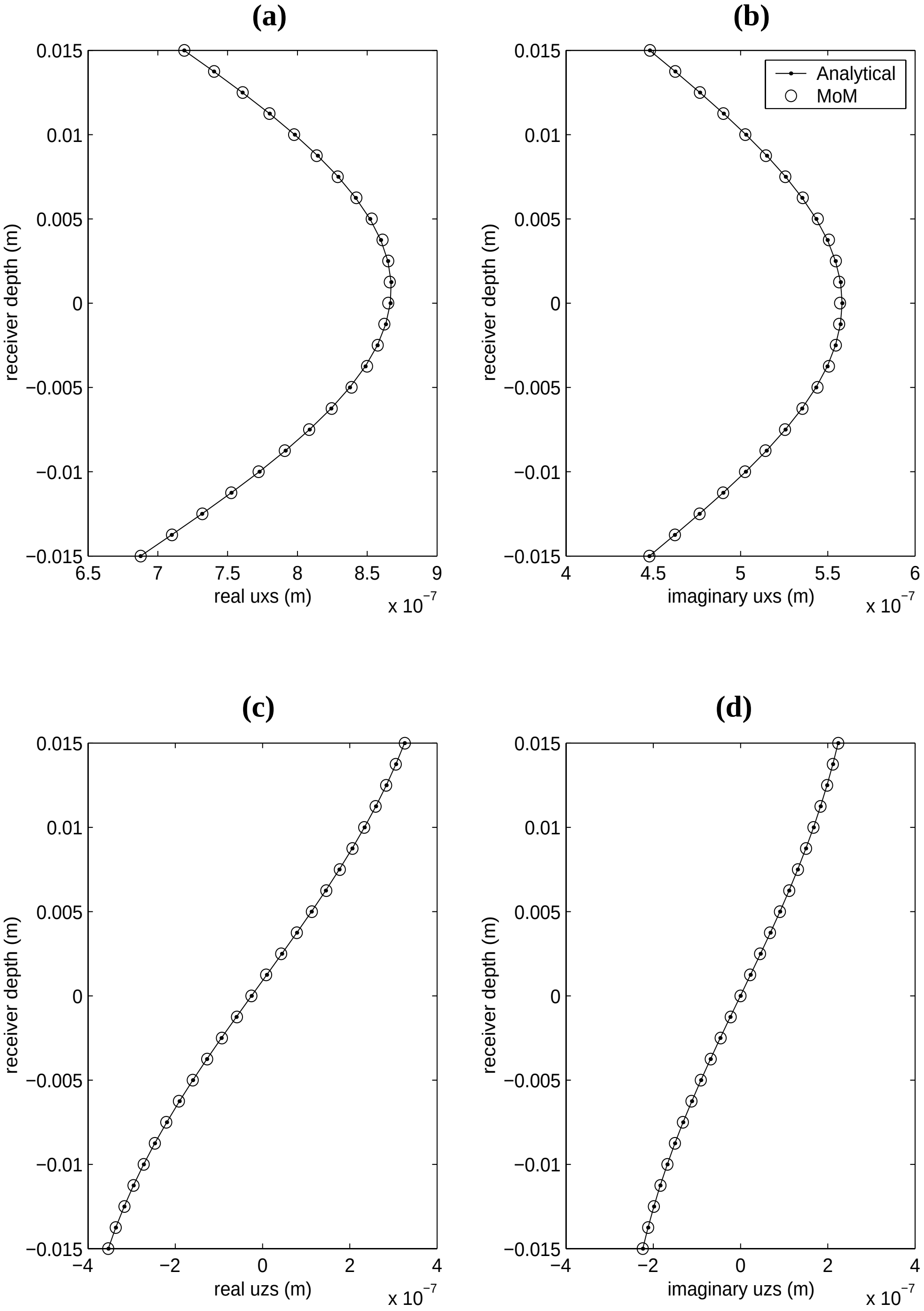

Figure 2.5: Comparison of the real (a) and imaginary (b) parts of the x component and the real (c) and imaginary (d) parts of the z component of the displacement of the scattered waves computed with the analytical solution, MoM, Born approximation, and extended Born approximation for $\delta\lambda$ variation only. The frequency of the source is 1 kHz. The compressional velocity of the scatterer is 1000 m/s higher than that of the background. For Figures 2.5 through 2.8, x_0, x_{rec}, r_a, and z_T are 0.03 m, 0.06 m, 0.025 m, and 0.03 m, respectively.

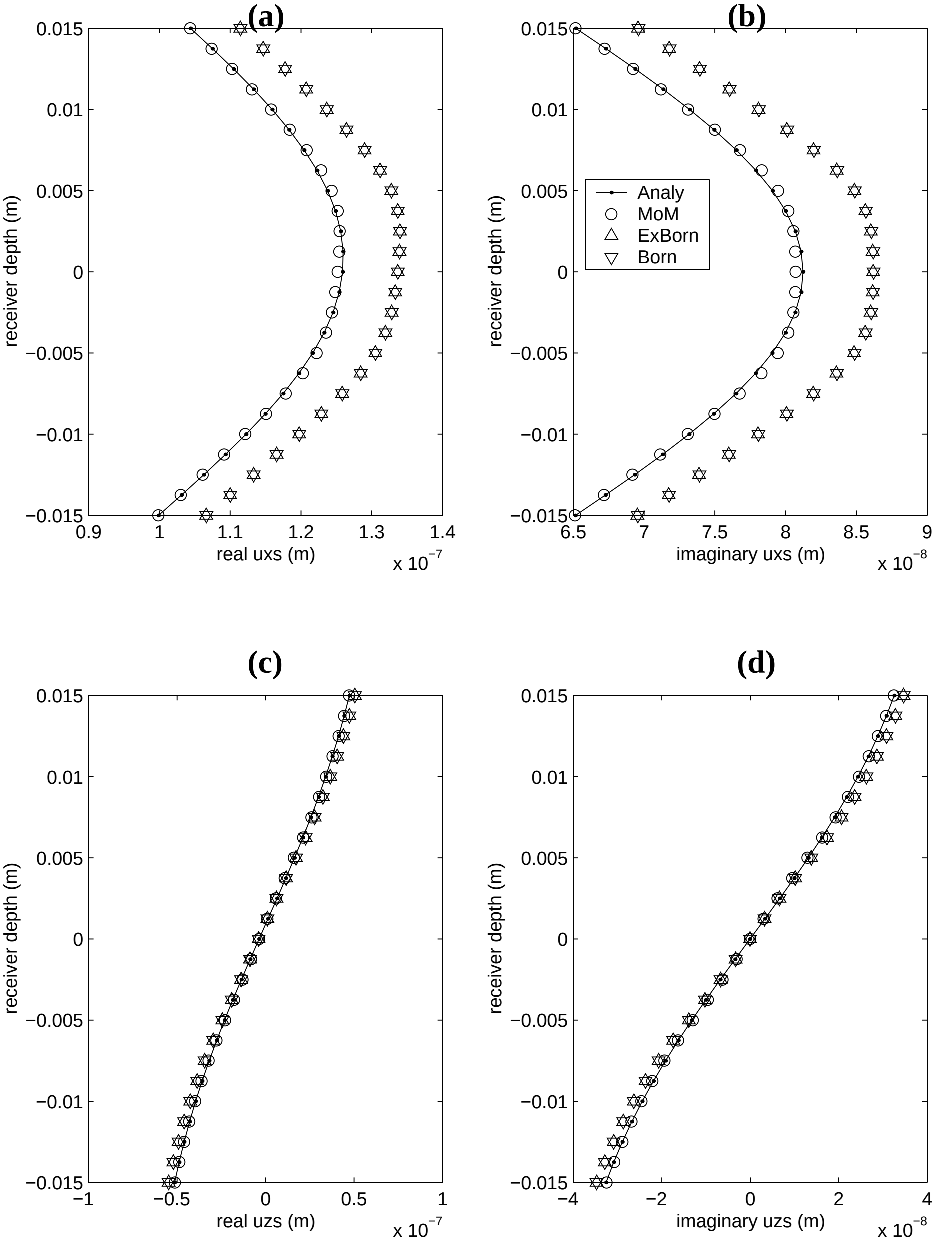

Figure 2.6: Comparison of the real (a) and imaginary (b) parts of the x component and the real (c) and imaginary (d) parts of the z component of the displacement of the scattered waves computed with the analytical solution, MoM, Born approximation, and extended Born approximation for $\delta\lambda$ variation only. The frequency of the source is 1 kHz. The $\delta\lambda$ variation is 20%.

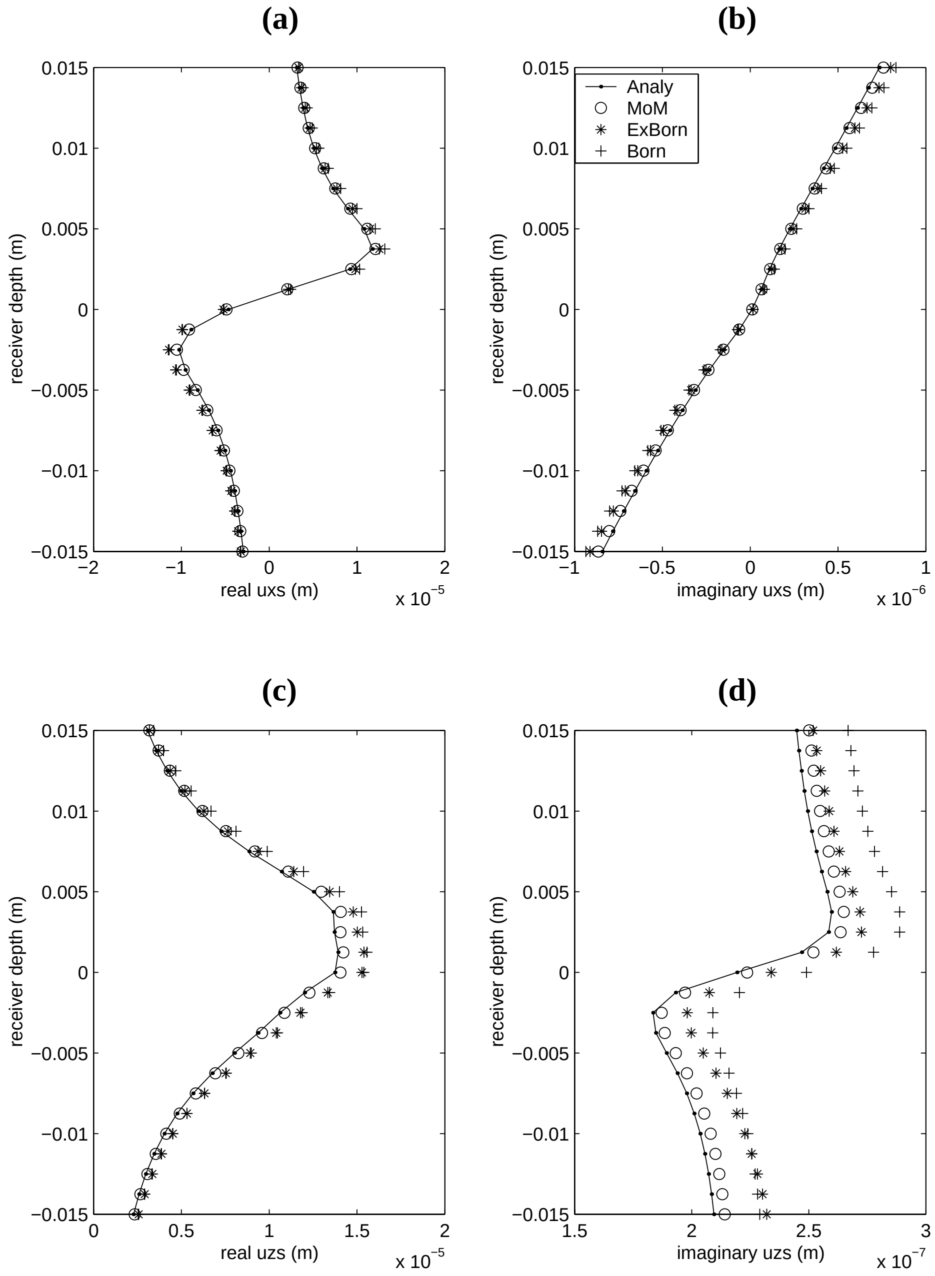

Figure 2.7: Comparison of the real (a) and imaginary (b) parts of the x component and the real (c) and imaginary (d) parts of the z component parts of the displacement of the scattered waves computed with the analytical solution, MoM, Born approximation, and extended Born approximation for simultaneous density, $\delta\lambda$, and $\delta\mu$ variations. The frequency of the source is 1 kHz. The density, $\delta\lambda$, and $\delta\mu$ of the scatterer are 5.0%, 1.4%, and 17.5% higher as compared to the background, respectively.

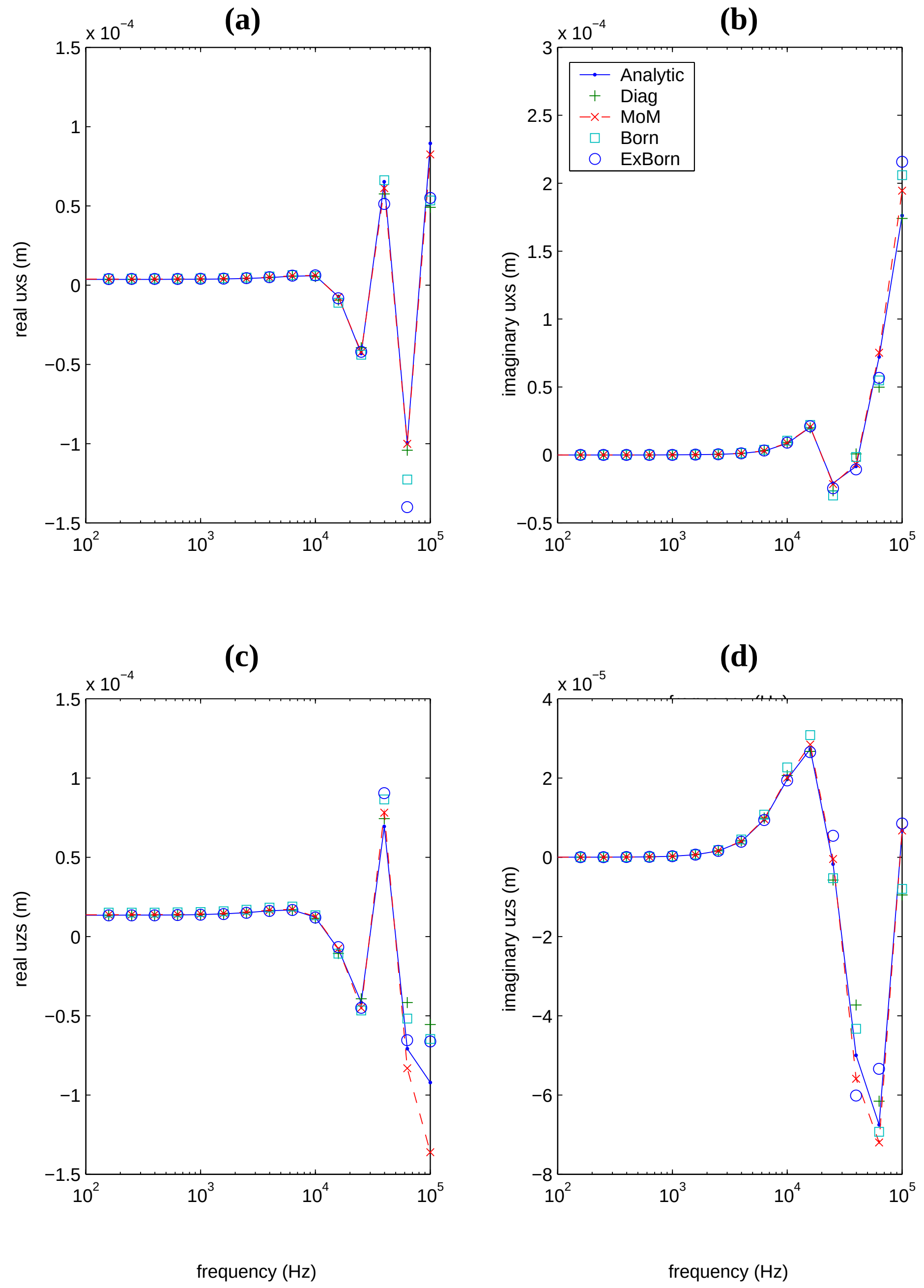

Figure 2.8: Comparison of the real (a) and imaginary (b) parts of the x component and the real (c) and imaginary (d) parts of the z component of the displacement of the scattered waves computed with the analytical solution, MoM, Born approximation, and extended Born approximation for simultaneous density, $\delta\lambda$, and $\delta\mu$ variations. The frequency of the source ranges from 100 Hz to 100 kHz. Diag denotes an approximation using the only diagonal entries of the stiffness matrix of the linear system in solving the system.

Chapter 3: Synthesis of Multipole Acoustic Logging Measurements Using the Generalized Reflection/Transmission Matrices Method

To date, the Thomson-Haskell method is the only analytical method available to simulate multipole acoustic logging measurements in the presence of cylindrically layered media. This method becomes numerically unstable for high-frequency problems. In this chapter, a new algorithm is developed based on the concept of generalized reflection and transmission matrices. The adoption of normalized Hankel functions and normalizing factors makes the method overcome the numerical instability that exists in the Thomson-Haskell method at high frequencies. Generalized reflection and transmission matrices of a given layer are reconstructed using the reflection coefficient of the outward-directed wave in that layer and the transmission coefficient of the incoming wave from the outlying layers, the An efficient recursive scheme is designed to compute the generalized reflection and transmission matrices. Subsequently, the displacement and stress can be computed for any layer. Discrete wavenumber integrals and fast Fourier transforms (FFT) are applied to transform the acoustic measurements from the frequency-wavenumber domain to the time-space domain.

This new formulation is verified by comparing simulation results to those of the Thomson-Haskell method for the cases of a simple borehole and complex mud-filtrate invasion zones. An example of using the new formulation to simulate multipole waveforms is described assuming a borehole surrounded by a complex mud-filtrate invasion zone due to water-base mud-filtrate invading a gas-bearing limestone formation. Velocity analysis is then performed to study the depth of investigation of a dipole tool in the case of complex radial invasion zones. P- and S-wave velocities obtained from the array dipole waveforms correspond to a depth of investigation of 1.7 m. In this case, the dipole tool senses about three times deeper into the formation than does a monopole tool.

3.1 INTRODUCTION

In a slow formation, the shear wave velocity is slower than the compressional velocity of the drilling fluid in the borehole. Because of the ability of a multipole tool to measure the shear velocity in a slow formation, the excitation and measurement of non-axially symmetric waves in boreholes have been examined extensively. In particular, dipole and quadrupole source tools, such as XMAC* and DSI** have been widely used by the hydrocarbon exploration and development industry. Theoretical and numerical investigations of non-axially symmetric wave propagation in a fluid-filled borehole are important for the design of logging tools. For a borehole penetrating an infinite homogeneous media, synthetic waveforms associated with multipole sources have been studied by White (1967), Roever et al. (1974), Winbow (1980), Tongtaow (1982), Kurkjian and Chang (1983, 1986), Winbow and Rice (1984), Kurkjian (1984), and many others. Schmitt (1988) analyzed the wave fields generated by multipole sources in the presence of radially multilayered elastic and transversely isotropic porous formations using the Thomson-Haskell method. Cheng et al. (1995) used a 3D finite-difference method to simulate acoustic propagation in heterogeneous formations. Tang et al. (2002) computed synthetic waveforms using a 3D finite-difference simulation and showed good agreements between the shear-wave velocity logs obtained using a Logging-While-Drilling quadrupole acoustic logging tool and a wireline dipole tool.

Because finite-difference simulations can be computationally intensive for radially layered media, analytical solutions offer a more efficient alternative to investigate wave propagation phenomena in boreholes. The Thomson-Haskell method is the only method that has been used in multipole waveform synthesis for radially multilayered formations. In the monopole source case, Chen et al. (1996) proposed an alternative approach, the generalized reflection and transmission (R/T) matrices method, to perform waveform synthesis in isotropic elastic media. The generalized R/T matrices method is widely used in modeling elastic waves in vertically layered media because of its computational stability and efficiency over the Thomson-Haskell method, especially for high-frequency problems (e.g., Dunkin, 1965, Luco and Apsel, 1983, Kennett, 1983, Tygel and Hubral, 1987, and Chen, 1993). Chen et al. (1996) derived a set of alternative formulations that are more stable and efficient than the previous methods for numerical computation. In their algorithm, Chen et al. (1996) introduced the concepts of modified and generalized reflection and transmission matrices for radially layered media and derived a recursive scheme to calculate them. Subsequently, they used the same matrices to compute wavefields. They demonstrated that the generalized R/T matrices method could efficiently simulate full waveform acoustic logs and crosswell seismic profiles in situations where borehole effects were significant. The generalized R/T matrices method also successfully simulated a high frequency propagation problem while the conventional formulation failed. However, their study was applicable only to the simulation of monopole logging measurements in isotropic elastic formations.

Multipole logging tools offer several advantages over monopole tools, such as a deeper depth of investigation (Baker et al., 1988), insensitivity to borehole washouts, and the ability to reliably measure shear wave speed in slow formations. Therefore, it is very important to develop algorithms that can simulate multipole acoustic logging measurements. In this study, the method of generalized reflection and transmission matrices is extended to compute seismograms due to multipole sources. To verify and benchmark the formulation, dipole and quadruple waveforms computed using the proposed algorithm are compared to those of Schmitt (1988) and Kurkjian et al. (1986).

The generalized reflection and transmission matrices method can also be extended to compute the acoustic waveforms in boreholes penetrating radially layered anisotropic formations. Finally, it is shown that the formulation for multipole sources is a general case of the monopole source formulation given by Chen et al. (1996).

3.2 FORMULATION OF THE GENERALIZED R/T MATRICES METHOD USING MULTIPOLE SOURCES

Simulation of borehole acoustic measurements due to a multipole source is formulated in cylindrical coordinates and in the frequency-wavenumber domain. The space-time domain response is obtained by applying a discrete wavenumber integral and an FFT to the analytical representation.

3.2.1 Mathematical Representation of a Multipole Source

A multipole acoustic source of order *n* is constructed by placing 2*n* monopoles in the same horizontal plane (Kurkjian and Chang, 1986). Each monopole is located at a distance δ from the axis of symmetry of the cylindrical coordinates $r = 0$. The expression for the displacement potential associated with the multipole source in a borehole fluid is given by

$$\phi_f = -\frac{i}{4} S(\omega) \frac{\varepsilon_n}{n!} \left(\frac{kp_f \delta}{2} \right)^n H_n^{(1)}\left(kp_f r\right) \cos(n\theta) e^{ikz}, \tag{3.1}$$

where $H_n^{(1)}$ denotes the Hankel function of the first kind and order *n*, ω is the angular frequency of the source, i is the imaginary unit $\left(\sqrt{-1}\right)$, S is the source frequency spectrum, kp_f and k are the radial and axial components of the fluid wavenumber, respectively, and ε_n is the Neumann's factor (defined to be 2 for all *n,* except for *n* = 0 in which case it takes the value of 1).

3.2.2 The Acoustic Field in the Borehole Fluid

The acoustic field in the borehole fluid excited by a multipole source also placed in the borehole fluid can be represented mathematically as the sum of two components: the first component is the contribution due to the source alone, while the second component is due to the interaction of the source with the formation. The total displacement potential in the borehole fluid can be written as

$$\phi_f = -\frac{i}{4} S(\omega) \frac{1}{n!} \left(\frac{k p_f \delta}{2} \right)^n \left[\varepsilon_n H_n^{(1)}\left(k p_f r\right) + A_n(k,\omega) J_n\left(k p_f r\right) \right] \cos(n\theta) e^{ikz} , \tag{3.2}$$

where the first term in equation (3.2) is the direct field term and the second term is the field due to the presence of rock formation surrounding the borehole. The term "reflected field" is used to indicate this type of contribution. The reflected field is of the same form as the direct field except that its radial dependence is that of a Bessel function, rather than of a Hankel function, and there is an additional *f-k* weighting function, $A_n(k,\omega)$, included as a multiplicative factor.

The displacement in the borehole fluid exhibits radial, azimuthal, and axial components, which can be written in terms of the displacement potential as

$$\mathbf{U} = u_f \hat{r} + v_f \hat{\theta} + w_f \hat{z} , \tag{3.3}$$

where

$$u_f = \frac{\partial \phi_f}{\partial r} , \tag{3.4}$$

$$v_f = \frac{1}{r} \frac{\partial \phi_f}{\partial \theta} , \tag{3.5}$$

$$w_f = \frac{\partial \phi_f}{\partial z} , \tag{3.6}$$

and $\hat{r}$, $\hat{\theta}$, and $\hat{z}$ are the unit vectors in the radial, azimuthal, and vertical directions, respectively.

The pressure P in the borehole fluid is equal to the negative value of the radial component of normal stress in the borehole fluid, and is given by

$$P = -\sigma_{rr} = \omega^2 \rho_f \phi_f \,, \tag{3.7}$$

where ρ_f is the density of the borehole fluid.

3.2.3 The Elastic Wavefield in the Formation

The elastic wave equation for an isotropic homogeneous solid is given by (Aki and Richards, 1980)

$$-\omega^2 \rho \mathbf{U} = (\lambda + 2\mu)\nabla(\nabla \cdot \mathbf{U}) - \mu \nabla \times (\nabla \times \mathbf{U}), \tag{3.8}$$

where λ and μ are the Lamé constants of the medium, and ρ is the density of the medium.

The displacement vector can be expressed in terms of potentials as

$$\mathbf{U} = \nabla \phi + \nabla \times (\chi \hat{z}) + \nabla \times \nabla \times (\gamma \hat{z}), \tag{3.9}$$

where ϕ is the compressional (P) wave potential, χ is the vertically polarized shear (SV) wave potential, and γ is the horizontally polarized shear (SH) wave potential. These displacement potentials satisfy the Helmholtz equations

$$\left(\nabla^2 + k_c^2\right)\phi = 0 \,, \tag{3.10}$$

$$\left(\nabla^2 + k_s^2\right)\chi = 0 \,, \tag{3.11}$$

and

$$\left(\nabla^2 + k_s^2\right)\gamma = 0 \,, \tag{3.12}$$

where k_c and k_s are the compressional and shear wavenumbers given by $k_c = \omega / v_c$ and $k_s = \omega / v_s$. Here v_c and v_s are the compressional and shear wave speeds of the formation, respectively.

The solution of equations (3.10) through (3.12) yields the potentials in the formation. In a radially multi-layered formation, let j be the layer index, with j = 1, 2, …, N. Within the borehole fluid, j=1. In layer j (j=2, …, N-1), both outward-directed and incoming (reflected) waves exist. In the outermost layer N, only outward-directed waves exist as required by the radiation condition.

Thus, the solution for the potentials corresponding to an *n*th-order multipole source in layer j (j=2, …, N-1) can be written as

$$\phi_j = \left[c_{P_j -} e^{ikp_j\left(r_j - r\right)} \overline{H}_n^{(2)}\left(kp_j r\right) + c_{P_j +} e^{ikp_j\left(r - r_{j-1}\right)} \overline{H}_n^{(1)}\left(kp_j r\right) \right] \cos(n\theta) e^{ikz}, \qquad (3.13)$$

$$\chi_j = \left[c_{SH_j -} e^{iks_j\left(r_j - r\right)} \overline{H}_n^{(2)}\left(ks_j r\right) + c_{SH_j +} e^{iks_j\left(r - r_{j-1}\right)} \overline{H}_n^{(1)}\left(ks_j r\right) \right] \sin(n\theta) e^{ikz}, \qquad (3.14)$$

and

$$\gamma_j = \left[c_{SV_j -} e^{iks_j\left(r_j - r\right)} \overline{H}_n^{(2)}\left(ks_j r\right) + c_{SV_j +} e^{iks_j\left(r - r_{j-1}\right)} \overline{H}_n^{(1)}\left(ks_j r\right) \right] \cos(n\theta) e^{ikz}, \qquad (3.15)$$

where the coefficients $c_{P_j -}$, $c_{P_j +}$, $c_{SH_j -}$, $c_{SH_j +}$, $c_{SV_j -}$ and $c_{SV_j +}$ are unknown, with the subscript "+" used to identify outward-directed waves and the subscript "-" used to identify incoming waves. In the same equations, kp_j and ks_j are the radial components of the compressional and shear wavenumbers, respectively, r_j and r_{j-1} are the outer and inner radius of layer j, and $\overline{H}_n^{(1)}\left(kp_f r\right)$ and $\overline{H}_n^{(2)}\left(kp_f r\right)$ are normalized Hankel functions. The adoption of normalized Hankel functions makes the algorithm numerically stable even for high-frequency problems, i.e., when the thickness of the radial formation layer is greater than the corresponding characteristic wavelength.

In the outermost layer (*j=N*), there exist only outward-directed waves, i.e.,

$$\phi_j = c_{P_j+} e^{ikp_j\left(r-r_{j-1}\right)} \overline{H}_n^{(1)}\left(kp_j r\right)\cos(n\theta)e^{ikz}, \tag{3.16}$$

$$\chi_j = c_{SH_j+} e^{iks_j\left(r-r_{j-1}\right)} \overline{H}_n^{(1)}\left(ks_j r\right)\sin(n\theta)e^{ikz}, \tag{3.17}$$

and

$$\gamma_j = c_{SV_j+} e^{iks_j\left(r-r_{j-1}\right)} \overline{H}_n^{(1)}\left(ks_j r\right)\cos(n\theta)e^{ikz}. \tag{3.18}$$

For j=1 (within the fluid-filled borehole), one can drop the coefficient $\frac{1}{n!}\left(\frac{kp_f\delta}{2}\right)^n$ in equation (3.1) and make use of the properties of Bessel functions, namely,

$$2J_n(kr) = H_n^{(1)}(kr) + H_n^{(2)}(kr), \tag{3.19}$$

to arrive at

$$\begin{aligned}\phi_f &= \left[cJ_n\left(kp_f r\right) + s_+ H_n^{(1)}\left(kp_f r\right)\right]\cos(n\theta)e^{ikz} \\ &= \left[c_{P_1-} e^{ikp_f\left(r_1-r\right)} \overline{H}_n^{(2)}\left(kp_f r\right) + \left(c_{P_1+} + s_+\right) e^{ikp_f r} \overline{H}_n^{(1)}\left(kp_f r\right)\right]\cos(n\theta)e^{ikz},\end{aligned} \tag{3.20}$$

where

$$c_{P_1+} = c_{P_1-} e^{ikp_f r_1} = \frac{c}{2}, \tag{3.21}$$

$$s_+ = -\frac{i\varepsilon_n}{4} S(\omega), \tag{3.22}$$

$$kp_f = \left(k_f^2 - k^2\right)^{1/2} \left[\operatorname{Im}\left(kp_f\right) > 0\right], \tag{3.23}$$

and

$$k_f = \frac{\omega}{v_f}, \tag{3.24}$$

where k_f is the acoustic wavenumber in the fluid, k is the axial component of a wavenumber, c is a coefficient yet to be determined, and J_n is the Bessel function of the first kind and order n. By comparing equation (3.20) to equation (3.2), it follows that

$$c = S(\omega)A_n(k,\omega). \tag{3.25}$$

Expressions for the radial, azimuthal, and axial components of the displacement can be written in terms of potentials as

$$u = \frac{\partial\phi}{\partial r} + \frac{1}{r}\frac{\partial\chi}{\partial\theta} + \frac{\partial^2\gamma}{\partial r\partial z}, \tag{3.26}$$

$$v = \frac{1}{r}\frac{\partial\phi}{\partial\theta} - \frac{\partial\chi}{\partial r} + \frac{1}{r}\frac{\partial^2\gamma}{\partial\theta\partial z}, \tag{3.27}$$

and

$$w = \frac{\partial\phi}{\partial z} - \nabla^2\gamma + \frac{\partial^2\gamma}{\partial z^2}. \tag{3.28}$$

The stresses in the formation are given in terms of the displacement and compressional potential by (Achenbach, 1973)

$$\sigma_{rr} = -\lambda k_c^2\phi + 2\mu\frac{\partial u}{\partial r}, \tag{3.29}$$

$$\sigma_{r\theta} = \mu\left[\frac{\partial v}{\partial r} - \frac{1}{r}v + \frac{1}{r}\frac{\partial u}{\partial\theta}\right], \tag{3.30}$$

and

$$\sigma_{rz} = \mu\left[\frac{\partial u}{\partial z} + \frac{\partial w}{\partial r}\right]. \tag{3.31}$$

Using the above potential solutions and their relationships with displacement and stress, one obtains radial, tangential, and azimuthal components of displacement and stress in solid layers, given by

$$\begin{bmatrix} u \\ v \\ w \\ \sigma_{rr} \\ \sigma_{r\theta} \\ \sigma_{rz} \end{bmatrix} = E_j \begin{bmatrix} c_{P_j-} \\ c_{SH_j-} \\ c_{SV_j-} \\ c_{P_j+} \\ c_{SH_j+} \\ c_{SV_j+} \end{bmatrix} = \begin{bmatrix} e_{11} & e_{12} & e_{13} & e_{14} & e_{15} & e_{16} \\ e_{21} & e_{22} & e_{23} & e_{24} & e_{25} & e_{26} \\ e_{31} & e_{32} & e_{33} & e_{34} & e_{35} & e_{36} \\ e_{41} & e_{42} & e_{43} & e_{44} & e_{45} & e_{46} \\ e_{51} & e_{52} & e_{53} & e_{54} & e_{55} & e_{56} \\ e_{61} & e_{62} & e_{63} & e_{64} & e_{65} & e_{66} \end{bmatrix} \begin{bmatrix} c_{P_j-} \\ c_{SH_j-} \\ c_{SV_j-} \\ c_{P_j+} \\ c_{SH_j+} \\ c_{SV_j+} \end{bmatrix} , \qquad (3.32)$$

where ***E_j*** is a 6 by 6 matrix whose entries $\{e_{mn}\}_j$ are derived in Appendix F.

For the borehole fluid layer, one has

$$\begin{bmatrix} u \\ \sigma_{rr} \end{bmatrix} = E_1 \begin{bmatrix} c_{P1-} \\ c_{P1+} + s_+ \end{bmatrix}, \qquad (3.33)$$

where E_1 is a 2 by 2 matrix whose entries $\{e_{mn}\}_j$ are derived in the Appendix F.

3.2.4 Boundary Conditions

To determine the unknown coefficients for each layer (i.e., c_{P_j-}, c_{P_j+}, c_{SH_j-}, c_{SH_j+}, c_{SV_j-} and c_{SV_j+}), one need to impose boundary conditions at each layer interface. For an interface between two solid layers, a welded contact boundary condition is imposed. In other words, one enforces the continuity of radial, tangential, and azimuthal components of displacement and stress. In matrix form, the boundary condition at $r = r_j$ (j=2, 3, …, N-1) can be written as:

$$\begin{bmatrix} u \\ v \\ w \\ \sigma_{rr} \\ \sigma_{r\theta} \\ \sigma_{rz} \end{bmatrix}_j = \begin{bmatrix} u \\ v \\ w \\ \sigma_{rr} \\ \sigma_{r\theta} \\ \sigma_{rz} \end{bmatrix}_{j+1} . \tag{3.34}$$

At the boundary between the borehole and the adjacent solid layer (formation or steel casing), boundary conditions require the continuity of the radial components of both displacement and stress. For this particular case, however, the tangential and azimuthal components of stress become zero. The tangential and azimuthal components of the displacement are not continuous since fluid in the borehole is free to move in the tangential and azimuthal directions. In matrix form, the corresponding boundary conditions can be written as

$$\begin{bmatrix} u \\ \sigma_{rr} \\ 0 \\ 0 \end{bmatrix}_{j=1} = \begin{bmatrix} u \\ \sigma_{rr} \\ \sigma_{r\theta} \\ \sigma_{rz} \end{bmatrix}_{j=2} . \tag{3.35}$$

To develop the formulation based on the generalized R/T matrices method, one first considers a simple borehole case, in which the borehole penetrates a homogeneous and isotropic infinite rock formation.

3.3 THE GENERALIZED R/T MATRICES FOR A SIMPLE BOREHOLE CASE

In the simple borehole case, there are only outward-directed waves in the formation in order to satisfy the radiation condition at infinity. The wave field in the borehole fluid can be decomposed into the outward-directed wave due to the source emission and the incoming wave due to reflection at the fluid-solid boundary. To effectively determine the unknown coefficients for each layer, the modified and generalized reflection and transmission matrices are introduced and computed using a recursive scheme (Chen et al., 1996). This is done as follows. The modified R/T matrices, $\mathrm{R}_{+-}^{(1)}$ and $\mathbf{T}_{+}^{(1)}$ are defined by the relations

$$\begin{cases} c_{-}^{(1)} = R_{+-}^{(1)}\left(c_{+}^{(1)} + s_{+}\right) \\ \mathbf{C}_{+}^{(2)} = \mathbf{T}_{+}^{(1)}\left(c_{+}^{(1)} + s_{+}\right) \end{cases} , \tag{3.36}$$

where $c_{\pm}^{(1)} = c_{P_1\pm}$, $R_{+-}^{(1)}$ is a scalar, and $\mathbf{T}_{+}^{(1)}$ is a 3 by 1 matrix, respectively. Substitution of equations (3.32) and (3.33) into equation (3.35), and comparison of the result with equation (3.36), yield the R/T matrices

$$\begin{bmatrix} R_{+-}^{(1)} \\ \mathbf{T}_{+}^{(1)} \end{bmatrix} = \begin{bmatrix} e_{11}^{(1)} & -e_{14}^{(2)} & -e_{15}^{(2)} & -e_{16}^{(2)} \\ e_{21}^{(1)} & -e_{44}^{(2)} & -e_{45}^{(2)} & -e_{46}^{(2)} \\ 0 & -e_{54}^{(2)} & -e_{55}^{(2)} & -e_{56}^{(2)} \\ 0 & -e_{64}^{(2)} & -e_{65}^{(2)} & -e_{66}^{(2)} \end{bmatrix}^{-1} \begin{bmatrix} -e_{12}^{(1)} \\ -e_{22}^{(1)} \\ 0 \\ 0 \end{bmatrix} . \tag{3.37}$$

The generalized R/T matrices $\hat{\mathbf{R}}_{+-}^{(j)}$ and $\hat{\mathbf{T}}_{+}^{(j)}$ are the same as the modified R/T matrices, respectively, namely,

$$\begin{cases} \hat{\mathbf{T}}_{+}^{(1)} = \mathbf{T}_{+}^{(1)} \\ \hat{R}_{+-}^{(1)} = R_{+-}^{(1)} \end{cases} , \tag{3.38}$$

where $\hat{\mathbf{T}}_{+}^{(1)}$ is a 3 by 1 matrix, and $\hat{R}_{+-}^{(1)} = R_{+-}^{(j)}$ is a scalar.

3.4 THE GENERALIZED R/T MATRICES FOR A RADIALLY MULTI-LAYERED BOREHOLE CASE

It is clear that the outward directed (+) wave in layer *j+1* is the superposition of the transmitted outward-directed wave from layer j and the reflected incoming (-) wave from layer *j+1*. Similarly, the incoming wave in layer j is the superposition of the transmitted incoming wave from layer *j+1* and the reflected outward-directed wave from layer j. Consequently, the modified R/T matrices, $\mathbf{R}_{+-}^{(j)}, \mathbf{T}_{-}^{(j)}, \mathbf{T}_{+}^{(j)}$, and $\mathbf{R}_{-+}^{(j)}$ for solid-solid interfaces are defined by the relations

$$\begin{cases} \mathbf{C}_{-}^{(j)} = \mathbf{R}_{+-}^{(j)}\mathbf{C}_{+}^{(j)} + \mathbf{T}_{-}^{(j)}\mathbf{C}_{-}^{(j+1)} \\ \mathbf{C}_{+}^{(j+1)} = \mathbf{T}_{+}^{(j)}\mathbf{C}_{+}^{(j)} + \mathbf{R}_{-+}^{(j)}\mathbf{C}_{-}^{(j+1)} \end{cases}, \text{ for } j = 2, 3, \ldots, N\text{-}1. \tag{3.39}$$

The modified R/T matrices are 3 by 3 matrices. For the first interface (fluid-solid), the modified R/T matrices, $\mathrm{R}_{+-}^{(1)}$ (scalar), $\mathbf{T}_{-}^{(1)}$, $\mathbf{T}_{+}^{(1)}$, and $\mathbf{R}_{-+}^{(1)}$ are defined by

$$\begin{cases} c_{-}^{(1)} = \mathrm{R}_{+-}^{(1)}\left(c_{+}^{(1)} + s_{+}\right) + \mathbf{T}_{-}^{(1)}\mathbf{C}_{-}^{(2)} \\ \mathbf{C}_{+}^{(2)} = \mathbf{T}_{+}^{(1)}\left(c_{+}^{(1)} + s_{+}\right) + \mathbf{R}_{-+}^{(1)}\mathbf{C}_{-}^{(2)} \end{cases}, \tag{3.40}$$

where $c_{\pm}^{(1)} = c_{P_1\pm}$, $R_{+-}^{(1)}$ is a scalar, and $\mathbf{T}_{-}^{(1)}, \mathbf{T}_{+}^{(1)}$ and $\mathbf{R}_{-+}^{(1)}$ are 1 by 3, 3 by 1, and 3 by 3 matrices, respectively.

From equation (3.34), it follows that block partition and multiplication of the *E* matrices and direct comparison with the R/T matrices relationship yield

$$\begin{bmatrix} \mathbf{R}_{+-}^{(j)} & \mathbf{T}_{-}^{(j)} \\ \mathbf{T}_{+}^{(j)} & \mathbf{R}_{-+}^{(j)} \end{bmatrix} = \begin{bmatrix} E_{:,1}^{(j)} & E_{:,2}^{(j)} & E_{:,3}^{(j)} & -E_{:,4}^{(j+1)} & -E_{:,5}^{(j+1)} & -E_{:,6}^{(j+1)} \end{bmatrix}^{-1} \times \begin{bmatrix} -E_{:,4}^{(j)} & -E_{:,5}^{(j)} & -E_{:,6}^{(j)} & E_{:,1}^{(j+1)} & E_{:,2}^{(j+1)} & E_{:,3}^{(j+1)} \end{bmatrix}, \tag{3.41}$$

where $E_{:,i}^{(j)}$ are column vectors whose 6 entries are the corresponding entries of matrix $\boldsymbol{E_j}$ ($j=2, 3, \ldots, N\text{-}1, i=1, 2, \ldots, 6$).

Similarly, for the fluid-solid interface, one has

$$\begin{bmatrix} R_{+-}^{(1)} & \mathbf{T}_{-}^{(1)} \\ \mathbf{T}_{+}^{(1)} & \mathbf{R}_{-+}^{(1)} \end{bmatrix} = \begin{bmatrix} e_{11}^{(1)} & -e_{14}^{(2)} & -e_{15}^{(2)} & -e_{16}^{(2)} \\ e_{21}^{(1)} & -e_{44}^{(2)} & -e_{45}^{(2)} & -e_{46}^{(2)} \\ 0 & -e_{54}^{(2)} & -e_{55}^{(2)} & -e_{56}^{(2)} \\ 0 & -e_{64}^{(2)} & -e_{65}^{(2)} & -e_{66}^{(2)} \end{bmatrix}^{-1} \times \begin{bmatrix} -e_{12}^{(1)} & e_{11}^{(2)} & e_{12}^{(2)} & e_{13}^{(2)} \\ -e_{22}^{(1)} & e_{41}^{(2)} & e_{42}^{(2)} & e_{43}^{(2)} \\ 0 & e_{51}^{(2)} & e_{52}^{(2)} & e_{53}^{(2)} \\ 0 & e_{61}^{(2)} & e_{62}^{(2)} & e_{63}^{(2)} \end{bmatrix}. \tag{3.42}$$

The generalized R/T matrices $\hat{\mathbf{R}}_{+-}^{(j)}$ and $\hat{\mathbf{T}}_{+}^{(j)}$ are defined by the relations

$$\begin{cases}\mathbf{c}_+^{(j+1)} = \hat{\mathbf{T}}_+^{(j)}\mathbf{c}_+^{(j)} \\ \mathbf{c}_-^{(j)} = \hat{\mathbf{R}}_{+-}^{(j)}\mathbf{c}_+^{(j)}\end{cases} \text{, for } j=2, 3, \ldots, N\text{-}1, \tag{3.43}$$

and

$$\begin{cases}\mathbf{c}_+^{(2)} = \hat{\mathbf{T}}_+^{(1)}\left(c_+^{(1)} + s_+\right) \\ c_-^{(1)} = \hat{R}_{+-}^{(j)}\left(c_+^{(1)} + s_+\right)\end{cases}. \tag{3.44}$$

By substituting equations (3.43) and (3.44) into equations (3.39) and (3.40), respectively, and by rearranging terms, one obtains the recursive relationship

$$\begin{cases}\hat{\mathrm{T}}_+^{(j)} = \left[\mathrm{I}\text{-}\mathrm{R}_{-+}^{(j)}\hat{\mathrm{R}}_{+-}^{(j+1)}\right]^{-1}\mathrm{T}_+^{(j)} \\ \hat{\mathrm{R}}_{+-}^{(j)} = \mathrm{R}_{+-}^{(j)} + \mathrm{T}_-^{(j)}\hat{\mathrm{R}}_{+-}^{(j+1)}\hat{\mathrm{T}}_+^{(j)}\end{cases} \text{, for j = N-1, N-2, …, 2, 1,} \tag{3.45}$$

where **I** is the identity matrix, $\hat{\mathbf{R}}_{+-}^{(j)}$ and $\hat{\mathbf{T}}_+^{(j)}$ are 3 by 3 matrices for $j > 1$, $\hat{\mathbf{T}}_+^{(1)}$ is a 3 by 1 matrix, and $\hat{\mathbf{R}}_{+-}^{(1)} = \hat{R}_{+-}^{(j)}$ is a scalar. In the outer-most layer, N, only outward-directed waves exist and the medium extends to infinity. Therefore, the generalized reflection matrix takes on the form

$$\hat{\mathbf{R}}_{+-}^{(N)} = 0 \, . \tag{3.46}$$

The recursive scheme to compute generalized reflection and transmission coefficients theoretically makes this algorithm more efficient than the Thomson-Haskell method. Simulation of full acoustic waveforms for an eight-receiver array using the method of generalized reflection and transmission matrices takes less than one minutes on a 1 GHz desktop PC. From the author’s experience, the same simulation job using a finite-difference code would take a few hours. Therefore, the newly developed simulation method is much more efficient than the finite-difference method.

3.5 WAVEFORM SYNTHESIS

Having obtained the generalized R/T matrices, the next step is to compute the unknown coefficients c_{P_j-}, c_{P_j+}, c_{SH_j-}, c_{SH_j+}, c_{SV_j-} and c_{SV_j+} for each layer. For the first layer, the unknown coefficients are given by

$$\begin{cases} c_{P_1-} = \hat{R}_{+-}^{(1)}\left(1-\hat{R}_{+-}^{(1)}e^{ikp_f r_1}\right)^{-1}s_+ \\ c_{P_1+}+s_+ = \left(1-\hat{R}_{+-}^{(1)}e^{ikp_f r_1}\right)^{-1}s_+ \end{cases}. \tag{3.47}$$

In multipole acoustic logging, depending on the order of the multipole, the receivers sense different physical properties. Displacement is recorded if the source is a dipole, the spatial derivative of radial displacement is recorded if the source is a quadrupole, and higher-order gradients are recorded for multipole sources of higher orders.

For a multipole of order n, the quantity measured in the fluid-filled borehole is given by

$$\begin{aligned} \phi_{total} &= \frac{\partial^n}{\partial r^n}\phi_f \\ &= \frac{\partial^n}{\partial r^n}\left[c_{P_1-}e^{ikp_f r_1}H_n^{(2)}\left(kp_f r\right)+\left(c_{P_1+}+s_+\right)H_n^{(1)}\left(kp_f r\right)\right]. \end{aligned} \tag{3.48}$$

Substitution of equation (3.47) into the above equation yields the solution in the *f*-*k* domain, namely,

$$\begin{aligned} \phi_{total} &= \frac{\partial^n}{\partial r^n}\left[\frac{\hat{R}_{+-}^{(1)}e^{ikp_f r_1}H_n^{(2)}\left(kp_f r\right)+H_n^{(1)}\left(kp_f r\right)}{1-\hat{R}_{+-}^{(1)}e^{ikp_f r_1}}\right]s_+ \\ &= \frac{\partial^n}{\partial r^n}\left[\frac{\hat{R}_{+-}^{(1)}e^{ikp_f r_1}\left(H_n^{(2)}\left(kp_f r\right)+H_n^{(1)}\left(kp_f r\right)\right)}{1-\hat{R}_{+-}^{(1)}e^{ikp_f r_1}}+H_n^{(1)}\left(kp_f r\right)\right]s_+ \\ &= \frac{\partial^n}{\partial r^n}\left[\frac{2J_n\left(kp_f r\right)\hat{R}_{+-}^{(1)}e^{ikp_f r_1}}{1-\hat{R}_{+-}^{(1)}e^{ikp_f r_1}}+H_n^{(1)}\left(kp_f r\right)\right]s_+ \end{aligned}. \tag{3.49}$$

It is remarked that the first term in the last line of equation (3.49) is the reflected field and that the second term is the direct field. Making use of the relationship

$$\left.\frac{\partial^n J_n(kp_f r)}{\partial r^n}\right|_{r=0} = \left(\frac{kp_f}{2}\right)^n \quad , \tag{3.50}$$

one can write the reflected field in the *f-k* domain as

$$\phi_{reflect}(r,\omega,k) = \frac{-i\varepsilon_n \delta^n}{2n!}\left(\frac{kp_f}{2}\right)^{2n} \frac{\hat{R}_{+-}^{(1)} e^{ikp_f r_1}}{1-\hat{R}_{+-}^{(1)} e^{ikp_f r_1}} S(\omega). \tag{3.51}$$

Similarly, for the direct field in the frequency-space domain one has

$$\phi_{direct}(r,z,\omega) = \frac{1}{2\pi}\left[\int_{-\infty}^{\infty} \frac{\partial^n}{\partial r^n} H_n^{(1)}(kp_f r) e^{ikz} dk\right] s_+$$

$$= \frac{-\varepsilon_n \delta^n}{4\pi n! 2^{2n}} \left\{\sum_{m=0}^{n} \binom{n}{m} \left(\frac{-2i\omega}{v_f}\right)^m \frac{(2n-m)!}{z^{2n-m+1}}\right\} e^{ik_f z} S(\omega). \tag{3.52}$$

In the space-time domain, the receiver response for a multipole source is given by

$$\phi_{total}(r,z,t) = \phi_{reflect}(r,z,t) + \phi_{direct}(r,z,t)$$

$$= \frac{1}{2\pi}\int_{-\infty}^{\infty} S(\omega) e^{-i\omega t} d\omega \ \times$$

$$\left[\phi_{direct}(r,z,\omega) + \frac{1}{2\pi}\int_{-\infty}^{\infty} \frac{-i\varepsilon_n \delta^n}{2n!}\left(\frac{kp_f}{2}\right)^{2n} \frac{\hat{R}_{+-}^{(1)} e^{ikp_f r_1}}{1-\hat{R}_{+-}^{(1)} e^{ikp_f r_1}} e^{ikz} dk\right]$$

$$= -\frac{1}{2\pi}\frac{\varepsilon_n \delta^n}{4\pi n! 2^{2n}}\int_{-\infty}^{\infty} S(\omega) e^{-i\omega t} d\omega \times$$

$$\left[\left\{\sum_{m=0}^{n} \binom{n}{m} \left(\frac{-2i\omega}{v_f}\right)^m \frac{(2n-m)!}{z^{2n-m+1}}\right\} e^{ik_f z} + i\int_{-\infty}^{\infty} \frac{\hat{R}_{+-}^{(1)} e^{ikp_f r_1}}{1-\hat{R}_{+-}^{(1)} e^{ikp_f r_1}} (kp_f)^{2n} e^{ikz} dk\right]. \tag{3.53}$$

3.6 RELATIONSHIP BETWEEN THE FORMULATION OF THE MULTIPOLE CASE AND THAT OF THE MONOPOLE CASE

When the source is a monopole (*n* = 0), only *P* and *SV* waves are generated in the formation. The boundary conditions are simplified since explicit enforcement of the continuity of azimuthal components of displacement and stress is not necessary. Therefore, all the expressions that involve the azimuth can be dropped from the multipole formulation. Because the SH wave is not excited in the formation, the coefficients of the SH wave potential are equal to zero. Therefore, the displacement-stress vector exhibits only four non-zero components, and the ***E*** matrix in equation (3.32) becomes a 4 by 4 matrix. By collecting the remaining terms in equation (3.32) and after some algebraic manipulation, the formulation presented in this study yields the same monopole-case formulation described by Chen et al. (1996).

As for the pressure measurements in the monopole case, directly from the expression for multipole measurements (equation (3.53)), one obtains

$$\phi_{total}(r,z,t) = -\frac{1}{2\pi}\frac{1}{4\pi}\int_{-\infty}^{\infty} S(\omega) e^{-i\omega t} d\omega \times \left[i\int_{-\infty}^{\infty} \frac{\hat{R}_{+-}^{(1)} e^{ikp_f r_1}}{1-\hat{R}_{+-}^{(1)} e^{ikp_f r_1}} e^{ikz} dk + \frac{e^{ik_f z}}{z} \right] . \tag{3.54}$$

This expression agrees with equation (20) in Chen et al. (1996) under the assumption of centered tools, in which case r = 0 and the source receiver distance R = z.

3.7 THEORETICAL COMPARISON BETWEEN THE THOMSON-HASKELL METHOD AND THE GENERALIZED R/T MATRICES METHOD

In this section, the example of a centered monopole source in the borehole (Figure 3.1) is used to perform a theoretical comparison between the Thomson-Haskell method and the generalized R/T matrices method. Because the configuration of the problem is radially symmetric, only *P* and *SV* waves are excited in the formation. Both methods are based on the potential solutions ϕ and χ of the Helmholtz equations (3.10) and (3.11) for *P* and *SV* waves, respectively. However, in the Thomson-Haskell method, the radial and axial displacements and stresses in the cylindrical solid layers are defined by

$$U_j(r) = D_j(r)C_j(r), \tag{3.55}$$

for layer j, where U_j is the displacement-stress vector, D_j is a propagator matrix whose entries are given in terms of Bessel functions, and C_j is the coefficient vector of the potential solutions. Layer j has an outer radius equal to r_j and an inner radius equal to r_{j-1}. By enforcing boundary conditions, the displacement-stress vector U_j can be related across the layer through the expression

$$U_j(r_j) = D_j(r_j)D_j^{-1}(r_{j-1})U_j(r_{j-1}). \tag{3.56}$$

Across solid layer boundaries, displacements and stresses are continuous. Thus, the coefficient vector of the outermost layer and that of the first solid layer are connected by the product of the propagator matrices. By applying the radiation condition at the outermost layer, only the coefficients for the outward-directed wave do not vanish. At the borehole wall, which is a fluid-solid interface, the radial displacement and stress are continuous; the axial displacement can be discontinuous, and the tangential stress is zero for an inviscid fluid. The reflection coefficient at the borehole wall can be determined through this boundary condition. Subsequently, the pressure response in the borehole can be computed with the formula given by Tsang and Rader (1979).

For the generalized R/T matrices method, the modified R/T matrices defined by equations (3.39) and (3.40) first relate reflection and transmission coefficients of incoming and outward-directed waves in each layer (Figure 3.1). By considering two adjacent solid layers *j* and *j+1*, in layer j, the incoming wave coefficient is the superposition of the transmitted incoming wave from layer *j+1* and the reflected outward-directed wave of layer j. In layer *j+1*, the coefficient for the outward-directed wave is the superposition of the transmitted outward-directed wave from layer j and the reflected incoming wave of layer *j+1*. By substituting the equations for displacement-stress vector into the equations for the boundary condition at the interface between layer j and *j+1*, and by comparing with equations (3.39) and (3.40), modified R/T matrices ensue for each layer.

The generalized R/T matrices are defined by equations (3.43) and (3.44) and are computed recursively using equation (3.45) from the modified R/T matrices. Given that the normalized Hankel functions and the normalization factors $e^{ikp_j r_j}$, $e^{iks_j r_j}$, $e^{-ikp_j r_{j-1}}$ and $e^{-iks_j r_{j-1}}$ in the potential solutions are used, the algorithm is numerically stable. When the generalized reflection coefficient at the borehole boundary is obtained, the receiver responses can be readily computed using equation (3.54).

3.8 VALIDATION OF THE GENERALIZED R/T MATRICES METHOD

To compute the receiver responses using equation (3.53), one first uses the discrete wavenumber integral method (Bouchon and Aki, 1977) to perform the summation over wavenumber domain. Subsequently, the fast Fourier transform (FFT) is used to transform the responses from the frequency to the time domain. For the verification of the formulation and implementation, simulation results are compared to those of the Thomson-Haskell method assuming both a simple borehole cases as well as cases of rock formations subject to mud-filtrate invasion.

3.8.1 Simple Borehole Cases

For cases in which the borehole penetrates a homogeneous formation, one makes use of the formulation developed by Kurkjian and Chang (1986), which is the simplest case of the Thomson-Haskell and the generalized R/T matrices methods. Both fast and slow formations are considered in the comparison. A formation is said to be fast when the shear velocity of the formation is faster than the compressional velocity of the borehole fluid. By contrast, when the shear velocity of the formation is slower than the compressional velocity of the borehole fluid, the formation is defined as a slow formation. The corresponding formation parameters and tool and borehole configurations are listed in Table 3.1.

It is assumed that the central frequency of the dipole and quadrupole sources is 4 kHz. The frequency spectra of the sources is that of a Ricker wavelet, given by

$$\left(\frac{\omega}{\omega_0}\right)^2 e^{-\left(\frac{\omega}{\omega_0}\right)^2}, \tag{3.57}$$

where ω and ω_0 are the angular frequency, and source central frequency, respectively. A Ricker wavelet is also used as the source wavelet throughout this chapter.

In Figure 3.2(a), the dipole waveforms for a fast formation (Table 3.1) calculated using the Thomson-Haskell (T-H) and the R/T matrices methods almost completely overlay each other. The difference between the two sets of waveforms shown in Figure 3.2(b) is negligible. Figure 3.3 shows the overlay of and the difference between the quadrupole waveforms calculated with the two simulation methods. Similar conclusions are drawn concerning the accuracy of the simulations. Therefore, by comparing the dipole and quadrupole waveforms in the case of a fast formation in Figures 3.2 and 3.3, a good agreement is found between the results yielded by the two methods. An excellent agreement between the results of the Thomson-Haskell (T-H) and the R/T matrices methods is also shown in Figures 3.4 and 3.5 for the case of a slow formation whose properties are described in Table 3.1.

3.8.2 Boreholes with Invaded Zones

For the case of a sharp-boundary invaded zone, simulation results are compared to those reported by Schmitt (1988) and computed using the Thomson-Haskell method. Table 3.2 describes the densities, velocities and quality factors of the fluid, invaded zone and formation. Attenuation is introduced through the use of a complex-valued velocity defined by

$$v(\omega) = v(\omega_0)\left[1 + \frac{1}{\pi Q}\ln\left(\frac{\omega_0}{\omega}\right) - \frac{i}{2Q}\right], \tag{3.58}$$

where Q is the quality factor for either P- or S-wave, and v is the P- or S-wave velocity. The multipole separation, δ, is 1 cm, while the borehole radius is 10 cm. Figure 3.6 shows waveforms computed with the generalized R/T and the Thomson-Haskell methods for a fast sandstone virgin formation and for formations with 8 and 16 cm invaded zones, respectively. In Figures 3.7(a) and 3.7(b), the waveforms in the top panel are computed assuming a slow sandstone formation, those in the middle panel correspond to the same formation with an 8 cm invaded zone near the wellbore, and those at the bottom are for a formation with a 16 cm invaded zone. In Figures 3.6 and 3.7, the central frequency of the dipole source is 3 kHz. The waveforms in Figures 3.6(a) and 3.7(a) are in excellent agreement with those shown in Figures 3.6(b) and 3.7(b), respectively.

3.8.3 Long-spacing Quadrupole Logging

Waveforms simulated using the generalized R/T matrices method indicate that a quadrupole tool investigates deeper into the formation than a monopole tool by a factor of

$$\frac{\alpha_3}{\alpha_2}+1, \tag{3.59}$$

where α_2 and α_3 are compressional velocities for the invaded zone and virgin formation, respectively. In practice, $\alpha_3 > \alpha_2$. Thus, higher-order multipole tools allow the measurement of two to three times the distance from the wellbore compared to monopole tools, and therefore exhibit more sensitivity to virgin formation properties (Baker et al. ,1988). Using the same model (Table 3.3) as that presented in Figure 3.6 of Baker et al. (1988), waveforms computed using both simulation methods are compared in Figures 3.8 and 3.9. The difference is that in the current simulations the receivers are centered and in Baker et al.'s (1988) paper they are 0.03 m off-centered. In Figure 3.8, one can see that when the source-receiver spacing is 3 m or longer, the P-wave arrivals for the virgin formation can be clearly detected using a 10 kHz quadrupole source even though the thickness of the invaded zone is 0.92 m. When the central frequency of the source is reduced to 5 kHz, shear arrivals from the virgin formation can be detected with a similar source-receiver spacing. However, the P wave trains are barely visible now.

3.9 FIELD STUDY: MULTIPOLE TOOL LOGGING IN A DEEPLY INVADED FORMATION

In this reservoir study, the well under consideration was drilled in a gas-bearing carbonate formation. The mud was heavy and fresh-water base, and the overbalance pressure was more than 1000 psi. Lithology in the gas-bearing zone consists of inter-layered carbonates along with fine-grained clastics and shales. Porosities are low, usually less than 15%, thereby contributing to deep mud-filtrate invasion. Gas saturation in the formation is about 80-85% with the remaining pore space occupied by irreducible connate water.

Simulation of mud-filtrate invasion was performed on a five-layer synthetic model reconstructed along the depth interval X493-X551 ft (George et al., 2003). A schematic of the model is shown in Figure 3.10. The analysis focuses on the radial invasion profiles within layer 2. Because of the large overbalance pressure caused by the heavy mud column, the invasion zone in this well is very deep. Radial profiles of the P-wave velocity and the formation bulk density are computed using the Biot-Gassmann fluid substitution procedure described by Smith et al. (2003). These profiles are plotted in Figure 3.11 and show the same decreasing trend of P-wave velocity in the radial direction as that of water saturation after 4 days of invasion (Figure 3.11 (a)). The density and P-wave velocity slowly decrease by 1.1% and 0.7% relative to the values measured at the borehole wall, respectively, from the borehole wall to 1.8 m into the formation. These values within 0.2 m to those of the virgin formation at a radial distance of approximately 2 m decrease quickly by 3.4% and 1.7% relative to the values at the borehole wall, respectively.

Depending upon the formation and fluid properties, radial changes in P- and S-wave velocities can be quite large. In the flow unit under consideration, the magnitude of the variations is approximately 2.4%, 2.3% and 4.8% relative to properties of the virgin formation for the P-wave velocity, S-wave velocity, and bulk density, respectively. Changes of S-wave velocity after invasion are approximately equal to the measurement errors recorded in field operations, i.e., around 2%. Therefore, the differences are not expected to be sensed with a standard borehole sonic tool and standard waveform processing technique. However, the difference in P-wave velocity after invasion may be detected if the source-receiver offsets are long enough and a multipole tool is used to perform the measurements.

It is assumed that logging measured are acquired 4 days after drilling the well. From the invasion profile, one can observe that mud-filtrate penetrates to a radial distance of approximately 2 m away from the wellbore. Waveform synthesis is performed assuming tools with dipole and quadrupole sources at different source-receiver offsets. It would be expected that from the multipole synthetic waveforms, one could estimate the virgin formation properties. Perfect dipole and quadrupole sources generate compressional signals. It has also been shown that within commercial logging frequency bands, the multipole logging tool can measure P-wave velocity two to three times farther away from the wellbore than a monopole tool and that the signal to noise ratio is higher (Baker et al., 1988).

In the current simulations, continuous profiles of the density and the P- and S-wave velocities are discretized into 12 radial layers to ensure accurate representation of the profiles described in Table 3.4. The configuration of the DSI tool is emulated in the simulations. For the Lower Dipole Mode, the 8 source-receiver offsets vary from 3.51 m (11.5ft) to 4.57 m (15ft) with a receiver spacing of 0.15 m (6 in). Here the central frequency of the sources is 1.4 kHz and 10 kHz, respectively, and the source spectrum is that of a Ricker wavelet.

In the low frequency dipole waveforms shown in Figure 3.12, P-wave arrivals are negligible. Figure 3.13 shows that the quadrupole waveforms primarily consist of quadrupole mode propagation. At a frequency of 10 kHz, stronger P-wave arrivals can be observed from the dipole waveforms (Figure 3.13(a)); P-wave arrivals in the quadrupole waveforms are much weaker (Figure 3.13(b)). In fact, it can be observed from the early arrivals of the dipole waveforms that there exist two P-wave arrivals on each wavetrain.

The compressional- and shear- velocities can be determined using industry standard slowness-time coherence (STC) array waveform processing techniques. From the STC contour plot shown in Figure 3.14, it can be seen that the P-wave component is not dispersive. The STC processing gives a P velocity of 4972 m/s. This velocity is very close to that of the virgin formation (4973 m/s). Therefore, the dipole tool can reliably measure P-wave velocity in this deep invasion case. Because the amplitude of the P-wave component is much smaller than that of the S-wave component, the feasibility of using a dipole tool to measure virgin formation property in deep invasion cases has to be investigated using field data. Similarly, the shear wave velocity is found to be 2796 m/s, which corresponds to the shear velocity of the invaded zone. This is because the STC processing results are complex functions of formation velocity, frequency, and window length (Kimball and Marzetta, 1986). Even though the properties of the virgin formation may be contained in the full waveforms, different processing techniques have to be used to extract that information.

Figure 3.15 show that dispersive analysis using the maximum likelihood method (Paillet and Cheng, 1991) yields a shear velocity of 2849 m/s at approximately 2.3 kHz. Such a shear velocity represents a more accurate result for this specific frequency (Kimball, 1995). By referring to Table 3.4, one can conclude that this value of shear velocity indicates that the depth of investigation of the low frequency component of the dipole shear wave is longer than 1.7 m.

For a radial distance shorter than 1.5 m, mud filtrate has replaced original gas in the formation, and hence the formation can be considered homogeneous in the invaded zone. The depth of investigation of a monopole tool can be approximated by the rule of thumb for a homogeneous formation. This states that the depth of investigation is about one P-wave wavelength. A simple calculation yields that the P-wave length in this limestone formation is about 0.5 m. Therefore, one can conclude that for this particular case a dipole tool can investigate approximately three times deeper than a monopole tool.

3.10 CONCLUSIONS

A new algorithm is developed for the synthesis of multipole acoustic logging measurements in radially layered media based on the method of generalized reflection and transmission coefficients. An exact frequency-wavenumber (*f*-*k*) domain solution of receiver responses associated with a multipole source in a fluid-filled borehole is formulated using the generalized reflection coefficients. The normalized Hankel functions and normalizing factors used in the formulation make the simulation algorithm computationally stable. A recursive scheme to compute generalized reflection and transmission coefficients is also implemented to further improve the efficiency of the algorithm. Validation of the algorithm is performed by comparing simulation results with those obtained using the Thomson-Haskell method assuming simple borehole and stepwise invasion-zone models. The dipole and quadrupole waveforms computed using the two methods show an excellent agreement.

The simulation algorithm is then applied to study the depth of investigation of a multipole tool in a gas reservoir case. It is assumed that borehole is surrounded by a radially multilayered formation. A Biot-Gassmann fluid substitution technique is used to convert the radial saturation profile into profiles of density and P- and S-wave velocities for each layer. In this specific formation, the relative P-wave amplitude of the flexural wave generated by the dipole source is stronger than that of the corresponding quadrupole waveforms. Using the STC algorithm and dispersion analysis to study dipole waveforms, it is found that a dipole tool emulating DSI with a wideband source can investigate about three times deeper than a monopole tool in the presence of a complex, deeply invaded zone. P- and S-wave velocities close to those of the virgin formation can be estimated from dipole waveform data by making use of dispersive processing techniques.

Table 3.1: Model parameters used for the numerical simulation described in Figures 3.2, 3.3, 3.4 and 3.5.

Parameter	Symbol	Fast Formation	Slow formation
Fluid speed (km/s)	v_f	1.50	1.50
Fluid density (kg/m^3)	ρ_f	1000	1000
Borehole radius (m)	r_1	0.10	0.10
Solid density (kg/m^3)	ρ	2000	2000
Shear speed (km/s)	v_s	2.0	1.20
Compr speed (km/s)	v_c	3.464	2.078
Multipole separation (m)	δ	0.01	0.01

Table 3.2: Model parameters used for the numerical simulation described in Figures 3.6 and 3.7.

Layer	α (m/s)	β (m/s)	ρ (kg/m^3)	Q_α	Q_β
Water	1500	0	1000	30	
Fast sandstone	4878	2601	2160	60	60
Invaded zone	4390	2341	2360	40	40
Slow sandstone	2751	1201	2100	50	50
Invaded zone	2338	1081	2000	40	40

Table 3.3: Model parameters used for the numerical simulation described in Figures 3.8 and 3.9.

Layer	Borehole	Invaded zone	Virgin formation
Inner radius (m)	0	0.122	1.04
ρ (g/cm^3)	1.0	2.0	2.2
V_p (m/s)	1520	2740	3350
V_s (m/s)	0	1680	1830

Table 3.4: Description of mud properties and discretized profiles of density and P- and S-wave velocities of the formation considered in the field study.

Layer	Inner radius (m)	ρ (g/cm^3)	U_p (m/s)	V_s (m/s)
1	0	1.1	1524	0
2	0.1	2.558	5092.3	2841.4
3	1.638	2.558	5091.6	2841.7
4	1.682	2.554	5086.3	2843.8
5	1.726	2.548	5079.1	2847.2
6	1.770	2.539	5069.9	2852.0
7	1.814	2.529	5058.7	2858.0
8	1.858	2.516	5045.5	2865.4
9	1.902	2.501	5030.4	2874.2
10	1.946	2.483	5013.2	2884.2
11	1.990	2.464	4994.1	2895.6
12	2.034	2.442	4973.0	2908.3

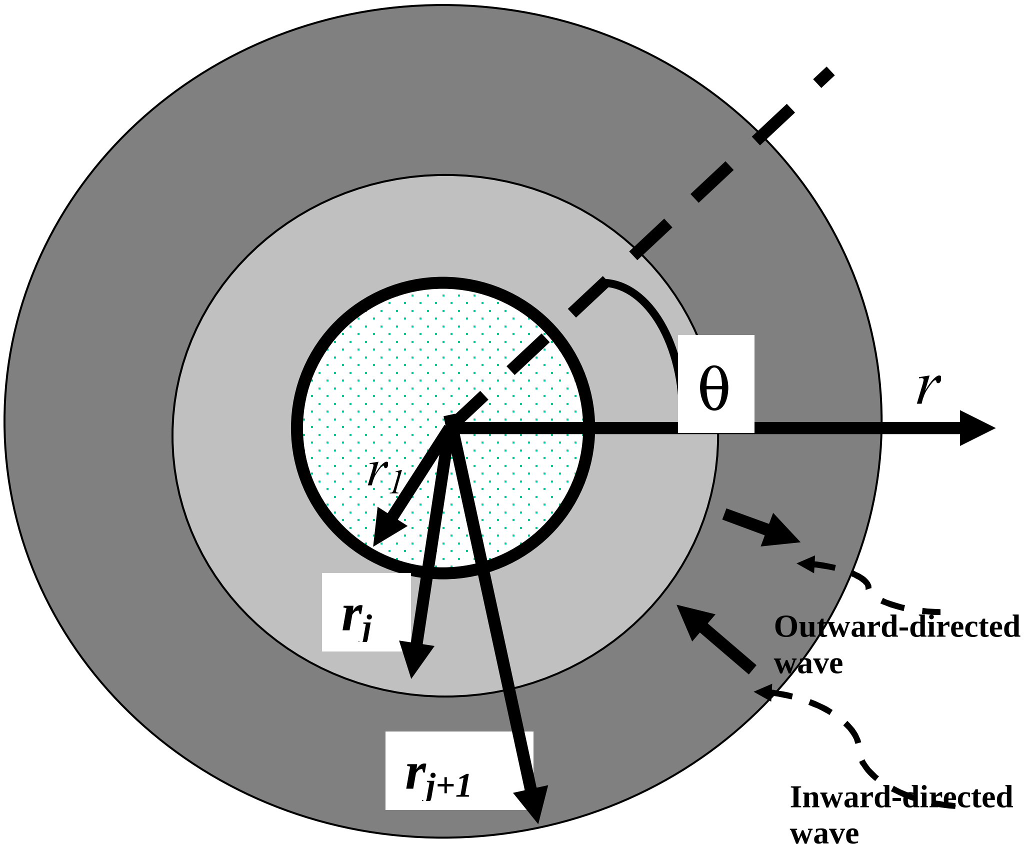

Figure 3.1: Schematic of a borehole in a radially layered formation model, with inward-directed and outward-directed waves supported within each layer except the outer-most layer, which only supports outward-directed waves.

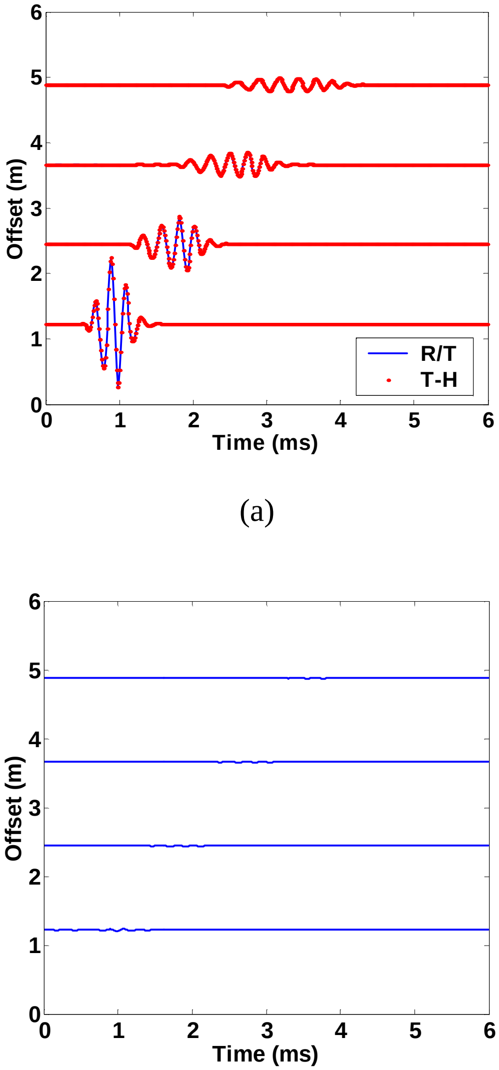

(a)

(b)

Figure 3.2: (a) Overlay of the dipole waveforms simulated using the Thomson-Haskell (T-H) and the R/T matrices methods; (b) the difference between the two sets of waveforms associated with the fast formation described in Table 1 for the simple borehole case. The central frequency of the source is 4 kHz.

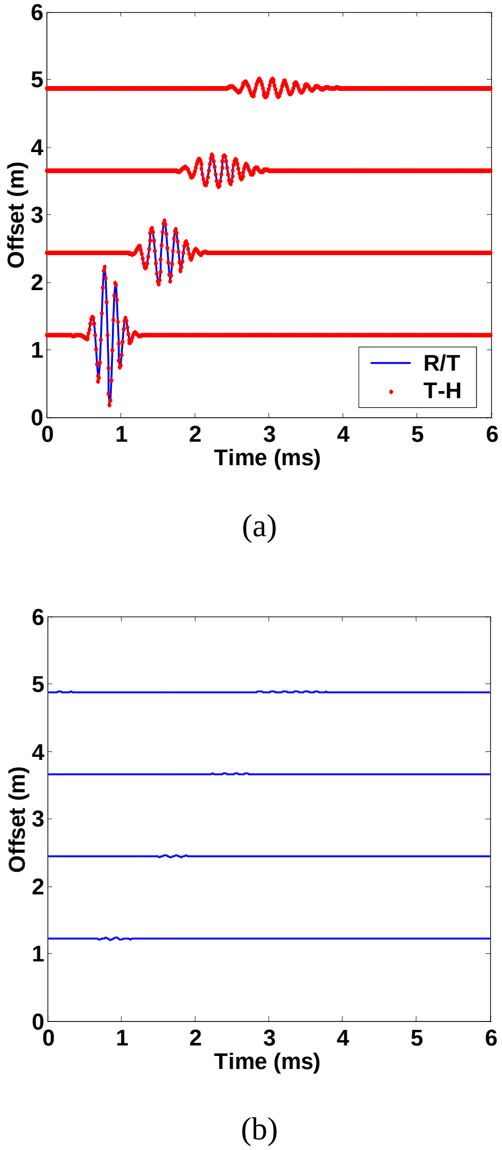

(a)

(b)

Figure 3.3: (a) Overlay of the quadrupole waveforms simulated using the Thomson-Haskell (T-H) and the R/T matrices methods; (b) the difference between the two sets of waveforms for a fast formation described in Table 1 for the simple borehole case. The central frequency of the source is 4 kHz.

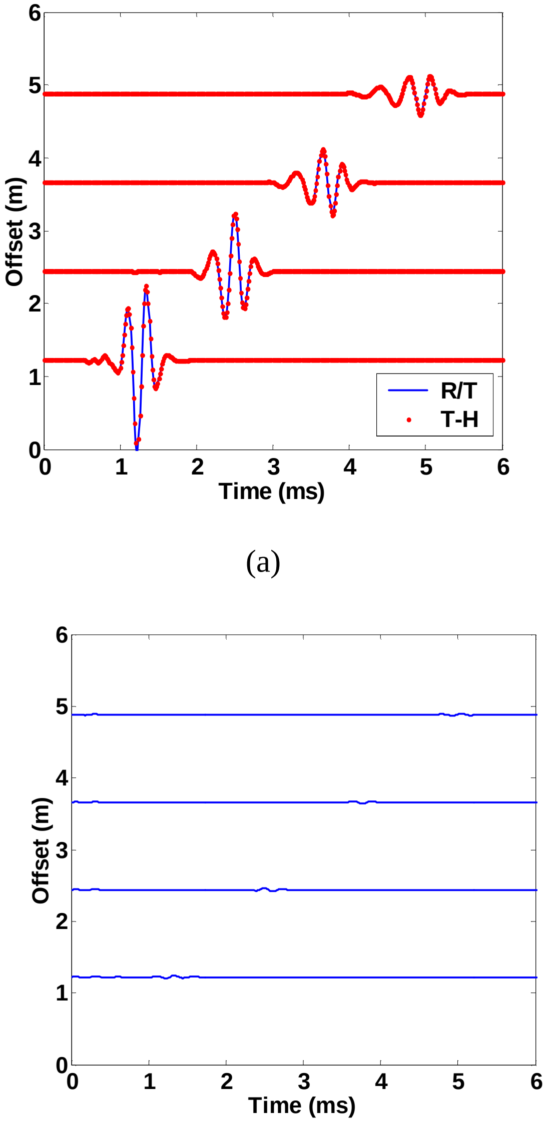

(a)

(b)

Figure 3.4: (a) Overlay of the dipole waveforms simulated using the Thomson-Haskell (T-H) and the R/T matrices methods; (b) the difference between the two sets of waveforms associated with the slow formation described in Table 3.1 for the simple borehole case. The central frequency of the source is 4 kHz.

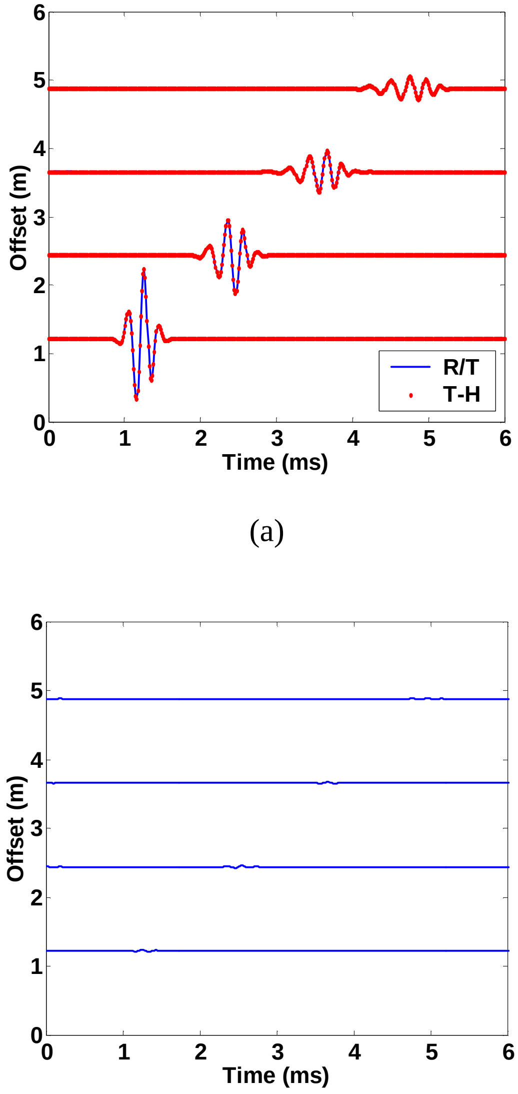

(a)

(b)

Figure 3.5: (a) Overlay of the quadrupole waveforms simulated using the Thomson-Haskell (T-H) and the R/T matrices methods; (b) the difference between the two sets of waveforms associated with the slow formation described in Table 3.1 for the simple borehole case. The central frequency of the source is 4 kHz.

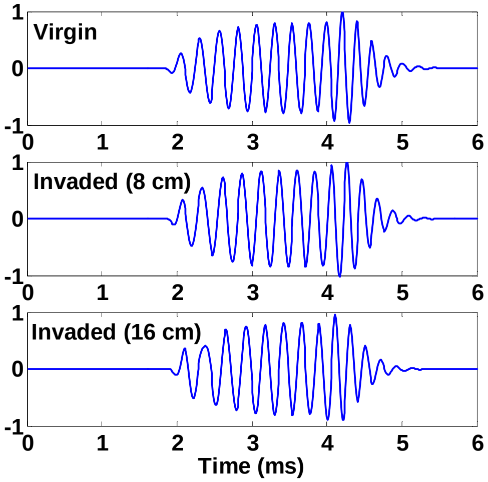

(a)

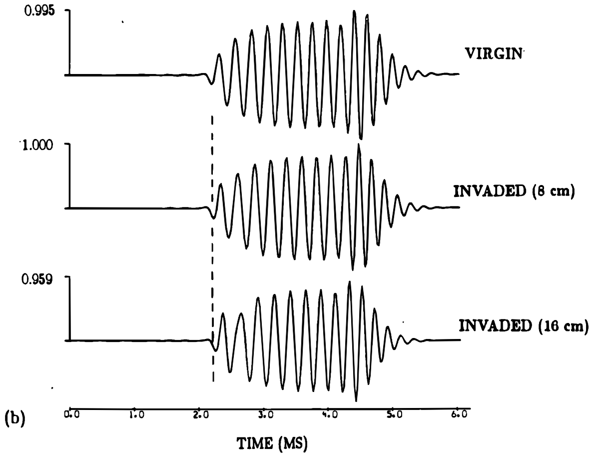

(b)

Figure 3.6 Dipole waveforms computed with (a) the generalized R/T method (b) the Thomson-Haskell method (after Schmitt, 1988, Fig. 10 (b)) associated with the borehole/formation models described in Table 3.2. Notice the effects of the invaded zone in the presence of a fast sandstone formation. The central frequency of the source is 3 kHz. Each trace is normalized with respect to its own maximum peak amplitude. The factors on the upper left corners of Figure 6(b) give the corresponding relative values.

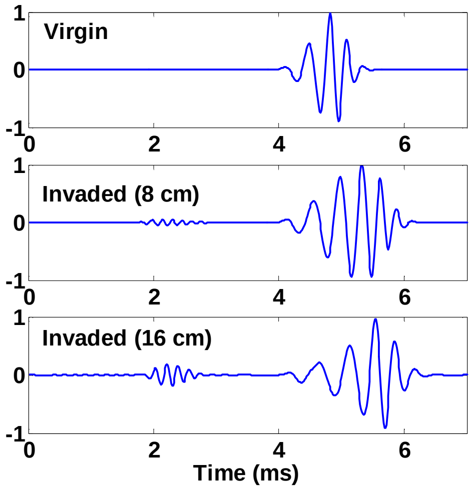

(a)

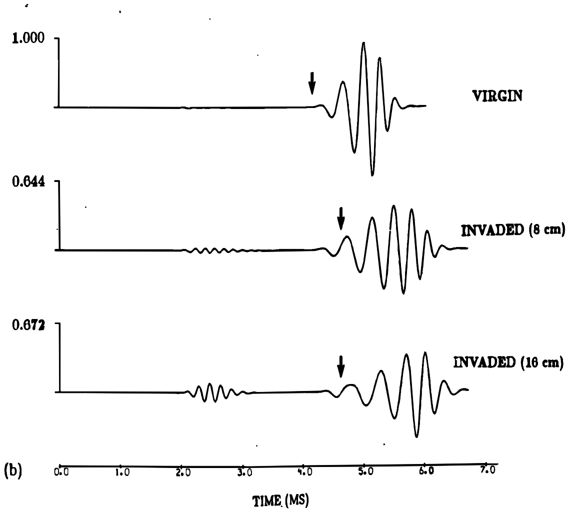

(b)

Figure 3.7: Similar to Figure 6. Dipole waveforms computed with (a) the generalized R/T method (b) the Thomson-Haskell method (after Schmitt, 1988, Fig. 12 (b)) associated with the borehole/formation models described in Table 3.2. Notice the effects of the invaded zone in the presence of a slow sandstone formation. The central frequency of the source is 3 kHz.

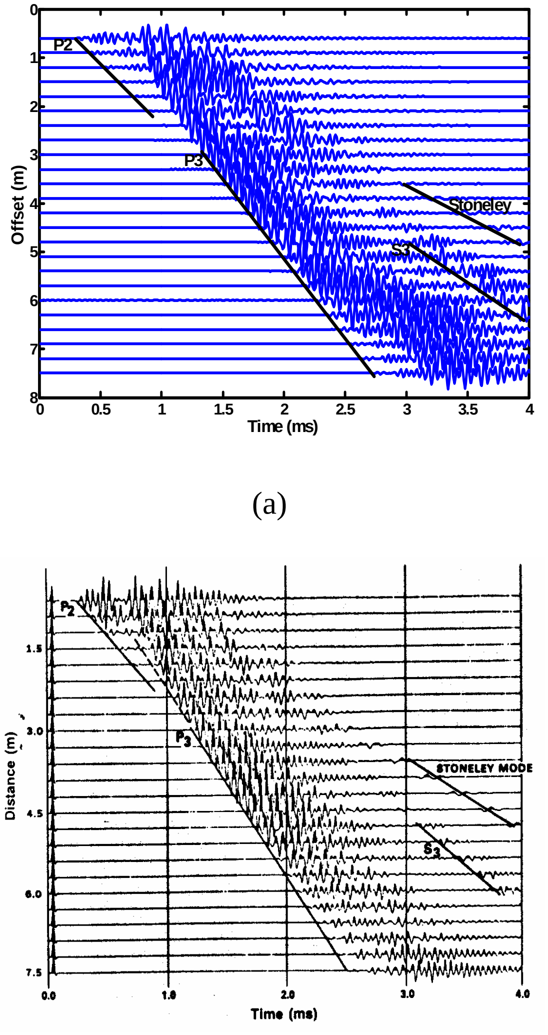

(a)

(b)

Figure 3.8: (a) Waveforms computed with the generalized R/T method assuming the damaged zone model described in Table 3.3. (b) Waveforms computed with the Thomson-Haskell method (after Baker et al., 1988, Fig. 9). The quadrupole tool with a source-receiver spacing of less than 3 meters measures the invaded zone P-wave velocity, P2, and measures the virgin formation P-wave velocity, P3 when the source-receiver spacing is larger than 3 meters. The central frequency of the quadrupole source is 10 kHz.

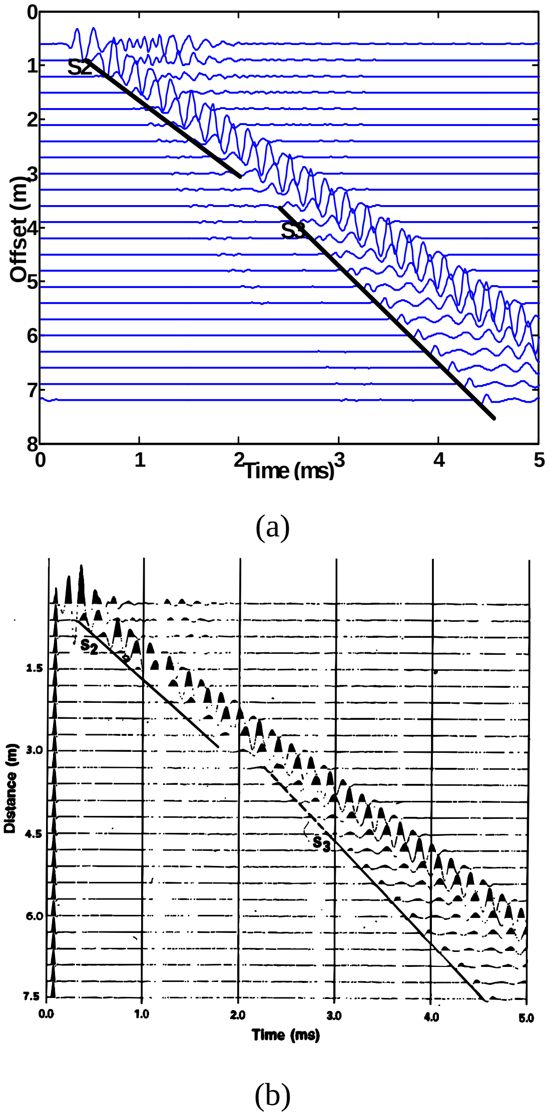

Figure 3.9: (a) Quadrupole waveforms computed with the generalized R/T method assuming a damaged zone model described in Table 3.3. (b) Quadrupole waveforms computed with the Thomson-Haskell method (after Baker et al., 1988, Fig. 10). The S-wave velocity of the invaded zone, S2, is detected when the source-receiver spacing is less than 3 meters. The S-wave velocity of the virgin formation, S3, is sensed when the source-receiver spacing is longer than 3 meters. The central frequency of the quadrupole source is 5 kHz.

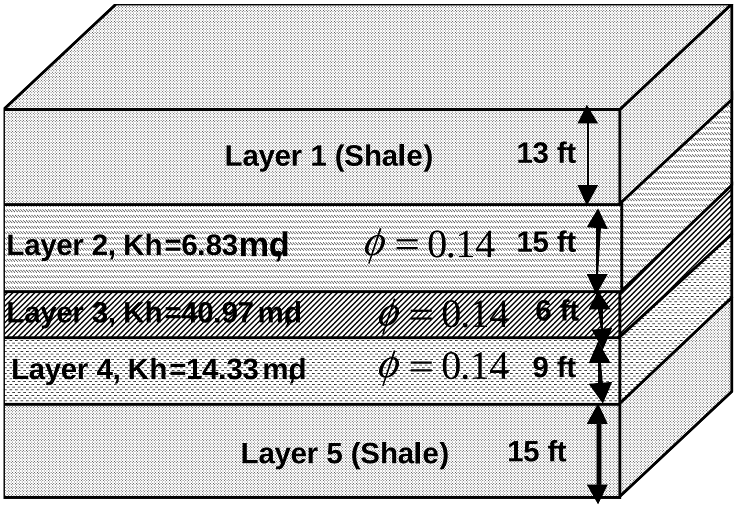

Figure 3.10: Description of the geometrical and petrophysical properties of the reservoir flow units considered in the field study.

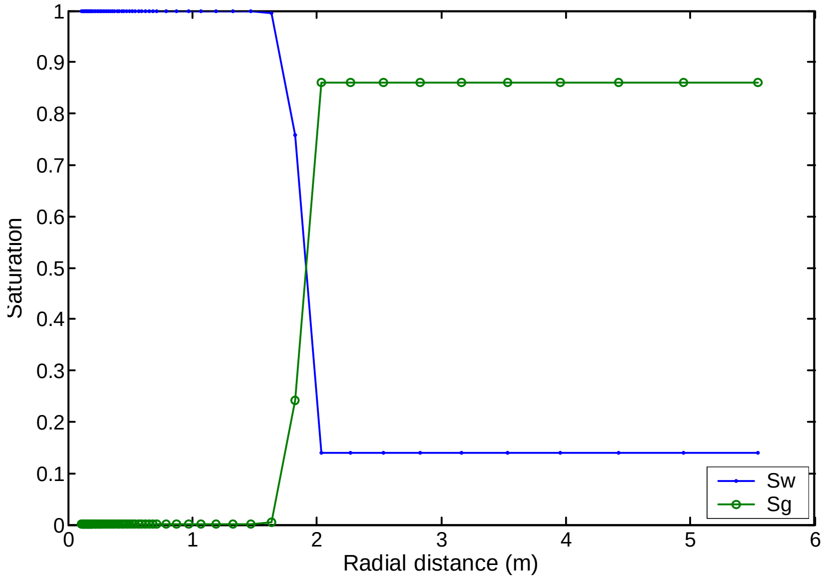

(a)

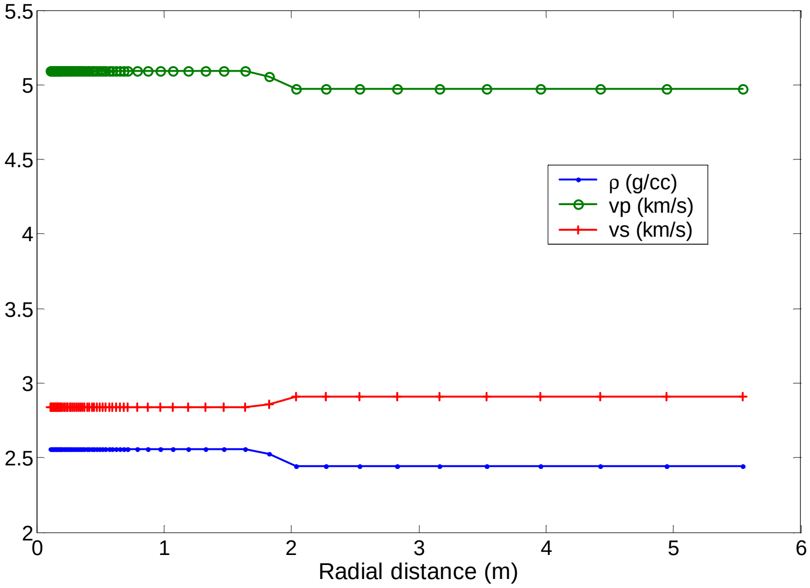

(b)

Figure 3.11: (a) Radial profiles of water and gas saturation in a permeable layer penetrated by the well considered in the field study. (b) Radial profiles of density, Vp, and Vs for the same layer. The discretized profiles are given in Table 3.4.

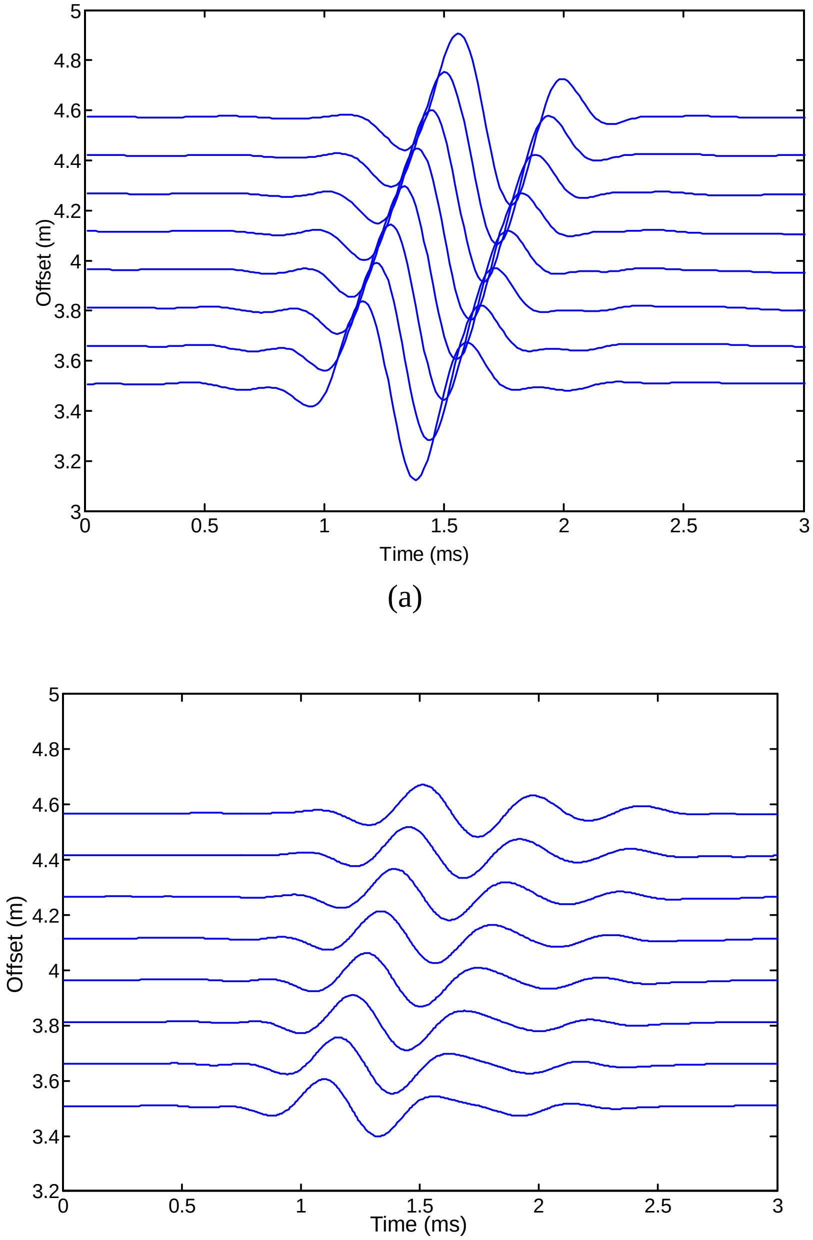

(a)

(b)

Figure 3.12: (a) Waveforms for the field study simulated assuming a DSI tool operating at the Lower Dipole Mode. The central frequency of the dipole source is 1.4 kHz. Model parameters are given in Table 3.4. (b) Waveforms simulated using a quadrupole source. All of the remaining model parameters are the same as those used in (a).

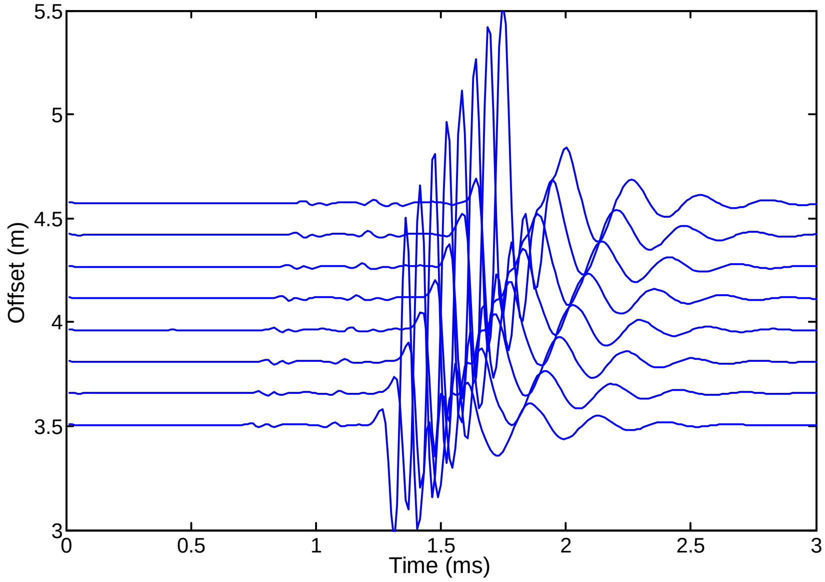

(a)

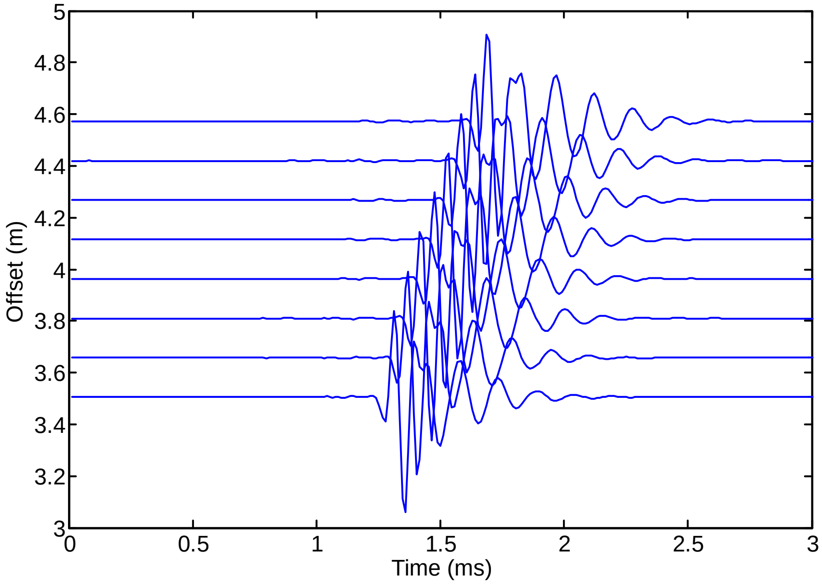

(b)

Figure 3.13: (a) Waveforms for the field study simulated assuming a DSI tool operating at the Lower Dipole Mode. The central frequency of the dipole source is 10 kHz. Model parameters are given in Table 3.4. (b) Waveforms simulated using a quadrupole source. All of the remaining model parameters are the same as those used in (a).

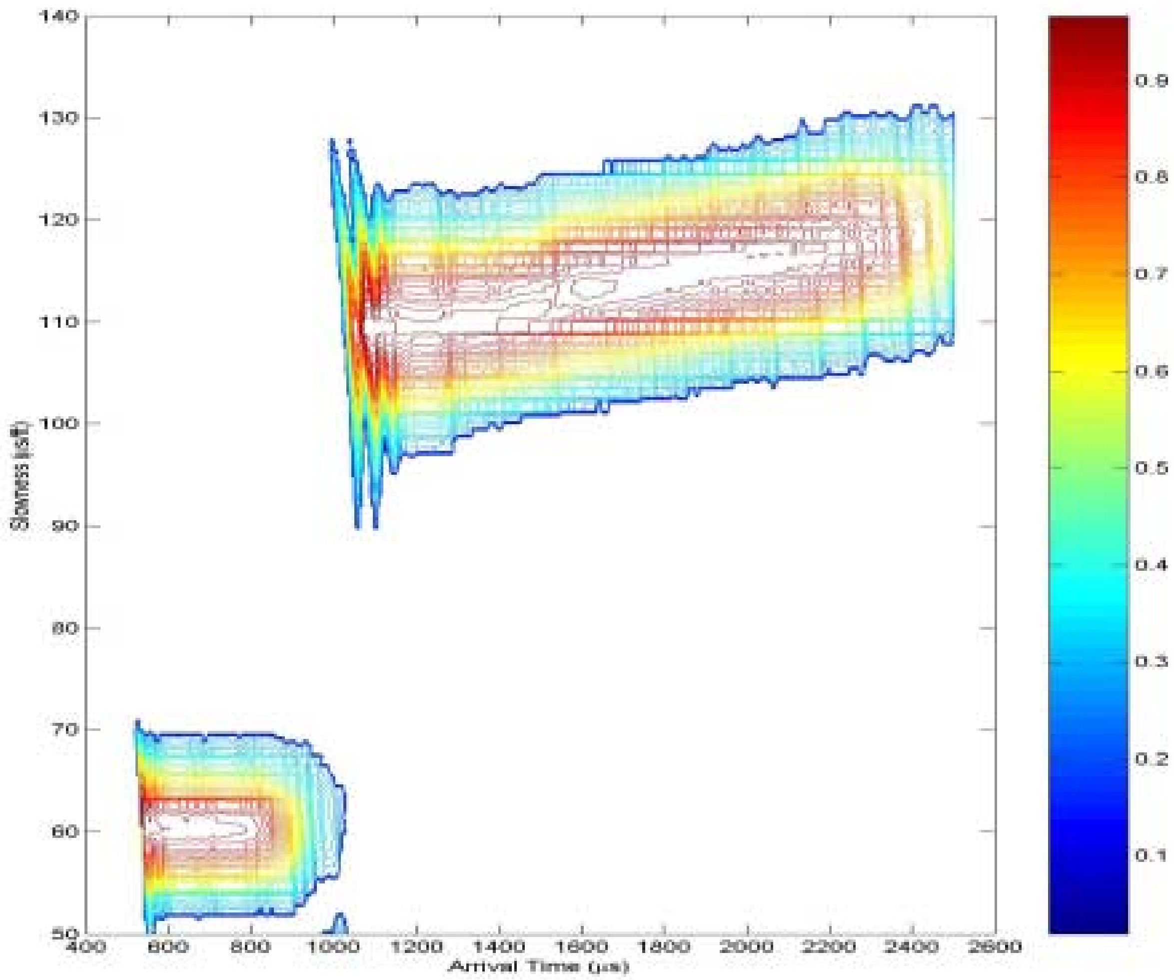

Figure 3.14: Slowness-time coherence (STC) contour plot of the dipole waveforms simulated for the field study case.

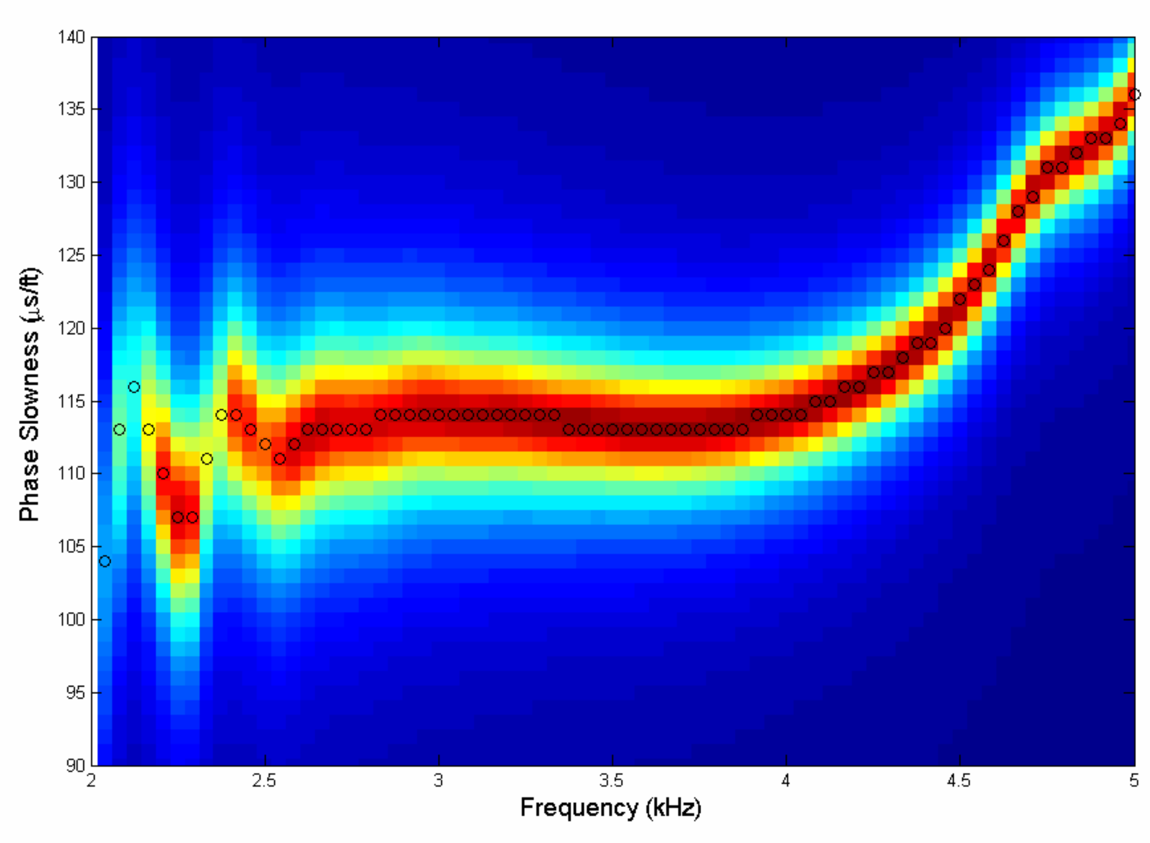

Figure 3.15: Dispersion analysis of the dipole waveforms simulated with a 10 kHz source for the field study case. The dispersion curve for the shear slowness is identified with the open circles. The shear slowness 107 us/ft at 2.3 kHz indicates that the shear wave senses the formation at a radial distance of 1.7 m.

Chapter 4: Assessment of Mud-Filtrate Invasion Effects on Open-Hole and Cased-Hole Acoustic Measurements

Mud-filtrate invasion modifies the connate fluid distribution in rock formations penetrated by a well. This in turn perturbs the density and P- and S-wave velocities in the near-wellbore region. Understanding the impact of the damaged zone on borehole acoustic measurements is significant for the interpretation and quantitative evaluation of the estimated formation velocities. This chapter assesses mud-filtrate invasion effects on borehole acoustic measurements. The radial saturation distribution of mud filtrate and connate formation fluids is first obtained by simulating the mud-filtrate invasion process in the near-wellbore region. Subsequently radial profiles of the elastic properties are calculated by applying a Biot-Gassmann fluid substitution model. By making use of the radial profiles of density and P- and S-wave velocities, monopole and dipole acoustic array waveforms are simulated in open- and cased-holes. The effects of mud-filtrate invasion on the arrival times and amplitudes of various wave modes are studied by comparing the monopole and dipole waveforms for homogeneous and radially layered formation models. An industry standard Slowness-Time-Coherence (STC) method is then used to extract P- and S-wave velocities from the simulated waveforms. Velocities from STC processing show that modern borehole sonic tools investigate beyond shallow invaded zones, but do not penetrate beyond deeply invaded zones.

In general, mud-filtrate invasion in the near-wellbore region reduces the P-wave amplitude and arrival time and increases the shear wave amplitude and arrival time. These observations provide a qualitative tool for monitoring fluid redistribution in the near-wellbore region via time-lapse logging. Since acoustic logs are influenced only in the presence of deeply invaded zones, log corrections with the Biot-Gassmann fluid substitution model are not appropriate for cases of shallow invasion.

4.1 INTRODUCTION

During and after drilling, the near-wellbore formation is often altered by stress and stress releases, mud-filtrate invasion, chemical reactions, and many other factors. These alterations cause some physical properties in the near-wellbore region to be different from those of the uninvaded rock formation.

Stress concentration around a wellbore may cause formation anisotropy and radial variation of velocities. The stress-induced anisotropy can be identified by dispersion analysis (Plona et al., 2000). If anisotropy becomes significant, then the Biot-Gassmann theory for fluid substitution is no longer valid. Positive radial velocity gradients focus the elastic waves propagating away from the wellbore back toward the borehole wall. This phenomenon can be easily identified from high-amplitude acoustic arrivals. Mechanical damage may decrease the measured velocities by approximately 10% (Winkler, 1997). In well-consolidated hard rock formations, mechanical damage is less pronounced than in soft formations and is a much more localized phenomenon than mud-filtrate invasion effects. This dissertation focuses on mud-filtrate invasion effects only.

It is well known that formation properties inferred from wireline logging measurements may not be the true properties of virgin formations. A realistic description of the invaded zone is important for the processing and interpretation of logs. Conventionally, in a damaged zone, the P-wave velocity of the formation near the wellbore is lower than the P-wave velocity of the virgin formation. In a flushed zone, the P-wave velocity is higher than that of the virgin formation. A common model used in the open literature assumes that a sharp interface exists between the altered zone and the undisturbed formation (Baker, 1986). The term “stepwise” is used to describe this type of mud-filtrate invasion model. Linear gradient models have been described for the syntheses of acoustic waveforms as well (Stephen et al., 1985). Actual radial profiles of elastic wave properties resulting from invasion can be quite complex and are dependent on the specific petrophysical properties of the rock as well as on the static and dynamic properties of the fluids involved. This chapter details a procedure for calculating the radial profiles of formation elastic properties with the Biot-Gassmann fluid substitution model starting from the numerically simulated saturation profiles.

Theoretical (Gassmann, 1951, Biot, 1956a, 1956b, Toksoz et al., 1976) and experimental studies (Geertsma and Smit, 1961, Domenico, 1976, Dutta and Ode, 1979a, 1979b, Murphy, 1982, etc.) have shown that rocks saturated with hydrocarbons and water can be differentiated with acoustic velocity measurements. Using time-lapse acoustic logging, bypassed zones can be identified and fluid movement in rock formations can be monitored in open- and cased-holes. Based on the difference between measured P-wave velocity (Vp) to shear-wave velocity ratio (Vs) and that predicted for a water-saturated rock, Williams (1990) proposed a method to identify hydrocarbon-saturated rocks using acoustic logs. The possibility of detecting hydrocarbon with acoustic velocities depends on the difference between the acoustic properties of the two fluids. In general, fluid properties exercise a large influence on elastic properties for high-porosity rocks than for low-porosity rocks (Gregory, 1976).

It has been shown that a low frequency dipole tool senses 2-3 borehole diameters into the formation (Plona, et al., 2002). If the invasion depth is approximately within 2-3 borehole diameters, the dipole tool can measure virgin formation properties. High frequency monopole tools penetrate one borehole diameter, thereby sensing only the damaged zone. When a logging tool can detect the virgin formation properties, the Vp/Vs ratio or else Poisson’s ratio can be used to quantify hydrocarbon saturations. If the invasion depth is beyond the depth of investigation of a logging tool, the measured velocities reflect those of the damaged zone and log corrections become necessary to estimate virgin formation velocities.

To enhance the productivity and to extend the economic life of mature fields, time-lapse acoustic logging has been used to assess fluid saturation through casing and to assist in well re-completion (Moos et al., 1996). However, most of the published studies have been performed on poorly consolidated sandstone reservoirs, wherein fluid effects are significant. In this chapter, the feasibility of detecting fluid saturation changes with time is investigated assuming consolidated sandstone and carbonate reservoirs.

4.2 NUMERICAL SIMULATION OF MUD-FILTRATE INVASION

Mud filtrate invasion is treated as a water or oil injection process into a gas or oil reservoir wherein two-phase immiscible fluid flow is assumed in the simulations. In order to study the effects of different types of mud filtration on gas or oil reservoirs, the following cases are selected: (a) water-base mud invades oil and gas reservoirs penetrated by open- and cased-holes, (b) oil-base mud invades gas reservoirs penetrated by open holes, and (c) oil-base mud invades gas reservoirs penetrated by cased holes. In each of these cases, it is assumed that a vertical well penetrates horizontally layered rock formations, and that the rock formation considered does not communicate hydraulically with its upper and lower shoulders. To study the sensitivity of mud-filtrate invasion to formation petrophysical properties, a low permeability (15 md) and low porosity (15 p.u.) reservoir and a high permeability (300 md) and high porosity (30 p.u.) reservoir are considered for cases (a) through (c). One exception is that for the case of water-base mud invading a gas reservoir in which only a low porosity carbonate reservoir is studied given that field data for the corresponding high porosity reservoir are not available.

Details of the numerical simulation of the process of mud-filtrate invasion in open holes can be found in Wu et al. (2001) and George et al. (2003). In the simulations, both dynamic growth of mud-cake and dynamic decrease of mud-cake permeability are coupled to formation properties. This process results in a dynamic monotonic decrease of flow rate into the formation. After a short initial spurt of mud filtrate invasion, the invasion process reaches a steady state. Cycles of mud-cake rub-off and buildup can also be taken into account.

A schematic of the process of mud-filtrate invading a permeable rock formation is illustrated in Figure 4.1. The invasion front moves deeper into the formation with time. Figure 4.2 shows the time-evolution of water-base mud filtrate saturation in the radial direction of a low porosity, low permeability, oil-bearing, sandstone formation. A finer numerical simulation grid can be used to smooth out the corners on the saturation profiles. The water-base mud filtrate reaches a radial distance of approximately 0.8 m after four days of invasion. Mud filtrate invasion is much shallower for the corresponding high porosity case. Figure 4.3 shows that mud filtrate penetrates to a radial distance of 0.5 m after four days of invasion. For a gas-producing carbonate reservoir case (after George et al., 2003), mud filtrate reaches a radial distance of approximately 2 m after four days of invasion primarily due to the combined effects of a large overbalance pressure and low formation porosity (14 p.u.).

Oil-base mud invades the gas-bearing sandstone formation at a much slower rate. Figure 4.4 shows that the time-evolution of oil-base mud filtrate saturation in the radial direction of a low porosity (15 p.u.) and low permeability (30 md) formation. Oil-base mud filtrate reaches a radial distance of approximately 0.2 m after four days of invasion. Figure 4.5 shows that mud filtrate primarily concentrates within a distance of 0.1 m away from the borehole wall.

When casing is set in place 16 days after drilling, it is assumed that the invasion process is stopped instantaneously and hence that filtrate dissipation starts to take place. The saturation in the near-wellbore region was simulated for 30 more days due to capillary and gravity effects (Lane, 1993).

4.3 RADIAL PROFILES OF DENSITY AND P- AND S-WAVE VELOCITIES IN AN INVADED ZONE

The work by Biot (1956) and Gassmann (1951) continues to be the foundation for quantifying the effects of rock and fluid parameters on acoustic velocities. Once invasion profiles are obtained from numerical simulations, profiles of elastic formation properties can be calcualted using the Biot-Gassmann fluid-substitution equations.

Following the tutorial presented by Smith et al. (2003), a calculation is first performed of the basic formation and fluid properties. Subsequently, for each point in the saturation profile one can calculate: (a) fluid properties, (b) saturated bulk modulus of the rock, (c) bulk density of the rock, and (d) compressional- and shear- velocities.

When computing fluid and formation properties after invasion, a careful selection is necessary of homogeneous or patchy saturation models. Over geologic time, fluids in the pores of the rocks become homogeneously distributed. This is one of the important assumptions for the application of Biot-Gassmann's fluid-substitution model. However, mud-filtrate invasion in the near wellbore region changes the connate fluid distribution. It may require more time to establish hydraulic equilibrium of the fluid phases involved than the time before logging. From the numerical simulation results described in this

Chapter, it is clear that the equilibrium of phases in the near-wellbore region is not established within a few days after the onset of the mud-filtrate invasion process. Wettability also causes segregated distribution of fluids. In the sonic logging frequency range, the time scale of wave propagation may be too short for the pressure to equilibrate. Therefore, it is more accurate to use a patchy saturation model to compute the corresponding bulk modulus (Hill, 1963).

4.4 NUMERICAL SIMULATION OF TIME-LAPSE BOREHOLE ACOUSTIC MEASUREMENTS

Once the radial profiles of density and P- and S-wave velocities are obtained, they are discretized and approximated with a concentrically multi-layered rock model. The radial discretization is fine enough to ensure accurate representation of the continuous profiles. A corresponding stepwise-invaded zone model is also used for the numerical simulation. The waveforms simulated for the multilayered- and stepwise-models are compared against each other with the objective of determining under what kind of situations the stepwise models are adequate to represent the invaded zone.

In the synthesis of array waveforms, the assumption is made of a source-receiver configuration that replicates the DSI* tool. For the monopole mode, the central frequency of the source is 10 kHz. The minimum source-receiver distance is 9 ft with the receiver array consisting of 8 receivers spaced at 6 in intervals. Dipole modes make use of a 1.5 kHz source and a minimum source-receiver separation of 11.5 ft. In the Lower Dipole Mode, the 8 source-receiver offsets vary from 3.51 m (11.5ft) to 4.57 m (15ft) with a receiver spacing of 0.15 m (6 in).

---

* Mark of Schlumberger

Sonic array waveforms are simulated for a homogeneous uninvaded formation as well as for the same formation after four days of mud-filtrate invasion. Casing is set in place 16 days after drilling. Because of the dissipation mechanism due to capillary forces and gravity segregation, simulations are performed again to obtain the radial profiles of fluid saturations in the near-wellbore region 30 days after setting casing. Radial profiles of elastic properties are computed once again assuming the simulated radial saturation profiles of the fluids in the near wellbore rocks. Likewise, array waveforms are simulated to study the effects of fluid movement on full waveform acoustic logging data acquired in cased holes.

4.5 PROCESSING AND INTERPRETATION OF MONOPOLE AND DIPOLE LOGGING DATA

The sensitivity of acoustic measurements to different invasion models and radial saturation profiles can be assessed by comparing the synthetic waveforms for homogeneous, stepwise, and multi-layered radial formation models. Arrival times and amplitudes of P-, S-, and Stoneley-wave modes are the main waveform features that are used to assess the effect of mud-filtrate invasion on borehole acoustic logging measurements.

An industry standard slowness-time coherence (STC) method (Kimball and Marzetta, 1986) is used to determine the velocities of P-, S-, and Stoneley-waves measured with array monopole logs. The STC method is well suited for non-dispersive waves. For the slightly dispersive Stoneley wave, the STC processing also provides accurate results. Interpolations in the time and slowness domains are performed to improve the accuracy of the computed velocities. The time-domain interpolation sharpens the peaks of coherence and hence the slowness-domain interpolation improves the accuracy of slowness at the respective contour peaks.

Radial depths of investigation for sonic tools depend on the formation type, shear and compressional slowness, the transmitter-to-receiver spacing, wavelength and wave mode considered, the source frequency and the type of signal, among others. Frequency determines the wavelength that drives the depth of investigation of the measurement. Low frequency waves penetrate deeper into the formation and hence are sensitive to radial zones beyond invaded/damaged regions. As a rule of thumb, the depth of investigation is approximately one wavelength of the particular type of wave. Therefore, a dipole tool can investigate 3-4 times deeper than a monopole tool because the frequency of the dipole source is 3-4 times lower than that of the monopole source. Ideally, if the P- and S-wave velocities can be accurately determined, the depth of investigation can be determined by referring to the radial velocity profiles. However, the number of samples and frequency content in the correlation window influences the accuracy of the STC method. The measurements errors are approximately 1% for P-wave and 2% for S-wave velocities, respectively. Quite often, velocity variations due to mud-filtrate invasion remain close to such errors. For example, the maximum variation of Vp and Vs is about 2% and 4%, respectively, for a consolidated gas reservoir exhibiting 30% porosity. For a low porosity (less than 15%) reservoir, the velocity variation may not be distinguishable from processing errors.

The current industry standard for processing array dipole waveforms is the dispersive STC method. In this Chapter, the effect of invasion on dipole acoustic measurements is interpreted by directly comparing the characteristics of full waveforms.

When correlating seismic data with acoustic logs, it is often found that synthetic seismograms do not match the measured seismograms. As a result, corrections to the acoustic logs via the Biot-Gassmann fluid substitution model are common practice used in the seismic industry to free sonic logs from mud-filtrate invasion effects. In this correction procedure, it is assumed that the measured velocities are those of the invaded zone saturated with mud filtrate. By displacing the saturation fluid in the invaded zone with the connate formation fluid and by applying the Biot-Gassmann fluid-substitution equation, new velocities are obtained and taken as the virgin formation velocities. Below, the validity of this practice is investigated through several case studies.

4.6 CASE STUDIES

4.6.1 A Deeply-Invaded Gas Reservoir Case

This unique field case can be used to quantify the effects of mud-filtrate invasion on measured formation velocities and to validate log corrections with the Biot-Gassmann fluid-substitution model. Attention is focused to well X-2, which is the same well described by George et al. (2003). The hydrocarbon field is located in North America, and comprises carbonate formations subject to production of natural gas. The well was drilled with a water-base mud, and a large overbalance pressure resulted deep invasion of the formation. A nearby well, here referred to as X-1, was drilled a few hundred feet away from well X-2. This well was drilled with light mud resulting in very shallow invasion. Well X-1 is considered a key well in the present study due to both negligible invasion and the availability of P- and S-wave log data. Well-log data acquired in well X-1 are used as a benchmark in the present study.

As shown in Figure 4.14 (a), water-base mud filtrate reaches a radial distance of approximately 2 m into the formation in well X-2. In this flow unit, P-wave velocity, S-wave velocity, and bulk density change approximately 2.4%, 2.3% and 4.8%, respectively, relative to the corresponding properties of the uninvaded formation. The change of S-wave velocity after invasion is approximately equal to the measurement errors recorded in field operations (approximately 2%). Therefore, it is difficult to sense differences in formation velocities due to invasion with a standard borehole sonic tool and a standard waveform processing method.

To assess the effects of the mud-filtrate invasion on elastic wave velocities, a numerical study of monopole and dipole waveforms is necessary. To this end, the continuous radial profiles of density and P- and S-wave velocities are discretized into 12 radial layers to ensure accurate representation of the profiles described in Table 3.4 of Chapter 3. Such radial profiles are shown in Figure 4.14(b). The eighth traces of the array waveforms shown in Figure 4.15 (a) are simulated using a monopole source for three types of formation model, namely, a homogeneous formation, a formation with a multilayered invasion zone, and a formation with a stepwise invasion zone. It is very clear that both the P- and S-wave arrivals for the stepwise model occur significantly later than those for the homogeneous and multilayered models. Therefore, the stepwise model for the invasion zone remains inadequate to describe the continuous invasion profile. In addition, Figure 4.15 (a) also shows that P wave arrives earlier and S wave arrives later for the multilayered model than that for the homogeneous model, and P- and S-wave amplitudes remain almost unchanged in the waveforms simulated for both models. In the dipole waveforms shown in Figure 4.15 (b), the S wave also arrives for the multilayered model with respect to that of the homogeneous model.

Shear-wave velocities for the stepwise and multilayered models are 2.0% and 3.4% lower than that of the true virgin formation. P-wave velocities for the two models are approximately 1.3% higher than the true compressional velocity. Theoretical results obtained using the Biot-Gassmann fluid substitution model predict a 2.3% decrease for shear velocity and a 2.4% increase for compressional velocity with respect to the true formation velocities. Slowness-Time-Coherence results for the homogeneous formation remain biased by more than 1% with respect to the true formation velocities shown in Table 4.3. This indicates that the STC processing yields velocities representative of the invaded zone for both stepwise and multilayered models.

To estimate true formation velocities, it is necessary to perform corrections to the logs that are influenced by mud-filtrate invasion. In the same flow unit, the P-wave velocities in well X-2 are consistently higher than those of well X-1. In well X-2, only a P-wave velocity log is available, whereas in well X-1, both P- and S-wave velocity logs are available. Because the Biot-Gassmann fluid-substitution procedure requires knowledge of both P- and S-wave velocities, the P-wave velocity log of well X-1 is first calculated assuming that the well is deeply invaded. As shown in Figure 4.17, the calculated P-wave velocity log assuming invasion matches the measured P-wave velocity log in well X-2 reasonably well. This example indicates that the application of fluid substitution in the deeply invaded reservoir formation remains valid even though the porosity and permeability are relatively low and the rock formation is a carbonate.

4.6.2 Sandstone Oil Reservoir Invaded with a Water-Base Mud

In onshore conventional drilling actives, water-base mud is still widely used because of its efficiency to balance formation pressure without substantially increasing costs. Elastic properties of oil in rock formations are much closer to those of mud filtrate derived from a water-base mud. Compared to the case of mud-filtrate invading a gas reservoir, it may be more difficult to distinguish mud-filtrate invasion effects on the measured velocities. Moreover, fluid-flow properties of oil and gas are also very different from each other. Therefore, smaller mud-filtrate invasion effects are expected in the cases that will be studied in this section than in the previous section. To study the sensitivity of the measured velocities to porosity and permeability, this section first considers a low porosity (15%) and low permeability (30 md) reservoir. Table 4.1 summarizes the petrophysical and fluid parameters used in the simulation of water-base mud invasion. Subsequently, attention is focused to the case of a high porosity (30%) and high permeability (300 md) reservoir. Saturation profiles of mud filtrate and oil in formations are simulated for 4 days of invasion. The latter profiles are used to calculate radial profiles of elastic parameters using the Biot-Gassmann fluid-substitution model.

Figure 4.2 shows the time evolution of mud-filtrate invasion for the case of water-base mud invading the oil-bearing sandstone reservoir of 15% porosity. Figure 4.8 shows the radial profiles of the density and P- and S-wave velocities. P-wave velocities estimated from the array waveforms simulated for stepwise and multilayered models remain 1.1% lower than the true formation velocity shown in Table 4.3. Moreover, these velocities do not exhibit the expected amount of increase in the invaded zone. It is therefore concluded that the P wave is sensitive to the radial region beyond the invaded zone. S-wave velocities remain 2% lower than that of the uninvaded formation. This indicates that S-wave propagation is sensitive to the presence of the invaded zone.

Figure 4.3 shows the time evolution of mud-filtrate invasion for the case of a 30% porosity reservoir. The corresponding radial profiles of the density and P- and S-wave velocities are plotted in Figure 4.9. Referring to Table 4.5, it is also concluded that the P wave is sensitive to the radial region beyond the invaded zone, whereas the S wave is sensitive to the invaded zone.

In summary, P waves are sensitive to virgin zones and S waves are sensitive to invaded zones when the mud-filtrate invasion depth is around 0.5-0.8 m in the two sandstone reservoirs considered in this section.

4.6.3 Sandstone Gas Reservoir Invaded with an Oil-Base Mud

In general, oil-base mud promotes shallower invasion than water-base mud and hence causes less formation damage. Since oil-base mud is also chemically less active compared to water-base mud, it is more effective in inhibiting shale swelling. Because of this, oil-base mud is widely used in drilling expensive offshore wells. The section below is intended to assess mud-filtrate invasion effects on acoustic measurements with the presence of oil-base mud invasion.

4.6.3.1 Open-Hole cases

Two synthetic cases are selected to study mud-filtrate effects on the measured velocities of sandstone formations exhibiting low and high porosities and permeabilities.

For the gas-bearing sandstone reservoir of 15% porosity invaded with an oil-base mud, the time evolution of mud-filtrate invasion front is shown in Figure 4.4, and the corresponding radial profiles of the density and P- and S-wave velocities are shown in Figure 4.10. Figure 4.12 shows the eighth traces of the (a) monopole and (b) dipole array waveforms. Waveforms for the stepwise and multilayered models agree with each other. It is found that the P-wave amplitudes become much smaller in the presence of invasion, and that the S- and Stoneley-wave amplitudes increase considerably for monopole waveforms simulated for the invaded formation models than for the virgin formation model. Dipole waveforms show that the S-wave amplitude also increases with the presence of invaded zones. Figure 4.12(a) shows that the presence of oil-base mud filtrate reduces the P-wave arrival times, but does increase the S-wave arrival time. Arrival times for dipole waves remain unchanged.

P-wave velocities estimated from array waveforms simulated for stepwise and multilayered models are approximately 1.0% higher than the true formation P-wave velocity described in Table 4.6. S-wave velocities are approximately 0.2% lower than the true formation S-wave velocity. Therefore, P- and S-wave velocities are slightly influenced by mud-filtrate invasion, and remain primarily sensitive to the radial region beyond the invaded zone.

For the 30% porosity case, Figure 4.5 shows the time evolution of the mud-filtrate invasion front for the case of oil-base mud invasion and Figure 4.11 shows the corresponding radial profiles of density and P- and S-wave velocities. It is observed from the monopole waveforms that the presence of invaded zones does not affect the P-wave arrival time, but it does delay the S-wave arrival time. On the other hand, P-wave amplitudes do not change appreciably, but S-wave amplitudes do increase. In the dipole waveforms, the change in S-wave arrival is negligible. Dipole waveforms for the stepwise model are significantly different from those simulated for the multilayered formation model.

Table 4.7 summarizes the velocities estimated from synthetic waveforms for homogeneous, multilayered, and stepwise models. By comparing the velocities for different models, it is concluded that P waves penetrate past the invaded zone. S-wave velocities estimated for the stepwise and multilayered models are approximately 1% lower than that for the virgin formation. According to the Biot-Gassmann fluid substitution model, formation saturated with 90% mud filtrate should exhibit a 4.3% S-wave velocity decrease compared to the S-wave velocity of the virgin formation. This indicates that the measured S-wave velocities remain influenced by mud filtrate in the near-wellbore region, but that S waved sense region partially saturated with mud filtrate. Similar conclusions can be drawn from Figure 4.13.

In all the cases studied in this section, both P and S waves are not sensitive to the invaded zones when the oil-base mud-filtrate invasion reaches a depth of approximately 0.3 m in sandstone reservoirs.

4.6.3.2 Cased-Hole Cases

Presence of casing and cement layers between the borehole and the formation significantly modifies the characteristics of full acoustic waveforms. Both casing and cement replace part of the wave path in fluid as compared to the situation of an open-hole. Shorter arrival times are then expected for both P and S waves.

For a cased-hole drilled in the gas-bearing sandstone reservoir of 15% porosity using oil-base mud, P- and S-wave velocities obtained from simulated waveforms for multilayered models are the same as those of homogeneous model shown in Table 4.8. Figure 4.16(a) shows that the presence of oil-base mud filtrate behind casing slightly reduces the P-wave arrival times, but increases the S-wave arrival time. Arrival times for dipole waves remain unchanged shown in Figure 4.16(b). This is consistent with Figure 4.6, which indicates that after 30 days of fluid dissipation, the saturation of mud filtrate reduces to 50% from 95% in the near-wellbore region. Except for P-wave amplitudes in the monopole waveform, amplitudes for the S- and Stoneley- waveforms are not affected by the time variation of fluid saturation behind casing.

For the 30% porosity case, mud-filtrate invasion does not affect the estimated formation velocities and arrival times, and produces a minor impact on the amplitudes of both P and S waves. Therefore, it is concluded that both formation velocities estimated from array waveforms measured in cased holes are not sensitive to the presence of either casing, cement, or invaded zones after 30 days of oil-base mud-filtrate dissipation in the sandstone reservoirs considered in this Chapter.

4.7 SUMMARY AND CONCLUSIONS

Detailed radial profiles of elastic properties in near-wellbore region caused by filtration are computed using a reservoir simulator and the Biot-Gassmann fluid substitution model. These radial profiles are used as input for the numerical simulation of sonic array waveforms. Mud filtrate displacing a lighter formation fluid causes the P-wave velocity to decrease and the S-wave velocity to increase in the radial direction away from the wellbore.

By direct comparison of time-lapse monopole waveforms, it was found that P wave arrives earlier, and that S- and Stoneley-waves arrive later for formation models with invaded zones than for homogeneous formation models in the cases of water-base mud invading oil-bearing sandstone reservoirs. P-wave amplitudes decrease by more than ten times because of the diverging effect of the monotonically decreasing profiles of density and P-wave velocity in the radial direction away from the borehole wall. On the other hand, S-wave amplitudes increase by a few percent due to the focusing effect of the monotonically increasing profiles of the S-wave velocity in the radial direction. P waves are sensitive to virgin zones and S waves are affected by invaded zones when the mud-filtrate invasion depth is around 0.5-0.8 m. For the cases of oil-base mud invading sandstone reservoirs, both P and S waves are insensitive to the presence of mud filtrate in the invaded zones. The difference in P-wave arrivals for homogeneous and multilayered formations is negligible even though the delays for S-wave arrivals are approximately 10-20 μs for the multilayered formation.

The stepwise models considered in this chapter represent invaded zones reasonably well for the sandstone reservoirs. However, for the case of the gas-bearing carbonate reservoir, a stepwise model cannot be used to accurately represent the invaded zone. The applicability of stepwise models for invaded zones depends on the shapes of the fluid-saturation profiles in the invaded zones and on the depth of mud-filtrate invasion. Time-lapse dipole waveforms show that the S-wave arrival is delayed by about the same amount with respect to monopole waveforms for the case of invaded formations. It is also found that the amplitude is affected in similar.

In cased holes, both P- and S-wave amplitudes decrease significantly and low-frequency Stoneley wave dominates the monopole waveforms due to the presence of a steel casing. Amplitudes of dipole waveforms for homogeneous and multilayered formation models hardly show any change because dipole waves propagate at low frequency and hence are sensitive primarily to virgin formations.

Mud-filtrate invasion effects are not observed on the P- and S-wave velocities estimated with industry standard STC processing for invasion depths around 2-3 borehole diameters. Therefore, log corrections are not necessary in these situations using the Biot-Gassmann fluid substitution model although discrepancies between seismic and acoustic velocities may still exist. However, fluid substitution effects are clearly shown in the gas reservoir study wherein the invasion length reaches approximately 2 m. For this particular case, log corrections using the Biot-Gassmann fluid substitution model were performed and validated using field data.

Table 4.1: Summary of geometrical, petrophysical, and fluid parameters used in the construction of sandstone reservoir models of water-base mud-filtrate invasion.

Variable	Units	Base
Mudcake Permeability	md	0.03
Mudcake porosity	fraction	0.30
Mud solid fraction	fraction	0.06
Mudcake maximum thickness	cm	1.00
Mudcake compressibility exponent v	fraction	0.40
Mudcake exponent multiplier δ	fraction	0.10
Water viscosity (filtrate)	cp	1.00
Oil viscosity	cp	3.00
Rock compressibility	1/psi	0.0E-6
Water compressibility	1/psi	0.0E-6
Initial formation pressure	psi	5000.00
Mud hydrostatic pressure	psi	5500.00
Formation permeability	md	300.00
Formation porosity	fraction	0.25
Permeability anisotropy	fraction	1.00
Total invasion time	hours	48.00
Mudcake rub-off time	hours	36.00
Wellbore radius	cm	10.00
Mud filtrate salinity	ppm	43,900.00
Formation water salinity	ppm	102,500.00
Irreducible water saturation	fraction	0.1

Table 4.2: Summary of properties used in the fluid substitution model for sandstone reservoirs.

Bulk modulus of mineral matrix	GPa	3.0E10
Shear modulus of mineral matrix	GPa	1.0E10
Bulk density of mineral matrix	Kg/m^3	2400
Bulk modulus of mud-filtrate	GPa	2.9E9
Density of mud-filtrate	Kg/m^3	1055
Bulk modulus of oil	GPa	2.0E9
Density of oil	Kg/m^3	800
Bulk modulus of gas	GPa	0.033
Density of gas	Kg/m^3	100

Table 4.3: P- and S-wave velocities for the virgin formation and the invaded zones and estimated velocities using monopole data for homogeneous, stepwise, and multilayered models reconstructed for the case of a carbonate gas reservoir.

Model	Vp (km/s)	Vp error (%)	Vs (km/s)	Vs error (%)
True	4973.0		2908.0	
Homogeneous	4916.1	-1.1	2867.4	-1.4
Invaded	5092.3	2.4	2841.4	-2.3
Stepwise	5038.2	1.3	2848.6	-2.0
Multilayered	5038.2	1.3	2809.2	-3.4

Table 4.4: P- and S-wave velocities for the virgin formation and the invaded zones and estimated velocities using monopole data for homogeneous, stepwise, and multilayered models for the case of an oil-bearing sandstone reservoir of 15% porosity.

Model	Vp (km/s)	Vp error (%)	Vs (km/s)	Vs error (%)
True	3806.2		2272.5	
Homogeneous	3819.5	0.4	2241.2	-1.4
Invaded	3844.9	1.0	2252.5	-0.8
Stepwise	3763.0	-1.1	2208.7	-2.8
Multilayered	3763.0	-1.1	2192.8	-3.5

Table 4.5: P- and S-wave velocities for the virgin formation and the invaded zones and estimated velocities using monopole data for homogeneous, stepwise, and multilayered models for the case of an oil-bearing sandstone reservoir of 30% porosity

Model	Vp (km/s)	Vp error (%)	Vs (km/s)	Vs error (%)
True	3360.6		2045.4	
Homogeneous	3349.5	-1.0	2014.4	-1.5
Invaded	3394.8	1.1	2004.9	-2.0
Stepwise	3349.5	-0.3	1966.5	-3.9
Multilayered	3349.5	-0.3	1961.4	-4.1

Table 4.6: P- and S-wave velocitiesfor the virgin formation and the invaded zones and estimated velocities using monopole data for homogeneous, stepwise, and multilayered models for a gas-bearing sandstone reservoir of 15% porosity.

Model	Vp (km/s)	Vp error (%)	Vs (km/s)	Vs error (%)
True	3516.3		2142.8	
Homogeneous	3544.2	0.8	2154.6	0.5
Invaded	3669.3	4.4	2122.4	-1.0
Stepwise	3569.1	1.5	2151.2	0.4
Multilayered	3577.5	1.7	2149.5	0.3

Table 4.7: P- and S-wave velocities for the virgin formation and the invaded zones and estimated velocities using monopole data for homogeneous, stepwise, and multilayered models for the case of a gas-bearing sandstone reservoir of 30% porosity.

Model	Vp (km/s)	Vp error (%)	Vs (km/s)	Vs error (%)
True	3277.7		2043.9	
Homogeneous	3249.5	-0.9	2042.9	0.0
Invaded	3344.4	2.0	1955.2	-4.3
Stepwise	3249.5	-0.9	2018.5	-1.2
Multilayered	3249.5	-0.9	2025.3	-0.9

Table 4.8: P- and S-wave velocities for the virgin formation and the invaded zones and estimated velocities using monopole data for homogeneous and multilayered models for the case of the gas-bearing sandstone reservoir of 15% porosity penetrated by a cased hole.

Model	Vp (km/s)	Vp error (%)	Vs (km/s)	Vs error (%)
True	3516.3		2142.8	
Homogeneous	3536.0	0.6	2146.5	0.2
Invaded	3669.3	4.4	2122.4	-1.0
Multilayered	3503.4	-0.4	2128.5	-0.7

Table 4.9: P- and S-wave velocities for the virgin formation and the invaded zones and estimated velocities using monopole data for homogeneous and multilayered models for the case of a gas-bearing sandstone reservoir of 30% porosity penetrated by a steel-cased borehole.

Model	Vp (km/s)	Vp error (%)	Vs (km/s)	Vs error (%)
True	3277.7		2043.9	
Homogeneous	3259.9	-0.5	2029.3	-0.7
Invaded	3344.4	2.0	1955.2	-4.3
Multilayered	3263.4	-0.4	2027.9	-0.8

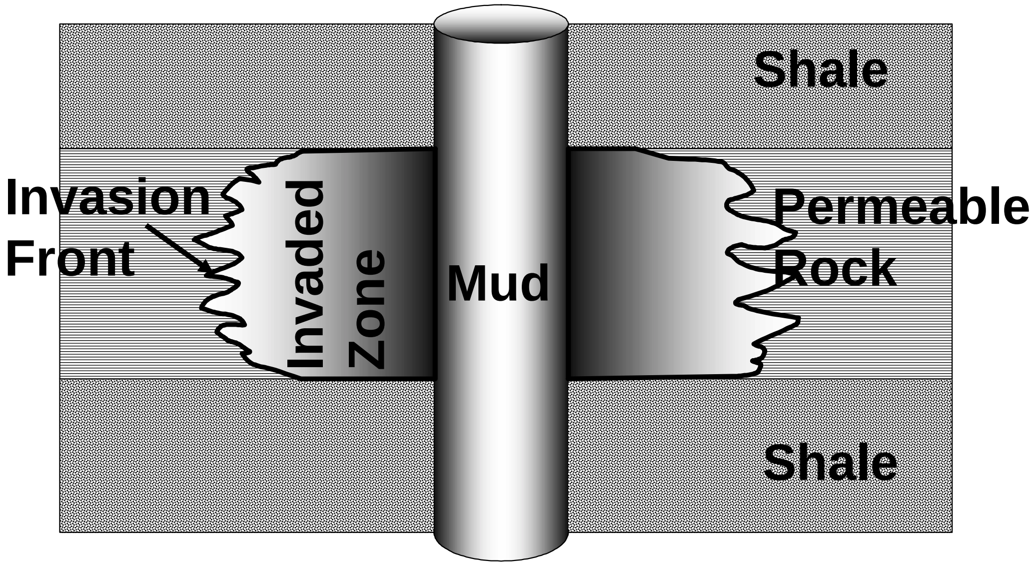

Figure 4.1: Schematic of mud-filtrate invasion in rock formations penetrated by a mud-filled borehole.

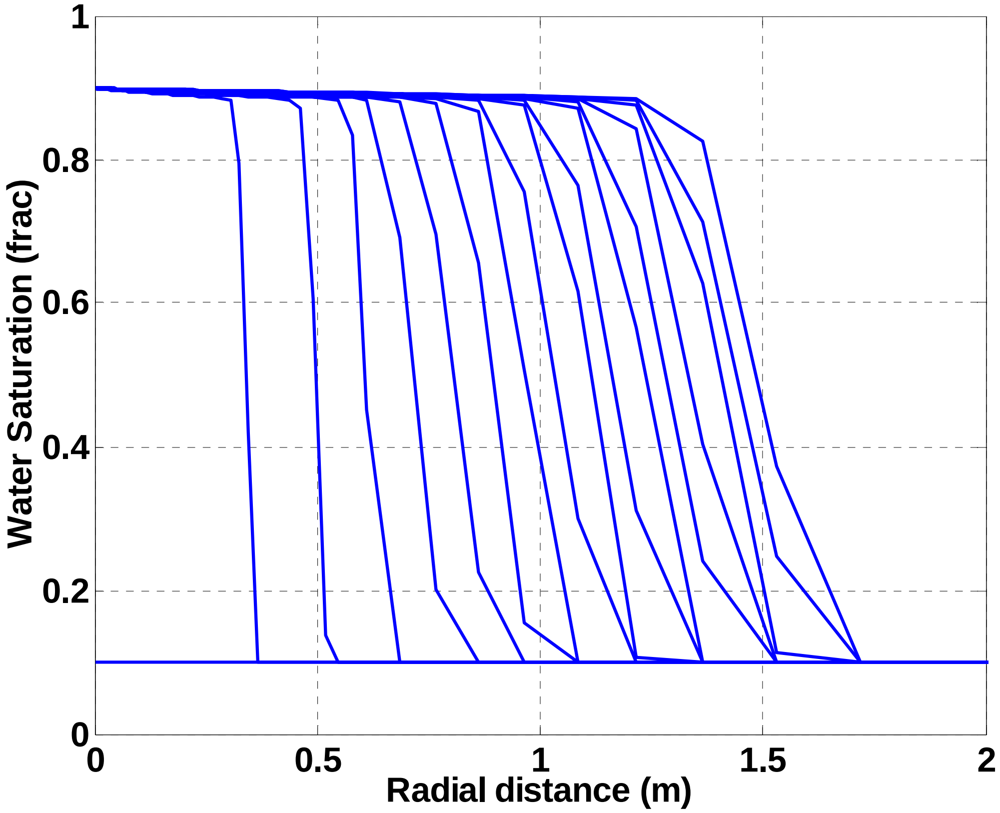

Figure 4.2: Time evolution of mud-filtrate invasion for the case of water-base mud invading a 15% porosity, oil-bearing reservoir. Plots of water saturation are shown for uniform time intervals of one day after the onset of mud-filtrate invasion. The first plot of water saturation corresponds to a time of one day after the onset of invasion.

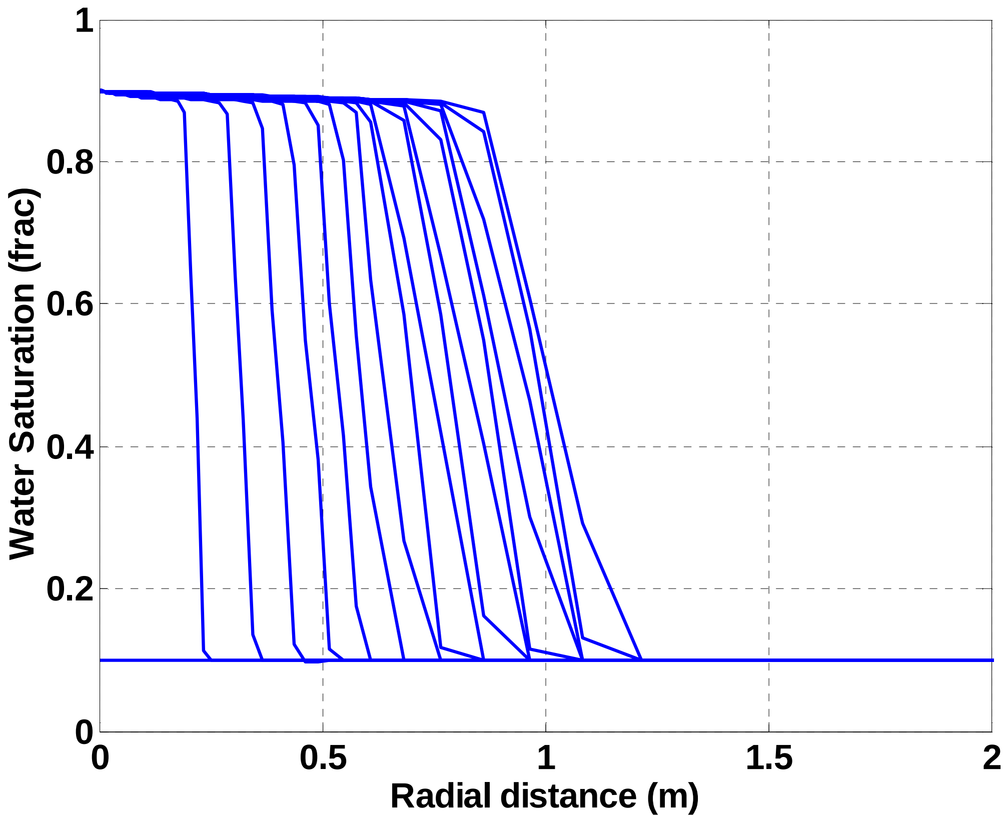

Figure 4.3: Time evolution of mud-filtrate invasion for the case of water-base mud invading a 30% porosity, oil-bearing reservoir. Each line denotes one-day invasion.

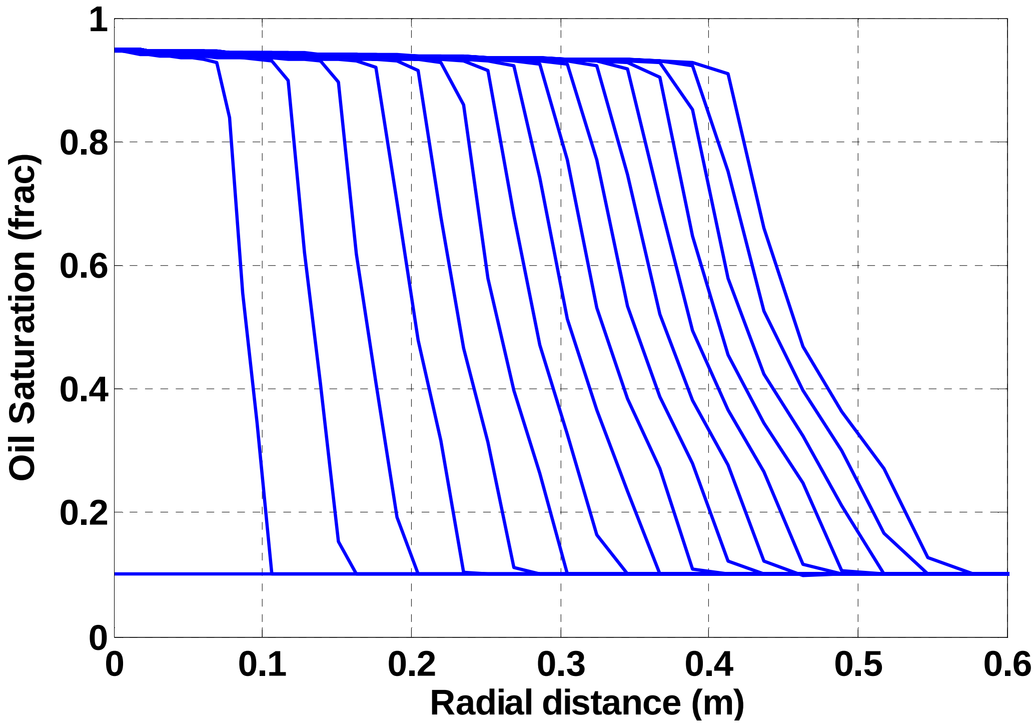

Figure 4.4: Time evolution of mud-filtrate invasion front for the case of oil-base mud invading a 15% porosity, gas-bearing reservoir. Each line denotes one-day invasion.

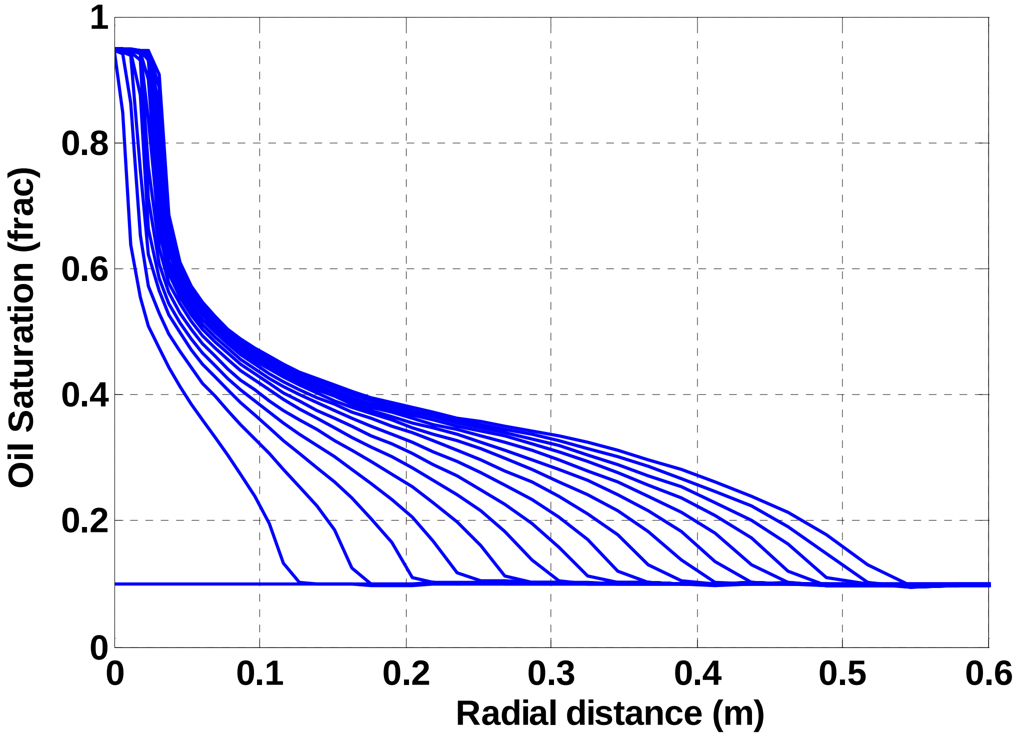

Figure 4.5: Time evolution of mud-filtrate invasion front for the case of oil-base mud invading a 30% porosity, gas-bearing reservoir. Each line denotes one-day invasion.

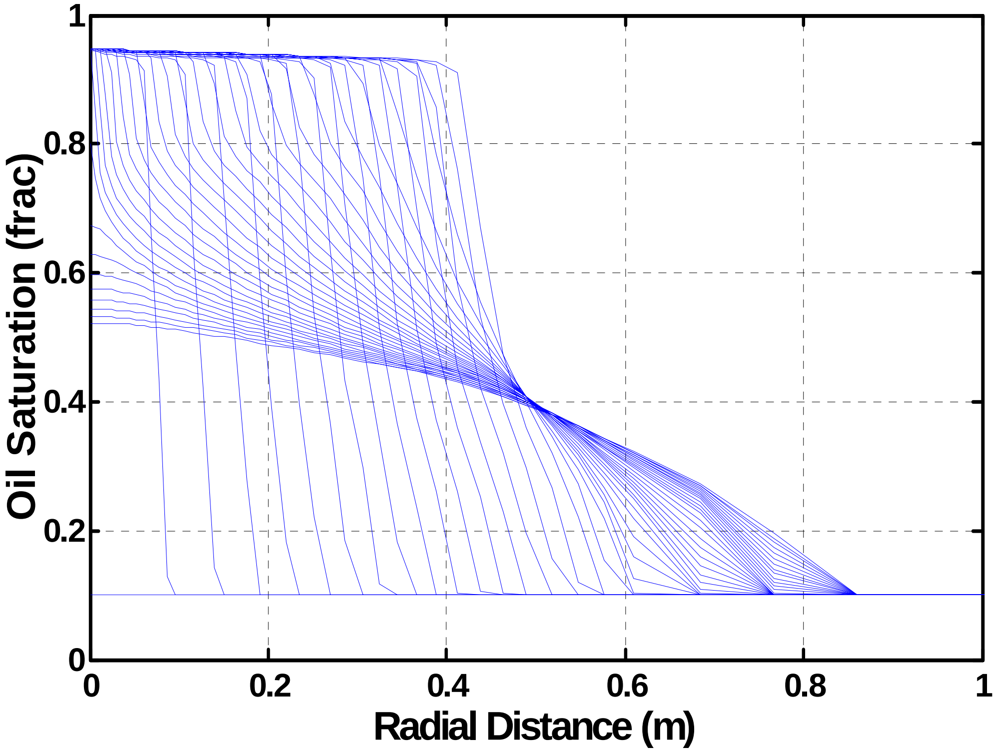

Figure 4.6: Time evolution of mud-filtrate invasion front for the case of oil-base mud invading a 15% porosity, gas-bearing reservoir in the cased-hole case. Each line denotes one-day invasion or dissipation.

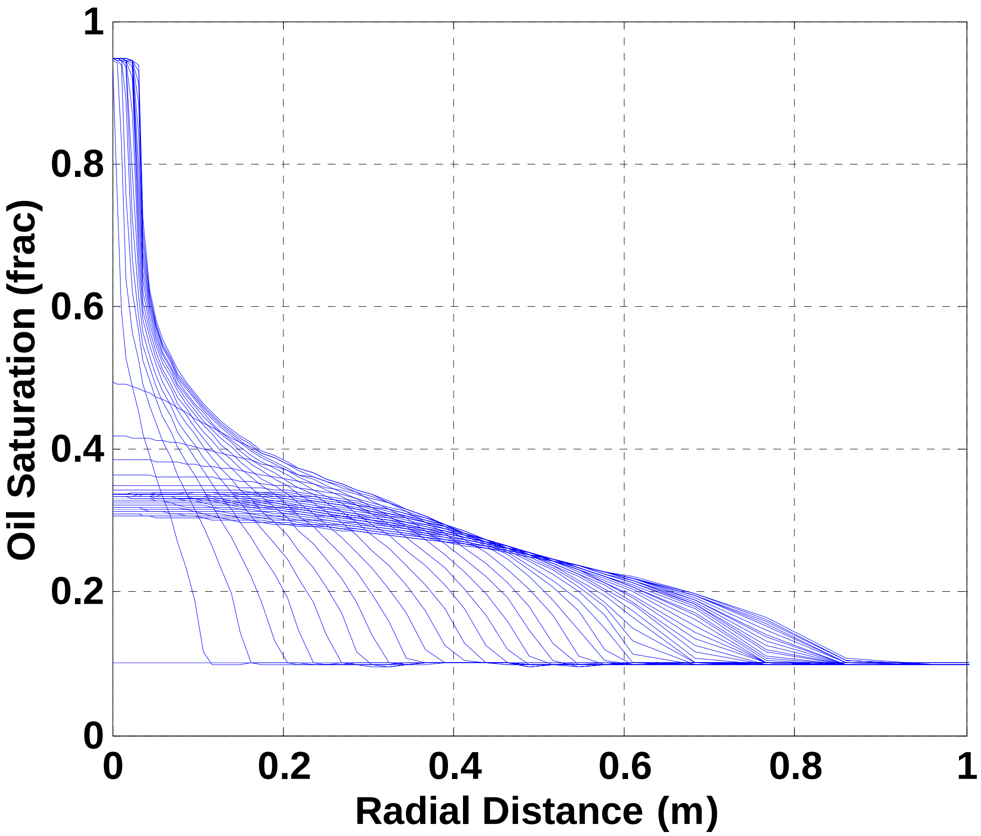

Figure 4.7: Time evolution of mud-filtrate invasion front for the case of oil-base mud invading a 30% porosity, gas-bearing reservoir in the cased-hole. Each line denotes one-day invasion or dissipation.

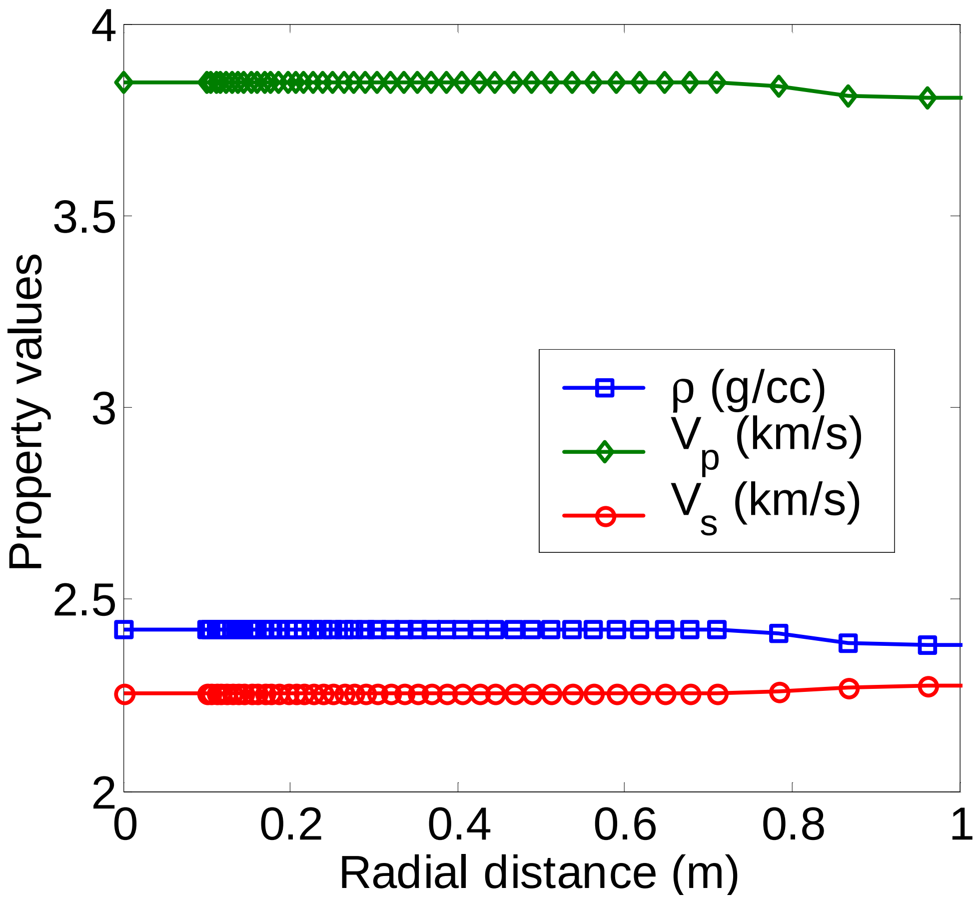

Figure 4.8: Radial profiles of density and P- and S-wave velocities for the case of water-base mud invading a 15% porosity, oil-bearing reservoir after 4 days of invasion.

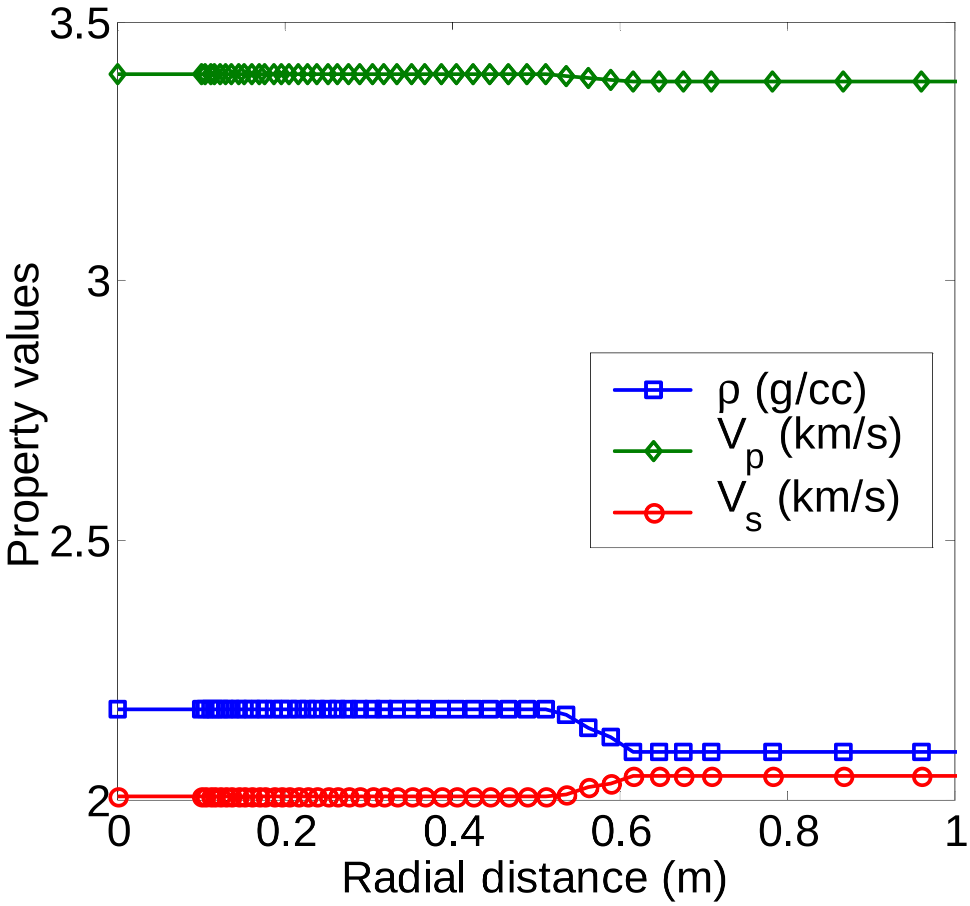

Figure 4.9: Radial profiles of density and P- and S-wave velocities for the case of water-base mud invading a 30% porosity, oil-bearing reservoir after 4 days of invasion.

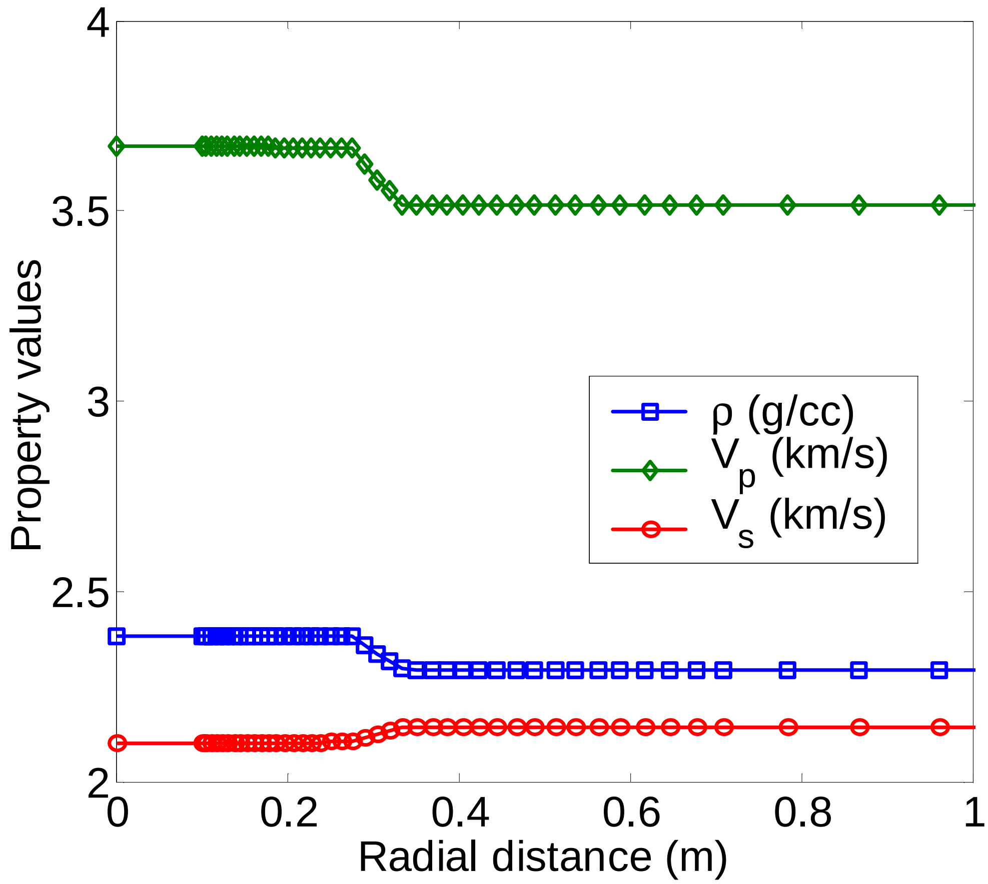

Figure 4.10: Radial profiles of density and P- and S-wave velocities for the case of oil-base mud invading a 15% porosity, gas-bearing reservoir after 4 days of invasion.

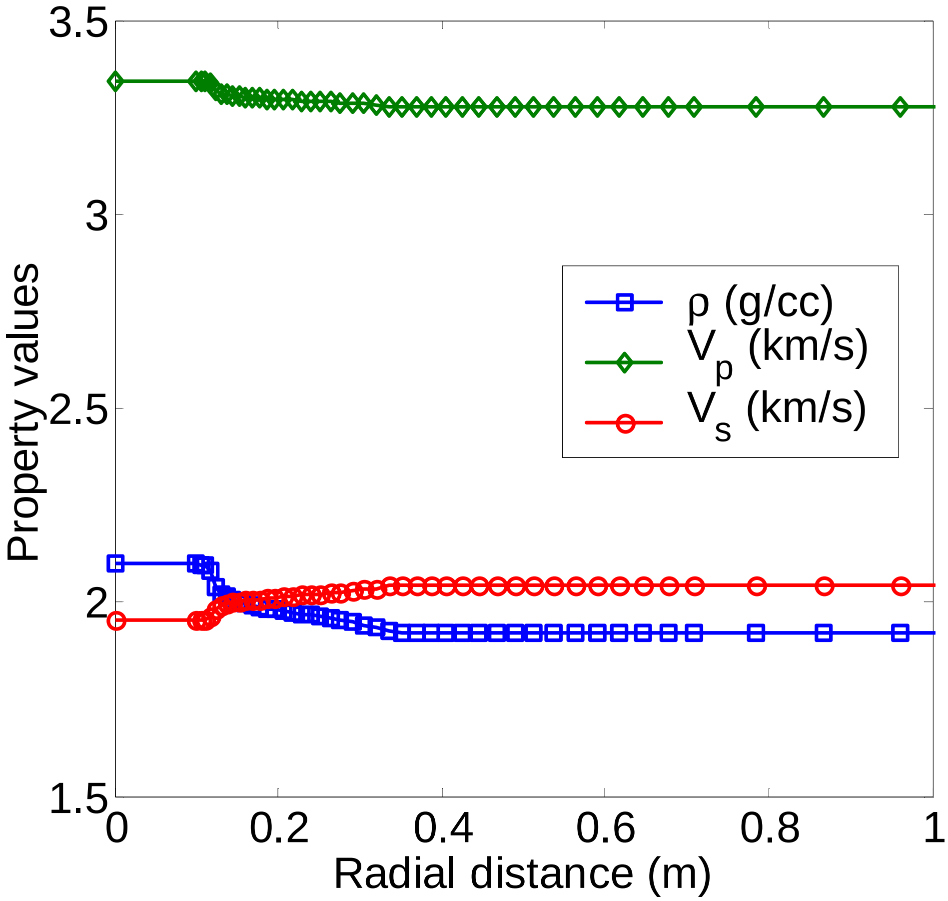

Figure 4.11: Radial profiles of density and P- and S-wave velocities for the case of oil-base mud invading a 30% porosity, gas-bearing reservoir after 4 days of invasion.

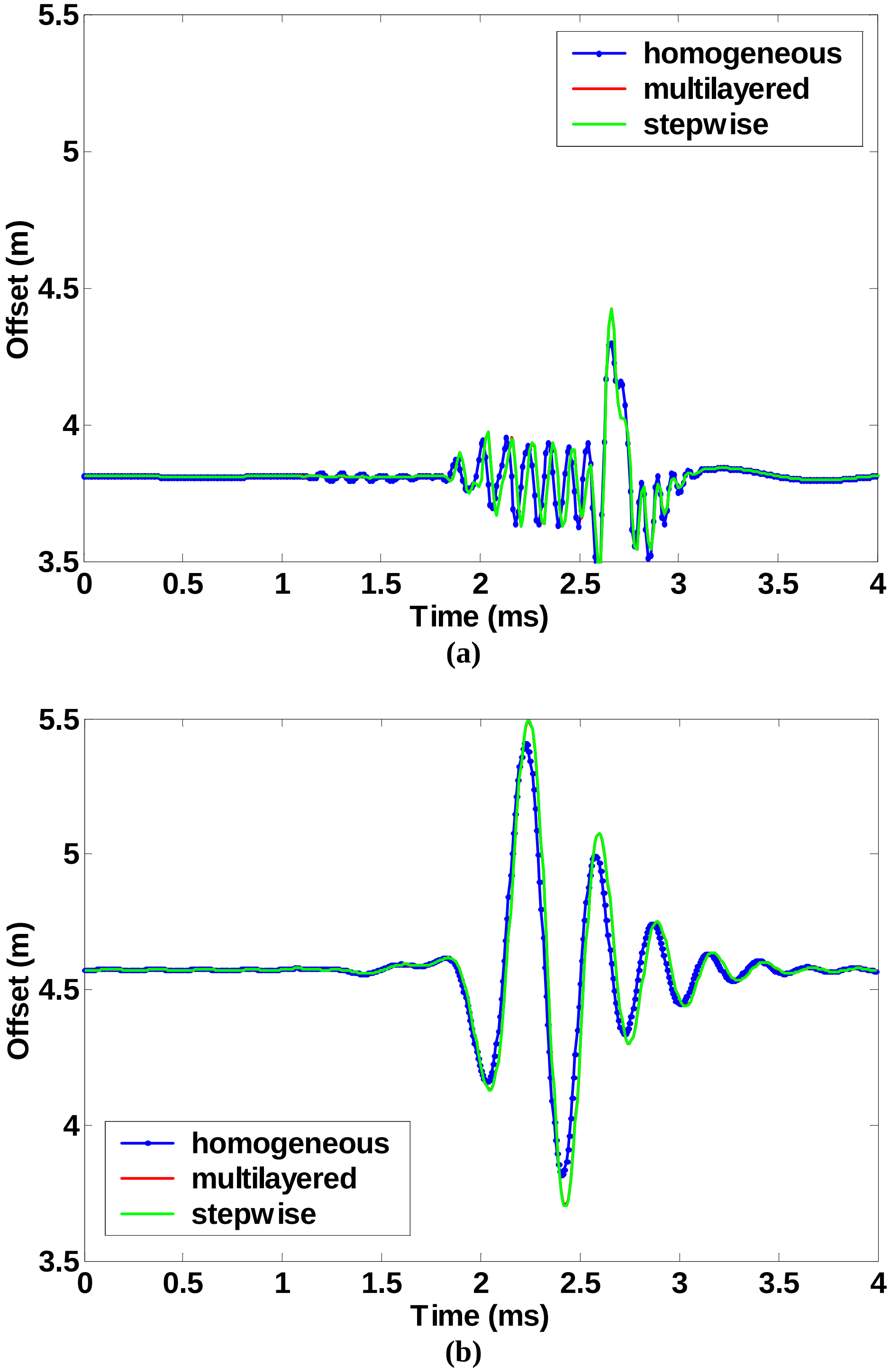

Figure 4.12: Simulated (a) monopole and (b) dipole waveforms for a homogeneous, stepwise, and multilayered formation model shown in Figure 4.8.

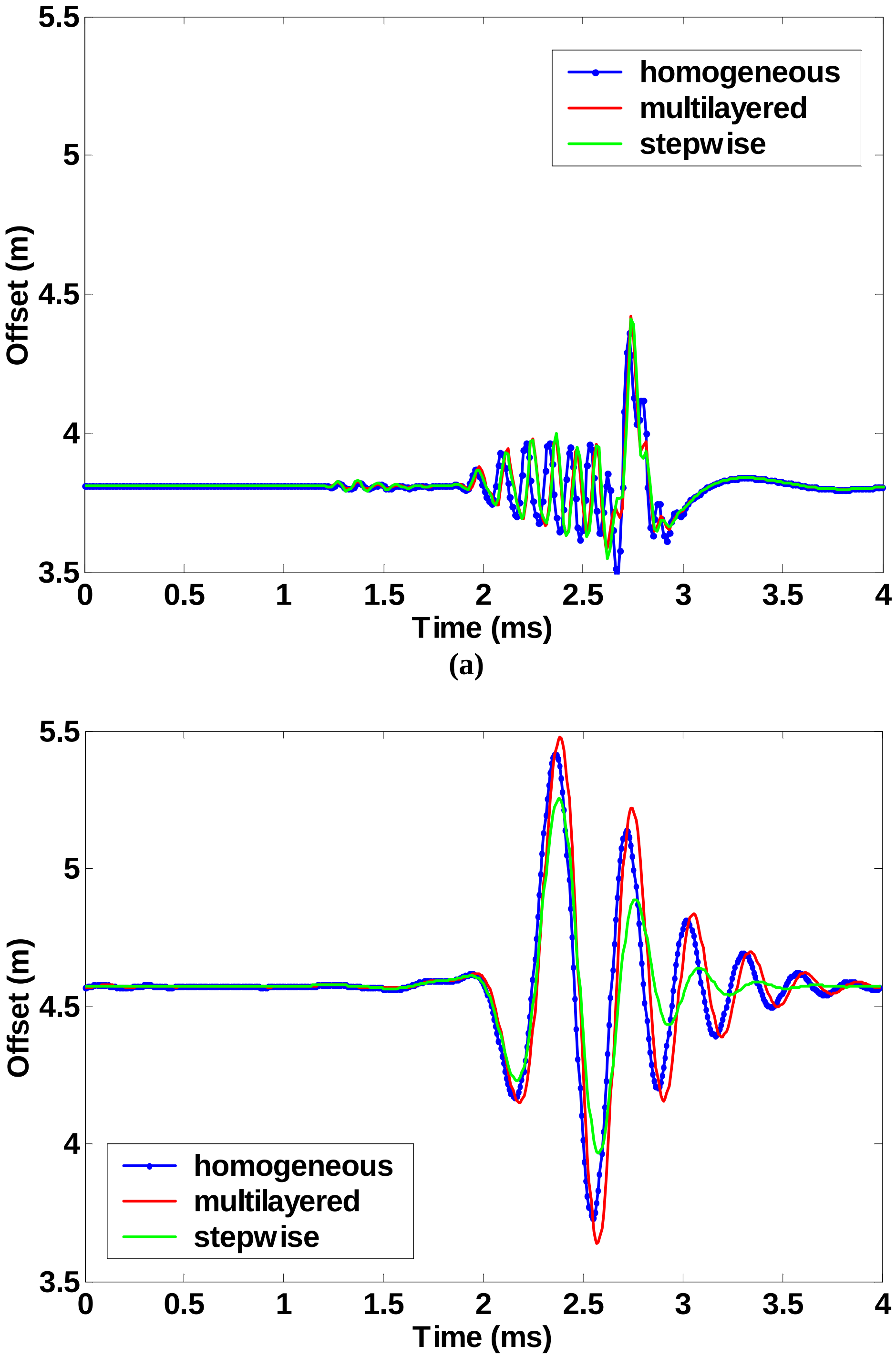

(a)

(b)

Figure 4.13: Simulated (a) monopole and (b) dipole waveforms for the case of a homogeneous, stepwise, and multilayered formation model invaded with oil-base mud after 4 days of invasion in a gas reservoir with a 30% porosity.

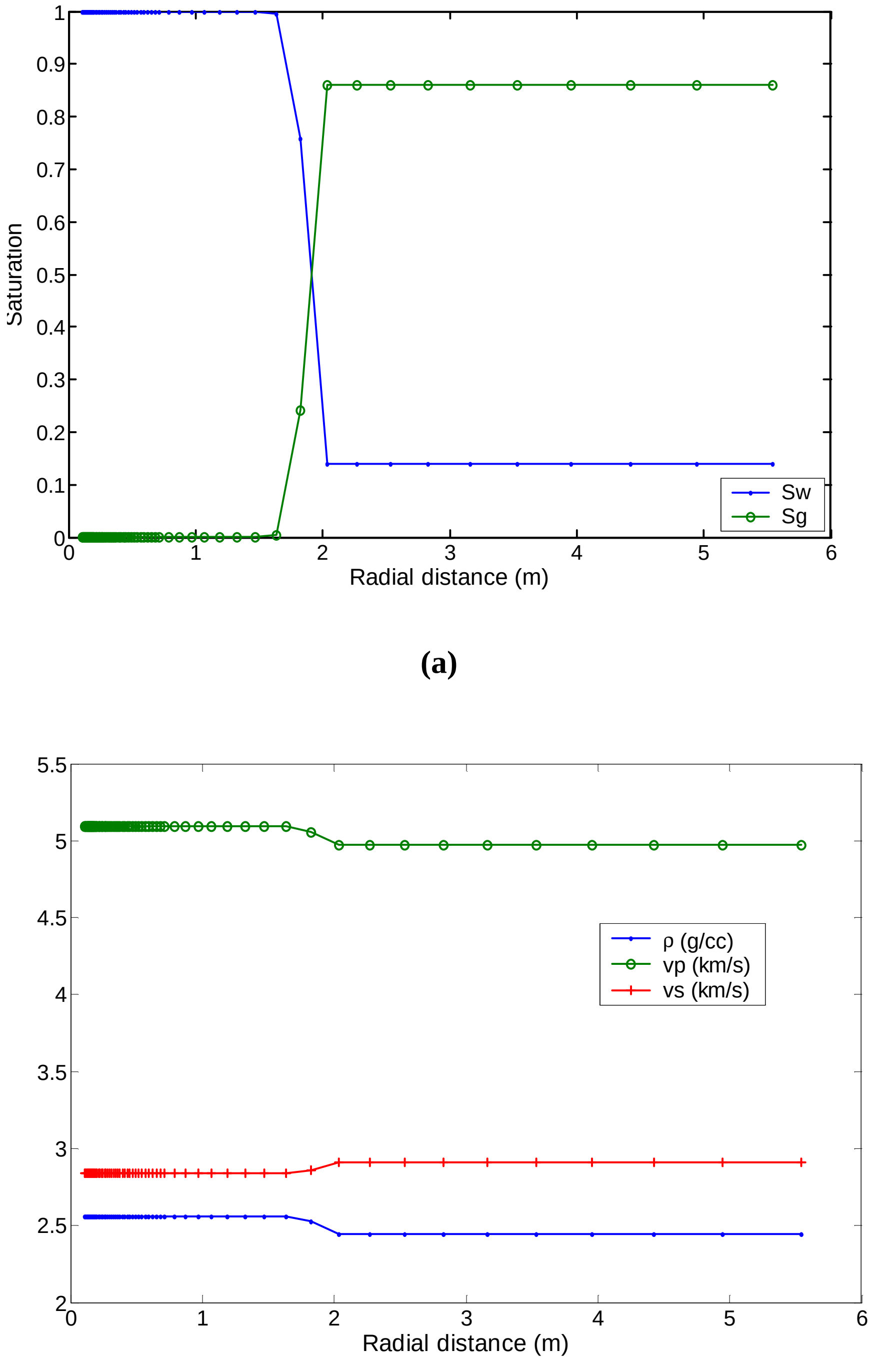

(a)

(b)

Figure 4.14: (a) Radial profiles of water and gas saturation in a layer of Well X2. (b) Radial profiles of density and P- and S-wave velocities in a layer of Well X2 for the Anadarko reservoir case.

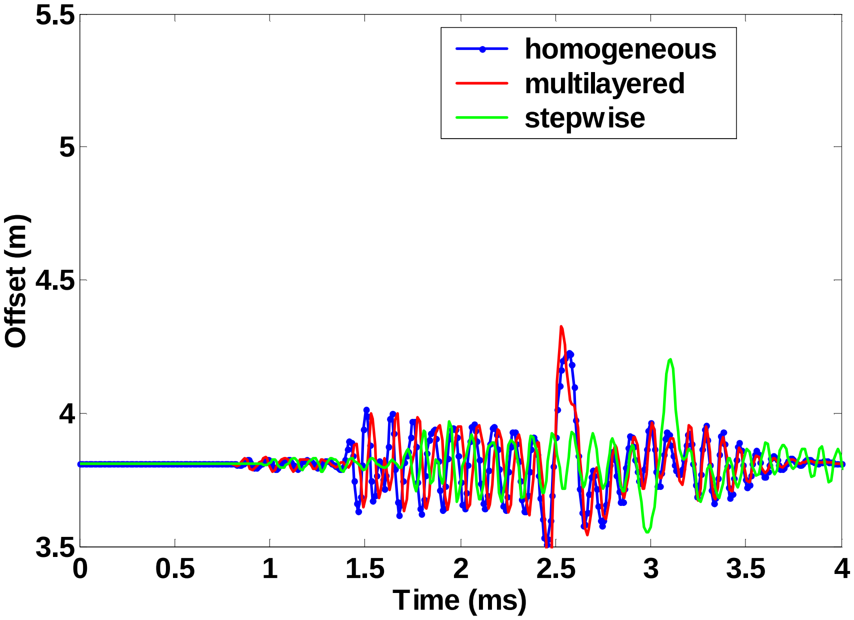

(a)

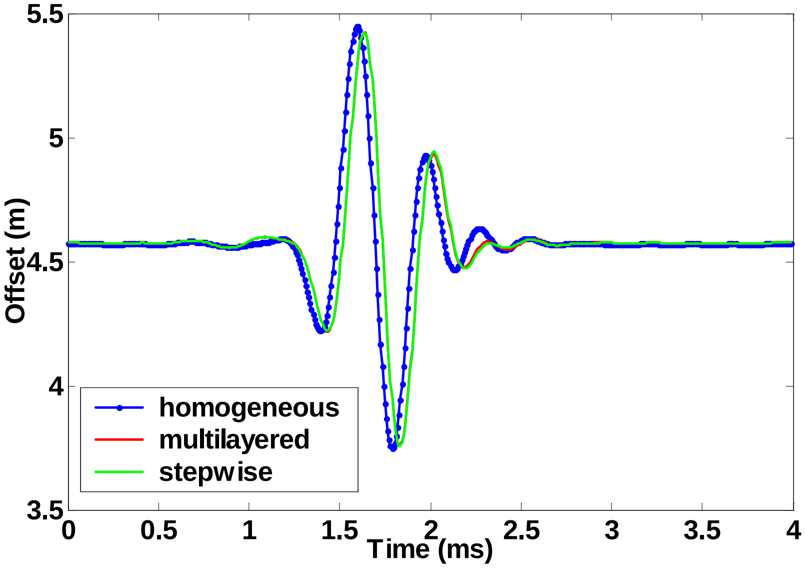

(b)

Figure 4.15: Comparison of (a) monopole (b) dipole waveforms for well X-2 for the case of homogeneous, multilayered, and stepwise radial invasion models.

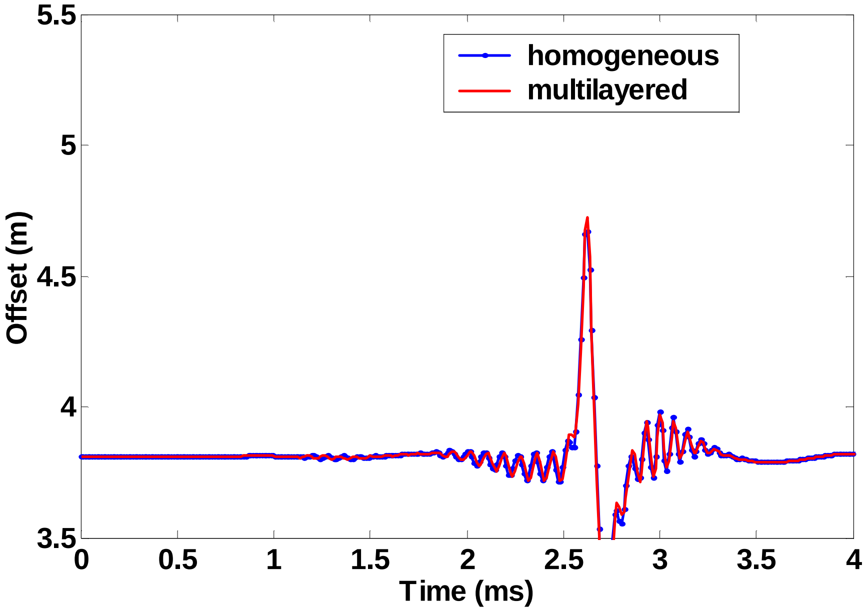

(a)

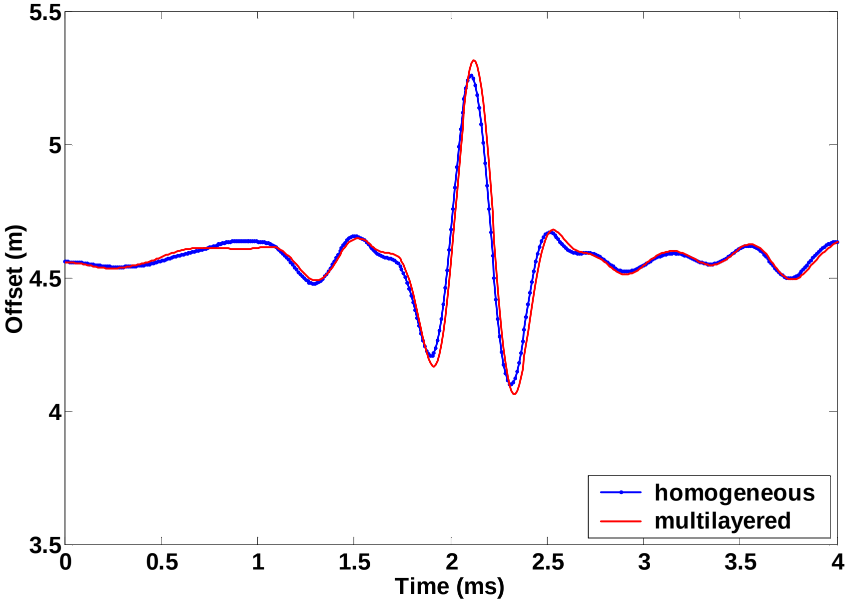

(b)

Figure 4.16. Comparison of (a) monopole (b) dipole waveforms acquired in cased holes for the case of homogeneous, multilayered, and stepwise radial invasion models in the gas reservoir exhibiting 15% porosity.

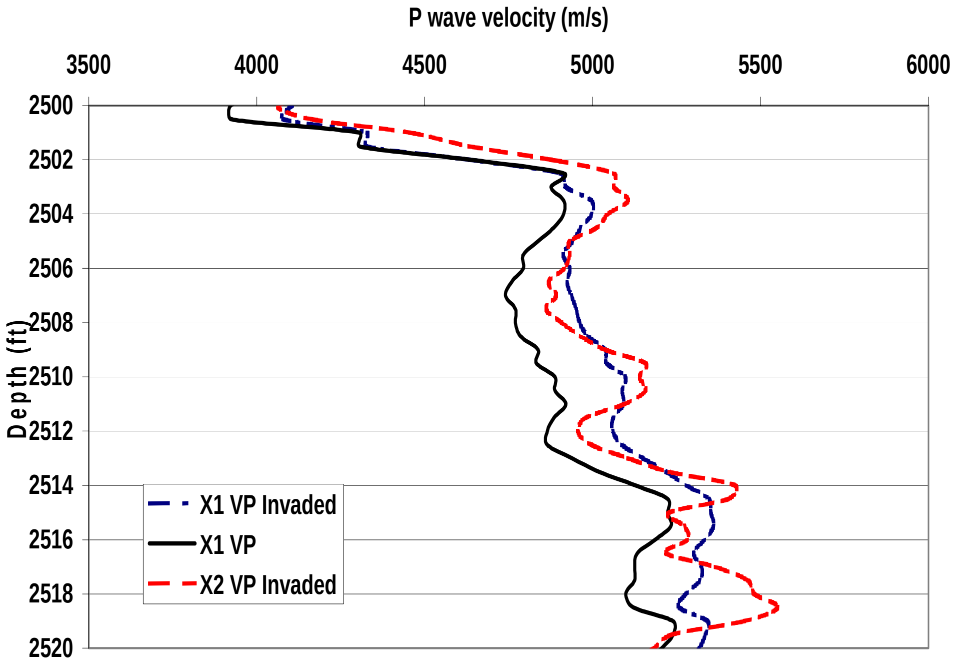

Figure 4.17: P-wave velocity logs in well X-1 drilled using a lightweight mud, and in well X-2 drilled using a water-base mud. The P-wave log in well X-1 is forward modeled to simulate the log under deep water-base mud invasion. Comparison of the P-wave logs in well X-2 with the calculated one in well X-1 indicates that well X-2 is deeply invaded by water-base mud.

Chapter 5: Radial Profiling Using Full Waveform Acoustic Logging Data

Rock formation velocities estimated with industry standard sonic data processing are often influenced by near-wellbore damages and mud-filtrate invasion. This may result in biased estimation of virgin formation properties. Moreover, full waveforms contain much more information than only the P- and S-wave velocities being routinely used in commercial logging applications. Inversion of acoustic full waveforms can be used to estimate radial profiles of velocities in the near-wellbore region. Such endeavor has been a challenging subject, partly because of the lack of precise knowledge of the mechanical coupling of the source with the borehole and the surrounding rock formations.

A method is proposed in this chapter to estimate radial profiles of density and P- and S-wave velocities using array full waveforms. Array waveforms are first transformed from the time domain to the frequency domain using a fast Fourier transform. A new array data set is obtained by normalizing the remaining traces using as a reference one of the available traces. Therefore, the complex-valued normalized spectra are rendered dimensionless. Since the normalized spectral ratios do not entail source information, the spectral normalization procedure does away with the need of source wavelet information for full-waveform inversion. The inversion algorithm minimizes the least-squared misfit between the measured normalized wavefield and the modeled normalized wavefield in a selected frequency band. This algorithm is successfully applied to the inversion of radial profiles of density and P- and S-wave velocities in the near wellbore regions in the presence of damaged and invaded zones.

5.1 INTRODUCTION

Practical uses of borehole acoustic measurements include the estimation of formation velocities, formation fluid identification, fluid permeability estimation, and saturation determination. Current industry practice of acoustic data processing makes use of the slowness-time coherence (STC) method to estimate in-situ velocities of rock formations. This type of processing yields values of P- and S-wave velocities, both of which are complex functions of formation and borehole properties, frequency, and number of time samples used in the window of the STC algorithm. When near-wellbore formation damage is significant, velocity logs obtained with the STC method may only reflect properties of the damaged zone even though modern acoustic tools are designed to sense past the damaged zone with the use of long source-receiver spacing and relatively low source frequencies. However, measured arrival times will be different in the presence of the damaged zone and will depend on the actual path that the elastic waves take from the source to the receivers. It becomes evident that a naïve implementation of STC processing to estimate velocities discards valuable information about near-wellbore formation properties.

In an effort to estimate near-wellbore formation properties, Hornby (1993) developed a tomographic reconstruction technique that yielded formation compressional velocities near the wellbore from sonic travel times. The estimation was performed using a series of linear inversions followed by ray tracing. However, traveltime tomography using ray tracing requires accurate picking of the refracted arrivals of each wavetrain and of the use of an accurate high-frequency ray-trace approximation; the maximum resolution is of the order of one wavelength (Sheng and Schuster, 2000). Furthermore, the method is limited to the reconstruction of the radial profile of compressional velocity in the near-wellbore region, though estimation of formation shear wave velocity has long been one of the major objectives of full waveform acoustic logging.

Shear moduli derived from formation shear velocity is important in a number of production problems, including hydraulic fracturing and wellbore stability analysis. P- to S-wave velocity ratio or, equivalently, the Poisson's ratio, is an excellent tool for lithology identification and for quantitative interpretation of saturating fluids. These velocities can be accurately measured in hard formations, where the S-wave velocity is faster than the acoustic velocity of the borehole fluid. However, in soft formations, where the S-wave velocity is slower than the acoustic velocity of the borehole fluid, shear wave components do not exist in logs acquired with monopole sources. An indirect method has to be used to determine the S-wave velocity of slow formations (Cheng, 1989). Multipole source tools can be used to estimate S-wave velocities in such environments, but the cost of the logging service can be high and the multipole data are not available in many mature fields. This Chapter develops a novel technique to estimate radial profiles of S-wave velocity in a soft formation using full waveform inversion.

A sizable number of studies in seismic full waveform inversion (e.g. Sen and Stoffa, 1991; Zhou et al., 1997; Pratt, 1999a, 1999b) show that the use of amplitude data can improve the vertical resolution of one-dimensional distributions of velocity and density. Amplitude and phase behavior of full waveform data are sensitive to the petrophysical properties of formations supporting the propagation of elastic waves. Therefore, full-waveform analysis has a significant potential in acoustic logging to estimate petrophysical properties of damaged zones and virgin formations. The reconstruction of formation slowness away from the borehole can provide valuable calibration factors for measurements acquired with shallow reading devices, for example, bulk density logging. Corrections provided by full-waveform inversion may be of primary importance for the robust and accurate computation of synthetic seismograms. There is, however, one major difficulty to overcome in full waveform inversion. In all field applications, the effective source wavelet, the coupling among source, borehole, and formation, and the coupling between receivers and formation depend on the in-situ borehole conditions. The practical difficulty in estimating the sonic source signature is probably the reason why very few attempts have been made to use the rich information contained in the full waveform of acoustic logging data.

Cheng (1989) described an indirect method for determining shear wave velocities from full waveform acoustic logs based on inversion. This method makes use of the spectral ratio of the P wavetrains at two source-receiver separations, and simultaneously inverts for both formation shear-wave velocity and compressional wave attenuation. In this Chapter, Cheng's (1989) approach based on spectral ratio data is extended to full waveform arrays to overcome the practical difficulty of unknown source output spectrum. Lee and Kim (2003) estimated compressional velocity structures from synthetic seismic data by using spectral ratio method. Frazer et al. (1997) and Frazer and Sun (1998) presented an inversion scheme for processing array full waveform data. Their approach does not require an exact source function although it is a necessary part of the inversion. Because of this, the chosen source function can affect the inversion results.

This inversion approach presented in this chapter first transforms array waveforms into the frequency domain to construct a set of normalized array sonic data. The normalized wavefield is independent of the spectrum of the source, and hence the proposed inversion method allows one to make use of the full waveform content of sonic data without requiring knowledge of the source signature. Previous studies of full waveform borehole acoustic measurements assumed a homogeneous and isotropic formation and a model for borehole wave propagation without surface irregularities. The developments considered in this chapter make the assumptions of a radially multilayered formation model and a cylindrical borehole.

5.2 NORMALIZED WAVEFIELD

Array full waveforms acquired with a monopole-logging source are simulated using the method of generalized reflection and transmission described in Chapter 3. The pressure response at a point located at (*r, z*) in cylindrical coordinates due to a source located at (0, 0) in a fluid-filled borehole is given by

$$\phi_{total}\left(r,z,t\right)=-\frac{1}{8\pi^2}\int_{-\infty}^{\infty}S\left(\omega\right)e^{-i\omega t}d\omega\times\left[i\int_{-\infty}^{\infty}\frac{\hat{R}_{+-}^{(1)}e^{ikp_f r_1}}{1-\hat{R}_{+-}^{(1)}e^{ikp_f r_1}}e^{ikz}dk+\frac{e^{ik_f z}}{z}\right]. \tag{5.1}$$

This model of wave propagation in a borehole assumes an isotropic, radially multilayered formation, with no irregularities along the borehole wall. As with any inversion procedure, the accuracy and reliability of the results will depend on how accurately the forward model describes actual in-situ conditions. In practical field studies, irregularities on the borehole wall can be quantified using caliper measurements. Consequently, vertical intervals of formation can be identified that are consistent with the assumption of a smooth borehole wall. Along the length of the receiver spacing (6 in), the formation can be regarded as homogeneous in the axial direction.

In practice, the effect of borehole-receiver coupling can be assumed negligibly small in comparison to source coupling. The spectral ratio of the pressure responses at two receiver locations, z_1 and z_2, from one common source can be written as

$$T_{12} = \frac{S(\omega)\left[i\int_{-\infty}^{\infty} \frac{\hat{R}_{+-}^{(1)} e^{ikp_f r_1}}{1-\hat{R}_{+-}^{(1)} e^{ikp_f r_1}} e^{ikz_2}\, dk + \frac{e^{ik_f z_2}}{z_2} \right]}{S(\omega)\left[i\int_{-\infty}^{\infty} \frac{\hat{R}_{+-}^{(1)} e^{ikp_f r_1}}{1-\hat{R}_{+-}^{(1)} e^{ikp_f r_1}} e^{ikz_1}\, dk + \frac{e^{ik_f z_1}}{z_1} \right]}, \tag{5.2}$$

where $S(\omega)$ is an effective source output spectrum. The source terms in equation (5.2) divide to 1, hence resulting in a final frequency representation independent of the source spectrum. This procedure indicates that knowledge about the source spectrum can be rendered obsolete for full-waveform inversion when spectral ratios are used in inversion. In fact, the term T_{12} in equation (5.2) is the transfer function between the two receivers. For practical applications, the source functions are never fully known due to the variability of mechanical coupling due to vertical variation of formation properties. The source independent formulation described by equation (5.2) summarizes the conceptual basis for a robust and efficient algorithm that can be used as the forward computational model for full-waveform inversion. Thus, within the context of full-waveform inversion, a computer algorithm based on equation (5.1) is used to simulate the response of modern logging tools that measure array waveforms from an array of receivers.

The transfer function T_{12} depends on both the formation and borehole properties. Specifically, factors that affect the transfer function include (a) elastic parameters of the formation, (b) borehole radius R, (c) acoustic velocity V_f, (d) density ρ_f, and (e) quality factors for formation and borehole fluid. Toksöz et al. (1985), Cheng et al. (1986), and Cheng (1989) have assessed some of these factors using forward modeling techniques. Because the primary goal of this chapter is to simultaneously invert radial profiles of density and P- and S-wave velocities, quality factors will not be subject to quantitative consideration. Sensitivity analysis is performed to quantify the influence of borehole radius, fluid acoustic velocity, and density in the simultaneous inversion assuming a simple borehole model.

5.3 FULL WAVEFORM INVERSION

The normalized wavefield (or the normalized spectrum) of full-waveforms constitute the measurement data input to the full-waveform inversion algorithm. A cost function that enforces the least-squared difference between the simulated and measured normalized-wavefields is used for inversion. In order to quantify the robustness of the inversion algorithm, this chapter also considers a sensitivity study to assess the influence of noise, normalization trace, and regularization parameter.

For the estimation of the radial distribution of elastic parameters, density and P- and S-wave velocities are assigned a constant value within each radial layer in the near-wellbore region. Let $\mathbf{m}$ be the size-N vector of unknown parameters that fully describe the radial distribution of elastic parameters, and $\mathbf{m}_R$ be a reference vector of the same size as $\mathbf{m}$ that has been determined from some a-priori information. The estimation (inversion) of $\mathbf{m}$ is undertaken from the measured data by minimizing a quadratic cost function, $C(\mathbf{m})$, defined as (Torres-Verdín and Habashy, 1994)

$$2C(\mathbf{m}) = \left[\left\| \mathbf{W}_d \cdot \left[\mathbf{d}(\mathbf{m}) - \mathbf{d}^{obs} \right] \right\|^2 - \chi^2 \right] + \lambda \left\| \mathbf{W}_m \cdot (\mathbf{m} - \mathbf{m}_R) \right\|^2, \qquad (5.3)$$

where $\mathbf{d}^{obs}$ is a size-M vector that contains the noisy measurements, and $\mathbf{W}_d \cdot \mathbf{W}_d^T$ is the inverse of the data covariance matrix. This data-weighing matrix describes the estimated variance for each particular measurement and the estimated correlation between measurements. The parameter χ denotes the prescribed value of enforced data misfit. A-priori estimates of the noise in the measurements are employed to determine the magnitude of χ. In equation (5.3), $\mathbf{d}(\mathbf{m})$ is the measurement vector numerically simulated for specific values of $\mathbf{m}$, $\mathbf{W}_m \cdot \mathbf{W}_m^T$ is the inverse of the model covariance matrix, used to enforce a quantitative degree of confidence in the reference model, $\mathbf{m}_R$, and to enforce a-priori information on $\mathbf{m}$, and λ is a Lagrange multiplier or regularization parameter.

The first additive term on the right-hand side of equation (5.3) drives the inversion toward fitting the measurements within the desired χ^2 value. The sole presence of such a term in the cost function, $C(\mathbf{m})$, will yield multi-valued solutions of the inverse problem as a result of both noisy measurements as well as insufficient and imperfect data sampling. Enforcing an extremely small data misfit may result in estimated models with exceedingly large norms (Torres-Verdín and Habashy, 1994). The second additive term on the right-hand-side of equation (5.3) is used to reduce non-uniqueness and to stabilize the inversion in the presence of noisy and sparse measurements. In this context, the Lagrange multiplier, λ, controls the relative weight of the two additive terms in the cost function. The developments considered in this chapter make use of relatively large regularization parameter at the outset, which monotonically decreases according to the number of iterations and according to the observed reduction of the cost function from iteration to iteration.

5.3.1 Measurement and Model Vectors

In the cost function equation (5.3), the measurement vector $\mathbf{d}^{obs}$ is constructed from the real and imaginary parts of the normalized spectra, $\mathrm{Re}(S)$ and $\mathrm{Im}(S)$, in the following organized fashion:

$$\mathbf{d}^{obs} = [\,\mathrm{Re}\left(S_1\right), \mathrm{Im}\left(S_1\right), \ldots, \mathrm{Re}\left(S_j\right), \mathrm{Im}\left(S_j\right), \ldots, \mathrm{Re}\left(S_M\right), \mathrm{Im}\left(S_M\right)]^T, \qquad (5.4)$$

where $j = 1, 2, \ldots, M$.

In equation (5.4), M is the number of actual frequency-domain measurements and the superscript T indicates transpose. The amplitude of the spectra can also be used as the measurement vector at the expense of losing phase information. The ordering procedure that assigns an index, j, to a given measurement is a function of frequency for the spectrum of each trace and receiver locations. Real and imaginary parts of one measurement are arranged next to each other. If the tool has NREC receivers, the normalized wavefield has NREC-1 traces because one trace is used to eliminate the source effect. If the number of frequencies used for each trace is NFREQ, and given that both real and imaginary parts of the spectra are used, the actual number of data points used for the inversion is 2M = 2*NFREQ*(NREC-1).

Similarly, the model vector can be assembled as

$$\mathrm{m} = [V_{\mathrm{p1}}, V_{\mathrm{p2}}, \ldots, V_{p1}, V_{\mathrm{s,2}}, \ \ldots, V_{\mathrm{s,N}}, \rho_1, \ldots, \rho_N\,]^T \qquad (5.5)$$

for the simultaneous inversion of P- and S-wave velocities and density for each radial layer, where V_p, V_S, and ρ denote P-wave velocity, S-wave velocity, and density in the radial layers numbered from 1 to N, respectively. By denoting the model parameters as $\mathbf{m}_i$, where $i = 1, 2, \ldots, 3N$, equation (5.5) can be written as

$$\mathbf{m} = [\mathbf{m}_1, \mathbf{m}_2, \ldots, \mathbf{m}_{3N}]^T. \qquad (5.6)$$

A model vector constructed with only the model parameter V_p is used for the independent inversion of P-wave velocity to perform a comparison against the tomographic inversion algorithm developed by Hornby (1993).

5.3.2 Gauss-Newton Fixed-point Iteration Search

A Gauss-Newton fixed-point iteration search is used (Gill et al., 1981) to determine a stationary point, $\mathbf{m}$, where the cost function attains a minimum. This method considers only first-order variations of the cost function in the neighborhood of a local iteration point. The corresponding iterated formula can be written as

$$\mathbf{m}^{k+1} = \left[\mathbf{J}^T(\mathbf{m}^k) \cdot \mathbf{W}_d^T \cdot \mathbf{W}_d \cdot \mathbf{J}(\mathbf{m}^k) + \lambda \mathbf{W}_m^T \cdot \mathbf{W}_m \right]^{-1}$$

$$\cdot \left\{ \mathbf{J}^T(\mathbf{m}^k) \cdot \mathbf{W}_d^T \cdot \mathbf{W}_d \cdot \left[\mathbf{d}(\mathbf{m}^k) - \mathbf{d}^{obs} + \mathbf{J}(\mathbf{m}^k) \cdot \mathbf{m}^k \right] + \lambda \mathbf{W}_m^T \cdot \mathbf{W}_m \cdot \mathbf{m}_R \right\} \qquad (5.7)$$

subject to

$$l_i \le m_i^{k+1} \le u_i, \text{ where } i = 1, 2, \ldots, N. \qquad (5.8)$$

In the above two expressions, the superscript k is used as an iteration count, and $J(\mathbf{m})$ is the Jacobian matrix of $C(\mathbf{m})$. Upper and lower bounds enforced on $\mathbf{m}^{k+1}$ are intended to have the iterated solution yield only physically consistent results. The fixed-point iteration search for a minimum of $C(\mathbf{m})$ is concluded when the measured data have been fit within the prescribed tolerance, χ^2.

Relative data misfits computed with the formula

$$\frac{\left\| \mathbf{W}_d \cdot \left[\mathbf{d}(\mathbf{m}^k) - \mathbf{d}^{obs} \right] \right\|^2}{\left\| \mathbf{W}_d \cdot \mathbf{d}^{obs} \right\|^2} \qquad (5.9)$$

are used in this chapter to enforce the convergence criterion.

5.4 NUMERICAL EXAMPLES

In the inversions, it is assumed that both borehole radius and fluid properties are known and that the formation elastic parameters are the objective of the inversion. This is a realistic assumption because drilling mud density is routinely assessed in drilling operations and mud velocity can be rather accurately estimated using Wood’s equation (1941). On the other hand, the borehole radius is measured by caliper logs. The sensitivity of the inversion to small variations (5%) of borehole radius and fluid properties, normalizing traces, and noises in measurements are discussed in the study. In all the following numerical examples except those mentioned specifically, the borehole radius, mud density, and acoustic velocity of mud are assumed to be 10 cm, 1000kg/m3, and 1500m/s, respectively.

5.4.1 Hornby's Tomographic Example

There are several difficulties associated with the ray-tracing inversion method. First, the ray tracing algorithm requires accurate picking of first arrival times of array waveforms and often this is very difficult to achieve. Second, the shear arrival times are even harder to pick because often the shear wave packages are interfered by the P-wave packages in the full waveforms. The proposed full waveform inversion technique does not face such difficulties.

The ray-tracing model example of Hornby (1993) is first used to demonstrate the applicability of the inversion technique proposed in this Chapter. This model assumes a damaged zone extending away from the borehole wall into the formation. The corresponding radial velocity profile ranges from 2118 m/s at the borehole wall to 2538 m/s at a distance of 0.46 m. Figure 5.3 is a plot of the model for one source position in the borehole. This numerical experiment assumes that there are 24 receivers and source-receiver offsets ranging from 0.91 m to 4.1 m.

First, it is shown that the normalized spectra of waveform traces are indeed source-independent. Figure 5.1 is a plot of the spectra of the waveforms recorded at receivers 2, 3, 23, and 24 computed assuming both a Ricker wavelet and a Tsang (Tsang and Rader, 1979) wavelet as sources. As shown in Figure 5.1, the spectra simulated for the two sources are quite different, especially for traces 2 and 3. Figures 5.2(a) and 5.2(b) show that the amplitude spectra of traces 2 and 3 normalized with respect to that of trace 1 and computed with the two types of sources are now identical. Similarly, Figures 5.2(c) and 5.2(d) show that the amplitude spectrum of traces 23 and 24 for the two types of sources becomes identical after normalization. It can also be shown those normalized phase spectra are source-independent. The inversion algorithm uses the real and imaginary parts of the spectrum and hence both amplitude and phase information are included in the estimation of elastic parameters.

Since the tomographic algorithm (Hornby, 1993) can only be used to invert radial profiles of P-wave velocity, the full waveform inversion is first tested to performing the same function. The starting model for the inversion is described in Figure 5.3 with a dashed line. This model consists of 10 radial layers, including one fluid layer in the borehole. The initial radial profile of formation P-wave velocity is constructed with a constant background virgin formation velocity of 2538 m/s, and the velocity of the fluid layer is given the value of 1500 m/s. No assumptions regarding radial changes in the near-wellbore velocity are made for the starting model. Figure 5.3 also shows the inverted radial profile of P-wave velocity after 65 iterations using sonic array data in the frequency band from 12 to 13 kHz. This inverted model is an accurate reconstruction of the actual model. The inversion exercise indicates that full waveform inversion yields a reconstruction similar to that obtained with tomographic methods. Figure 5.4 shows the evolution of the data misfit and cost functions with the number of iterations used to invert the model shown in Figure 5.3. The reduction of these two functions is not monotonic, but the inversion algorithm does eventually converge to the expected solution.

Figure 5.5 shows the inverted radial profile of P-wave velocity after 65 iterations using data in the frequency band from 11 to 14 kHz. The reconstruction of the model shown in Figure 5.3 is not correct. The inversion remains trapped in a local minimum and the misfit cannot be further reduced. A large Langrage parameter λ with a value of 100 is also experimented to see if a better result can be obtained. Figures 5.6(a) and (b) show that the misfit and cost functions become less oscillating than shown in Figure 5.5. However, the inverted radial profile of P-wave velocity does not improve. Therefore, further experiments with a large Langrage parameter λ are not conducted.

From this exercise, it follows that the use of data with a relatively narrow frequency band leads itself to a more stable and robust inversion result.

5.4.2 Cases of a Simple Borehole

In the previous example, it was shown that full waveform inversion is efficient in reconstructing the near-wellbore features of the radial profile of the P-wave velocity. In this section, the inversion approach is used to simultaneously invert density and P- and S-wave velocities for a homogeneous and isotropic formation surrounding a borehole. The array waveforms are first simulated assuming a Ricker wavelet in the time domain, and then they are fast-Fourier transformed into the frequency domain. Finally, the simulated frequency-domain array sonic data are normalized with respect to the spectrum of the first trace. The frequency-normalized traces are used as input data to the inversion algorithm.

5.4.2.1 Case of a Fast Rock Formation

It is well known that both P- and S-wave components are identifiable in full waveforms acquired in boreholes penetrating fast formations. In the cases of a simple borehole, the inversion method can be used as an alternative interpretation algorithm to the STC processing to estimate formation velocities and the bulk density.

Model parameters shown in Table 5.1 are chosen from those of an actual gas-bearing carbonate reservoir. The borehole fluid parameters are $V_f = 1500$ m/s and $\rho_f = 1.0\, g/cm^3$, and the borehole radius is 10 cm. A source-receiver configuration identical to that of the DSI[*] tool is used to simulate the array sonic data. In the Monopole Mode, the existing 8 source-receiver offsets vary from 2.74 m (9 ft) to 3.81 m (12.5 ft) with a receiver spacing of 0.15 m (6 inch). Here, the central frequency of the source is assumed to be 10 kHz. Data from the 2 to 20 kHz frequency band are used to perform the inversion. Figure 5.2 shows that the normalized spectra can exhibit prominent spikes and hence can be very difficult to match by the inversion. Therefore, a decision is made to use only data from the frequency band of 2-7 kHz in the inversion. Model parameters used to initialize the inversion are 20% higher than the actual model parameters. This is a reasonable assumption to make given that the density log and standard STC processing can give measurements of formation density and velocities within 5% of those of the virgin formation. The inversion algorithm monotonically converges to actual model parameters after 10 iterations. Inversion results are listed in Table 5.1; the corresponding errors are within 1% relative to the actual values.

---

[*] Mark of Schlumberger

5.4.2.2 Case of a Slow Rock Formation

Shear wave components are not present in full waveforms acquired with a monopole tool in soft rock formations. Thus, the STC method cannot be used to estimate the formation shear-wave velocity. In many situations, such as mature oil fields and offshore scientific research drilling, only monopole logs are acquired and hence it is either impossible or not economically to re-log the wells again using multipole tools. Thus, estimation of formation shear-wave velocity using full wave monopole data becomes a very attractive alternative.

Model parameters shown in Table 5.2 are taken from the full waveform inversion example described by Cheng (1989). The formation parameters are typical of marine sediments. Borehole parameters are the same as those for the fast formation case discussed earlier. The configuration of the tool is that of the DSI*. In a slow formation, the central frequency of the source output is lower than that of a fast formation. Thus data from the frequency band 2-5.5 kHz are used in the inversion. Figure 5.7 shows the evolution of the misfit and cost functions with the number of iterations. Model parameters used to initialize the inversion are 20% higher than the actual model parameters. As shown in Table 5.2, for this case the inversion monotonically converges to the actual model parameters after 20 iterations.

This example shows that the inversion algorithm can be used to reliably estimate formation density and P- and S-wave velocities from full waveforms acquired with a monopole tool in boreholes penetrating soft formations.

5.4.3 Cases of a Multilayered Formation

The simple borehole cases described earlier indicate that the inversion algorithm allows the reliable estimation of formation velocities as well as of bulk density for homogenous fast and slow formations. In this section, the inversion algorithm is further tested to estimate elastic parameters in radially multilayered formations.

5.4.3.1 Case of a Fast Rock Formation

This case makes use of realistic elastic parameters for a fast formation model (Schmitt, 1988), which consists of six radial layers, including a fluid layer in the borehole. Table 5.5 describes the actual fluid and formation parameters and the radial discretization grid used for the inversion. The tool and source configurations are the same as those of previously discussed simple borehole cases. Amplitude spectra of the simulated waveforms indicate that the main energy is located within the frequency band 9-16 kHz. Data from the frequency band 11-14 kHz are used in the inversion to speed up the convergence of the inversion algorithm.

Figure 5.9 shows radial profiles and cross-plots of actual and inverted elastic parameters after 26 iterations of the inversion algorithm. The radial profiles of the inverted elastic parameters show a good agreement with the actual parameters. Global correlation coefficients are calculated between the inverted and the actual values of elastic parameters (see Figure 5.9d). All of the inverted elastic parameters exhibit high global correlation coefficients with the original model parameters (0.932, 1, and 1 for P- and S-wave velocities and density, respectively).

5.4.3.2 Case of a Slow Rock Formation

This example is an extension of the slow formation model in the simple borehole cases described by Cheng (1989) within the context of marine sediments. Table 5.6 describes the model, which consists of six radial layers, including one fluid layer in the borehole. The tool and source configurations are the same as those of previously discussed for simple borehole cases. Given that the low frequency contents of the full waveforms are more important in soft formations than in fast formations, data from the frequency band 2-5 kHz are used in the inversion. Inversion results from this example not only estimate the virgin formation elastic parameter but also give a description of near-wellbore damage.

Inversions performed with no assumption of an increasing value of the elastic parameters away from the borehole wall converge to local minima without exception. Figure 5.10 shows the profiles and the cross-plots of actual and inverted elastic parameters after 20 iterations for a slow formation under the assumption of monotonically increasing values of the elastic parameters. The inversion also stops at a local minimum as can be observed from the evolution of the data misfit and cost functions shown in Figures 5.10 (a) and 5.10(b), respectively. Global correlation coefficients for the inverted and the actual velocities exhibit good correlation (0.83 and 0.83 for P- and S-wave velocities, respectively). However, for bulk density the correlation coefficient is -0.45. This indicates the relatively low sensitivity of data in the frequency band (2-5 kHz) to radial variations of density. Overall, the inversion algorithm provides a means of estimating radial profiles of elastic parameters in soft formation. This is a valuable tool for detailed analysis of acoustic logging data in offshore wells.

5.5 SENSITIVITY OF INVERSION RESULTS TO BOREHOLE PROPERTIES

Borehole parameters input to the inversion, namely, borehole radius, borehole fluid density, and acoustic velocity, are often measured within a certain degree of accuracy in field operations. In this section, a sensitivity analysis of the above parameters is performed by way of inversion. Tables 5.3 and 5.4 summarize the results for the cases of fast and slow formations considered in the sensitivity analysis, respectively. Simple borehole models of fast and slow formations are used in this sensitivity study. The assumed borehole properties are also the same as those used in the simple borehole cases, namely, the actual acoustic velocity of drilling mud is 1500 m/s, mud density is $1.0\, g/cm^3$, and the borehole radius is equal to 10 cm.

5.5.1 Sensitivity of Inversion Results to Borehole Radius

For a fast formation, Table 5.3 shows that a 5% overestimation of borehole radius results in a 10% increase in both formation density and P-wave velocity and in a 4% decrease in S-wave velocity. A 5% underestimation of the borehole radius has a negligible effect on the inverted velocities, though the inverted density exhibits an increase of 3.3%.

For a slow formation, Table 5.4 shows that an overestimation (5%) of borehole radius decreases the inverted P- and S-wave velocities of the slow formation by approximately 6% and 24%, respectively. On the other hand, an underestimation by the same amount has a negligible effect on the inverted velocities. The inverted formation density values increase over 14% when the borehole radius is either over- or under-estimated by 5%.

5.5.2 Sensitivity of Inversion Results to Borehole Fluid Velocity

Incorrect estimations of velocity of borehole fluid cause the inverted density and P- and S-wave velocities to change over 10% for the fast formation case. For the case of a slow formation, a 5% overestimation or underestimation of borehole fluid velocities do not significantly affect the inverted velocities; however, they do cause the inverted density to increase by 14% and to decrease by 30%, respectively.

5.5.3 Sensitivity of Inversion Results to Borehole Fluid Density

Finally, an erroneous input (5% deviation from the true value) of borehole fluid density does not affect the inverted P- and S-wave velocities, but it does change the inverted formation density by 5% for both fast and slow formations.

5.6 SENSITIVITY OF INVERSION RESULTS TO MODEL FLATNESS

The iteration formula for estimating a model solution [equation (5.7)] contains a smoothness matrix $\mathbf{W_m}$. In previous examples, this matrix is chosen to be a unity diagonal matrix. Inversion results exhibit good agreement with actual models. To enforce smoothness upon the inverted model (Constable, 1987), matrix, can also be constructed as

$$\mathbf{W_m} = \begin{bmatrix} 0 & & & & & \\ -\Delta r & \Delta r & & & & 0 \\ & -\Delta r & \Delta r & & & \\ & & -\Delta r & \Delta r & & \\ & & & & \cdots & \\ & & 0 & & -\Delta r & \Delta r \end{bmatrix}, \tag{5.10}$$

where Δr is the radial length of each cell in the formation. It has been reported that smooth models can be obtained by this form of $\mathbf{W_m}$ in the Gauss-Newton inversions

(Constable, 1987). The same approach is adopted here to simultaneously invert radial profiles of density and P- and S-wave velocities in the case of multilayered fast formation.

As in the previous example for the case of the multilayered fast formation, data from the frequency band 11-14 kHz are used in this inversion exercise. Figure 5.11 shows the radial profiles of actual and inverted elastic parameters after 26 iterations. A good agreement is obtained between the radial profiles of the inverted and actual elastic parameters. The global correlation coefficients between the inverted and the actual values of elastic parameters are 0.679, 0.967, and 0.978 for P- and S-wave velocities and density, respectively. Comparison of inversion results with those obtained with the use of a unity diagonal matrix for $\mathbf{W_m}$ shows that the enforcement of a "flatness" model does not improve the behavior of the inverted radial profiles. This observation is reasonable given that excitation of waves propagating in boreholes is a highly nonlinear function of elastic formation parameters. As a consequence of this example, usage of a smoothness model is not considered for further inversion experiments.

5.7 SENSITIVITY OF INVERSION RESULTS TO NORMALIZING TRACES

All of the previous inversion examples were carried out using the spectrum of the first trace to normalize the spectra of the remaining traces. This section considers the problem of how a different normalizing trace may affect the inversion results. The eighth trace is selected as an alternative to trace one for spectrum normalization.

The case of the multilayered fast formation is used as example using array sonic data sampled in the frequency band from 11 to 14 kHz. Figure 5.11 shows radial profiles of actual and inverted elastic parameters after 26 iterations of the inversion algorithm. The global correlation coefficients between the inverted and the actual values of elastic parameters reach the highest possible value of 1 for P- and S-wave velocities and bulk density. This exercise indicates that the inversion algorithm is somewhat sensitive to the selection of the normalizing trace. However, as shown in Figure 5.9, using trace one as the normalizing trace also yields excellent results. Therefore, selection of normalizing traces does not seem to be a critical issue for the performance of the inversion algorithm.

5.8 SENSITIVITY OF INVERSION RESULTS TO NOISE IN THE MEASUREMENTS

This section uses the same example of a multilayered fast formation to assess the influence of noise in the measurements on the inverted model parameters. The array waveform data in the time domain are contaminated with 2% and 5% zero-mean Gaussian random additive noise. Figure 5.9(a) shows the noise-free array waveforms, whereas Figure 5.13(a) shows the array waveforms contaminated with 5% zero-mean random Gaussian noise. Subsequently, the normalized spectra are obtained by transforming the contaminated data into the frequency domain and by applying the normalization procedure discussed earlier in this Chapter. Data from the same frequency band considered in previous exercises, 11-14 kHz, are used in this inversion. Figure 5.13(c) indicates that the inversion converges in 10 iterations. Radial profiles of actual and inverted elastic parameters after 26 iterations are described in Figure 5.13(d). A good agreement is obtained between the radial profiles of the inverted and actual elastic parameters. Figure 5.13(b) shows that the data residuals entailed by the inversion are negligible in the time domain. Correlation coefficients between the inverted and the actual values of elastic parameters remain very high (0.822, 0.962, and 0.931 for P- and S-wave velocities and density, respectively).

When the noise level decreases to 2% in the time domain data, the inversion algorithm converges faster than for the case of 5% noise and the resolution of the inverted radial profiles increases. For the case of 2% additive noise, correlation coefficients between the inverted and the actual values of elastic parameters are 0.941, 0.995, and 0.991 for P- and S-wave velocities and density, respectively. This exercise shows that the inversion algorithm remains stable and robust when the noise level reaches 5% of the energy of the acoustic measurements.

5.9 FIELD STUDY

This example assesses the feasibility and performance of the inversion algorithm when applied to field data. Full waveform acoustic data were acquired with the DSI* tool in the depth from 13000 ft to 13050 ft within a well penetrating a tight-gas sandstone reservoir. Core data and log measurements (shown on the second panel from the right hand of Figure 5.14) show that the porosity of the fine-grained sandstone formation is below 9%. Formation gas saturation ranges from 80% to 95%. Figure 5.14 shows a section of logs acquired in this well. The caliper log in panel 2 indicates that the wellbore is in excellent condition and the borehole diameter is 6.4 in. On the other hand, the density log in panel 4 and the slowness logs in panel 5 show that the rock formation is highly homogenous in the axial direction of the borehole. These observations indicate that the assumptions of the forward model algorithm for simulation of wave propagation are satisfied for the most part and that the inversion algorithm can be used to estimate formation elastic parameters from measured data.

Figure 5.15(a) is a display of the array waveform data acquired at the depth of 13030 ft. The bottom four traces show very similar characteristics in the number of wave modes and in the amplitudes of each wave mode. The top four traces, however, show a totally different character. Figure 5.15(b) displays the amplitude spectra of the array waveform data. The main energy of the waveforms is contained in the frequency band from 9 to 14 kHz. Input data to the inversion algorithm are chosen to be the normalized frequency data in the band of 11-14 kHz given that previous examples show that data from a narrower frequency data band facilitate the convergence of the algorithm. The STC processing method yields formation P- and S-wave slowness of 66.33 and 108.01

us/ft, which are used as the initial parameters for the inversion, respectively. Likewise, the density log reads a value of 2.504 gm/cc for bulk formation density. The mud density at this depth in the borehole is known to be 14 ppg (1678 kg/m^3), whereas acoustic velocity of the mud is approximately 1186 m/s. Mud-filtrate invasion studies (Salazar et al., 2003) indicate that mud filtrate reaches a radial distance of approximately 1.5 ft in the flow unit of interest after 24 hrs of drilling (rock type 1A). Thus, A five-radial-layer model is used to describe the near-wellbore invasion zone. The inner radii of the radial formation layers are 0.07, 0.15, 0.30, 0.40, and 0.45 m, respectively, and the outmost layer is assumed to be unbounded in the radial direction. Within each radial zone, the formation elastic parameters are assumed to be constant.

First, normalized frequency data from traces one to four in the band from 11 to 14 kHz are used as input data for the inversion. Data misfits are reduced by 4% after 20 iterations. Figure 5.15 (c) indicates that the formation P- and S-wave velocities increase and bulk density decreases in the radial direction. It is well known that formation damage caused by drilling decreases the formation velocities and that mud-filtrate invasion in the near-wellbore region increases the bulk density. The inverted radial profiles indicate that a damaged zone exists in the near-wellbore region even though the borehole is in excellent condition. Such a result also agrees with the high-amplitude P-wave components that can be observed from traces one through four of the array sonic waveforms. A radial profile of monotonically increasing P-wave velocity focuses the elastic waves propagating away from the wellbore back toward the borehole wall and increases the P-wave amplitude (Winkler, 1997, and Chen et al., 1996). The radial profile of decreasing density can be interpreted as mud-filtrate displacing gas in the formation. This inversion exercise indicates that the algorithm can be used to estimate reliable radial profiles of formation elastic parameters in the near-wellbore region.

5.10 CONCLUSIONS

A novel full waveform inversion algorithm was developed that makes use of a normalized frequency spectrum. Normalized frequency spectrum for a source depends only on the borehole and formation models and on the position of the source, but does remain independent of the source spectrum. The validity of the algorithm was successfully assessed using both simple and radially multilayered 1-D synthetic models. An additional test of the inversion algorithm with field data acquired in a tight-gas reservoir also yields reasonable results.

This Chapter shows that full waveform inversion can be performed with spectrum-normalized sonic data for the cases of both fast and slow formations. The proposed inversion method does not require of specific knowledge of the source wavelet. Inversions using the Gauss-Newton method construct radial profiles of formation density and P- and S-wave velocities for synthetic models. For the case of a multilayered slow formation, inversions using the low frequency array data converge to a local minimum. This indicates that the low frequency content of the full waveform data is sensitive to formation elastic parameters far from the borehole wall. For the case of a multilayered fast formation, data from the frequency band 11-14 kHz are used and the inverted radial profiles of formation elastic parameters entail a very high correlation with the actual formation elastic parameters. This exercise shows that the high frequency component of the array sonic data may be preferable for estimating the radial distribution of elastic parameters in the near-wellbore region.

Inversion exercises performed on the ray-tracing example indicate that full waveform inversion yields a reconstruction of P-wave velocity profiles similar to that of tomographic methods. In addition, the proposed inversion algorithm can be used to invert radial profiles of bulk density and S-wave velocity.

Sensitivity studies indicate that correct values for borehole fluid velocity are required by the inversion method. A 5% underestimation of borehole radius and inaccurate borehole fluid density do not significantly affect the inverted formation P- and S-wave velocities even though the inverted formation density can deviate from the actual values by at least 5%.

Inversion exercises performed with noisy synthetic data indicate that small amounts of noise do not significantly bias the estimated radial profiles of elastic parameters. Finally, the choice of normalizing trace has negligible effect on the inverted radial profiles. These sensitivity studies indicate that the inversion algorithm is rather robust and stable for estimating radial profiles of formation elastic parameters.

Table 5.1: Input and inverted model parameters for the case of a fast formation and a simple borehole model. The model parameters used to initialize the inversion are 20% higher than the actual model parameters.

Layer	Model	Start	Inversion	Error (%)
ρ (g/cm^3)	2.442	2.930	2.435	0.3
V_p (m/s)	4973	5968	5004	0.6
V_s (m/s)	2908	3490	2908	0.0

Table 5.2: Input and inverted model parameters for the case of a slow formation and a simple borehole model. The model parameters used to initialize the inversion are 20% higher than the actual model parameters.

Layer	Model	Start	Inversion	Error (%)
ρ (g/cm^3)	2.100	2.520	2.100	0.0
V_p (m/s)	2500	3000	2500	0.0
V_s (m/s)	1240	1488	1240	0.0

Table 5.3: Model parameters inverted after 20 iterations for various borehole parameters (shown in first column of the table) for the case of a fast formation and simple borehole model. The actual acoustic velocity of mud $V_f = 1500$ m/s, mud density $\rho_f = 1.0\, g/cm^3$, and the borehole radius R = 10 cm.

Input	ρ (g/cm^3)	V_p (m/s)	V_s (m/s)	ρ error (%)	V_p error (%)	V_s error (%)
1.05 R	2.903	5621	2789	18.8	13.0	-4.1
0.95 R	2.522	4983	2896	3.3	0.2	-0.3
1.05 V_f	1.967	4449	2292	-19.5	-10.5	-21.2
0.95 V_f	2.929	5669	3275	19.9	14	12.6
1.05 ρ_f	2.564	4996	2905	5.0	0.5	-0.1
0.95 ρ_f	2.324	4963	2907	-4.8	-0.2	0.0

Table 5.4: Model parameters inverted after 20 iterations for various borehole parameters (shown in first column of the table) for the case of a slow formation and simple borehole model. The actual acoustic velocity of mud $V_f = 1500$ m/s, mud density $\rho_f = 1.0\, g/cm^3$, and the borehole radius R = 10 cm.

Input	ρ (g/cm^3)	V_p (m/s)	V_s (m/s)	ρ error (%)	V_p error (%)	V_s error (%)
1.05 R	2.480	2352	937	18.1	-5.9	-24.4
0.95 R	2.394	2420	1248	14.0	-3.2	0.6
1.05 V_f	2.394	2393	1192	14.0	-4.2	-3.9
0.95 V_f	1.471	2503	1202	-30.0	0.1	-3.0
1.05 ρ_f	2.205	2500	1240	5.0	0.0	0.0
0.95 ρ_f	1.995	2500	1240	-5.0	0.0	0.0

Table 5.5: Description of mud properties and of the actual profiles of density and P- and S-wave velocities for the multilayered fast formation.

Layer	Inner radius (m)	ρ (g/cm^3)	V_p (m/s)	V_s (m/s)
1	0	1.0	1500	0
2	0.10	2.36	4390	2341
3	0.18	2.31	4512	2406
4	0.26	2.26	4634	2471
5	0.34	2.21	4756	2536
6	0.42	2.16	4878	2601

Table 5.6: Description of mud properties and of actual profiles of density and P- and S-wave velocities for the multilayered slow formation.

Layer	Inner radius (m)	ρ (g/cm^3)	V_p (m/s)	V_s (m/s)
1	0	1.000	1500	0
2	0.10	2.000	2300	1000
3	0.18	2.025	2350	1060
4	0.26	2.050	2400	1120
5	0.34	2.075	2450	1180
6	0.42	2.100	2500	1240

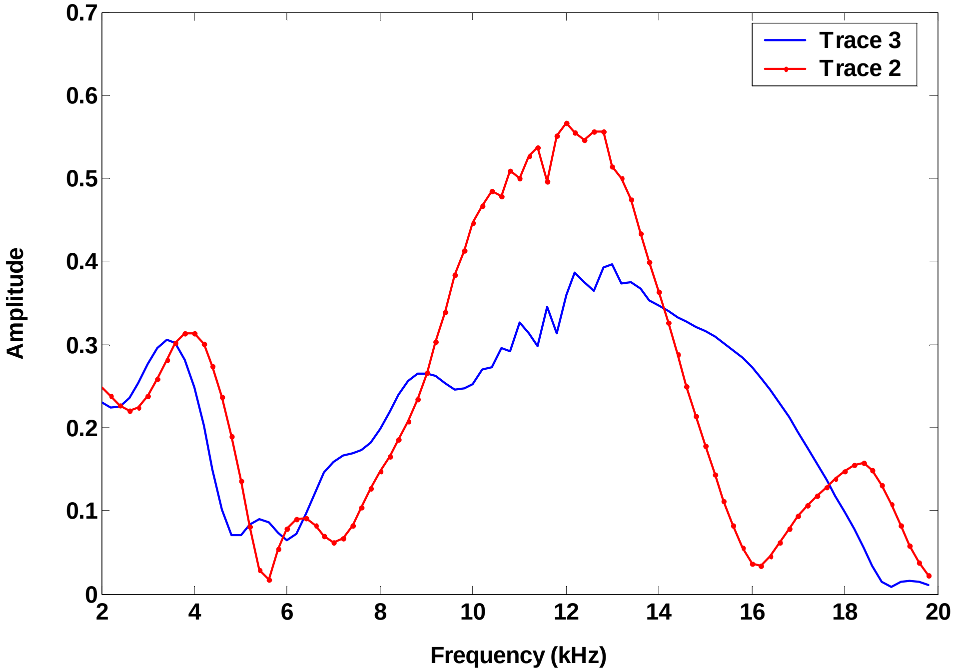
Trace 3
Trace 2
Amplitude
Frequency (kHz)
0
0.1
0.2
0.3
0.4
0.5
0.6
0.7
2
4
6
8
10
12
14
16
18
20

(a)

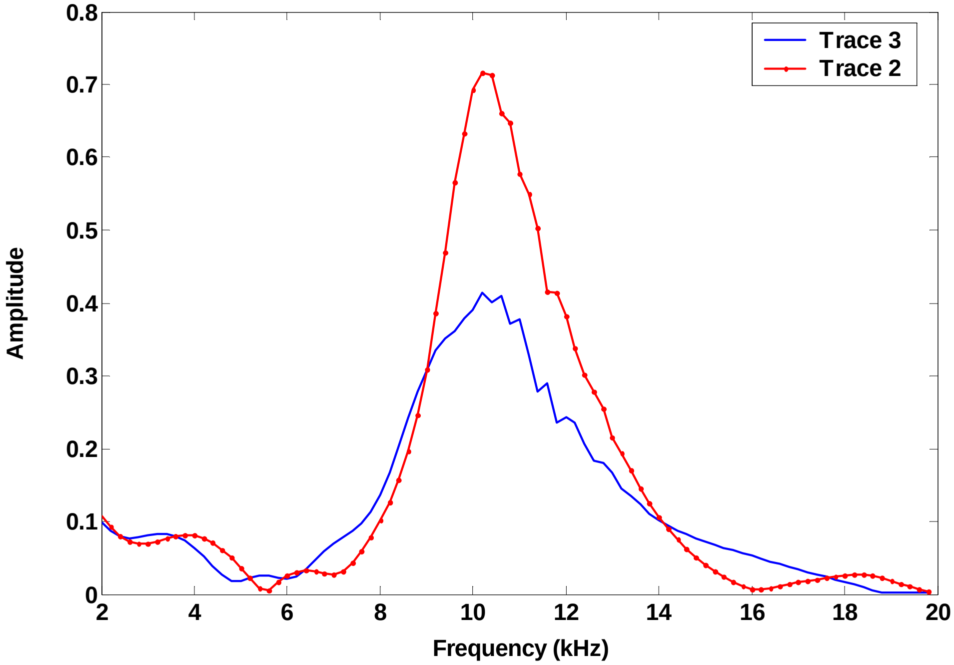
Trace 3
Trace 2
Amplitude
Frequency (kHz)
0
0.1
0.2
0.3
0.4
0.5
0.6
0.7
0.8
2
4
6
8
10
12
14
16
18
20

(b)

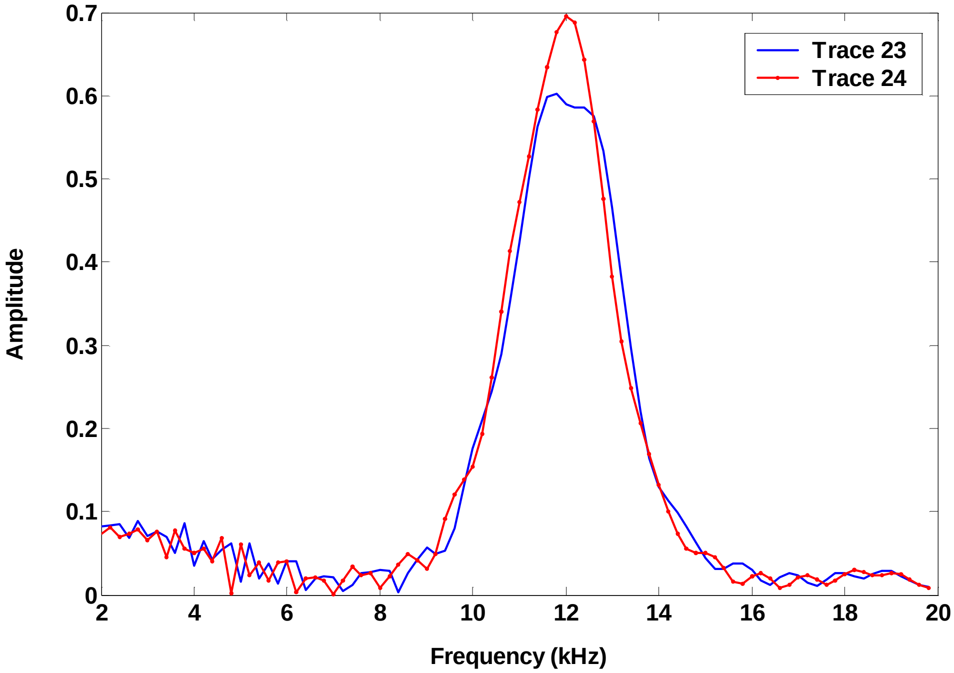

(c)

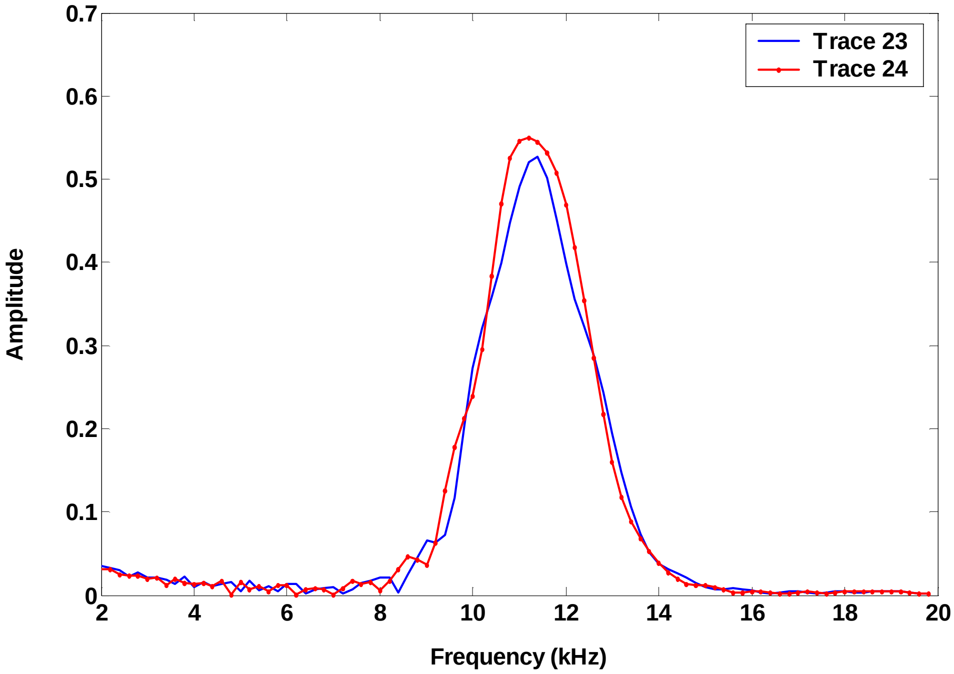

(d)

Figure 5.1: Amplitude spectra of sonic traces 2 and 3 computed using (a) a Ricker wavelet source and (b) a Tsang type source for Hornby’s model. Plots (c) and (d) are the amplitude spectra of trace 23 and 24 calculated with the corresponding wavelet sources.

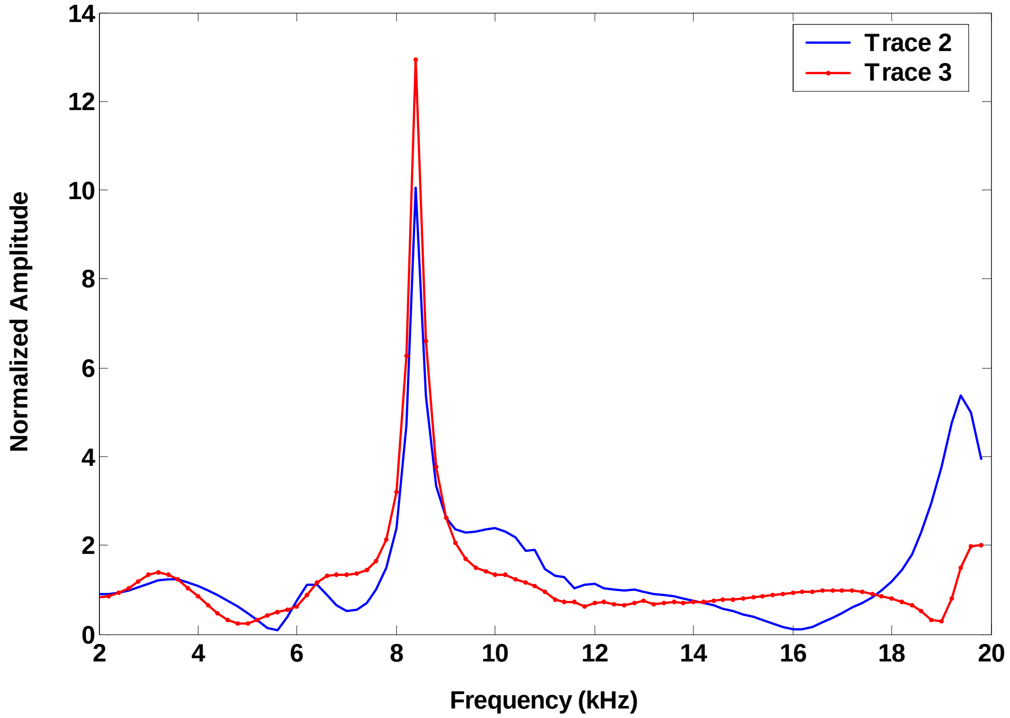
Trace 2
Trace 3
Normalized Amplitude
Frequency (kHz)
0
2
4
6
8
10
12
14
2
4
6
8
10
12
14
16
18
20

(a)

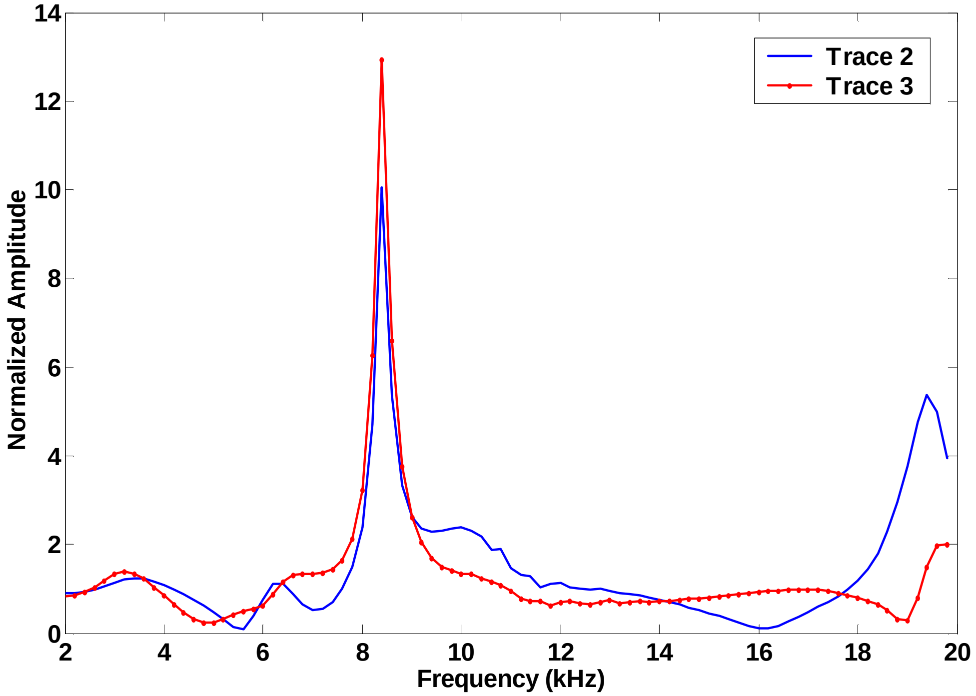
Trace 2
Trace 3
Normalized Amplitude
Frequency (kHz)
0
2
4
6
8
10
12
14
2
4
6
8
10
12
14
16
18
20

(b)

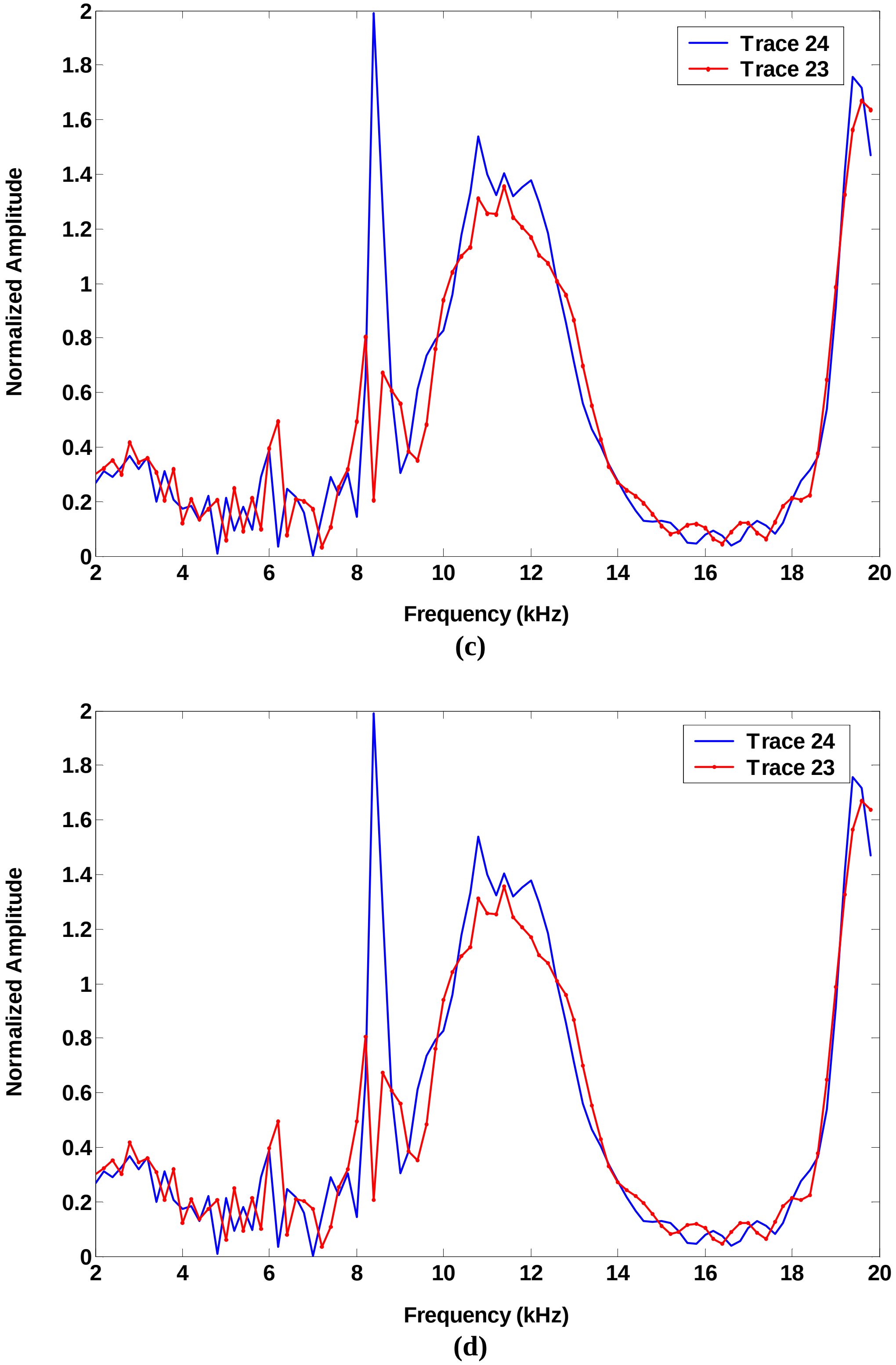

(c)

(d)

Figure 5.2: Amplitude spectra normalized with respect to trace 1 of the amplitude spectra shown in Figure 5.1.

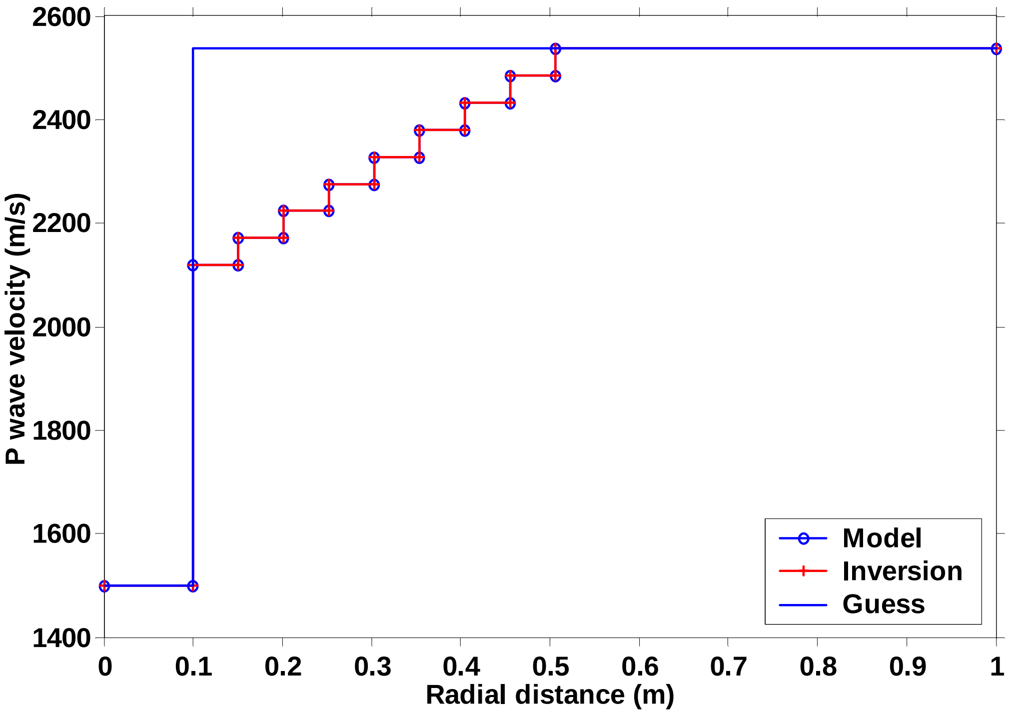

Figure 5.3: Radial model used to simulate a damaged zone extending away from the borehole wall. The velocity profile ranges from 2118 m/s at the borehole wall to 2538 m/s at a distance of 0.51 m from the borehole wall. The formation is divided into 9 radial layers with the outermost layer extending to infinity. There are 24 receivers and source receiver offsets ranging from 0.91 m (3ft) to 4.1 m (13.5 ft). The actual model is represented by a solid line with open circles; the dash line indicates the starting model used for the inversion, and the solid line with crosses identifies the inverted radial profile of P-wave velocity after 65 iterations using frequency normalized data in the band from 12 to 13 kHz. The background formation P-wave velocity is used to initialize the inversion. No assumptions are made regarding the near-borehole slowness.

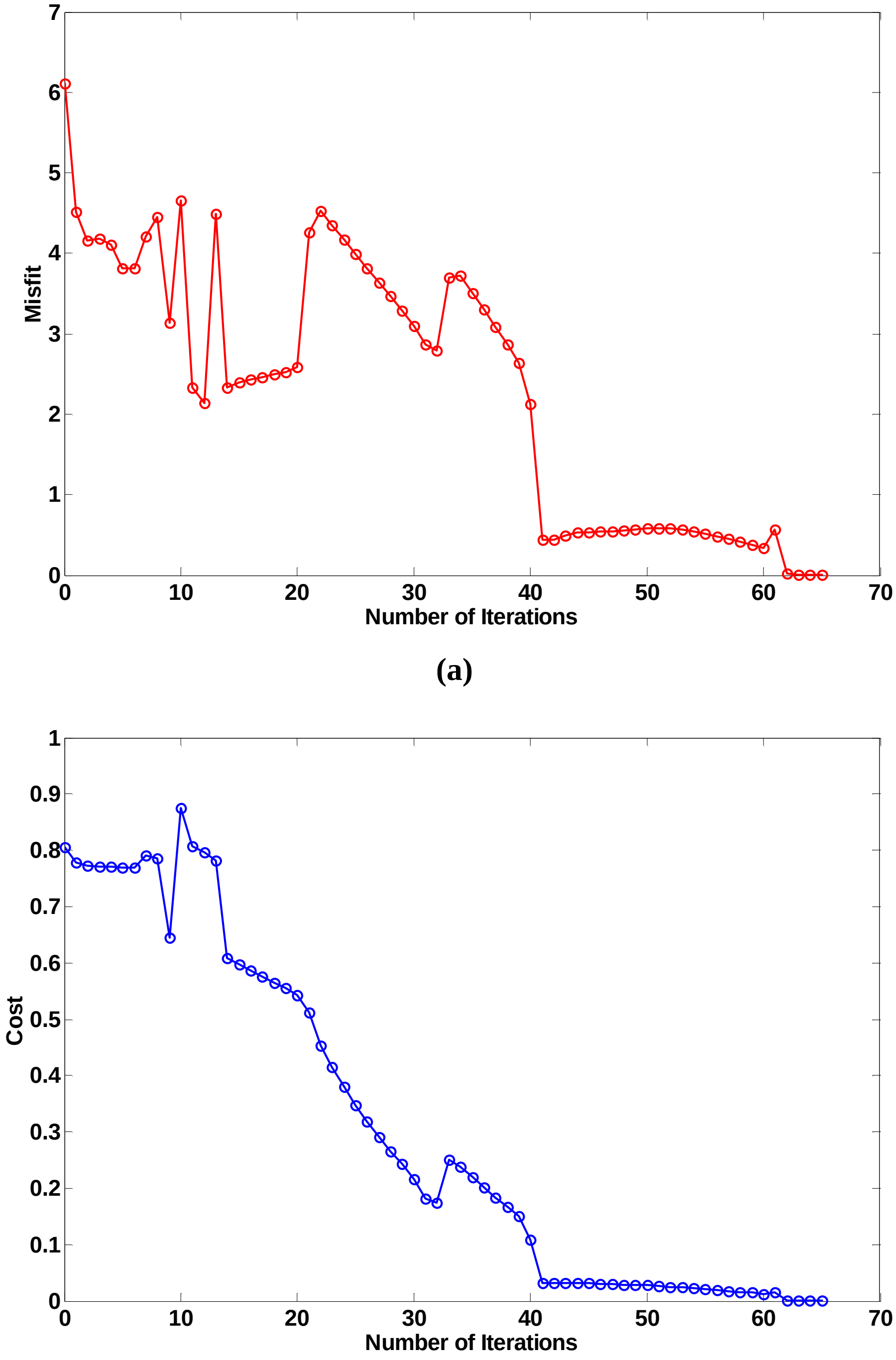

(a)

(b)

Figure 5.4: Evolution of data misfit and cost function with the number of iterations for the inversion of the radial P-wave velocity model shown Figure 5.3.

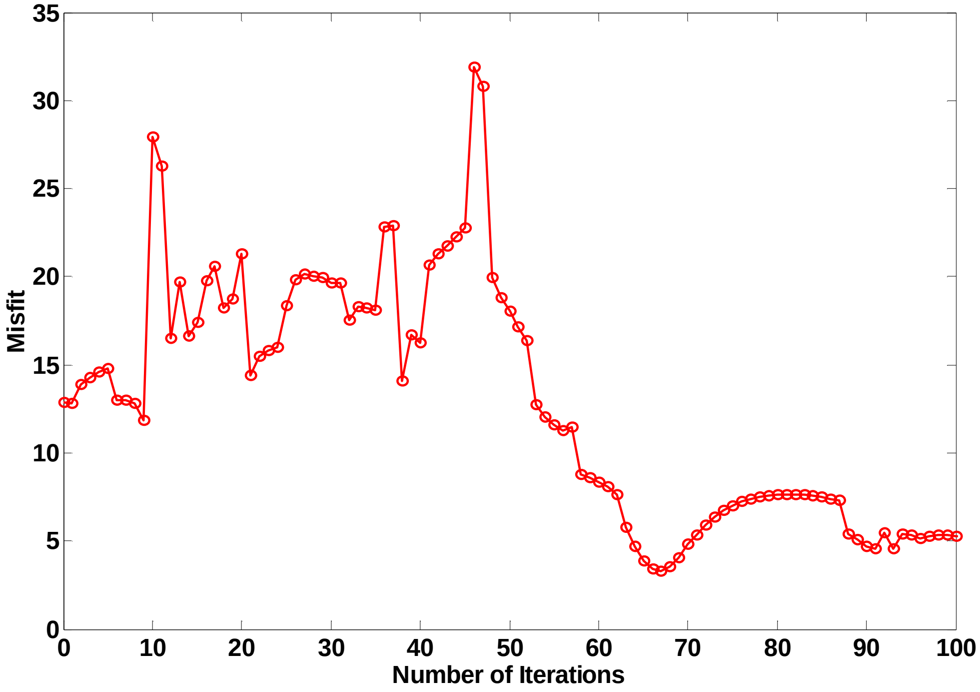
Misfit
0
5
10
15
20
25
30
35
0
10
20
30
40
50
60
70
80
90
100
Number of Iterations

(a)

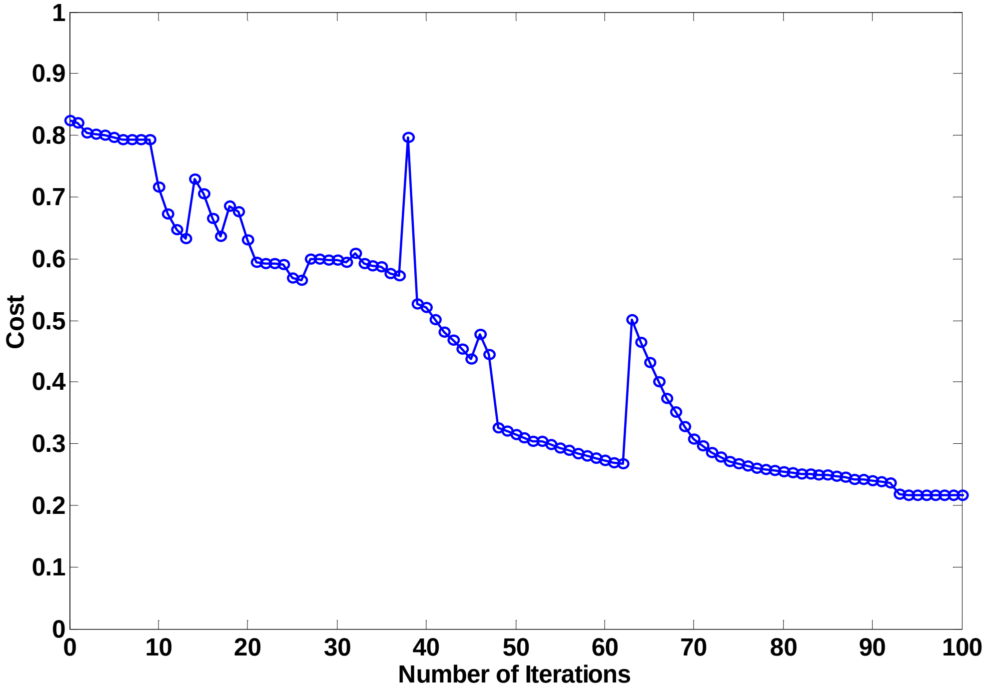
Cost
0
0.1
0.2
0.3
0.4
0.5
0.6
0.7
0.8
0.9
1
0
10
20
30
40
50
60
70
80
90
100
Number of Iterations

(b)

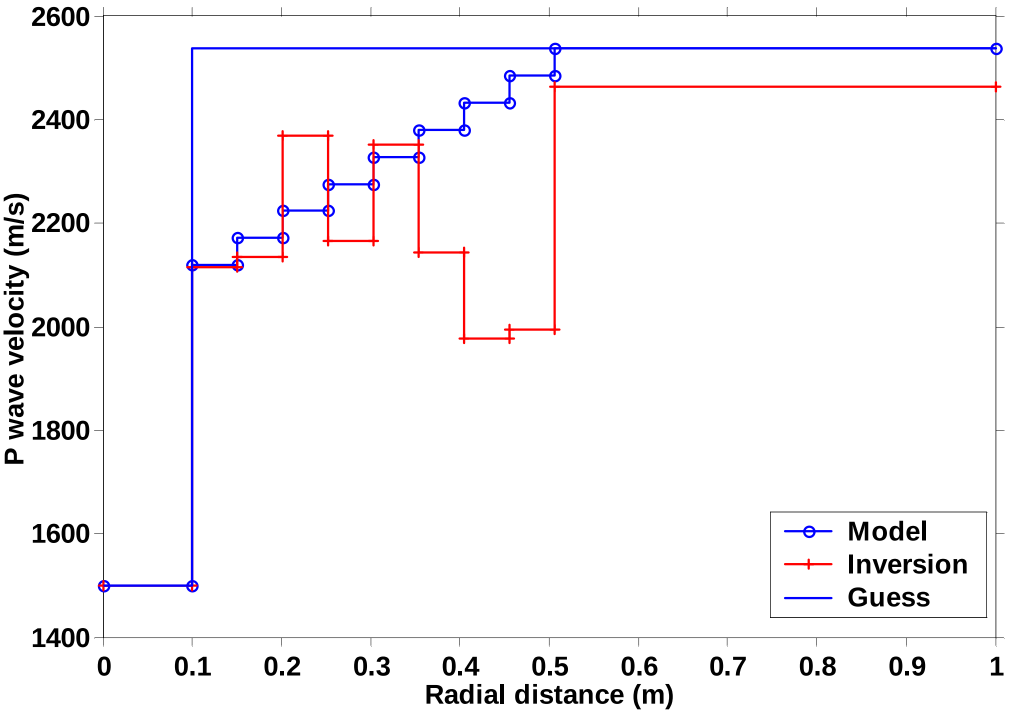

(c)

Figure 5.5: Evolution of (a) data misfit and (b) cost functions with the number of iterations for the inversion of the radial profile of P-wave velocity of Hornby's model (c) after 65 iterations using frequency normalized data in the frequency band 11-14 kHz. The Lagrange regularization parameter starts from 0.001 and is reduced by half at each iteration until it reaches the value of 10^{-9}.

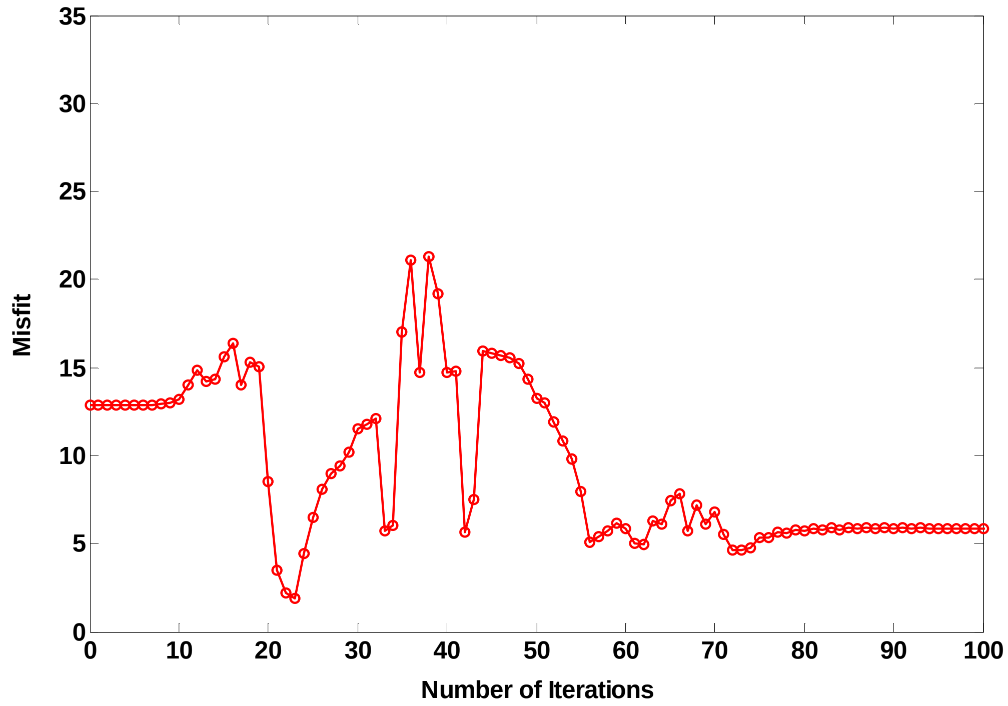
35
30
25
20
15
10
5
0
Misfit
0
10
20
30
40
50
60
70
80
90
100
Number of Iterations

(a)

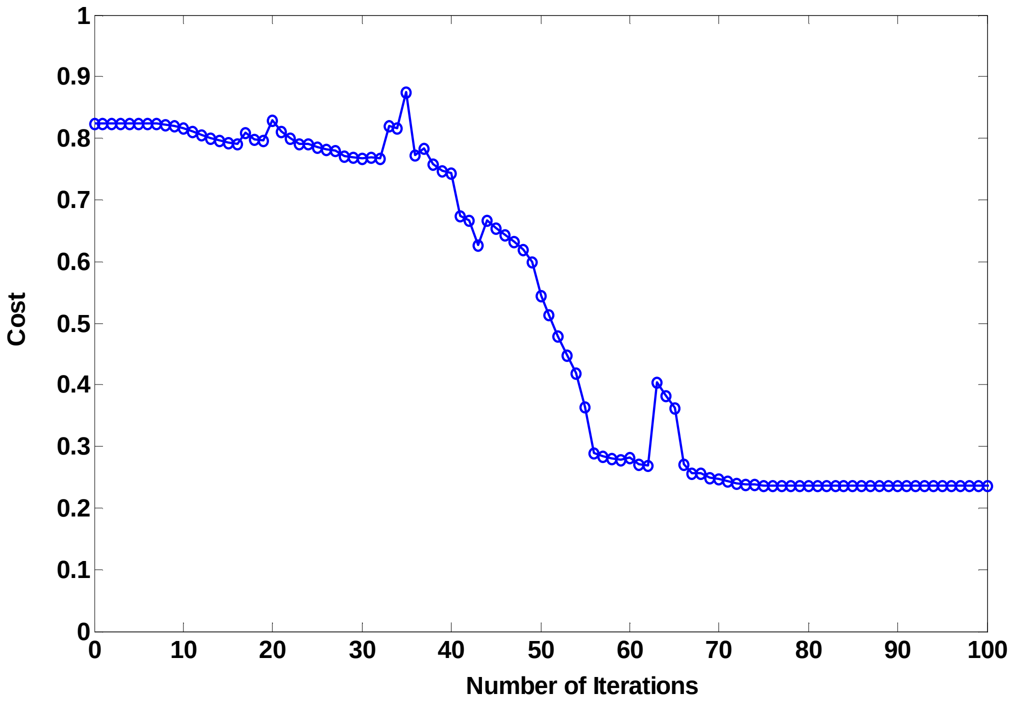
1
0.9
0.8
0.7
0.6
0.5
0.4
0.3
0.2
0.1
0
Cost
0
10
20
30
40
50
60
70
80
90
100
Number of Iterations

(b)

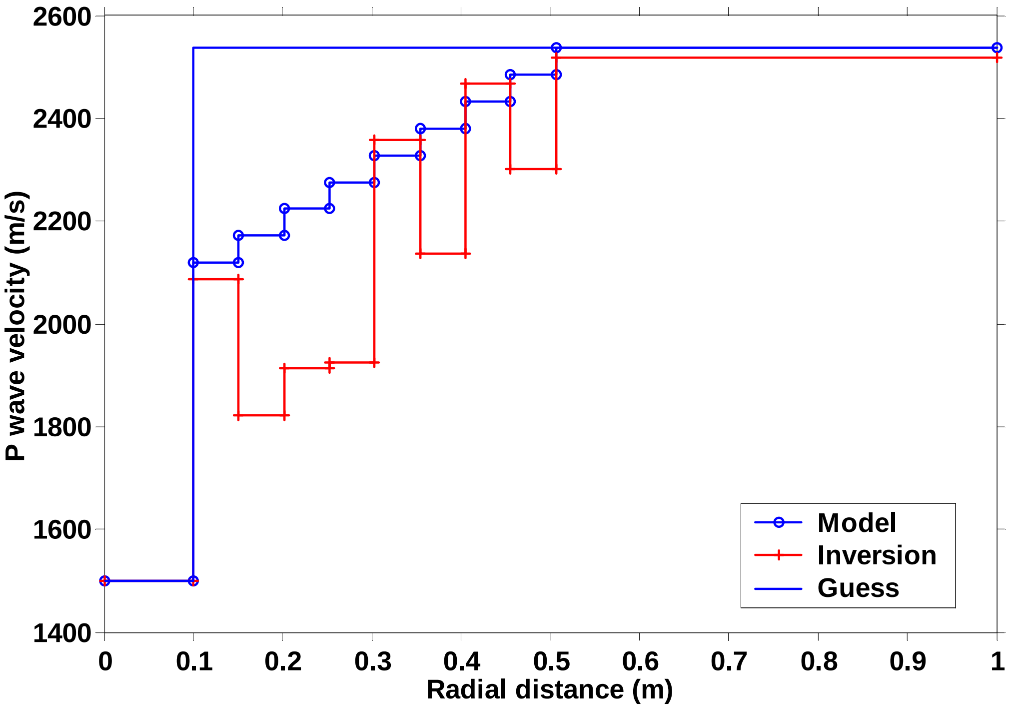

(c)

Figure 5.6: Evolution of (a) data misfit and (b) cost functions with the number of iterations for the inversion of the radial profile of P-wave velocity of Hornby's model (c) after 65 iterations using frequency normalized data in the frequency band 11-14 kHz. The Lagrange regularization parameter starts from a value of 100 and is reduced by half at each iteration until it reaches the value of 10^{-9}.

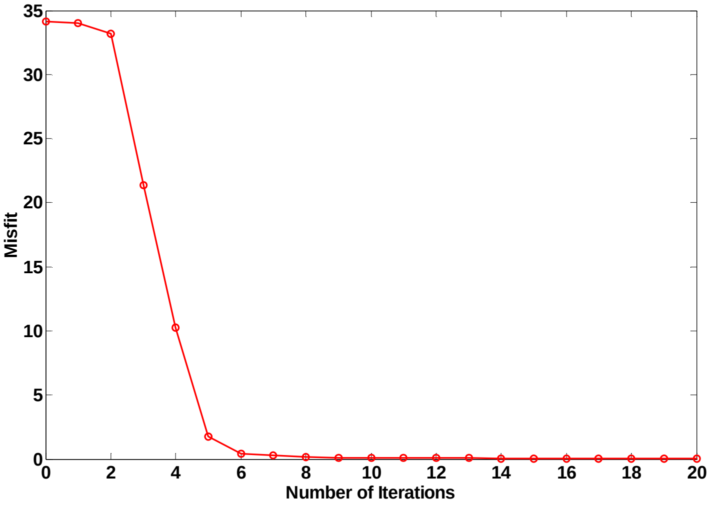

(a)

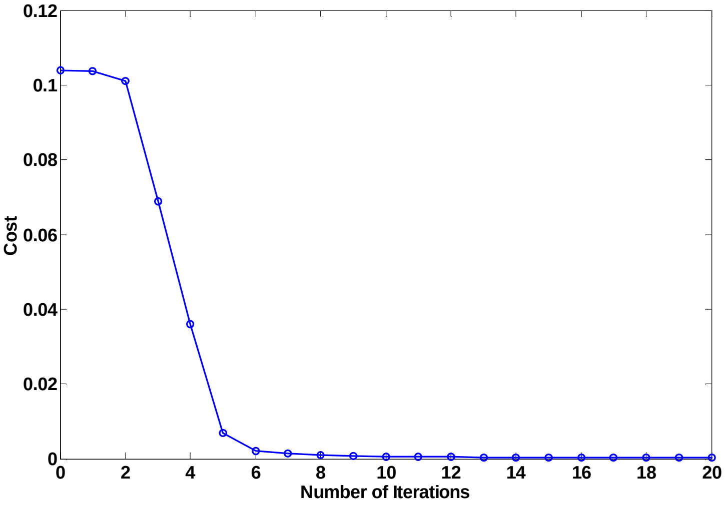

(b)

Figure 5.7: Evolution of (a) data misfit and (b) cost functions with the number of iterations for the inversion using normalized array sonic data in the 2-7 kHz frequency band. The inversion converges to the actual parameters shown in Table 5.1 for the model of a simple borehole penetrating a fast formation.

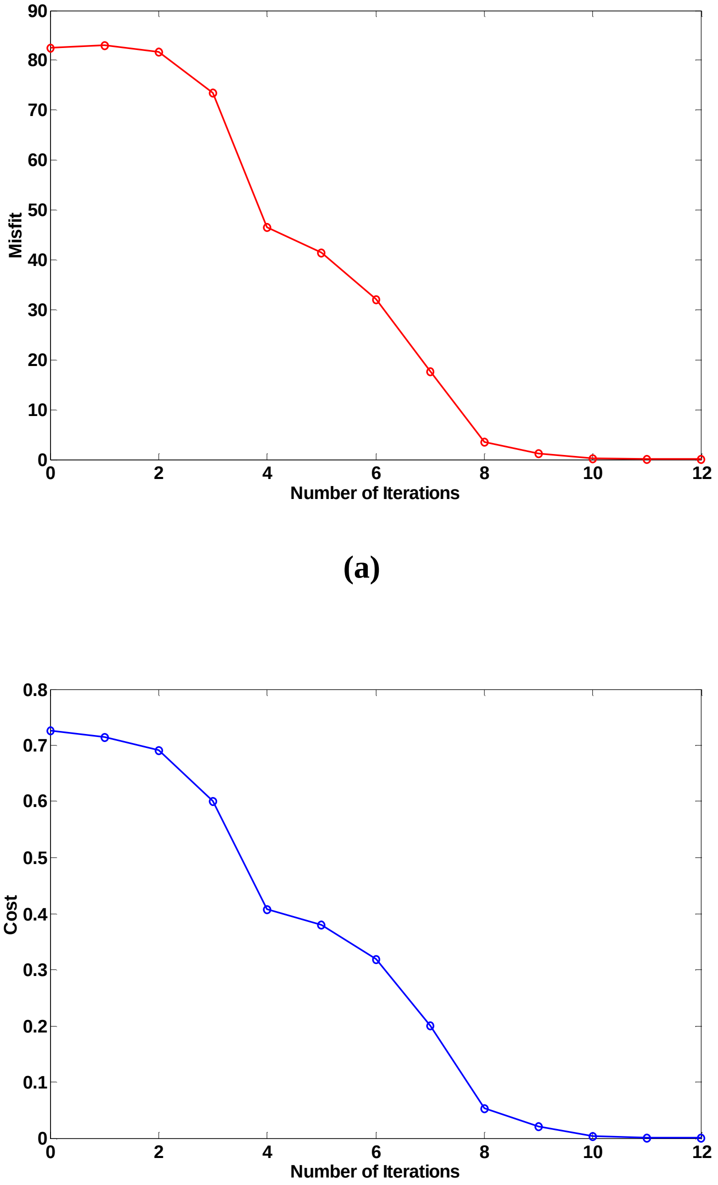

(a)

(b)

Figure 5.8: Evolution of (a) data misfit and (b) cost functions with the number of iterations for the inversion using the normalized array sonic data in the 2-5.5 kHz frequency band. The inversion converges to the actual parameters shown in Table 5.2 for the model of a simple borehole penetrating a slow formation.

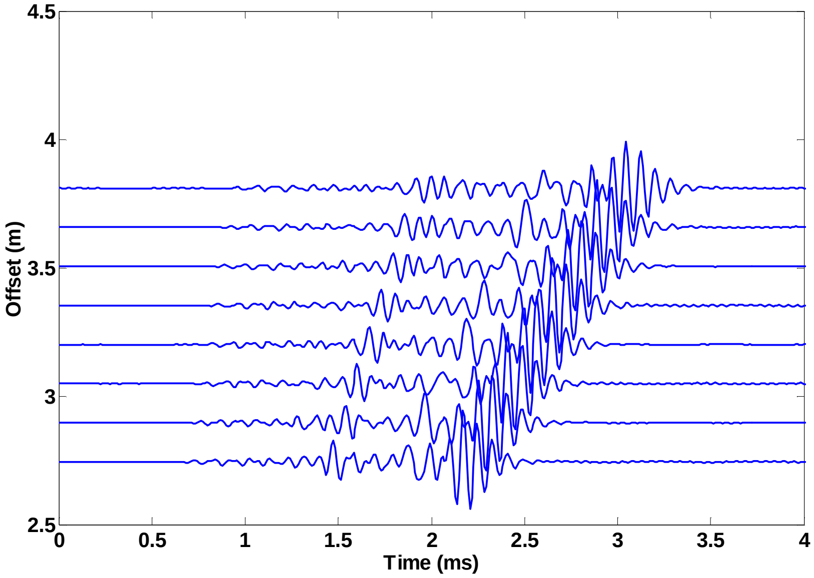
4.5
4
3.5
3
2.5
Offset (m)
0
0.5
1
1.5
2
2.5
3
3.5
4
Time (ms)

(a)

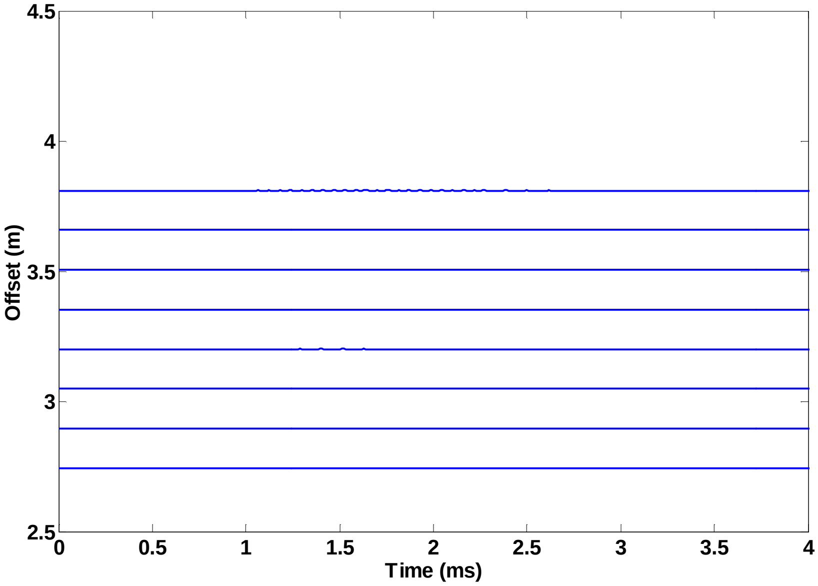
4.5
4
3.5
3
2.5
Offset (m)
0
0.5
1
1.5
2
2.5
3
3.5
4
Time (ms)

(b)

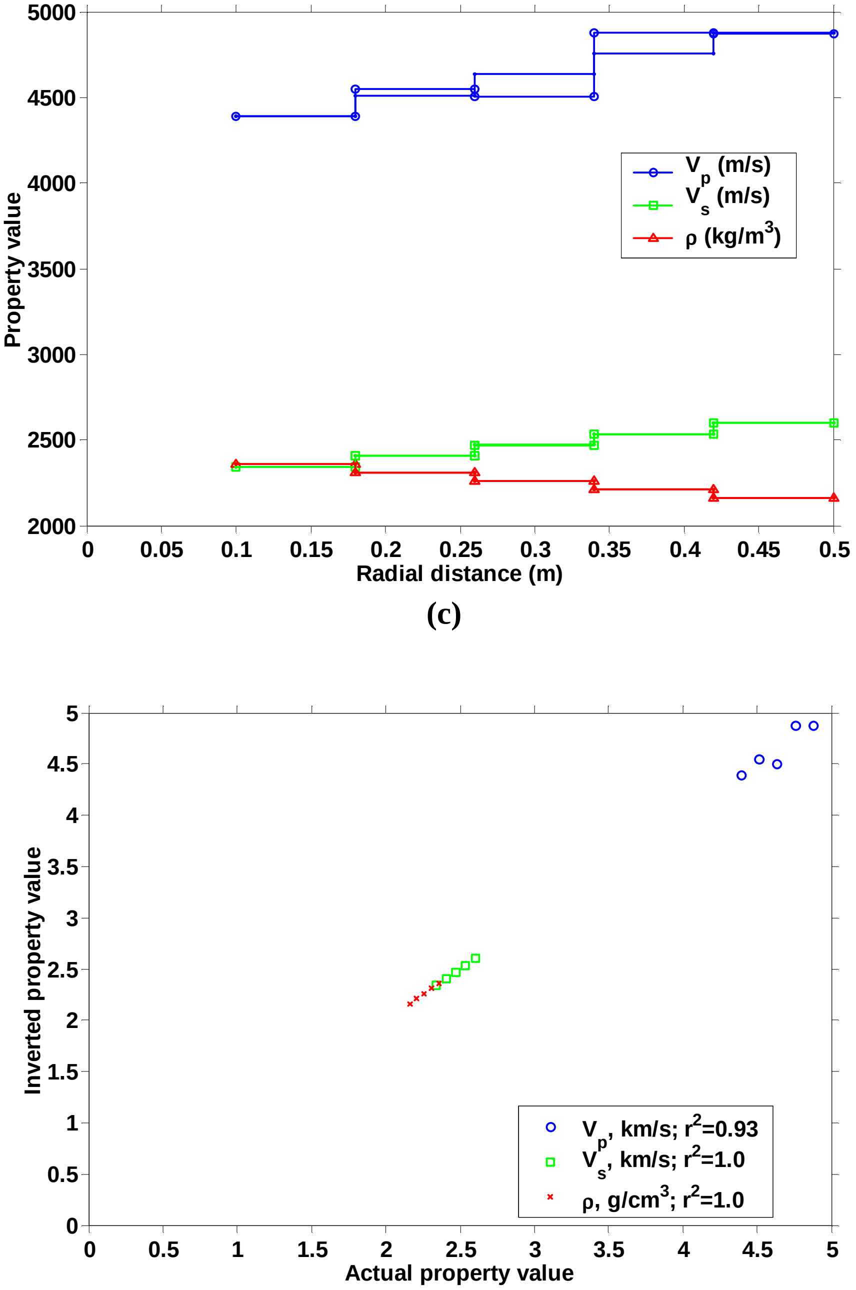

(c)

(d)

Figure 5.9: Simultaneous inversion of radial profiles of elastic parameters for a six-layer fast formation using noise-free normalized spectra of array waveform data. Panel (a) shows the array waveform in the time domain and panel (b) shows the data residuals yielded by the inversion. In panel (c), the inverted radial distributions of elastic parameters are identified with solid lines plus open circles, and in panel (b), r^2 is the correlation coefficient between the inverted and actual elastic parameters.

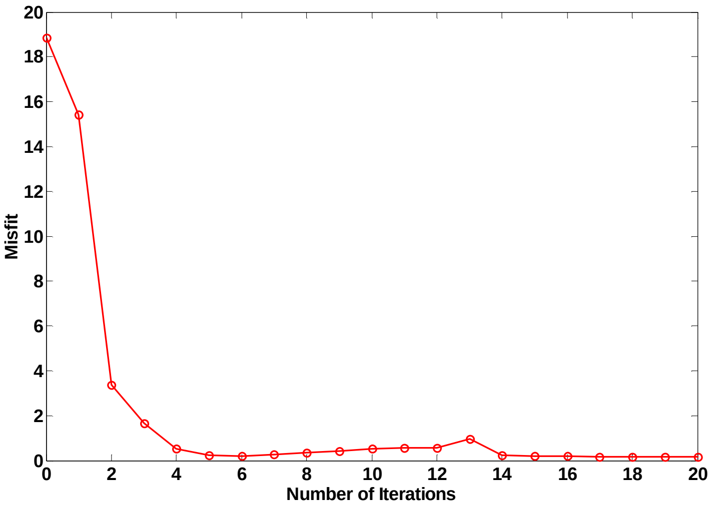
Misfit
20
18
16
14
12
10
8
6
4
2
0
0
2
4
6
8
10
12
14
16
18
20
Number of Iterations

(a)

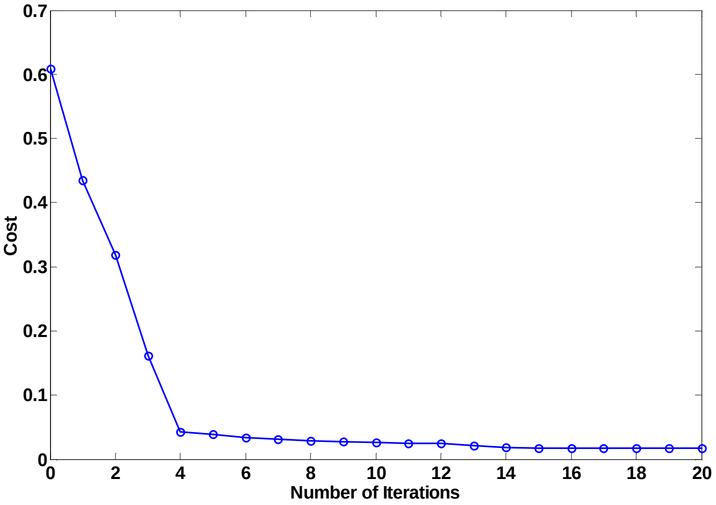
Cost
0.7
0.6
0.5
0.4
0.3
0.2
0.1
0
0
2
4
6
8
10
12
14
16
18
20
Number of Iterations

(b)

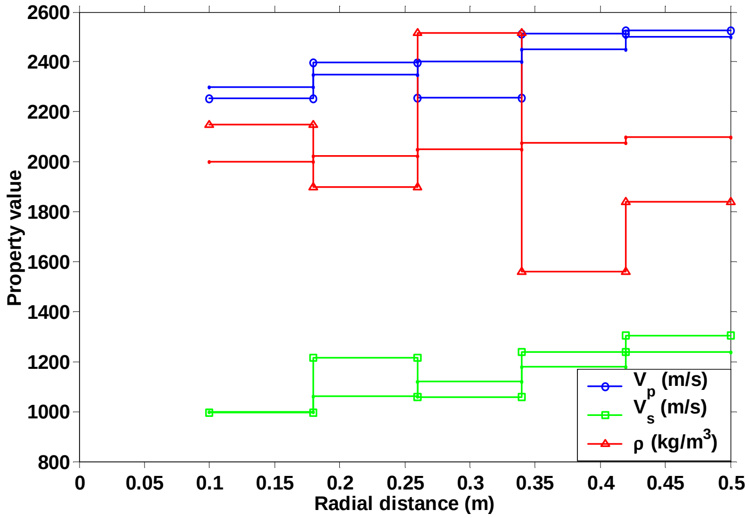

(c)

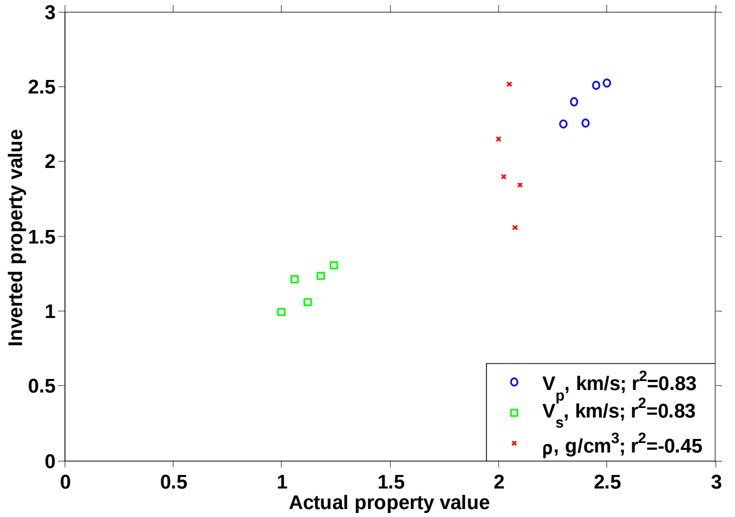

(d)

Figure 5.10: Radial profiles and cross-plots of the actual and inverted elastic parameters for a six-layer slow formation. The evolution of the data misfit and cost functions with iteration number is shown in plot (a) and (b), respectively. In plot (c), the inverted radial distributions of elastic parameters are identified with open circles, and in plot (d), r^2 is the correlation coefficient.

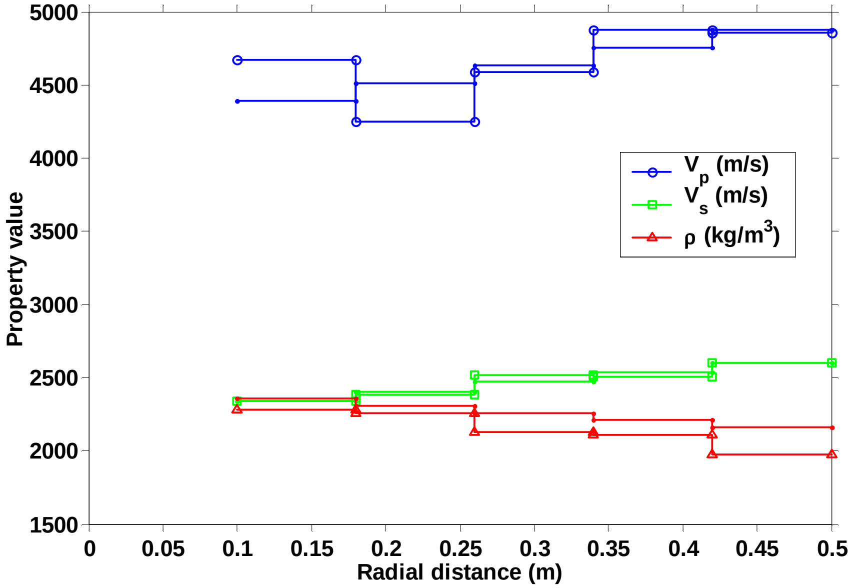

Figure 5.11: Radial profiles of the actual and inverted elastic parameters for a six-layer fast formation obtained by enforcing model flatness. Actual parameters are identified with solid lines. Correlation coefficients are 0.679, 0.967, and 0.978 for P- and S-wave velocities and density, respectively.

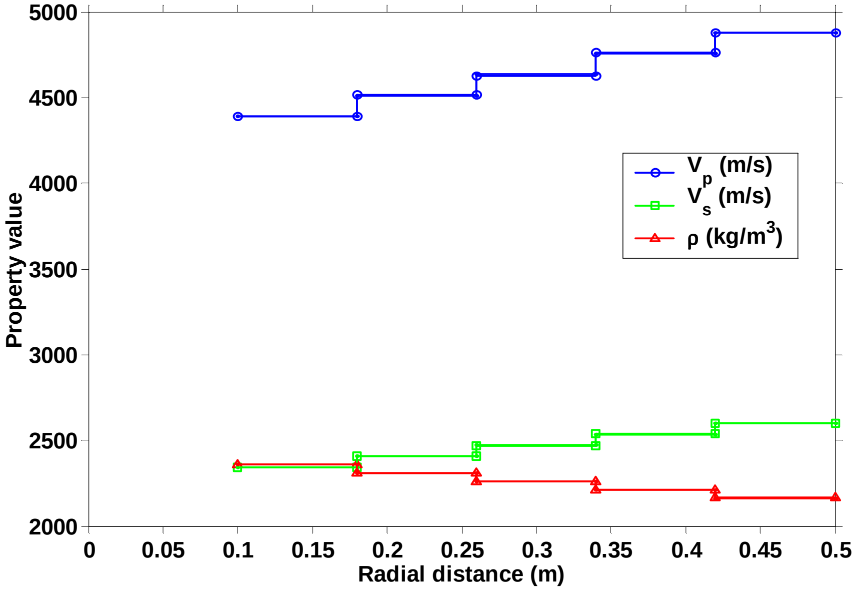

Figure 5.12: Radial profiles of the actual and inverted elastic parameters for a six-layer fast formation. Actual parameters are identified with solid lines. The frequency array sonic data are normalized by trace 8 instead of trace 1.

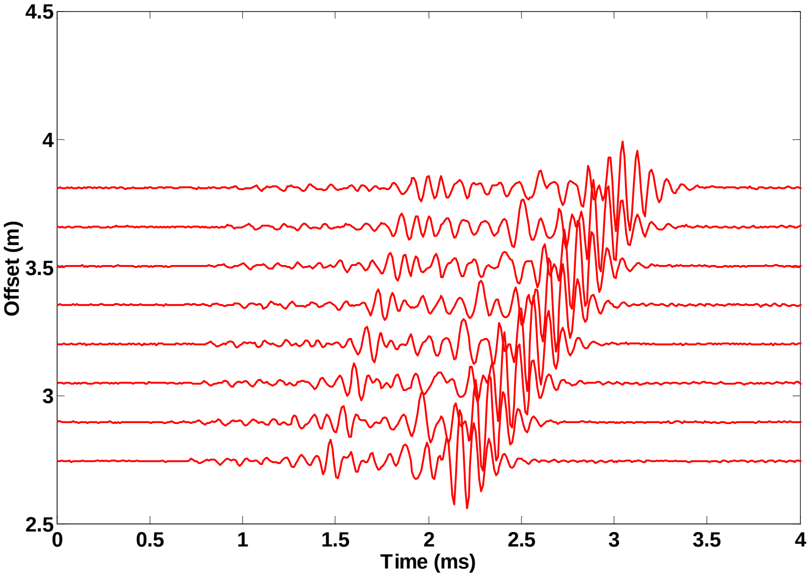

(a)

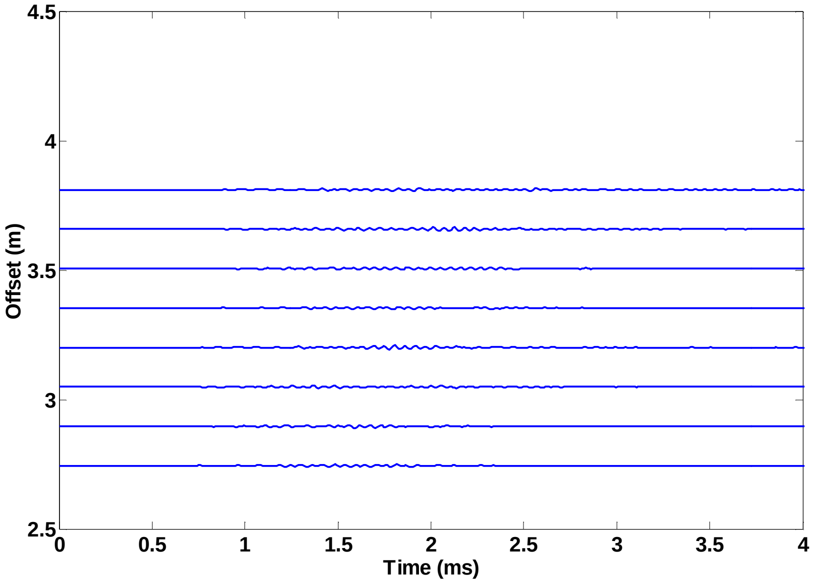
Offset (m)
4.5
4
3.5
3
2.5
0
0.5
1
1.5
2
2.5
3
3.5
4
Time (ms)

(b)

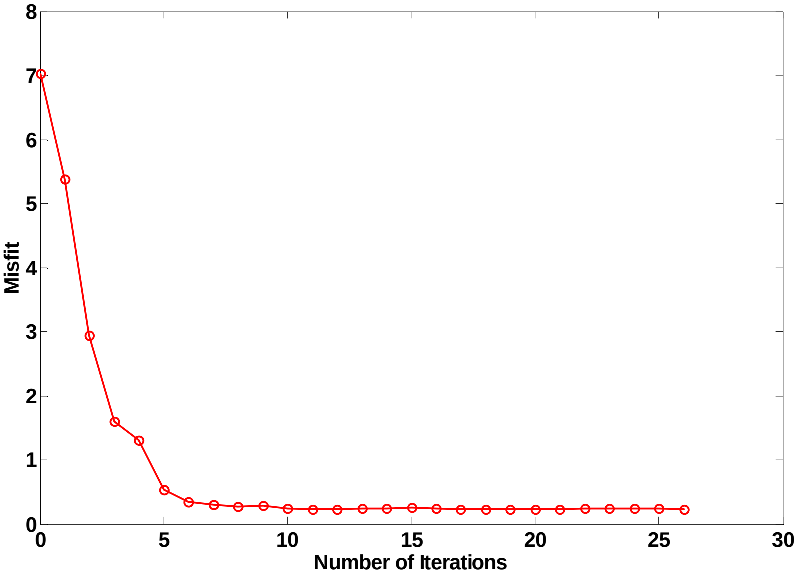
Misfit
8
7
6
5
4
3
2
1
0
0
5
10
15
20
25
30
Number of Iterations

(c)

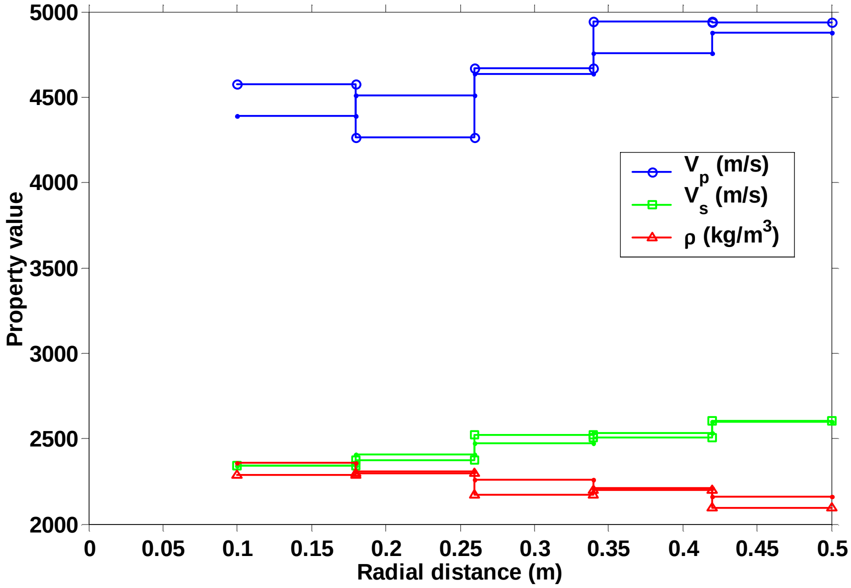

(d)

Figure 5.13: Simultaneous inversion of radial profiles of elastic parameters for a six-layer fast formation using normalized spectra of array waveform data contaminated with 5% zero-mean Gaussian noise. Panel (a) shows the array waveform in the time domain and panel (b) shows the data residuals yielded by the inversion. In panel (d), the inverted radial distributions of elastic parameters are identified with solid lines and open circles, and panel (c) shows the reduction of the misfit function with the number of iterations.

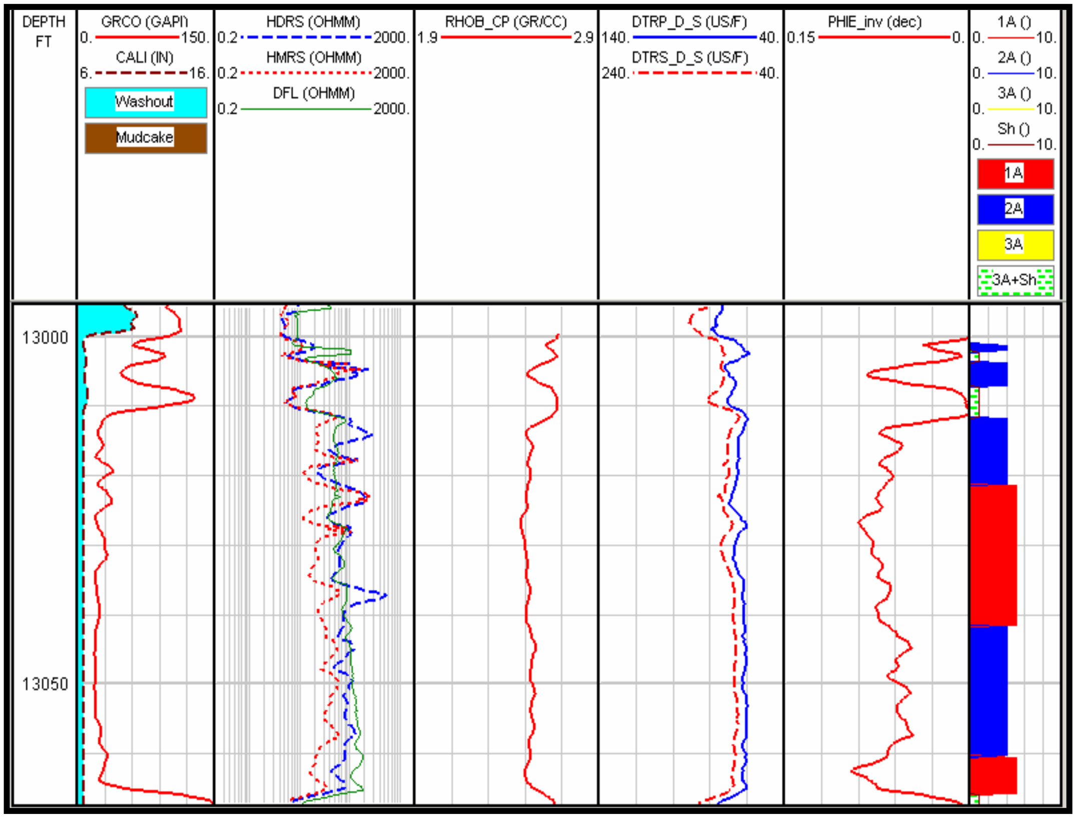

Figure 5.14**:** Plot of the basic suite of measured wireline logs including dipole sonic logs and rock types along Anderson well #2.

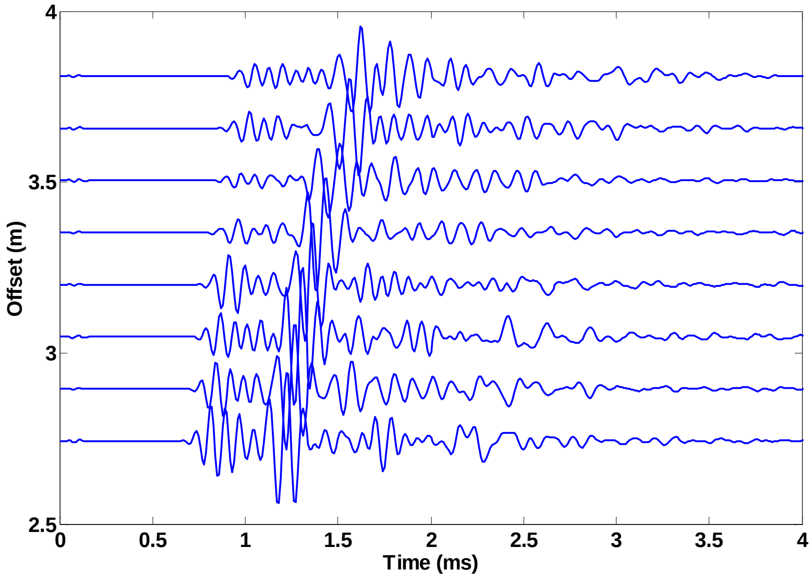

(a)

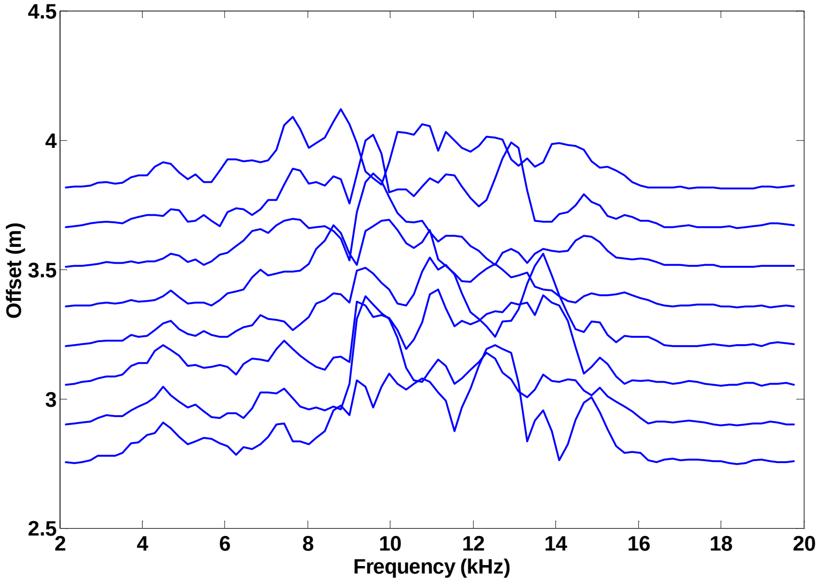

(b)

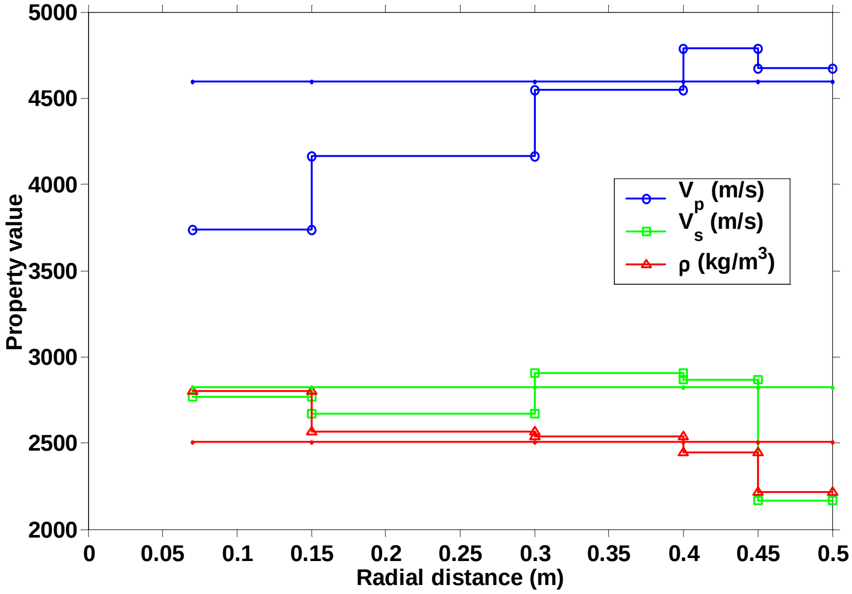

(c)

Figure 5.15: Simultaneous inversion of radial profiles of elastic parameters using array waveform data acquired in Anderson well #2 located in a tight-gas reservoir. Panel (a) shows the array waveforms in the time domain and the amplitude spectra are shown in panel (b). Panel (c) shows the homogeneous formation model used to initialize the inversion and inverted profiles of formation elastic parameters.

Chapter 6: Summary, Conclusions and Recommendations for Future Research

6.1 SUMMARY

The main thrust of this dissertation was to obtain more reliable estimates of formation velocities from industry standard borehole acoustic logging data. This goal was achieved by (a) development of an efficient numerical simulation in boreholes surrounded by radially layered formations, (b) a detailed assessment of mud-filtrate invasion effects on borehole acoustic measurements, (c) evaluations of the applicability of log correction with the Biot-Gassmann fluid substitution model, and (d) radial profiling of formation elastic parameters. The new forward modeling algorithm for simulating wave propagation in boreholes is a key component for accomplishing this goal. An inversion algorithm is also developed to estimate the radial distributions of elastic formation parameters. Such radial profiles provide a quantitative description of near-wellbore formation damages and true formation parameters in the vicinity of the borehole. A Gauss-Newton method using normalized array full waveform data in the frequency domain is the essence of the inversion algorithm. The main contribution of this dissertation can be summarized as follows:

1. Developed integral equation formulations and approximations that are amenable to simulate elastic wave scattering.
2. Established a procedure for calculating realistic radial profiles of formation elastic parameters due to mud-filtrate invasion.
3. Developed and implemented an efficient and stable algorithm for the synthesis of multipole acoustic logging measurements in radially layered

media based on the method of generalized reflection and transmission coefficients.

4. Concluded that log corrections using the Biot-Gassmann fluid substitution model are only needed in presence of deeply invaded zones.
5. Presented an efficient and stable inversion procedure that makes use of array normalized-frequency spectrum to estimate radial profiles of formation elastic parameters. The proposed inversion method does not require of specific knowledge of the source wavelet.

Specifically, to simulate wave propagation in a fluid-filled borehole, an integral equation representation is first used to study elastic wave propagation in solid media. The method of moments and various approximations are explored to numerically solve elastic scattering problems due to inhomogeneous inclusions in a homogeneous background. This serves as a methodological research for the feasibility of the integral equation method to simulate wave propagation in a fluid-filled borehole. It is revealed that the Green's tensor necessary for simulating the acoustic propagation in boreholes is much more complicated than that of a homogeneous medium.

An efficient algorithm for forward modeling is developed using the recommended Green's tensor from the research in Chapter 2. The new algorithm, based on the concept of generalized reflection and transmission matrices, performs numerical simulation of multipole acoustic logging measurements in the presence of cylindrically layered media in an efficient and stable manner. This new formulation is verified by comparing simulation results to those of the Thomson-Haskell method in cases of simple borehole and complex mud-filtrate invasion zones.

Using the newly developed forward modeling tool, mud-filtrate invasion effects on borehole acoustic measurements are assessed through the simulation of time-lapse logging measurements in the presence of complex invasion zones. By simulating the mud-filtrate invasion process in the near-wellbore region, one can obtain radial distributions of saturation of mud filtrate and connate formation fluid. Subsequently, radial profiles of formation elastic properties are obtained by applying the Biot-Gassmann fluid substitution model. Monopole and dipole acoustic array waveforms are simulated in open- and cased-holes by making use of the calculated radial profiles of density and P- and S-wave velocities. The effect of mud-filtrate invasion on the arrival times and amplitudes of various wave modes are studied by comparing monopole and dipole waveforms for homogeneous and radially layered formation models. An industry standard STC method is used to extract P- and S-wave velocities from the simulated waveforms. The STC processing results suggest that modern borehole sonic tools investigate beyond shallow invaded zones, but not within deeply invaded zones. In general, mud-filtrate invasion in the near-wellbore region reduces the P-wave amplitude and increases the shear wave amplitude. P-wave arrivals occur earlier and S-wave arrivals occur later for models with invaded zones with respect for wave arrivals for virgin (uninvaded) formations. The differences are visually identifiable and are approximately tens of microseconds. These observations can be used to detect the mud-filtrate invasion effects and fluid movement. In most cases, the Biot-Gassmann fluid substitution model is found appropriate for performing sonic log corrections in the presence of deeply invasion zones.

Finally, an inversion algorithm using a Gauss-Newton method is developed for estimating radial profiles of density and P- and S-wave velocities of rock formation in using array full waveforms. The array waveforms are first transformed from the time to the frequency domain using a fast Fourier transform. A new array data set is obtained by normalizing the remaining traces using one of the traces as reference. Therefore, the normalized, complex-valued wavefield remains dimensionless and source independent. The inversion algorithm minimizes the least-squared misfit between the measured normalized wavefield and the numerically modeled normalized wavefield in the selected frequency band. This algorithm was successfully applied in the inversion of radial profiles of density and P- and S-wave velocities in the near wellbore regions. Sensitivity analysis showed that accurate input of borehole fluid velocity is required for the stable and reliable estimation of elastic parameters.

6.2 CONCLUSIONS

The following conclusions can be drawn from the dissertation:

1. The study of simulation of borehole acoustic logging measurements using the integral equation method provides an intuitive understanding of the physics involved in wave propagation in boreholes. To make the problem tractable, a Green’s tensor is required that can take into account discontinuities in the integral equation representation of wave propagation in fluid-filled boreholes. The Green’s tensor necessary for the solution of secondary wavefield propagation is that for a multilayered, elastic medium penetrated by an infinite borehole.
2. A new algorithm developed in the dissertation for the synthesis of multipole acoustic logging measurements in radially layered media is based on the method of generalized reflection and transmission coefficients. An exact frequency-wavenumber (*f*-*k*) domain solution of the

Green's tensor associated with a multipole source in a fluid-filled borehole is formulated using the generalized reflection coefficient method. Normalized Hankel functions, normalizing amplitude factors, and a recursive scheme to compute generalized reflection and transmission coefficients are used to render the algorithm stable and efficient. The algorithm is benchmarked and validated by comparing simulation results with those of the Thomson-Haskell method for simple borehole and stepwise invasion zone models. Dipole and quadrupole waveforms computed using the two simulation methods show an excellent agreement.

3. Using a reservoir simulator and the Biot-Gassmann fluid substitution model, detailed radial profiles of elastic properties in the near-wellbore region due to mud-filtrate invasion are computed and used as the input model for waveform simulation. Fluid-substitution effects cause a decrease in the P-wave velocity and an increase in the S-wave velocity in the radial direction away from the wellbore.
4. The simulation of radial elastic properties is applied to investigate the depth of penetration of a multipole tool in a gas-saturated reservoir. Using the STC algorithm and dispersion analysis to study the dipole waveforms simulated for a radially multilayered formation, it is found that a dipole tool emulating Dipole Sonic Imager with a wideband source can investigate about three times deeper than a monopole source.
5. By comparing time-lapse logging waveforms, it is found that P waves arrives earlier and that S- and Stoneley- waves arrive later for formation model with invaded zones than for homogeneous formation model. P-

wave amplitudes decrease because of the diverging effect of the decreasing density and P-wave velocity in the radial direction away from the borehole wall. On the other hand, S-wave amplitudes increase by a few percent because of the focusing effect of the increasing S-wave velocity in the radial direction.

6. Mud-filtrate invasion effects are not observed on the P- and S-wave velocity logs calculated with industry standard STC processing for invasion depths around 2-3 borehole diameters. Therefore, log corrections are not necessary in these situations using the Biot-Gassmann fluid substitution model although discrepancies between seismic and acoustic velocities may still exist. Such effects are clearly shown in the gas reservoir study described in Chapter 4 wherein the invasion length reaches approximately 2 m. A log correction using the Biot-Gassmann fluid substitution model is performed and validated using field data. However, different formation solid composition and fluid properties may limit the practical use of the Biot-Gassmann fluid substitution model.
7. The inversion procedure proposed in the dissertation uses normalized spectra of the array waveforms, which by construction is independent of the source spectrum. If the formation across the receiver section is very heterogeneous, the effective source spectra for each trace of recorded waveforms will be different. Because of this, the normalization procedure can break down. By matching the real and imaginary parts of the spectra, the Gauss-Newton non-linear method yields reliable radial profiles of formation density and P- and S-wave velocities for the cases of synthetic

models. The inversion algorithm is stable when one makes use of the low frequency component of the array data. Inverted radial profiles of elastic properties using measurements contaminated by Gaussian noises exhibit high correlation coefficients (over 0.82) with the actual distributions of elastic properties. Additional tests of the algorithm using field data acquired in a low-porosity gas field also yield reasonable near-wellbore distribution of elastic properties.

8. Sensitivity studies with respect to borehole fluid property and geometry indicate that the inversion algorithm is sensitive to borehole fluid velocity, but not to borehole fluid density. Overestimation of borehole radius causes significant errors in the inversion results, but underestimation does not significantly affect the inverted P- and S-wave velocities.

6.3 RECOMMENDATIONS FOR FUTURE RESEARCH

The simulation and inversion algorithms developed in the dissertation are based on radially multilayered formation models. The forward modeling algorithm does not involve the logging tool in the simulation. Presence and eccentricity of an elastic tool in a borehole can significantly change the number of wave modes and the space-time properties of full waveforms. In the field, borehole conditions such as borehole washouts, shale swelling and many other factors can be quite complex. Formations along the borehole axial direction are commonly inhomogeneous due to layering of sedimentary rocks. In these situations, a finite-difference simulation method becomes more appropriate to reproduce acoustic wave propagation in rock formations penetrated by a borehole, including tool effects.

The nonlinear inversion algorithm using the Gauss-Newton method is subject to the problem of local convergence. A global inversion method, such as simulated annealing, is worth considering for the accurate and reliable estimation of radial profiles of formation properties.

Dispersion curves of guided wave modes in borehole acoustic logging, such as the flexural wave in dipole logging, are monotonic functions of frequency. Moreover, they are also source independent and sensitive to density and P- and S-wave velocities. Radial profiling using the guided wave dispersion properties should render the inversion algorithm stable and efficient.

Expensive drilling operations in deep water environments promote the need of acoustic logging-while-drilling (LWD) practices. Extensive modeling research is required to understand wave propagation phenomena in the presence of a large steel drill collar in the borehole. The thin fluid annulus between the collar and the wellbore requires of a very fine spatial grid to be used in the finite-difference simulation, and a stretched grid method may be necessary to insure the accurate enforcement of arbitrary boundary conditions. However, for the isotropic model and centered-tool case, the method developed in the dissertation may be used to accurately simulate wave propagation in LWD environments.

Lastly, it is strongly suggested that the inversion algorithm developed in the dissertation be applied to more field data sets to further evaluate the feasibility and practical limitations of noisy and imperfect acoustic logging measurements to estimate radial and vertical profiles of elastic parameters.

Appendix A: Analytical Solution to the Elastic Scattering Problem

Consider a harmonic dilatational line source located at an off-centered position in the solid, and oscillating with an angular frequency ω. Elastic wave scattering due to the infinite long solid cylinder shown in Figure 2.1 becomes a two-dimensional (2-D) problem. The scalar wave equations lead to two Helmholtz equations, whose solutions can be expressed in terms of a single dilatational potential for the incident waves, together with a set of potentials for scattered waves within both the background and the scatterer.

The displacement vector both in the background and in the scattering cylinder can be expressed in terms of classical dilatational and shear potentials, ϕ and ψ, respectively. This is written as

$$\overline{u} = \nabla\phi + \nabla\times\left(\hat{y}\psi\right). \tag{A-1}$$

A.1 INCIDENT FIELD

The incident dilatational potential ϕ^{inc} is obtained from the expression of a line source, i.e.,

$$\phi^{inc}(r,\theta) = \frac{i}{4} f_T \frac{k_{cb}^2}{\omega^2} H_0^{(1)}\left(k_{cb}\left|\overline{r}_s - \overline{r}\right|\right), \tag{A-2}$$

where i is the imaginary unit$\left(\sqrt{-1}\right)$, f_T is the moment of the source, k_{cb} is the compressional wavenumber, $H_0^{(1)}$ denotes the Hankel function of the first kind and order 0, and $\overline{r_s}$ and $\overline{r}$ are the locations of the source and the receiver, respectively

Equation (A-2) expresses the incident field in terms of waves centered at the source point, and not at the axis of the cylinder. Graf's addition theorem is used to express the incident potential in terms of waves centered at the origin, leading to the expressions (in cylindrical coordinates)

$$\phi^{inc}(r,\theta)=\frac{i}{4}f_T\frac{k_{cb}^2}{\omega^2}\left[H_0^{(1)}(k_{cb}r_s)J_0(k_{cb}r)+2\sum_{n=1}^{\infty}H_n^{(1)}(k_{cb}r_s)J_n(k_{cb}r)\cos n(\theta_s-\theta)\right] \quad \text{(A-3)}$$

when $r \leq r_s$, and

$$\phi^{inc}(r,\theta)=\frac{i}{4}f_T\frac{k_{cb}^2}{\omega^2}\left[H_0^{(1)}(k_{cb}r)J_0(k_{cb}r_s)+2\sum_{n=1}^{\infty}H_n^{(1)}(k_{cb}r)J_n(k_{cb}r_s)\cos n(\theta_s-\theta)\right] \quad \text{(A-4)}$$

when $r > r_s$, where $H_n^{(1)}$ denotes Hankel functions of the first kind and order n, and J_n denotes Bessel functions of order n, θ is the azimuth, *r* is the distance to the receiver and r_s is the distance from the source to the cylinder's origin.

Using the property $\cos n(\theta_s-\theta)=\cos n\theta_s\cos n\theta+\sin n\theta_s\sin n\theta$, the incident field can be separated into cosine and sine equations.

A.2 SCATTERED FIELD

In the frequency-wavenumber domain, the scattered field in the background medium can be expressed using a form similar to that of the incident field, namely

$$\begin{aligned}\phi^{sc}(r,\theta)&=A_0H_0^{(1)}(k_{cb}r)/H_0^{(1)}(k_{cb}a)\\&\quad+2\sum_{n=1}^{\infty}\left[A_n\cos n\theta+A_n'\sin n\theta\right]H_n^{(1)}(k_{cb}r)/H_n^{(1)}(k_{cb}a),\end{aligned} \quad \text{(A-5)}$$

and

$$\psi^{sc}(r,\theta)=2\sum_{n=1}^{\infty}\left[B_n\cos n\theta+B_n'\sin n\theta\right]H_n^{(1)}(k_{sb}r)/H_n^{(1)}(k_{sb}a), \quad \text{(A-6)}$$

where the superscript ‘sc’ denotes the scattered field, and A_n, A'_n, B_n, and B'_n are unknown coefficients to be determined by enforcing the appropriate boundary conditions.

A.3 INTERNAL FIELD

The internal (refracted) field in the solid cylindrical formation consists of standing waves, which can be expressed as

$$\begin{aligned}\phi^{\mathrm{int}}(r,\theta) &= C_0 J_0(k_c r)/J_0(k_c a)\\ &\quad + 2\sum_{n=1}^{\infty}\left[C_n \cos n\theta + C_n^{'} \sin n\theta\right] J_n(k_c r)/J_n(k_c a),\end{aligned} \tag{A-7}$$

and

$$\psi^{\mathrm{int}}(r,\theta) = 2\sum_{n=1}^{\infty}\left[D_n \cos n\theta + D_n^{'} \sin n\theta\right] J_n(k_s r)/J_n(k_s a), \tag{A-8}$$

where the superscript ‘int’ identifies the internal field, and the symbols C_n, C'_n, D_n, and D'_n denote unknown coefficients to be determined by enforcing the appropriate boundary conditions; k_{cb} and k_{sb} are compressional and shear wave numbers of the background medium, respectively, and k_c and k_s are compressional and shear wave numbers of the circular cylinder medium, respectively.

The use of constant denominators and the particular form of shear potentials in equations (A-5) through (A-8) makes the formulation numerically stable.

A.4 BOUNDARY CONDITIONS

The commonly used boundary conditions in elastic scattering in solid media are the welded-contact conditions. Accordingly, the radial displacement continuity is

$$u_r^{\mathrm{int}}(r=a,\theta) = u_r^{ext}(r=a,\theta), \tag{A-9}$$

the tangential displacement continuity is given by

$$u_\theta^{\text{int}}(r=a,\theta)=u_\theta^{ext}(r=a,\theta), \tag{A-10}$$

the radial stress continuity is

$$\sigma_{rr}^{\text{int}}(r=a,\theta)=\sigma_{rr}^{ext}(r=a,\theta), \tag{A-11}$$

and the angential stress continuity is

$$\sigma_{r\theta}^{\text{int}}(r=a,\theta)=\sigma_{r\theta}^{ext}(r=a,\theta). \qquad . \tag{A-12}$$

A.5 SOLUTION

In cylindrical coordinates, the displacement and stress components are given by

$$u_r=\frac{\partial\phi}{\partial r}+\frac{1}{r}\frac{\partial\psi}{\partial\theta}, \tag{A-13}$$

$$u_\theta=\frac{1}{r}\frac{\partial\phi}{\partial\theta}-\frac{\partial\psi}{\partial r}, \tag{A-14}$$

$$\sigma_{rr}=\lambda\nabla^2\phi+2\mu\frac{\partial u_r}{\partial r}, \tag{A-15}$$

and

$$\sigma_{r\theta}=\mu\left(\frac{\partial u_\theta}{\partial r}-\frac{u_\theta}{r}+\frac{1}{r}\frac{\partial u_r}{\partial\theta}\right). \tag{A-16}$$

Moreover, the potentials satisfy the Helmholtz equations

$$\nabla^2\phi+k^2\phi=0, \tag{A-17}$$

and

$$\nabla^2\psi+k^2\psi=0. \tag{A-18}$$

In order to simplify the notation, one defines the two ratios

$$RZ'(r)=\frac{Z'(r)}{Z(r)}, \tag{A-19}$$

and

$$RZ^{''}(r) = \frac{Z^{''}(r)}{Z(r)}, \tag{A-20}$$

where $Z(r)$ is a Bessel or Hankel function. The above short-handed notation will be used in the remainder of the derivations developed in this appendix. Likewise, only the case $r \le r_s$ is considered for the analysis.

By substituting the field potentials into the boundary conditions, one obtains a linear system of equations for the unknown coefficients. A special case of the linear system can be obtained when n = 0, from which A_0 and C_0 can be solved. Namely, from the condition of continuity of radial displacement, one obtains

$$k_{cb} r H_0^{'(1)}(k_{cb} a) A_0 - k_c r J_0^{'}(k_c a) C_0 = -S k_{cb} H_0^{(1)}(k_{cb} r_s) J_0^{'}(k_{cb} a), \tag{A-21}$$

where

$$S = \frac{i}{4} f_T \frac{k_{cb}^2}{\omega^2}.$$

From the condition of continuity of the radial stress, one obtains

$$\begin{aligned} &k_{cb}^2\left(-\lambda_b + 2\mu_b \cdot r H_0^{''(1)}(k_{cb} a)\right) A_0 - k_c^2\left(-\lambda + 2\mu \cdot r J_0^{''}(k_c a)\right) C_0 \\ &= -S k_{cb}^2\left(-\lambda_b J_0(k_{cb} a) + 2\mu_b \cdot r J_0^{''}(k_{cb} a)\right) H_0^{(1)}(k_{cb} r_s). \end{aligned} \tag{A-22}$$

When n > 0, A_n, $A_n^{'}$, B_n, $B_n^{'}$, C_n, $C_n^{'}$, D_n, and $D_n^{'}$ can be obtained by solving the linear system of equations

$$A_{4\times 4} X_{4\times 1} = B_{4\times 1}, \tag{A-23}$$

where

$$A_{4\times 4} = \begin{bmatrix} a_{11} & a_{12} & a_{13} & a_{14} \\ a_{21} & a_{22} & a_{23} & a_{24} \\ a_{31} & a_{32} & a_{33} & a_{34} \\ a_{41} & a_{42} & a_{43} & a_{44} \end{bmatrix}, \text{ and } B_{4\times 1} = \begin{bmatrix} b_1 \\ b_2 \\ b_3 \\ b_4 \end{bmatrix}. \tag{A-24}$$

The entries of matrix *A* and vector *B* are derived by making use of the continuity equations. From the condition of continuity of radial displacement, one has

$$\begin{aligned} a_{11} &= k_{cb} \cdot rH_0^{'(1)}\left(k_{cb}a\right), \\ a_{12} &= \frac{n}{a}, \\ a_{13} &= -k_c \cdot rJ_0^{'}\left(k_c a\right), \end{aligned}$$

and

$$a_{14} = -\frac{n}{a}. \tag{A-25}$$

From the condition of continuity of tangential displacement, one has

$$\begin{aligned} a_{21} &= \frac{n}{a}, \\ a_{22} &= k_{sb} \cdot rH_0^{'(1)}\left(k_{sb}a\right), \\ a_{23} &= -\frac{n}{a}, \end{aligned}$$

and

$$a_{24} = k_s \cdot rJ_0^{'}\left(k_s a\right). \tag{A-26}$$

From the condition of continuity of radial stress, one has

$$\begin{aligned} a_{31} &= k_{cb}^2\left(-\lambda_b + 2\mu_b \cdot rH_0^{''(1)}\left(k_{cb}a\right)\right), \\ a_{32} &= 2\mu_b k_{sb}\,\frac{n}{a} \cdot \left(rH_0^{'(1)}\left(k_{sb}a\right) - \frac{1}{k_{sb}a} \right), \\ a_{33} &= -k_c^2\left(-\lambda + 2\mu \cdot rJ_0^{''}\left(k_c a\right)\right), \end{aligned}$$

and

$$a_{34} = -2\mu k_s\,\frac{n}{a} \cdot \left(rJ_0^{'}\left(k_s a\right) - \frac{1}{k_s a} \right). \tag{A-27}$$

From the condition of continuity of tangential stress, one has

$$a_{41} = 2\mu_b k_{cb}\,\frac{n}{a}\left(rH_0^{'(1)}\left(k_{cb}a\right) - \frac{1}{k_{cb}a} \right),$$

$$a_{42} = -\mu_b k_{sb}^2 \left(-rH_0^{''(1)}\left(k_{sb}a\right) + \frac{rH_0^{''(1)}\left(k_{sb}a\right)}{k_{sb}a} - \left(\frac{n}{k_{sb}a}\right)^2 \right),$$

$$a_{42} = -2\mu k_c\,\frac{n}{a}\left(rJ_0^{'}\left(k_c a\right) - \frac{1}{k_c a} \right),$$

and

$$a_{44} = \mu k_s^2 \left(-rJ_0^{''}\left(k_s a\right) + \frac{rJ_0^{''}\left(k_s a\right)}{k_s a} - \left(\frac{n}{k_s a}\right)^2 \right). \qquad \text{(A-28)}$$

As mentioned in section A.1 of this appendix, the incident field can be separated into sine and cosine equations. The scattered field can be obtained for each set of equations by solving for the unknown coefficients. Superposition can then be applied to obtain the total scattered field by adding the solutions for the sine and cosine equations of the incident field. Specifically, for the cosine equation, one has

$$b_1 = -Sk_{cb}H_n^{(1)}\left(k_{cb}r_s\right)J_n^{'}\left(k_{cb}a\right)\cos n\theta_s,$$

$$b_2 = -S\frac{n}{a}H_n^{(1)}\left(k_{cb}r_s\right)J_n\left(k_{cb}a\right)\cos n\theta_s,$$

$$b_3 = -Sk_{cb}^2\left(-\lambda_b J_n\left(k_{cb}a\right) + 2\mu_b \cdot rJ_n^{''}\left(k_{cb}a\right)\right)H_n^{(1)}\left(k_{cb}r_s\right)\cos n\theta_s,$$

and

$$b_4 = -2S\mu_b k_{cb}\,\frac{n}{a}\left(J_n^{'}\left(k_{cb}a\right) - \frac{J_n\left(k_{cb}a\right)}{k_{cb}a} \right)H_n^{(1)}\left(k_{cb}r_s\right)\cos n\theta_s. \qquad \text{(A-29)}$$

In this case, only the coefficients of cosine terms in the potential expressions of the scattered and internal fields are not zero. These coefficients A_n, $B_n^{'}$, C_n, and $D_n^{'}$ can be obtained by solving the linear system (A-23).

Similarly, for the sine equation one has

$$b_1 = -Sk_{cb} H_n^{(1)}(k_{cb} r_s) J_n^{'}(k_{cb} a) \sin n\theta_s,$$

$$b_2 = -S \frac{n}{a} H_n^{(1)}(k_{cb} r_s) J_n(k_{cb} a) \sin n\theta_s,$$

$$b_3 = -Sk_{cb}^2 \left(-\lambda_b J_n(k_{cb} a) + 2\mu_b \cdot r J_n^{''}(k_{cb} a)\right) H_n^{(1)}(k_{cb} r_s) \sin n\theta_s,$$

and

$$b_4 = -2S\mu_b k_{cb} \frac{n}{a} \left(J_n^{'}(k_{cb} a) - \frac{J_n(k_{cb} a)}{k_{cb} a} \right) H_n^{(1)}(k_{cb} r_s) \sin n\theta_s. \tag{A-30}$$

Coefficients for the sine terms in the scattered and internal fields, $A_n^{'}$, B_n, $C_n^{'}$, and D_n can be obtained from the above expressions.

Displacement fields can be determined from equations (A-13) and (A-14). The displacement fields in the background are the sum of the incident field and scattered field, i.e.,

$$u_r^{sc} = \frac{\partial \phi^{sc}}{\partial r} + \frac{1}{r} \frac{\partial \psi^{sc}}{\partial \theta}, \tag{A-31}$$

and

$$u_r = u_r^{inc} + u_r^{sc} = \frac{\partial \left(\phi^{inc} + \phi^{sc}\right)}{\partial r} + \frac{1}{r} \frac{\partial \psi^{sc}}{\partial \theta}. \tag{A-32}$$

The radial stress field can be obtained as follows

$$\sigma_{rr} = \lambda_{cb} \nabla^2 \left(\phi^{inc} + \phi^{sc}\right) + 2\mu_{cb} \frac{\partial u_r}{\partial r} = -\lambda_{cb} k_{cb}^2 \left(\phi^{inc} + \phi^{sc}\right) + 2\mu_{cb} \frac{\partial u_r}{\partial r}. \tag{A-33}$$

Appendix B: Numerical Integration of the Green's Tensor

This appendix provides details on the integration of the Green's tensor in 2-D rectangular cells.

Consider the following equation

$$f(\bar{r}) = k_b^2 \int_\tau g(\bar{r},\bar{r}_0)d\bar{r}_0 \ , \tag{B-1}$$

where the function $g(\bar{r},\bar{r}_0)$ satisfies the Helmholtz equation

$$k_b^2 \mathrm{g}(\bar{r},\bar{r}_0) = -\nabla^2 g(\bar{r},\bar{r}_0) - \delta(\bar{r}-\bar{r}_0) . \tag{B-2}$$

Substituting (B-2) into (B-1) yields

$$\begin{aligned} f(\bar{r}) &= -\int_\tau \nabla^2 g(\bar{r},\bar{r}_0)d\bar{r}_0 - \int_\tau \delta(\bar{r}-\bar{r}_0)d\bar{r}_0 \\ &= \nabla \cdot \int_\tau \nabla_0 g(\bar{r},\bar{r}_0)d\bar{r}_0 - D(\bar{r}) \end{aligned} \quad , \tag{B-3}$$

where

$$D(\bar{r}) = \begin{cases} 1 & if \quad \bar{r} \in \tau \\ 0 & if \quad \bar{r} \notin \tau \end{cases} ,$$

and the subscript "0" for the ∇ operator indicates differentiation with respect to $\bar{r}_0$.

Applying the gradient theorem to the integral on the right-hand side of equation (B-3) gives

$$f(\bar{r}) = \nabla \cdot \oint_{\partial\tau} g(\bar{r},\bar{r}_0)\hat{\mathrm{n}}(\bar{r}_0)\mathrm{ds}_0 - D(\bar{r}), \tag{B-4}$$

where $\partial\tau$ is the enclosing surface boundary of τ, $\hat{\mathrm{n}}(\bar{r}_0)$ is the normal unit vector pointing outward from τ, and ds_0 is the differential surface element.

In a similar way, one obtains

$$\begin{aligned}\nabla\nabla f(\bar{r}) &= \nabla\int_{\tau}\nabla g(\bar{r},\bar{r}_0)d\bar{r}_0 = -\nabla\int_{\tau}\nabla_0 g(\bar{r},\bar{r}_0)d\bar{r}_0 \\ &= \nabla\oint_{\partial\tau} g(\bar{r},\bar{r}_0)\hat{\mathrm{n}}(\bar{r}_0)\mathrm{ds}_0\,.\end{aligned} \tag{B-5}$$

Consequently, then tensor

$$\overline{\overline{\Lambda}}(\bar{r}) = \nabla\nabla\int_{\tau} g_C(\bar{r},\bar{r}_0)dr' - \left(\kappa_{sb}^2\bar{I} + \nabla\nabla\right)\int_{\tau} g_S(\bar{r},\bar{r}_0)d\bar{r}_0 \tag{B-6}$$

can be written as

$$\begin{aligned}\overline{\overline{\Lambda}}(\bar{r}) &= -\nabla\oint_{\partial\tau} g_C(\bar{r},\bar{r}_0)\hat{\mathrm{n}}(\bar{r}_0)\mathrm{ds}_0 \\ &\quad + \overline{\overline{I}}D(\bar{r}) - \overline{\overline{I}}\nabla\cdot\oint_{\partial\tau} g_S(\bar{r},\bar{r}_0)\hat{\mathrm{n}}(\bar{r}_0)\mathrm{ds}_0 + \nabla\oint_{\partial\tau} g_S(\bar{r},\bar{r}_0)\hat{\mathrm{n}}(\bar{r}_0)\mathrm{ds}_0\,\cdot\end{aligned} \tag{B-7}$$

Now consider a two-dimensional (2-D) rectangular cell, whose geometrical center is located at (x_0, z_0) and whose side lengths in x, and z direction are 2a and 2c, respectively. The scalar Green's tensor in two dimensions becomes the Hankel function $\frac{\mathrm{i}}{4}H_0^{(1)}(\kappa_b\bar{\rho})$. Accordingly, equation (B-7) reduces to the following 2-D form

$$\begin{aligned}\overline{\overline{\Lambda}}(\bar{\rho}) &= -\frac{i}{4}\nabla\oint_{\partial S} H_0^{(1)}\left(\kappa_{cb}|\bar{\rho}-\bar{\rho}_0|\right)\hat{\mathrm{n}}(\bar{\rho}_0)\mathrm{d}\ell' \\ &\quad + \overline{\overline{I}}D(\bar{\rho}) - \frac{i}{4}\overline{\overline{I}}\nabla\cdot\oint_{\partial S} H_0^{(1)}\left(\kappa_{sb}|\bar{\rho}-\bar{\rho}_0|\right)\hat{\mathrm{n}}(\bar{\rho}_0)\mathrm{d}\ell' + \frac{i}{4}\nabla\oint_{\partial S} H_0^{(1)}\left(\kappa_{sb}|\bar{\rho}-\bar{\rho}_0|\right)\hat{\mathrm{n}}(\bar{\rho}_0)\mathrm{d}\ell'\,,\end{aligned} \tag{B-8}$$

where $\partial\mathrm{S}$ is the closed perimeter around S and $\mathrm{d}\ell$ is the corresponding differential length element. In two dimensions, the unit tensor is given by

$$\overline{\overline{I}} = \hat{x}\hat{x} + \hat{z}\hat{z}\,.$$

Thus, equation (B-8) can be written explicitly as

$$
\begin{aligned}
&\overline{\overline{\Lambda}}(\overline{\rho}) = -\nabla\left[\ell_{cx}(\overline{\rho})\hat{x} + \ell_{cz}(\overline{\rho})\hat{z}\right] \\
&+ \left\{D(\overline{\rho}) - \nabla\cdot\left[\ell_{x}(\overline{\rho})\hat{x} + \ell_{z}(\overline{\rho})\hat{z}\right]\right\}\overline{\overline{I}} + \nabla\left[\ell_{x}(\overline{\rho})\hat{x} + \ell_{z}(\overline{\rho})\hat{z}\right] \\
&= -\left\{\upsilon_{cxx}(\overline{\rho})\hat{x}\hat{x} + \upsilon_{cxz}(\overline{\rho})\hat{x}\hat{z} + \upsilon_{czx}(\overline{\rho})\hat{z}\hat{x} + \upsilon_{czz}(\overline{\rho})\hat{z}\hat{z}\right\} \\
&+ \left\{D(\overline{\rho}) - \upsilon_{xx}(\overline{\rho}) - \upsilon_{zz}(\overline{\rho})\right\}\overline{\overline{I}} + \upsilon_{xx}(\overline{\rho})\hat{x}\hat{x} + \upsilon_{xz}(\overline{\rho})\hat{x}\hat{z} + \upsilon_{zx}(\overline{\rho})\hat{z}\hat{x} + \upsilon_{zz}(\overline{\rho})\hat{z}\hat{z} \\
&= \left[D(\overline{\rho}) - \upsilon_{zz}(\overline{\rho}) - \upsilon_{cxx}(\overline{\rho})\right]\hat{x}\hat{x} + \left[\upsilon_{xz}(\overline{\rho}) - \upsilon_{cxz}(\overline{\rho})\right]\hat{x}\hat{z} \\
&+ \left[\upsilon_{zx}(\overline{\rho}) - \upsilon_{czx}(\overline{\rho})\right]\hat{z}\hat{x} + \left[D(\overline{\rho}) - \upsilon_{xx}(\overline{\rho}) - \upsilon_{czz}\right]\hat{z}\hat{z},
\end{aligned}
\qquad \text{(B-9)}
$$

where

$$
\begin{aligned}
\ell_{x}(\overline{\rho}) = \frac{i}{4}\Bigg\{&\int_{z_0-c}^{z_0+c} H_0^{(1)}\left[\kappa_{sb}\sqrt{(x-x_0-a)^2+(z'-z)^2}\right]dz' \\
&- \int_{z_0-c}^{z_0+c} H_0^{(1)}\left[\kappa_{b}\sqrt{(x-x_0+a)^2+(z'-z)^2}\right]dz'\Bigg\} \quad ,
\end{aligned}
\qquad \text{(B-10)}
$$

$$
\begin{aligned}
\ell_{z}(\overline{\rho}) = \frac{i}{4}\Bigg\{&\int_{x_0-c}^{x_0+c} H_0^{(1)}\left[\kappa_{sb}\sqrt{(z-z_0-c)^2+(x'-x)^2}\right]dx' \\
&- \int_{x_0-c}^{x_0+c} H_0^{(1)}\left[\kappa_{b}\sqrt{(z-z_0+c)^2+(x'-x)^2}\right]dx'\Bigg\} \quad ,
\end{aligned}
\qquad \text{(B-11)}
$$

$$
\begin{aligned}
&\upsilon_{xx}(\overline{\rho}) = \frac{\partial \ell_{x}(\overline{\rho})}{\partial x} \\
&= -\frac{i}{4}\kappa_{sb}\left\{(x-x_0-a)\int_{z_0-c}^{z_0+c}\frac{H_1^{(1)}\left[\kappa_{sb}\sqrt{(x-x_0-a)^2+(z'-z)^2}\right]}{\sqrt{(x-x_0-a)^2+(z'-z)^2}}dz'\right. \\
&\left.-(x-x_0+a)\int_{z_0-c}^{z_0+c}\frac{H_1^{(1)}\left[\kappa_{sb}\sqrt{(x-x_0+a)^2+(z'-z)^2}\right]}{\sqrt{(x-x_0+a)^2+(z'-z)^2}}dz'\right\} \quad ,
\end{aligned}
\qquad \text{(B-12)}
$$

$$
\begin{aligned}
&\upsilon_{zz}(\overline{\rho}) = \frac{\partial \ell_{z}(\overline{\rho})}{\partial z} \\
&= -\frac{i}{4}\kappa_{sb}\left\{(z-z_0-c)\int_{x_0-a}^{x_0+a}\frac{H_1^{(1)}\left[\kappa_{sb}\sqrt{(x'-x)^2+(z-z_0-c)^2}\right]}{\sqrt{(x'-x)^2+(z-z_0-c)^2}}dx'\right. \\
&\left.-(z-z_0+c)\int_{x_0-a}^{x_0+a}\frac{H_1^{(1)}\left[\kappa_{sb}\sqrt{(x'-x)^2+(z-z_0+c)^2}\right]}{\sqrt{(x'-x)^2+(z-z_0+c)^2}}dx'\right\} \quad ,
\end{aligned}
\qquad \text{(B-13)}
$$

and

$$\begin{aligned}
\upsilon_{xz}(\bar{\rho}) &= \frac{\partial \ell_{z}(\bar{\rho})}{\partial x} \\
&= \frac{i}{4}\kappa_{sb}\left\{\int_{x_0-a}^{x_0+a}(x'-x)\frac{H_1^{(1)}\left[\kappa_{sb}\sqrt{(x'-x)^2+(z-z_0-c)^2}\right]}{\sqrt{(x'-x)^2+(z-z_0-c)^2}}dx'\right. \\
&\left.-\int_{x_0-a}^{x_0+a}(x'-x)\frac{H_1^{(1)}\left[\kappa_{sb}\sqrt{(x'-x)^2+(z-z_0+c)^2}\right]}{\sqrt{(x'-x)^2+(z-z_0+c)^2}}dx'\right\} \\
&= -\frac{i}{4}\left\{H_0^{(1)}\left[\kappa_{sb}\sqrt{(a+x_0-x)^2+(c+z_0-z)^2}\right]\right. \\
&\quad -H_0^{(1)}\left[\kappa_{sb}\sqrt{(a+x_0-x)^2+(c-z_0+z)^2}\right] \\
&\quad +H_0^{(1)}\left[\kappa_{sb}\sqrt{(a-x_0+x)^2+(c-z_0+z)^2}\right] \\
&\quad \left.-H_0^{(1)}\left[\kappa_{sb}\sqrt{(a-x_0+x)^2+(c+z_0-z)^2}\right]\right\} \\
&= \frac{\partial \ell_{x}(\bar{\rho})}{\partial z} = \upsilon_{zx}(\bar{\rho}) \qquad . \qquad \text{(B-14)}
\end{aligned}$$

The final solutions for ℓ_{cx}, ℓ_{cz}, υ_{cxx}, υ_{cxz}, υ_{czx}, and υ_{czz} are obtained from equations (B-10) through (B-14), by replacing k_{sb} for k_{cb}. Consequently, the corresponding relationships are given by

$\ell_{x} \Rightarrow \ell_{cx}$,

$\ell_{z} \Rightarrow \ell_{cz}$,

$\upsilon_{zz} \Rightarrow \upsilon_{czz}$,

$\upsilon_{zx} \Rightarrow \upsilon_{czx}$,

$\upsilon_{xz} \Rightarrow \upsilon_{cxz}$,

and

$\upsilon_{xx} \Rightarrow \upsilon_{cxx}$.

The entries of matrix A, $\overline{\overline{a_{ij}}}$, introduced in Chapter 2 for solving the elastic scattering problem, can then be written as follows

$$\overline{\overline{a_{ij}}} = -\delta\rho_j \int_{\tau_j} \overline{\overline{G}}(\bar{r}_i, \bar{r}_0)\mathrm{d}r' = \frac{\delta\rho_j}{\omega^2 \rho_j} \overline{\overline{\Lambda}}(\bar{r}_i), \tag{B-15}$$

for $\mathrm{i} \neq \mathrm{j}$, where i, j=1, 2, … N, and

$$\overline{\overline{a_{ij}}} = \overline{\overline{I}} - \delta\rho_j \int_{\tau_j} \overline{\overline{G}}(\bar{r}_i, \bar{r}_0)\mathrm{d}r' = \overline{\overline{I}} - \frac{\delta\rho_j}{\omega^2 \rho_j} \overline{\overline{\Lambda}}(\bar{r}_i), \tag{B-16}$$

for $\mathrm{i} = \mathrm{j}$, where i, j=1, 2, … N.

In two dimensions, one obtains the following expression for $\overline{\overline{\Lambda}}(\bar{\rho})$:

$$\overline{\overline{\Lambda}}(\bar{\rho}) = \begin{bmatrix} D(\bar{\rho}) - \upsilon_{zz}(\bar{\rho}) - \upsilon_{cxx}(\bar{\rho}) & \upsilon_{xz}(\bar{\rho}) - \upsilon_{cxz}(\bar{\rho}) \\ \upsilon_{xz}(\bar{\rho}) - \upsilon_{cxz}(\bar{\rho}) & D(\bar{\rho}) - \upsilon_{xx}(\bar{\rho}) - \upsilon_{czz}(\bar{\rho}) \end{bmatrix}. \tag{B-17}$$

By substituting equation (B-17) into (B-15) and (B-16), one obtains

$$\overline{\overline{a_{ij}}} = \begin{cases} \begin{bmatrix} 1 + C_j\left[D(\bar{\rho}_i) - \upsilon_{zz}(\bar{\rho}_i) - \upsilon_{cxx}(\bar{\rho}_i)\right] & C_j\left[\upsilon_{xz}(\bar{\rho}_i) - \upsilon_{cxz}(\bar{\rho}_i)\right] \\ C_j\left[\upsilon_{xz}(\bar{\rho}_i) - \upsilon_{cxz}(\bar{\rho}_i)\right] & 1 + C_j\left[D(\bar{\rho}_i) - \upsilon_{xx}(\bar{\rho}_i) - \upsilon_{czz}(\bar{\rho}_i)\right] \end{bmatrix}, if \quad i = j \\ \\ \begin{bmatrix} C_j\left[D(\bar{\rho}_i) - \upsilon_{zz}(\bar{\rho}_i) - \upsilon_{cxx}(\bar{\rho}_i)\right] & C_j\left[\upsilon_{xz}(\bar{\rho}_i) - \upsilon_{cxz}(\bar{\rho}_i)\right] \\ C_j\left[\upsilon_{xz}(\bar{\rho}_i) - \upsilon_{cxz}(\bar{\rho}_i)\right] & C_j\left[D(\bar{\rho}_i) - \upsilon_{xx}(\bar{\rho}_i) - \upsilon_{czz}(\bar{\rho}_i)\right] \end{bmatrix}, if \quad i \neq j \end{cases},$$

(B-18)

where

$C_j = \frac{\delta\rho_j}{\omega^2 \rho_j}$, and i, j =1, 2, …N.

The integral contained in equations (B-12) and (B-13) can be evaluated numerically with the use of Gaussian quadrature formulae.

Appendix C: Derivation of $\nabla \cdot \bar{u}_b$, $\nabla\nabla \cdot \bar{u}_b$, and Partial Derivatives of $\bar{u}_b$

The incident field for an infinite long dilatational line source is given by

$$\bar{u}_b(R) = -\frac{i f_T k_{cb}^3}{4\omega^2} H_1^{(1)}(R) \bar{e}_R , \tag{C-1}$$

where R is the distance between the source and the center of a cell inside the scatterer.

By making use of the relationships

$$\nabla \cdot [\bar{e}_R F(R)] = F'(R) + \frac{2}{R} F(R) = -\nabla_0 \cdot [\bar{e}_R F(R)], \tag{C-2}$$

and

$$\frac{d}{dR} H_0^{(1)}(k_{cb}R) = k_{cb}\left[H_0^{(1)}(k_{cb}R) - \frac{H_1^{(1)}(k_{cb}R)}{k_{cb}R} \right], \tag{C-3}$$

one obtains

$$\nabla \cdot \bar{u}_b(R) = -\frac{i f_T k_{cb}^4}{4\omega^2} \left[H_0^{(1)}(k_{cb}R) + \frac{H_1^{(1)}(k_{cb}R)}{k_{cb}R} \right]. \tag{C-4}$$

The subsequent application of $\nabla F(R) = \bar{e}_R F'(R)$ yields

$$\nabla\nabla \cdot \bar{u}_b(R) = -\frac{i f_T k_{cb}^5}{4\omega^2} \left[\frac{H_0^{(1)}(k_{cb}R)}{k_{cb}R} - \left(1 + \frac{2}{k_{cb}^2 R^2}\right) H_1^{(1)}(k_{cb}R) \right]. \tag{C-5}$$

For the solution of Born and extended Born approximations and the method of moments, one needs to know the background field and its first order partial derivatives to solve for the scattered field. The following derivation shows how the latter may be obtained in an efficient manner.

First define

$$\Delta x = x - x_0 , \Delta z = z - z_0 ,$$

and

$$R = \left| \bar{r} - \bar{r}_0 \right|, \ \bar{r} = x\hat{x} + z\hat{z}, \bar{r}_0 = x_0\hat{x} + z_0\hat{z} .$$

In Cartesian coordinates, the x and z components of the displacement vector are given by

$$u_{bx}(r) = -\frac{if_T k_{cb}^3}{4\omega^2} H_1^{(1)}(k_{cb}R)\frac{\Delta x}{R} , \tag{C-6}$$

and

$$u_{bz}(r) = -\frac{if_T k_{cb}^3}{4\omega^2} H_1^{(1)}(k_{cb}R)\frac{\Delta z}{R} , \tag{C-7}$$

respectively. From the identities

$$\nabla\left[u\bar{f}\right] = \nabla u \bar{f} + u\nabla\bar{f} ,$$

and

$$\nabla\bar{R} = \bar{\bar{I}} ,$$

one obtains

$$\begin{aligned} \nabla\left[f\bar{e}_R\right] &= \nabla\left[\frac{f}{R}\bar{R}\right] = \nabla\left[\frac{f}{R}\right]\bar{R} + \left[\frac{f}{R}\right]\nabla\bar{R} \\ &= \left[\frac{f'}{R} - \frac{f}{R^2}\right]\bar{e}_R\bar{R} + \left[\frac{f}{R}\right]\bar{\bar{I}} \\ &= \left[f' - \frac{f}{R}\right]\bar{e}_R\bar{e}_R + \left[\frac{f}{R}\right]\bar{\bar{I}} \qquad . \end{aligned} \tag{C-8}$$

It is also known that

$$\frac{d}{dr}H_1^{(1)}(k_{cb}r) = k_{cb}\left[H_0^{(1)}(k_{cb}r) - \frac{H_1^{(1)}(k_{cb}r)}{k_{cb}r}\right]. \tag{C-9}$$

Thus, one has

$$\nabla\bar{u}_b(r) = -\frac{if_T k_{cb}^4}{4\omega^2}\left[H_0^{(1)}(k_{cb}R) - 2\frac{H_1^{(1)}(k_{cb}R)}{k_{cb}R}\right]\bar{e}_R\bar{e}_R - \frac{if_T k_{cb}^4}{4\omega^2}\frac{H_0^{(1)}(k_{cb}R)}{k_{cb}R}\bar{\bar{I}} . \tag{C-10}$$

In Cartesian coordinates,

$$\begin{aligned}\nabla\bar{u}_b(r) &= \left(\bar{e}_x\frac{\partial}{\partial x}+\bar{e}_z\frac{\partial}{\partial z}\right)\left(\bar{e}_x u_{bx}+\bar{e}_z u_{bz}\right)\\ &= \bar{e}_x\bar{e}_x u_{bx,x}+\bar{e}_x\bar{e}_z u_{bz,x}+\bar{e}_z\bar{e}_x u_{bx,z}+\bar{e}_z\bar{e}_z u_{bz,z}\end{aligned}\quad. \tag{C-11}$$

Conversion of the above expression from cylindrical to Cartesian coordinates yields

$$\begin{aligned}\nabla\bar{u}_b(r) &= -\frac{if_T k_{cb}^4}{4\omega^2}\left[H_0^{(1)}(k_{cb}R)-2\frac{H_1^{(1)}(k_{cb}R)}{k_{cb}R}\right]\bar{e}_R\bar{e}_R-\frac{if_T k_{cb}^4}{4\omega^2}\frac{H_1^{(1)}(k_{cb}R)}{k_{cb}R}\bar{\bar{I}}\\ &= -\frac{if_T k_{cb}^4}{4\omega^2}\left\{\left[H_0^{(1)}(k_{cb}R)-2\frac{H_1^{(1)}(k_{cb}R)}{k_{cb}R}\right]\frac{\Delta x^2}{R^2}+\frac{H_1^{(1)}(k_{cb}R)}{k_{cb}R}\right\}\bar{e}_x\bar{e}_x\\ &\quad-\frac{if_T k_{cb}^4}{4\omega^2}\left\{\left[H_0^{(1)}(k_{cb}R)-2\frac{H_1^{(1)}(k_{cb}R)}{k_{cb}R}\right]\frac{\Delta x\Delta z}{R^2}\right\}\bar{e}_x\bar{e}_z\\ &\quad-\frac{if_T k_{cb}^4}{4\omega^2}\left\{\left[H_0^{(1)}(k_{cb}R)-2\frac{H_1^{(1)}(k_{cb}R)}{k_{cb}R}\right]\frac{\Delta x\Delta z}{R^2}\right\}\bar{e}_z\bar{e}_x\\ &\quad-\frac{if_T k_{cb}^4}{4\omega^2}\left\{\left[H_0^{(1)}(k_{cb}R)-2\frac{H_1^{(1)}(k_{cb}R)}{k_{cb}R}\right]\frac{\Delta z^2}{R^2}+\frac{H_1^{(1)}(k_{cb}R)}{k_{cb}R}\right\}\bar{e}_z\bar{e}_z\end{aligned}\quad, \tag{C-12}$$

By comparing equations (C-11) and (C-12), one finds

$$u_{bx,x}=-\frac{if_T k_{cb}^4}{4\omega^2}\left\{\left[H_0^{(1)}(k_{cb}R)-2\frac{H_1^{(1)}(k_{cb}R)}{k_{cb}R}\right]\frac{\Delta x^2}{R^2}+\frac{H_1^{(1)}(k_{cb}R)}{k_{cb}R}\right\}, \tag{C-13}$$

$$u_{bz,x}=-\frac{if_T k_{cb}^4}{4\omega^2}\left[H_0^{(1)}(k_{cb}R)-2\frac{H_1^{(1)}(k_{cb}R)}{k_{cb}R}\right]\frac{\Delta x\Delta z}{R^2}, \tag{C-14}$$

$$u_{bx,z}=-\frac{if_T k_{cb}^4}{4\omega^2}\left[H_0^{(1)}(k_{cb}R)-2\frac{H_1^{(1)}(k_{cb}R)}{k_{cb}R}\right]\frac{\Delta x\Delta z}{R^2}, \tag{C-15}$$

$$u_{bz,z}=-\frac{if_T k_{cb}^4}{4\omega^2}\left\{\left[H_0^{(1)}(k_{cb}R)-2\frac{H_1^{(1)}(k_{cb}R)}{k_{cb}R}\right]\frac{\Delta z^2}{R^2}+\frac{H_1^{(1)}(k_{cb}R)}{k_{cb}R}\right\}, \tag{C-16}$$

and

$$v_b=u_{bx,z}+u_{bz,x}=-\frac{if_T k_{cb}^4}{4\omega^2}\left[H_0^{(1)}(k_{cb}R)-2\frac{H_1^{(1)}(k_{cb}R)}{k_{cb}R}\right]\frac{2\Delta x\Delta z}{R^2}. \tag{C-17}$$

Appendix D: Derivation of the Expression for the Divergence of the Integral of the Green's tensor

In this appendix, two closed-form expressions for the divergence of the Green's tensor are derived assuming a circular cross section.

D.1 FIRST DERIVATION

Start by defining the expression

$$\overline{\overline{\Lambda}}(R) = \int_{\tau_i} d\overline{r_0}\,\overline{\overline{G}}(\overline{r},\overline{r_0}), \tag{D-1}$$

where $R = |\overline{r} - \overline{r}_i|$ is the distance between the receiver and the center of the cell, and $\overline{r}_i$ is the center of the i-th cell.

When $R < a$, it has been shown that

$$f(R) = \int_{\tau} d\overline{r_0}\, g(\overline{r},\overline{r_0}) = -\frac{1}{k^2} + \frac{i\pi a}{2k} H_1^{(1)}(ka) J_0(kR), \tag{D-2}$$

where

$$g(\overline{r},\overline{r}_0) = \frac{e^{ik|\overline{r}-\overline{r}_0|}}{4\pi|\overline{r}-\overline{r}_0|}, \tag{D-3}$$

and a is the radius of the scattering cylinder. Notice that

$$\nabla\nabla f(r) = \left[f''(r) - \frac{f'(r)}{r} \right]\hat{r}\hat{r} + \frac{f'(r)}{r}\overline{\overline{\mathrm{I}}} - \frac{f'(r)}{r}\hat{y}\hat{y}. \tag{D-4}$$

Therefore,

$$\begin{aligned} \overline{\overline{\Lambda}}(R) &= \int_{\tau_i} d\overline{r_0}\,\overline{\overline{G}}(\overline{r},\overline{r_0}) = -\nabla\nabla f_c(R) + k_{sb}^2 \overline{\overline{\mathrm{I}}} f_s(R) + \nabla\nabla f_s(R) \\ &= h(R)\overline{\overline{\mathrm{I}}} + g(R)\hat{r}\hat{r} + \gamma(R)\hat{y}\hat{y}, \end{aligned} \tag{D-5}$$

where

$$h(r) = k_{sb}^2 f_s(r) + \frac{1}{R}\frac{df_s(r)}{dR} - \frac{1}{R}\frac{df_c(r)}{dR} \ . \tag{D-6}$$

By making use of the recurrence and differential relations of Bessel functions, namely,

$$\frac{2m}{x} Z_m(x) = Z_{m-1}(x) + Z_{m+1}(x), \tag{D-7}$$

and

$$\begin{aligned} \frac{d}{dx} Z_m(x) &= \frac{1}{2}\left[Z_{m-1}(x) - Z_{m+1}(x)\right] \\ &= Z_{m-1}(x) - \frac{m}{x} Z_m(x) = -Z_{m+1}(x) + \frac{m}{x} Z_m(x) \ , \end{aligned} \tag{D-8}$$

one obtains

$$f'(R) = -\frac{i\pi a}{2} H_1^{(1)}(ka) J_1(kR), \tag{D-9}$$

$$f''(R) = -\frac{i\pi ak}{2} H_1^{(1)}(ka)\left(J_0(kR) - \frac{J_1(kR)}{kR} \right), \tag{D-10}$$

and

$$f'''(R) = -\frac{i\pi ak^2}{2} H_1^{(1)}(ka)\left(-J_1(kR) - \frac{J_0(kR)}{kR} + \frac{2J_1(kR)}{k^2R^2} \right). \tag{D-11}$$

From the relationships

$$\nabla F(R) = \bar{e}_R F'(R) = -\nabla_0 F(R) \, , \tag{D-12}$$

$$\nabla \cdot (\nabla F) = \nabla^2 F \, , \tag{D-13}$$

and

$$\nabla^2 (\nabla F) = \nabla(\nabla^2 F), \tag{D-14}$$

one obtains

$$\begin{aligned}\bar{I}_c &= \int_{\tau_i} d\bar{r}_0 \nabla_0 \cdot \nabla_0 \nabla_0 g_c\left(\bar{r},\bar{r}_0\right)\\ &= \int_{\tau_i} d\bar{r}_0 \nabla_0^2 \nabla_0 g_c\left(\bar{r},\bar{r}_0\right)\\ &= \int_{\tau_i} d\bar{r}_0 \nabla_0 \nabla_0^2 g_c\left(\bar{r},\bar{r}_0\right)\\ &= -\nabla \int_{\tau_i} d\bar{r}_0 \nabla_0^2 g_c\left(\bar{r},\bar{r}_0\right)\\ &= k_{cb}^2 \nabla \int_{\tau_i} d\bar{r}_0 g_c\left(\bar{r},\bar{r}_0\right) + \nabla \int_{\tau_i} d\bar{r}_0 \delta\left(\bar{r}-\bar{r}_0\right).\end{aligned} \tag{D-15}$$

It is obvious that

$$\int_{\tau_i} d\bar{r}_0 \delta\left(\bar{r}-\bar{r}_0\right) = \begin{cases} 1 & if \quad \bar{r} \in \tau_i \\ 0 & if \quad \bar{r} \notin \tau_i \end{cases}, \tag{D-16}$$

and hence,

$$\nabla \int_{\tau_i} d\bar{r}_0 \delta\left(\bar{r}-\bar{r}_0\right) = 0. \tag{D-17}$$

When $R > a$, it has been shown that

$$f(R) = \int_{\tau} d\bar{r}_0 g\left(\bar{r},\bar{r}_0\right) = \frac{i\pi a}{2k} J_1(ka) H_0^{(1)}(kR), \tag{D-18}$$

and

$$f'(R) = -\frac{i\pi a}{2} J_1(ka) H_1^{(1)}(kR). \tag{D-19}$$

Therefore,

$$\bar{I}_c = -\frac{i\pi a k_{cb}^2}{2} H_1^{(1)}\left(k_{cb}R\right) J_1\left(k_{cb}a\right) \bar{e}_R. \tag{D-20}$$

By making use of the relationship $\nabla \cdot \left\lfloor \bar{\bar{I}} F(R) \right\rfloor = \nabla F(R)$ one obtains

$$\begin{aligned}\bar{I}_s &= -\int_{\tau_i} d\bar{r}_0 \nabla_0 \cdot \nabla_0 \nabla_0 g_s\left(\bar{r},\bar{r}_0\right) - \int_{\tau_i} d\bar{r}_0 \nabla_0 \cdot \left\lfloor k_{sb}^2 \bar{\bar{I}} g_s\left(\bar{r},\bar{r}_0\right)\right\rfloor\\ &= -k_{sb}^2 \nabla \int_{\tau_i} d\bar{r}_0 g_s\left(\bar{r},\bar{r}_0\right) + \nabla \cdot \left[k_{sb}^2 \bar{\bar{I}} \int_{\tau_i} d\bar{r}_0 g_s\left(\bar{r},\bar{r}_0\right)\right]\\ &= -k_{sb}^2 \nabla \int_{\tau_i} d\bar{r}_0 g_s\left(\bar{r},\bar{r}_0\right) + k_{sb}^2 \nabla \int_{\tau_i} d\bar{r}_0 g_s\left(\bar{r},\bar{r}_0\right)\\ &= 0.\end{aligned} \tag{D-21}$$

Therefore,

$$\bar{q}_i(R) = \bar{I}_c = -\frac{i\pi a k_{cb}^2}{2} H_1^{(1)}(k_{cb}R) J_1(k_{cb}a)\bar{e}_R\,. \qquad \text{(D-22)}$$

D.2 ALTERNATIVE DERIVATION

From the relationships

$$\nabla F(R) = \bar{e}_R F'(R) = -\nabla_0 F(R)\,,$$

$$\nabla \cdot (\nabla F) = \nabla^2 F\,,$$

and

$$\nabla^2 (\nabla F) = \nabla(\nabla^2 F),$$

one obtains

$$\begin{aligned}
\bar{I}_c &= \int_{\tau_i} d\bar{r}_0 \nabla_0 \cdot \nabla_0 \nabla_0 g_c(\bar{r}, \bar{r}_0) \\
&= \int_{\tau_i} d\bar{r}_0 \nabla_0^2 \nabla_0 g_c(\bar{r}, \bar{r}_0) \\
&= \int_{\tau_i} d\bar{r}_0 \nabla_0 \nabla_0^2 g_c(\bar{r}, \bar{r}_0) \\
&= -\nabla \int_{\tau_i} d\bar{r}_0 \nabla_0^2 g_c(\bar{r}, \bar{r}_0) \\
&= k_{cb}^2 \nabla \int_{\tau_i} d\bar{r}_0 g_c(\bar{r}, \bar{r}_0) + \nabla \int_{\tau_i} d\bar{r}_0 \delta(\bar{r} - \bar{r}_0)\cdot
\end{aligned} \qquad \text{(D-23)}$$

Also, from the property

$$\int_{\tau_i} d\bar{r}_0 \delta(\bar{r} - \bar{r}_0) = \begin{cases} 1 & if \quad \bar{r} \in \tau_i \\ 0 & if \quad \bar{r} \notin \tau_i \end{cases},$$

it follows that

$$\nabla \int_{\tau_i} d\bar{r}_0 \delta(\bar{r} - \bar{r}_0) = 0\,.$$

When $R < a$, it has been shown that

$$f(r) = \int_{\tau} d\bar{r}_0 g(\bar{r}, \bar{r}_0) = -\frac{1}{k^2} + \frac{i\pi a}{2k} H_1^{(1)}(ka) J_0(kR)\,,$$

and

$$f'(r) = -\frac{i\pi a}{2} H_1^{(1)}(ka) J_1(kR),$$

where *a* is the radius of the scattering cylinder. Therefore,

$$\begin{aligned} \overline{I}_c &= k_{cb}^2 \nabla \int_{\tau_i} d\overline{r_0} g_c(\overline{r}, \overline{r}_0) \\ &= -\frac{i\pi a k_{cb}^2}{2} H_1^{(1)}(k_{cb} a) J_1(k_{cb} R) \overline{e}_R \,. \end{aligned} \tag{D-24}$$

Making use of the relationship

$$\nabla \cdot \left[\overline{\overline{\mathrm{I}}} F(R) \right] = \nabla F(R)$$

gives

$$\begin{aligned} \overline{I}_s &= -\int_{\tau_i} d\overline{r_0} \nabla_0 \cdot \nabla_0 \nabla_0 g_s(\overline{r}, \overline{r}_0) - \int_{\tau_i} d\overline{r_0} \nabla_0 \cdot \left[k_{sb}^2 \overline{\overline{\mathrm{I}}} g_s(\overline{r}, \overline{r}_0) \right] \\ &= -k_{sb}^2 \nabla \int_{\tau_i} d\overline{r_0} g_s(\overline{r}, \overline{r}_0) + \nabla \cdot \left[k_{sb}^2 \overline{\overline{\mathrm{I}}} \int_{\tau_i} d\overline{r_0} g_s(\overline{r}, \overline{r}_0) \right] \\ &= -k_{sb}^2 \nabla \int_{\tau_i} d\overline{r_0} g_s(\overline{r}, \overline{r}_0) + k_{sb}^2 \nabla \int_{\tau_i} d\overline{r_0} g_s(\overline{r}, \overline{r}_0) \\ &= 0 \,. \end{aligned} \tag{D-25}$$

Therefore,

$$\overline{q}_i(r) = \overline{I}_c = -\frac{i\pi a k_{cb}^2}{2} H_1^{(1)}(k_{cb} a) J_1(k_{cb} R) \overline{e}_R \,. \tag{D-26}$$

Starting from the relationships

$$\nabla \cdot [\overline{e}_R F(R)] = F'(R) + \frac{1}{R} F(R)$$

and

$$\frac{d}{dR} J_1(k_{cb} R) = k_{cb} \left[J_0(k_{cb} R) - \frac{J_1(k_{cb} R)}{k_{cb} R} \right]$$

gives

$$\nabla \cdot \overline{I}_c = -\frac{i\pi a k_{cb}^3}{2} H_1^{(1)}(k_{cb}a) J_0(k_{cb}R). \tag{D-27}$$

Therefore,

$$\nabla \cdot \overline{q}_i(r) = \nabla \cdot \overline{I}_c = -\frac{i\pi a k_{cb}^3}{2} H_1^{(1)}(k_{cb}a) J_0(k_{cb}R), \tag{D-28}$$

where a_i is the radius of equivalent cylinder of the i-th cell.

When $R > a$, it has been shown

$$f(r) = \int_\tau d\overline{r_0} g(\overline{r}, \overline{r_0}) = \frac{i\pi a}{2k} J_1(ka) H_0^{(1)}(kR).$$

Similarly,

$$f'(r) = -\frac{i\pi a}{2} J_1(ka) H_1^{(1)}(kR),$$

$$\overline{q}_i(r) = \overline{I}_c = -\frac{i\pi a k_{cb}^2}{2} H_1^{(1)}(k_{cb}R) J_1(k_{cb}a) \overline{e}_R, \tag{D-29}$$

and

$$\nabla \cdot \overline{q}_i(r) = \nabla \cdot \overline{I}_c = -\frac{i\pi a k_{cb}^3}{2} J_1(k_{cb}a) H_0^{(1)}(k_{cb}R). \tag{D-30}$$

Appendix E: Expressions for the Derivatives of the Volume Integral of the Green's Tensor

E.1: VOLUME INTEGRAL OF THE GREEN'S TENSOR

As a first step, an explicit solution is found for the volume integral of the Green's tensor.

When $R < a$, it has been shown that

$$f(r) = \int_{\tau} d\overline{r}_0 g\left(\overline{r}, \overline{r}_0\right) = -\frac{1}{k^2} + \frac{i\pi a}{2k} H_1^{(1)}(ka) J_0(kR), \tag{E-1}$$

$$f'(r) = -\frac{i\pi a}{2} H_1^{(1)}(ka) J_1(kR), \tag{E-2}$$

and

$$f''(r) = -\frac{i\pi ak}{2} H_1^{(1)}(ka)\left(J_0(kR) - \frac{J_1(kR)}{kR}\right). \tag{E-3}$$

Making use of the two dimensional identities

$$\nabla\left[\overline{e}_r F(r)\right] = \left[F'(r) - \frac{F(r)}{r}\right]\overline{e}_r\overline{e}_r + \frac{F(r)}{r}\overline{\overline{I}}, \tag{E-4}$$

and

$$\nabla F(R) = \overline{e}_R F'(R), \tag{E-5}$$

one has

$$\nabla\nabla f(r) = \left[f''(r) - \frac{f'(r)}{r}\right]\overline{e}_R\overline{e}_R + \frac{f'(r)}{r}\overline{\overline{I}}. \tag{E-6}$$

Consequently,

$$\begin{aligned}\int_{\tau_i} d\overline{r_0}\,\overline{\overline{G}}\left(\overline{r},\overline{r_0}\right) &= \frac{1}{\rho_b\omega^2}\int_{\tau_i}\left\{-\nabla\nabla g_c\left(\overline{r},\overline{r_0}\right)+\left(k_{sb}^2\overline{\overline{I}}+\nabla\nabla\right)g_s\left(\overline{r},\overline{r_0}\right)\right\}d\overline{r_0}\\ &= -\frac{1}{\rho_b\omega^2}\nabla\nabla\int_{\tau_i} d\overline{r_0}\,g_c\left(\overline{r},\overline{r_0}\right)+\frac{1}{\rho_b\omega^2}\left(k_{sb}^2\overline{\overline{I}}+\nabla\nabla\right)\int_{\tau_i} d\overline{r_0}\,g_s\left(\overline{r},\overline{r_0}\right)\\ &= -\frac{1}{\rho_b\omega^2}\nabla\nabla f_c(r)+\frac{1}{\rho_b\omega^2}\left(k_{sb}^2\overline{\overline{I}}+\nabla\nabla\right)f_s(r)\\ &= g(r)\overline{e}_R\overline{e}_R+h(r)\overline{\overline{I}},\end{aligned} \qquad \text{(E-7)}$$

where

$$h(r)=\frac{1}{\rho_b\omega^2}\left[k_{sb}^2 f_s(r)+\frac{1}{R}f_s'(r)-\frac{1}{R}f_c'(r)\right], \qquad \text{(E-8)}$$

and

$$g(r)=\frac{1}{\rho_b\omega^2}\left[f_s''(r)-\frac{1}{R}f_s'(r)-f_c''(r)+\frac{1}{R}f_c'(r)\right]. \qquad \text{(E-9)}$$

Substitution of equations of (E-1), (E-2), and (E-3) into (E-8) and (E-9) yields

$$\begin{aligned}h(r)=&\frac{1}{2}\frac{1}{\rho_b\omega^2}i\pi a k_{cb}H_1^{(1)}\left(k_{cb}a\right)\frac{J_1\left(k_{cb}R\right)}{k_{cb}R}\\ &+\frac{1}{2}\frac{1}{\rho_b\omega^2}i\pi a k_{sb}H_1^{(1)}\left(k_{sb}a\right)\left(J_0\left(k_{sb}R\right)-\frac{J_1\left(k_{sb}R\right)}{k_{sb}R}\right)-\frac{1}{\rho_b\omega^2},\end{aligned} \qquad \text{(E-10)}$$

and

$$\begin{aligned}g(r)=&\frac{1}{2}\frac{1}{\rho_b\omega^2}i\pi a k_{cb}H_1^{(1)}\left(k_{cb}a\right)\left(J_0\left(k_{cb}R\right)-\frac{2J_1\left(k_{cb}R\right)}{k_{cb}R}\right)\\ &-\frac{1}{2}\frac{1}{\rho_b\omega^2}i\pi a k_{sb}H_1^{(1)}\left(k_{sb}a\right)\left(J_0\left(k_{sb}R\right)-\frac{2J_1\left(k_{sb}R\right)}{k_{sb}R}\right),\end{aligned} \qquad \text{(E-11)}$$

respectively.

When $R > a$, it has been shown that

$$f(r)=\int_{\tau} d\overline{r_0}\,g\left(\overline{r},\overline{r_0}\right)=\frac{i\pi a}{2k}J_1(ka)H_0^{(1)}(kR), \qquad \text{(E-12)}$$

$$f'(r) = -\frac{i\pi a}{2} J_1(ka) H_1^{(1)}(kR), \tag{E-13}$$

and

$$f''(r) = -\frac{i\pi ak}{2} J_1(ka)\left(H_0^{(1)}(kR) - \frac{H_1^{(1)}(kR)}{kR} \right). \tag{E-14}$$

Consequently,

$$\begin{aligned} h(r) = {} & \frac{1}{2}\frac{1}{\rho_b \omega^2} i\pi a k_{cb} J_1(k_{cb}a) \frac{H_1^{(1)}(k_{cb}R)}{k_{cb}R} \\ & + \frac{1}{2}\frac{1}{\rho_b \omega^2} i\pi a k_{sb} J_1(k_{sb}a) \left(H_0^{(1)}(k_{sb}R) - \frac{H_1^{(1)}(k_{sb}R)}{k_{sb}R} \right), \end{aligned} \tag{E-15}$$

and

$$\begin{aligned} g(r) = {} & \frac{1}{2}\frac{1}{\rho_b \omega^2} i\pi a k_{cb} J_1(k_{cb}a) \left(H_0^{(1)}(k_{cb}R) - \frac{2H_1^{(1)}(k_{cb}R)}{k_{cb}R} \right) \\ & - \frac{1}{2}\frac{1}{\rho_b \omega^2} i\pi a k_{sb} J_1(k_{sb}a) \left(H_0^{(1)}(k_{sb}R) - \frac{2H_1^{(1)}(k_{sb}R)}{k_{sb}R} \right), \end{aligned} \tag{E-16}$$

whereupon,

$$g_{xx} = h(r) + \frac{\Delta x^2}{R^2} g(r), \tag{E-17}$$

$$g_{xz} = g_{zx} = \frac{\Delta x \Delta z}{R^2} g(r), \tag{E-18}$$

and

$$g_{zz} = h(r) + \frac{\Delta z^2}{R^2} g(r). \tag{E-19}$$

E.2: DERIVATIVES OF THE INTEGRAL OF THE GREEN’S TENSOR

In this section, the derivatives of the functions h and g defined in equation (E-7) are obtained using the differential relationships of Bessel functions. For $R < a$, one has

$$\frac{d}{dR} J_0(kR) = -kJ_1(kR), \tag{E-20}$$

$$\frac{d}{dR} J_1(kR) = k\left[J_0(kR) - \frac{J_1(kR)}{kR} \right], \tag{E-21}$$

and

$$\begin{aligned} \frac{d}{dR}\left(\frac{J_1(kR)}{kR} \right) &= \frac{J_1'(kR)}{kR} - \frac{kJ_1(kR)}{(kR)^2} \\ &= \frac{k}{kR}\left[J_0(kR) - \frac{J_1(kR)}{kR} \right] - \frac{kJ_1(kR)}{(kR)^2} \\ &= k\left[\frac{J_0(kR)}{kR} - \frac{2J_1(kR)}{(kR)^2} \right] \qquad . \end{aligned} \tag{E-22}$$

Consequently,

$$\begin{aligned} h'(r) = {} & \frac{1}{2}\frac{1}{\rho_b \omega^2} i\pi a k_{cb}^2 H_1^{(1)}(k_{cb}a)\left(\frac{J_0(k_{cb}R)}{k_{cb}R} - \frac{2J_1(k_{cb}R)}{(k_{cb}R)^2} \right) \\ & + \frac{1}{2}\frac{1}{\rho_b \omega^2} i\pi a k_{sb}^2 H_1^{(1)}(k_{sb}a)\left(-\frac{J_0(k_{sb}R)}{k_{sb}R} + \frac{2J_1(k_{sb}R)}{(k_{sb}R)^2} - J_1(k_{sb}R) \right), \end{aligned} \tag{E-23}$$

and

$$\begin{aligned} g'(r) = {} & \frac{1}{2}\frac{1}{\rho_b \omega^2} i\pi a k_{cb}^2 H_1^{(1)}(k_{cb}a)\left(-\frac{2J_0(k_{cb}R)}{k_{cb}R} + \frac{4J_1(k_{cb}R)}{(k_{cb}R)^2} - J_1(k_{cb}R) \right) \\ & - \frac{1}{2}\frac{1}{\rho_b \omega^2} i\pi a k_{sb}^2 H_1^{(1)}(k_{sb}a)\left(-\frac{2J_0(k_{sb}R)}{k_{sb}R} + \frac{4J_1(k_{sb}R)}{(k_{sb}R)^2} - J_1(k_{sb}R) \right) . \end{aligned} \tag{E-24}$$

In order to obtain the second-order derivatives of the functions $h(r)$ and $g(r)$, one makes use of the following relationships

$$\frac{d}{dR}\left(\frac{J_0(kR)}{kR}\right)=\frac{J_0'(kR)}{kR}-\frac{kJ_0(kR)}{(kR)^2}$$

$$=k\left[-\frac{J_1(kR)}{kR}-\frac{J_0(kR)}{(kR)^2}\right], \tag{E-25}$$

and

$$\frac{d}{dR}\left(\frac{J_1(kR)}{(kR)^2}\right)=\frac{J_1'(kR)}{(kR)^2}-\frac{2kJ_1(kR)}{(kR)^3}$$

$$=k\left[\frac{J_0(kR)}{(kR)^2}-\frac{3J_1(kR)}{(kR)^3}\right]. \tag{E-26}$$

Substitution of equations (E-25) and (E-26) into the expression of the second derivatives of the functions $h(r)$ and $g(r)$ yields

$$\begin{aligned}h''(r)=&\frac{1}{2}\frac{1}{\rho_b\omega^2}i\pi a k_{cb}^3 H_1^{(1)}(k_{cb}a)\left(-\frac{3J_0(k_{cb}R)}{(k_{cb}R)^2}-\frac{J_1(k_{cb}R)}{k_{cb}R}+\frac{6J_1(k_{cb}R)}{(k_{cb}R)^3}\right)\\&+\frac{1}{2}\frac{1}{\rho_b\omega^2}i\pi a k_{sb}^3 H_1^{(1)}(k_{sb}a)\left(-J_0(k_{sb}R)+\frac{3J_0(k_{sb}R)}{(k_{sb}R)^2}+\frac{2J_1(k_{sb}R)}{k_{sb}R}-\frac{6J_1(k_{sb}R)}{(k_{sb}R)^3}\right),\end{aligned} \tag{E-27}$$

and

$$\begin{aligned}g''(r)=&\frac{1}{2}\frac{1}{\rho_b\omega^2}i\pi a k_{cb}^3 H_1^{(1)}(k_{cb}a)\left(-J_0(k_{cb}R)+\frac{6J_0(k_{cb}R)}{(k_{cb}R)^2}+\frac{3J_1(k_{cb}R)}{k_{cb}R}-\frac{12J_1(k_{cb}R)}{(k_{cb}R)^3}\right)\\&-\frac{1}{2}\frac{1}{\rho_b\omega^2}i\pi a k_{sb}^3 H_1^{(1)}(k_{sb}a)\left(-J_0(k_{sb}R)+\frac{6J_0(k_{sb}R)}{(k_{sb}R)^2}+\frac{3J_1(k_{sb}R)}{k_{sb}R}-\frac{12J_1(k_{sb}R)}{(k_{sb}R)^3}\right)\ .\end{aligned} \tag{E-28}$$

Similarly, when $R>a$, one has

$$\begin{aligned}h'(r)=&\frac{1}{2}\frac{1}{\rho_b\omega^2}i\pi a k_{cb}^2 J_1(k_{cb}a)\left(\frac{H_0^{(1)}(k_{cb}R)}{k_{cb}R}-\frac{2H_1^{(1)}(k_{cb}R)}{(k_{cb}R)^2}\right)\\&+\frac{1}{2}\frac{1}{\rho_b\omega^2}i\pi a k_{sb}^2 J_1(k_{sb}a)\left(-\frac{H_0^{(1)}(k_{sb}R)}{k_{sb}R}+\frac{2H_1^{(1)}(k_{sb}R)}{(k_{sb}R)^2}-H_1^{(1)}(k_{sb}R)\right),\end{aligned} \tag{E-29}$$

$$g'(r)=\frac{1}{2}\frac{1}{\rho_b\omega^2}i\pi a k_{cb}^2 J_1(k_{cb}a)\left(-\frac{2H_0^{(1)}(k_{cb}R)}{k_{cb}R}+\frac{4H_1^{(1)}(k_{cb}R)}{(k_{cb}R)^2}-H_1^{(1)}(k_{cb}R)\right)$$
$$-\frac{1}{2}\frac{1}{\rho_b\omega^2}i\pi a k_{sb}^2 J_1(k_{sb}a)\left(-\frac{2H_0^{(1)}(k_{sb}R)}{k_{sb}R}+\frac{4H_1^{(1)}(k_{sb}R)}{(k_{sb}R)^2}-H_1^{(1)}(k_{sb}R)\right), \quad \text{(E-30)}$$

$$h''(r)=\frac{1}{2}\frac{1}{\rho_b\omega^2}i\pi a k_{cb}^3 J_1(k_{cb}a)\left(-\frac{3H_0^{(1)}(k_{cb}R)}{(k_{cb}R)^2}-\frac{H_1^{(1)}(k_{cb}R)}{k_{cb}R}+\frac{6H_1^{(1)}(k_{cb}R)}{(k_{cb}R)^3}\right)$$
$$+\frac{1}{2}\frac{1}{\rho_b\omega^2}i\pi a k_{sb}^3 J_1(k_{sb}a)\left(-H_0^{(1)}(k_{sb}R)+\frac{3H_0^{(1)}(k_{sb}R)}{(k_{sb}R)^2}+\frac{2H_1^{(1)}(k_{sb}R)}{k_{sb}R}-\frac{6H_1^{(1)}(k_{sb}R)}{(k_{sb}R)^3}\right),$$

(E-31)

and

$$g''(r)=\frac{1}{2}\frac{1}{\rho_b\omega^2}i\pi a k_{cb}^3 J_1(k_{cb}a)\left(-H_0^{(1)}(k_{cb}R)+\frac{6H_0^{(1)}(k_{cb}R)}{(k_{cb}R)^2}+\frac{3H_1^{(1)}(k_{cb}R)}{k_{cb}R}-\frac{12H_1^{(1)}(k_{cb}R)}{(k_{cb}R)^3}\right)$$
$$-\frac{1}{2}\frac{1}{\rho_b\omega^2}i\pi a k_{sb}^3 J_1(k_{sb}a)\left(-H_0^{(1)}(k_{sb}R)+\frac{6H_0^{(1)}(k_{sb}R)}{(k_{sb}R)^2}+\frac{3H_1^{(1)}(k_{sb}R)}{k_{sb}R}-\frac{12H_1^{(1)}(k_{sb}R)}{(k_{sb}R)^3}\right).$$

(E-32)

The second step of the derivation consists of obtaining explicit expressions for the derivatives of the integral of the Green's tensor. This is done as follows. Start with

$$\nabla\overline{\overline{\Lambda}}=\nabla\int_\tau\overline{\overline{G}}(\bar{r},\bar{r}_0)d\bar{r}_0=\nabla\left(h(r)\overline{\overline{\mathrm{I}}}\right)+\nabla\left(g(r)\bar{e}_R\bar{e}_R\right). \quad \text{(E-33)}$$

By making use of the relationship $\nabla\left(u\overline{\overline{U}}\right)=(\nabla u)\overline{\overline{U}}+u\nabla\overline{\overline{U}}$, one obtains

$$\nabla\left(u\overline{\overline{I}}\right)=(\nabla u)\overline{\overline{I}}+u\nabla\overline{\overline{I}}=(\nabla u)\overline{\overline{I}}, \quad \text{(E-34)}$$

and

$$\nabla\overline{\overline{\Lambda}}=\nabla(h(r))\overline{\overline{\mathrm{I}}}+\nabla(g(r))\bar{e}_R\bar{e}_R+g(r)\nabla\left(\bar{e}_R\bar{e}_R\right). \quad \text{(E-35)}$$

From the relationship $\nabla\left(\bar{f}\bar{g}\right)=\nabla\left(\bar{f}\right)\bar{g}+\left(\bar{f}\nabla\bar{g}\right)^{213}$, and $\left(\bar{a}\bar{b}\bar{c}\right)^{213}=\bar{b}\bar{a}\bar{c}$, one obtains

$$\nabla\left(\bar{e}_R\bar{e}_R\right)=\nabla\left(\bar{e}_R\right)\bar{e}_R+\left(\bar{e}_R\nabla\bar{e}_R\right)^{213}. \quad \text{(E-36)}$$

It can be proved that in two or three dimensions,

$$\nabla\overline{R} = \overline{\overline{I}}\,. \tag{E-37}$$

Recall that $\nabla\left(u\overline{f}\right) = u\nabla\left(\overline{f}\right) + \left(\nabla u\right)\overline{f}$ and $\nabla F(R) = F'(R)\overline{e}_R$, whereupon,

$$\begin{aligned}
\nabla\overline{e}_R &= \nabla\left(\frac{\overline{R}}{R}\right) = \nabla\left(\frac{1}{R}\right)\overline{R} + \frac{1}{R}\nabla\overline{R} \\
&= -\frac{1}{R^2}\overline{e}_R\overline{R} + \frac{1}{R}\overline{\overline{I}} \\
&= \frac{1}{R}\left(\overline{\overline{I}} - \overline{e}_R\overline{e}_R\right).
\end{aligned} \tag{E-38}$$

Consequently,

$$\begin{aligned}
\left(\overline{e}_R\nabla\overline{e}_R\right)^{213} &= \frac{1}{R}\left(\overline{e}_R\overline{\overline{I}} - \overline{e}_R\overline{e}_R\overline{e}_R\right)^{213} \\
&= \frac{1}{R}\left(\overline{e}_R\left(\overline{e}_x\overline{e}_x + \overline{e}_y\overline{e}_y + \overline{e}_z\overline{e}_z\right) - \overline{e}_R\overline{e}_R\overline{e}_R\right)^{213} \\
&= \frac{1}{R}\left(\overline{e}_x\overline{e}_R\overline{e}_x + \overline{e}_y\overline{e}_R\overline{e}_y + \overline{e}_z\overline{e}_R\overline{e}_z - \overline{e}_R\overline{e}_R\overline{e}_R\right),
\end{aligned} \tag{E-39}$$

$$\begin{aligned}
\nabla\left(\overline{e}_R\overline{e}_R\right) &= \nabla\left(\overline{e}_R\right)\overline{e}_R + \left(\overline{e}_R\nabla\overline{e}_R\right)^{213} \\
&= \frac{1}{R}\left[\overline{\overline{I}}\overline{e}_R + \left(\overline{e}_R\overline{\overline{I}}\right)^{213} - 2\overline{e}_R\overline{e}_R\overline{e}_R\right],
\end{aligned} \tag{E-40}$$

$$\nabla h(r) = h'(r)\overline{e}_R\,, \tag{E-41}$$

and

$$\nabla g(r) = g'(r)\overline{e}_R\,. \tag{E-42}$$

Thus, in cylindrical coordinates,

$$\nabla\overline{\overline{\Lambda}} = h'(r)\overline{e}_R\overline{\overline{\mathrm{I}}} + g'(r)\overline{e}_R\overline{e}_R\overline{e}_R + \frac{g(r)}{R}\left[\overline{\overline{I}}\overline{e}_R + \left(\overline{e}_R\overline{\overline{I}}\right)^{213} - 2\overline{e}_R\overline{e}_R\overline{e}_R\right]. \tag{E-43}$$

In Cartesian coordinates, one has

$$\overline{\overline{I}} = \overline{e}_x\overline{e}_x + \overline{e}_z\overline{e}_z\,, \tag{E-44}$$

$$\bar{e}_R = \frac{1}{R}\left(\Delta x \bar{e}_x + \Delta z \bar{e}_z\right), \tag{E-45}$$

$$\bar{e}_R \bar{\bar{I}} = \frac{1}{R}\left(\Delta x \bar{e}_x \bar{e}_x \bar{e}_x + \Delta z \bar{e}_z \bar{e}_x \bar{e}_x + \Delta x \bar{e}_x \bar{e}_z \bar{e}_z + \Delta z \bar{e}_z \bar{e}_z \bar{e}_z\right), \tag{E-46}$$

$$\bar{\bar{I}} \bar{e}_R = \frac{1}{R}\left(\Delta x \bar{e}_x \bar{e}_x \bar{e}_x + \Delta z \bar{e}_x \bar{e}_x \bar{e}_z + \Delta x \bar{e}_z \bar{e}_z \bar{e}_x + \Delta z \bar{e}_z \bar{e}_z \bar{e}_z\right), \tag{E-47}$$

$$\begin{aligned}\left(\bar{e}_R \bar{\bar{I}}\right)^{213} &= \bar{e}_x \bar{e}_R \bar{e}_x + \bar{e}_z \bar{e}_R \bar{e}_z \\ &= \frac{1}{R}\left(\Delta x \bar{e}_x \bar{e}_x \bar{e}_x + \Delta z \bar{e}_x \bar{e}_x \bar{e}_z + \Delta x \bar{e}_z \bar{e}_z \bar{e}_x + \Delta z \bar{e}_z \bar{e}_z \bar{e}_z\right),\end{aligned} \tag{E-48}$$

$$\begin{aligned}\bar{e}_R \bar{e}_R \bar{e}_R &= \frac{1}{R^3}\left(\Delta x \bar{e}_x + \Delta z \bar{e}_z\right)\left(\Delta x \bar{e}_x + \Delta z \bar{e}_z\right)\left(\Delta x \bar{e}_x + \Delta z \bar{e}_z\right) \\ &= \frac{1}{R^3}\left(\Delta x^2 \bar{e}_x \bar{e}_x + \Delta x \Delta z \bar{e}_x \bar{e}_z + \Delta z \Delta x \bar{e}_z \bar{e}_x + \Delta z^2 \bar{e}_z \bar{e}_z\right)\left(\Delta x \bar{e}_x + \Delta z \bar{e}_z\right) \\ &= \frac{1}{R^3}\left(\Delta x^3 \bar{e}_x \bar{e}_x \bar{e}_x + \Delta x^2 \Delta z \bar{e}_x \bar{e}_x \bar{e}_z + \Delta x^2 \Delta z \bar{e}_x \bar{e}_z \bar{e}_x + \Delta x \Delta z^2 \bar{e}_x \bar{e}_z \bar{e}_z \right. \\ &\quad \left. + \Delta x^2 \Delta z \bar{e}_z \bar{e}_x \bar{e}_x + \Delta z^2 \Delta x \bar{e}_z \bar{e}_x \bar{e}_z + \Delta z^2 \Delta x \bar{e}_z \bar{e}_z \bar{e}_x + \Delta z^3 \bar{e}_z \bar{e}_z \bar{e}_z\right)\end{aligned} ,\tag{E-49}$$

and

$$\begin{aligned}\nabla \bar{\bar{\Lambda}} &= \left(\bar{e}_x \frac{\partial}{\partial x} + \bar{e}_z \frac{\partial}{\partial z}\right)\left(g_{xx} \bar{e}_x \bar{e}_x + g_{xz} \bar{e}_x \bar{e}_z + g_{zx} \bar{e}_z \bar{e}_x + g_{zz} \bar{e}_z \bar{e}_z\right) \\ &= g_{xx,x} \bar{e}_x \bar{e}_x \bar{e}_x + g_{xz,x} \bar{e}_x \bar{e}_x \bar{e}_z + g_{zx,x} \bar{e}_x \bar{e}_z \bar{e}_x + g_{zz,x} \bar{e}_x \bar{e}_z \bar{e}_z \\ &\quad + g_{xx,z} \bar{e}_z \bar{e}_x \bar{e}_x + g_{xz,z} \bar{e}_z \bar{e}_x \bar{e}_z + g_{zx,z} \bar{e}_z \bar{e}_z \bar{e}_x + g_{zz,z} \bar{e}_z \bar{e}_z \bar{e}_z \quad .\end{aligned} \tag{E-50}$$

By comparing the two equations (E-43) and (E-50) and by collecting the corresponding terms yields

$$g_{xx,x} = \frac{\Delta x}{R} h' + \frac{\Delta x^3}{R^3} g' + 2\left(\frac{\Delta x}{R^2} - \frac{\Delta x^3}{R^4}\right) g, \tag{E-51}$$

$$g_{zz,z} = \frac{\Delta z}{R} h' + \frac{\Delta z^3}{R^3} g' + 2\left(\frac{\Delta z}{R^2} - \frac{\Delta z^3}{R^4}\right) g, \tag{E-52}$$

$$g_{xx,z} = \frac{\Delta z}{R} h' + \frac{\Delta x^2 \Delta z}{R^3} g' - \frac{2\Delta x^2 \Delta z}{R^4} g, \tag{E-53}$$

$$g_{zz,x} = \frac{\Delta x}{R} h' + \frac{\Delta z^2 \Delta x}{R^3} g' - \frac{2\Delta z^2 \Delta x}{R^4} g \,, \tag{E-54}$$

$$g_{xz,x} = g_{zx,x} = \frac{\Delta x^2 \Delta z}{R^3} g' + \left(\frac{\Delta z}{R^2} - \frac{2\Delta x^2 \Delta z}{R^4} \right) g \,, \tag{E-55}$$

and

$$g_{xz,z} = g_{zx,z} = \frac{\Delta z^2 \Delta x}{R^3} g' + \left(\frac{\Delta x}{R^2} - \frac{2\Delta z^2 \Delta x}{R^4} \right) g \,. \tag{E-56}$$

In what follows, auxiliary expressions are derived prior to obtaining expressions for the second-order derivatives of the integral of the Green's tensor.

Recall that

$$\frac{\partial R}{\partial x} = \frac{\Delta x}{R} \,, \tag{E-57}$$

$$\frac{\partial f(R)}{\partial x} = \frac{\partial R}{\partial x} \frac{df(R)}{dR} = \frac{\Delta x}{R} f'(R), \tag{E-58}$$

and

$$\frac{\partial}{\partial x} \frac{1}{R^n} = \frac{\partial R}{\partial x} \frac{-n}{R^{n+1}} = \frac{-n\Delta x}{R^{n+2}} \,. \tag{E-59}$$

Similar equations follow for the derivative with respect to z.

For the second-order derivatives, one makes use of the symmetry properties of the Green's integral to obtain the expressions

$$\begin{aligned} g_{xx,xx} = {} & \left(1 - \frac{\Delta x^2}{R^2}\right) \frac{h'}{R} + \frac{\Delta x^2}{R^2} h'' \\ & + \left(1 - \frac{5\Delta x^2}{R^2} + \frac{4\Delta x^4}{R^4}\right) \frac{2g}{R^2} + 5\left(\frac{\Delta x^2}{R^2} - \frac{\Delta x^4}{R^4}\right) \frac{g'}{R} + \frac{\Delta x^4}{R^4} g'' \,, \end{aligned} \tag{E-60}$$

$$\begin{aligned} g_{xx,xz} &= -\frac{\Delta x\Delta z}{R^2}\frac{h'}{R} + \frac{\Delta x\Delta z}{R^2}h'' \\ &\quad + \left(-\frac{2\Delta x\Delta z}{R^2} + \frac{4\Delta x^3\Delta z}{R^4}\right)\frac{2g}{R^2} + \left(\frac{2\Delta x\Delta z}{R^2} - \frac{5\Delta x^3\Delta z}{R^4}\right)\frac{g'}{R} + \frac{\Delta x^3\Delta z}{R^4}g'', \end{aligned} \tag{E-61}$$

$$g_{xx,zx} = g_{xx,xz}, \tag{E-62}$$

$$\begin{aligned} g_{xx,zz} &= \left(1 - \frac{\Delta z^2}{R^2}\right)\frac{h'}{R} + \frac{\Delta z^2}{R^2}h'' \\ &\quad + \left(-\frac{\Delta x^2}{R^2} + \frac{4\Delta x^2\Delta z^2}{R^4}\right)\frac{2g}{R^2} + \left(\frac{\Delta x^2}{R^2} - \frac{5\Delta x^2\Delta z^2}{R^4}\right)\frac{g'}{R} + \frac{\Delta x^2\Delta z^2}{R^4}g'', \end{aligned} \tag{E-63}$$

$$\begin{aligned} g_{zz,zz} &= \left(1 - \frac{\Delta z^2}{R^2}\right)\frac{h'}{R} + \frac{\Delta z^2}{R^2}h'' \\ &\quad + \left(1 - \frac{5\Delta z^2}{R^2} + \frac{4\Delta z^4}{R^4}\right)\frac{2g}{R^2} + 5\left(\frac{\Delta z^2}{R^2} - \frac{\Delta z^4}{R^4}\right)\frac{g'}{R} + \frac{\Delta z^4}{R^4}g'', \end{aligned} \tag{E-64}$$

$$\begin{aligned} g_{zz,xz} &= -\frac{\Delta x\Delta z}{R^2}\frac{h'}{R} + \frac{\Delta x\Delta z}{R^2}h'' \\ &\quad + \left(-\frac{2\Delta x\Delta z}{R^2} + \frac{4\Delta x\Delta z^3}{R^4}\right)\frac{2g}{R^2} + \left(\frac{2\Delta x\Delta z}{R^2} - \frac{5\Delta x\Delta z^3}{R^4}\right)\frac{g'}{R} + \frac{\Delta x\Delta z^3}{R^4}g'', \end{aligned} \tag{E-65}$$

$$g_{zz,zx} = g_{zz,xz}, \tag{E-66}$$

$$\begin{aligned} g_{zz,xx} &= \left(1 - \frac{\Delta x^2}{R^2}\right)\frac{h'}{R} + \frac{\Delta x^2}{R^2}h'' \\ &\quad + \left(-\frac{\Delta z^2}{R^2} + \frac{4\Delta x^2\Delta z^2}{R^4}\right)\frac{2g}{R^2} + \left(\frac{\Delta z^2}{R^2} - \frac{5\Delta x^2\Delta z^2}{R^4}\right)\frac{g'}{R} + \frac{\Delta x^2\Delta z^2}{R^4}g'', \end{aligned} \tag{E-67}$$

$$g_{xz,xx} = \left(-\frac{3\Delta x\Delta z}{R^2} + \frac{4\Delta x^3\Delta z}{R^4}\right)\frac{2g}{R^2} + \left(\frac{3\Delta x\Delta z}{R^2} - \frac{5\Delta x^3\Delta z}{R^4}\right)\frac{g'}{R} + \frac{\Delta x^3\Delta z}{R^4}g'', \tag{E-68}$$

$$g_{xz,zz} = \left(-\frac{3\Delta x\Delta z}{R^2} + \frac{4\Delta x\Delta z^3}{R^4}\right)\frac{2g}{R^2} + \left(\frac{3\Delta x\Delta z}{R^2} - \frac{5\Delta x\Delta z^3}{R^4}\right)\frac{g'}{R} + \frac{\Delta x\Delta z^3}{R^4}g'', \tag{E-69}$$

$$g_{xz,xz} = \left(-\frac{1}{2} + \frac{4\Delta x^2\Delta z^2}{R^4}\right)\frac{2g}{R^2} + \left(1 - \frac{5\Delta x^2\Delta z^2}{R^4}\right)\frac{g'}{R} + \frac{\Delta x^2\Delta z^2}{R^4}g'', \tag{E-70}$$

$$g_{xz,zx} = g_{xz,xz}\,, \tag{E-71}$$

$$g_{zx,zx} = g_{xz,zx}\,, \tag{E-72}$$

$$g_{zx,xz} = g_{xz,zx}\,, \tag{E-73}$$

$$g_{zx,xx} = g_{xz,xx}\,, \tag{E-74}$$

and

$$g_{zx,zz} = g_{xz,zz}\,. \tag{E-75}$$

By definition,

$$R^2 = \Delta x^2 + \Delta z^2\,. \tag{E-76}$$

Therefore,

$$\begin{aligned} g_{xx,xz} + g_{xz,xx} &= \left(-\frac{\Delta x\Delta z}{R^2}\right)\frac{h'}{R} + \frac{\Delta x\Delta z}{R^2}h'' \\ &\quad + \frac{\Delta x\Delta z}{R^2}\left(\frac{8\Delta x^2}{R^2} - 5\right)\frac{2g}{R^2} + \frac{5\Delta x\Delta z}{R^2}\left(1 - \frac{2\Delta x^2}{R^2}\right)\frac{g'}{R} + \frac{2\Delta x^3\Delta z}{R^4}g'' \\ &= \frac{\Delta x\Delta z}{R^2}\left(h'' - \frac{h'}{R} + 5\cdot\frac{g'}{R} - 5\cdot\frac{2g}{R^2}\right) + \frac{2\Delta x^3\Delta z}{R^4}\left(4\cdot\frac{2g}{R^2} - 5\cdot\frac{g'}{R} + g''\right), \end{aligned} \tag{E-77}$$

$$\begin{aligned} g_{xx,zz} + g_{zz,xx} + g_{zx,xz} + g_{zx,xz} &= h'' + \frac{h'}{R} \\ &\quad + \left(\frac{8\Delta x^2\Delta z^2}{R^4} - 1\right)\frac{2g}{R^2} + \left(1 - \frac{10\Delta x^2\Delta z^2}{R^4}\right)\frac{g'}{R} + \frac{2\Delta x^2\Delta z^2}{R^4}g'' \\ &\quad + \left(\frac{8\Delta x^2\Delta z^2}{R^4} - 1\right)\frac{2g}{R^2} + \left(2 - \frac{10\Delta x^2\Delta z^2}{R^4}\right)\frac{g'}{R} + \frac{2\Delta x^2\Delta z^2}{R^4}g'' \\ &= h'' + \frac{h'}{R} + 3\cdot\frac{g'}{R} - 2\cdot\frac{2g}{R^2} + \frac{4\Delta x^2\Delta z^2}{R^4}\left(4\cdot\frac{2g}{R^2} - 5\cdot\frac{g'}{R} + g''\right), \end{aligned} \tag{E-78}$$

and

$$g_{zx,zz}+g_{zz,zx}=\left(-\frac{\Delta x\Delta z}{R^2}\right)\frac{h'}{R}+\frac{\Delta x\Delta z}{R^2}h''$$

$$+\frac{\Delta x\Delta z}{R^2}\left(\frac{8\Delta z^2}{R^2}-5\right)\frac{2g}{R^2}+\frac{5\Delta x\Delta z}{R^2}\left(1-\frac{2\Delta z^2}{R^2}\right)\frac{g'}{R}+\frac{2\Delta z^3\Delta x}{R^4}g''$$

$$=\frac{\Delta x\Delta z}{R^2}\left(h''-\frac{h'}{R}+5\cdot\frac{g'}{R}-5\cdot\frac{2g}{R^2}\right)+\frac{2\Delta x\Delta z^3}{R^4}\left(4\cdot\frac{2g}{R^2}-5\cdot\frac{g'}{R}+g''\right). \tag{E-79}$$

E.3: SELF-CELL CONTRIBUTION

In the method of moments formulation, one needs to calculate the self-cell contribution. To do so, the asymptotic solutions for the coefficients of the linear system of equations need to be obtained when the distance between two cells approaches zero.

The Taylor series expansions of the zero- and first-order Bessel functions are

$$J_0(x)=1-\frac{x^2}{4}+\frac{1}{4}\left(\frac{x}{2}\right)^4-\ldots\quad , \tag{E-80}$$

and

$$J_1(x)=\frac{x}{2}-\frac{x^3}{16}+\frac{1}{12}\left(\frac{x}{2}\right)^5-\ldots\ , \tag{E-81}$$

respectively.

Therefore, in the limit when x tends zero, one has

$$J_0(x)=1-\frac{x^2}{4}+O\left(x^4\right), \tag{E-82}$$

$$J_1(x)=\frac{x}{2}-\frac{x^3}{16}+O\left(x^5\right), \tag{E-83}$$

and

$$\frac{J_1(x)}{x}=\frac{1}{2}-\frac{x^2}{16}+O\left(x^4\right). \tag{E-84}$$

For $R < a$, one has

$$
\begin{aligned}
h(r) &= \frac{1}{2}\frac{1}{\rho_b\omega^2} i\pi a k_{cb} H_1^{(1)}(k_{cb}a)\frac{J_1(k_{cb}R)}{k_{cb}R} \\
&\quad + \frac{1}{2}\frac{1}{\rho_b\omega^2} i\pi a k_{sb} H_1^{(1)}(k_{sb}a)\left(J_0(k_{sb}R) - \frac{J_1(k_{sb}R)}{k_{sb}R}\right) - \frac{1}{\rho_b\omega^2} \\
&= \frac{1}{2}\frac{1}{\rho_b\omega^2} i\pi a k_{cb} H_1^{(1)}(k_{cb}a)\left(\frac{1}{2} - \frac{(k_{cb}R)^2}{16} + O(k_{cb}R)^4 \right) \\
&\quad + \frac{1}{2}\frac{1}{\rho_b\omega^2} i\pi a k_{sb} H_1^{(1)}(k_{sb}a)\left(\frac{1}{2} - \frac{3(k_{sb}R)^2}{16} + O(k_{sb}R)^4 \right) - \frac{1}{\rho_b\omega^2} \\
&= -\frac{1}{\rho_b\omega^2} + \frac{1}{2}\frac{1}{\rho_b\omega^2} i\pi a k_{cb} H_1^{(1)}(k_{cb}a)\left(\frac{1}{2} - \frac{(k_{cb}R)^2}{16} \right) \\
&\quad + \frac{1}{2}\frac{1}{\rho_b\omega^2} i\pi a k_{sb} H_1^{(1)}(k_{sb}a)\left(\frac{1}{2} - \frac{3(k_{sb}R)^2}{16} \right) + O(R)^4
\end{aligned}
\quad , \qquad \text{(E-85)}
$$

and

$$
\begin{aligned}
g(r) &= \frac{1}{2}\frac{1}{\rho_b\omega^2} i\pi a k_{cb} H_1^{(1)}(k_{cb}a)\left(J_0(k_{cb}R) - \frac{2J_1(k_{cb}R)}{k_{cb}R}\right) \\
&\quad - \frac{1}{2}\frac{1}{\rho_b\omega^2} i\pi a k_{sb} H_1^{(1)}(k_{sb}a)\left(J_0(k_{sb}R) - \frac{2J_1(k_{sb}R)}{k_{sb}R}\right) \\
&= \frac{1}{2}\frac{1}{\rho_b\omega^2} i\pi a k_{cb} H_1^{(1)}(k_{cb}a)\left(-\frac{(k_{cb}R)^2}{8} \right) \\
&\quad - \frac{1}{2}\frac{1}{\rho_b\omega^2} i\pi a k_{sb} H_1^{(1)}(k_{sb}a)\left(-\frac{(k_{sb}R)^2}{8} \right) + O(R)^4
\end{aligned}
\quad . \qquad \text{(E-86)}
$$

Therefore,

$$
\lim_{R\to 0} h(r) = -\frac{1}{\rho_b\omega^2} + \frac{1}{4}\frac{1}{\rho_b\omega^2} i\pi a k_{cb} H_1^{(1)}(k_{cb}a) + \frac{1}{4}\frac{1}{\rho_b\omega^2} i\pi a k_{sb} H_1^{(1)}(k_{sb}a), \qquad \text{(E-87)}
$$

$$
\lim_{R\to 0} g(r) = 0, \qquad \text{(E-88)}
$$

$$
\frac{2g(r)}{R^2} = \frac{1}{\rho_b\omega^2} i\pi a k_{cb}^3 H_1^{(1)}(k_{cb}a)\left(-\frac{1}{8}\right) - \frac{1}{\rho_b\omega^2} i\pi a k_{sb}^3 H_1^{(1)}(k_{sb}a)\left(-\frac{1}{8}\right) + O(R)^2, \qquad \text{(E-89)}
$$

and

$$\lim_{R\to 0}\frac{2g(r)}{R^2}=-\frac{1}{8}\frac{1}{\rho_b\omega^2}i\pi a k_{cb}^3 H_1^{(1)}(k_{cb}a)+\frac{1}{8}\frac{1}{\rho_b\omega^2}i\pi a k_{sb}^3 H_1^{(1)}(k_{sb}a). \qquad \text{(E-90)}$$

The first-order derivatives can be written in an expansion form as

$$\begin{aligned}h'(r)&=\frac{1}{2}\frac{1}{\rho_b\omega^2}i\pi a k_{cb}^2 H_1^{(1)}(k_{cb}a)\left(-\frac{(k_{cb}R)}{8}\right)\\&\quad+\frac{1}{2}\frac{1}{\rho_b\omega^2}i\pi a k_{sb}^2 H_1^{(1)}(k_{sb}a)\left(-\frac{3(k_{sb}R)}{8}\right)+O(R)^3,\end{aligned} \qquad \text{(E-91)}$$

$$\begin{aligned}g'(r)&=\frac{1}{2}\frac{1}{\rho_b\omega^2}i\pi a k_{cb}^2 H_1^{(1)}(k_{cb}a)\left(-\frac{(k_{cb}R)}{4}\right)\\&\quad-\frac{1}{2}\frac{1}{\rho_b\omega^2}i\pi a k_{sb}^2 H_1^{(1)}(k_{sb}a)\left(-\frac{(k_{sb}R)}{4}\right)+O(R)^3,\end{aligned} \qquad \text{(E-92)}$$

$$\begin{aligned}\frac{h'(r)}{R}&=\frac{1}{2}\frac{1}{\rho_b\omega^2}i\pi a k_{cb}^3 H_1^{(1)}(k_{cb}a)\left(-\frac{1}{8}\right)\\&\quad+\frac{1}{2}\frac{1}{\rho_b\omega^2}i\pi a k_{sb}^3 H_1^{(1)}(k_{sb}a)\left(-\frac{3}{8}\right)+O(R)^2.\end{aligned} \qquad \text{(E-93)}$$

and

$$\begin{aligned}\frac{g'(r)}{R}&=\frac{1}{2}\frac{1}{\rho_b\omega^2}i\pi a k_{cb}^3 H_1^{(1)}(k_{cb}a)\left(-\frac{1}{4}\right)\\&\quad-\frac{1}{2}\frac{1}{\rho_b\omega^2}i\pi a k_{sb}^3 H_1^{(1)}(k_{sb}a)\left(-\frac{1}{4}\right)+O(R)^2.\end{aligned} \qquad \text{(E-94)}$$

It follows that

$$\lim_{R\to 0}\frac{h'(r)}{R}=-\frac{1}{16}\frac{1}{\rho_b\omega^2}i\pi a k_{cb}^3 H_1^{(1)}(k_{cb}a)-\frac{3}{16}\frac{1}{\rho_b\omega^2}i\pi a k_{sb}^3 H_1^{(1)}(k_{sb}a), \qquad \text{(E-95)}$$

and

$$\lim_{R\to 0}\frac{g'(r)}{R}=-\frac{1}{8}\frac{1}{\rho_b\omega^2}i\pi a k_{cb}^3 H_1^{(1)}(k_{cb}a)+\frac{1}{8}\frac{1}{\rho_b\omega^2}i\pi a k_{sb}^3 H_1^{(1)}(k_{sb}a). \qquad \text{(E-96)}$$

The second-order derivatives can be written in an expansion form as

$$h''(r) = \frac{1}{2}\frac{1}{\rho_b\omega^2} i\pi a k_{cb}^3 H_1^{(1)}(k_{cb}a)\left(-\frac{1}{8}\right) + \frac{1}{2}\frac{1}{\rho_b\omega^2} i\pi a k_{sb}^3 H_1^{(1)}(k_{sb}a)\left(-\frac{3}{8}\right) + O(R)^2, \tag{E-97}$$

and

$$g''(r) = \frac{1}{2}\frac{1}{\rho_b\omega^2} i\pi a k_{cb}^3 H_1^{(1)}(k_{cb}a)\left(-\frac{1}{4}\right) - \frac{1}{2}\frac{1}{\rho_b\omega^2} i\pi a k_{sb}^3 H_1^{(1)}(k_{sb}a)\left(-\frac{1}{4}\right) + O(R)^2, \tag{E-98}$$

It follows that

$$\lim_{R\to 0} h''(r) = -\frac{1}{16}\frac{1}{\rho_b\omega^2} i\pi a k_{cb}^3 H_1^{(1)}(k_{cb}a) - \frac{3}{16}\frac{1}{\rho_b\omega^2} i\pi a k_{sb}^3 H_1^{(1)}(k_{sb}a)\ . \tag{E-99}$$

and

$$\lim_{R\to 0} g''(r) = -\frac{1}{8}\frac{1}{\rho_b\omega^2} i\pi a k_{cb}^3 H_1^{(1)}(k_{cb}a) + \frac{1}{8}\frac{1}{\rho_b\omega^2} i\pi a k_{sb}^3 H_1^{(1)}(k_{sb}a). \tag{E-100}$$

By making use of the equations (E-94), (E-95), (E-99), and (E-100), one obtains

$$\lim_{R\to 0}\frac{2g}{R^2} = \lim_{R\to 0}\frac{g'}{R} = \lim_{R\to 0} g'', \tag{E-101}$$

and

$$\lim_{R\to 0}\frac{h'}{R} = \lim_{R\to 0} h''. \tag{E-102}$$

By definition

$$R = \sqrt{\Delta x^2 + \Delta z^2}\ , \tag{E-103}$$

whereupon

$$-1 \le \left(\frac{\Delta x}{R}\right)^n \le 1,\ -1 \le \lim_{R\to 0}\left(\frac{\Delta x}{R}\right)^n \le 1, \text{ and } -1 \le \lim_{R\to 0}\frac{\Delta x^m \Delta z^n}{R^{m+n}} \le 1, \tag{E-104}$$

where the variables *m* and *n* are positive integers.

From the above results, it follows that, in the limit as R approaches zero, one has

$$\begin{aligned}\lim_{R\to 0} g_{xx} &= \lim_{R\to 0} h + \lim_{R\to 0} \frac{\Delta x^2}{R^2} \cdot \lim_{R\to 0} g \\ &= \lim_{R\to 0} h + \lim_{R\to 0} \frac{\Delta x^2}{R^2} \cdot 0 \\ &= -\frac{1}{\rho_b \omega^2} + \frac{1}{4} \frac{1}{\rho_b \omega^2} i\pi a k_{cb} H_1^{(1)}\left(k_{cb} a\right) + \frac{1}{4} \frac{1}{\rho_b \omega^2} i\pi a k_{sb} H_1^{(1)}\left(k_{sb} a\right),\end{aligned} \quad \text{(E-105)}$$

$$\begin{aligned}\lim_{R\to 0} g_{zz} &= \lim_{R\to 0} h + \lim_{R\to 0} \frac{\Delta z^2}{R^2} \cdot \lim_{R\to 0} g \\ &= \lim_{R\to 0} h + \lim_{R\to 0} \frac{\Delta z^2}{R^2} \cdot 0 \\ &= -\frac{1}{\rho_b \omega^2} + \frac{1}{4} \frac{1}{\rho_b \omega^2} i\pi a k_{cb} H_1^{(1)}\left(k_{cb} a\right) + \frac{1}{4} \frac{1}{\rho_b \omega^2} i\pi a k_{sb} H_1^{(1)}\left(k_{sb} a\right),\end{aligned} \quad \text{(E-106)}$$

$$\begin{aligned}\lim_{R\to 0} g_{zx} &= \lim_{R\to 0} g_{xz} = \lim_{R\to 0} \frac{\Delta x \Delta z}{R^2} \cdot \lim_{R\to 0} g \\ &= 0\end{aligned} \quad , \qquad \text{(E-107)}$$

and

$$\begin{aligned}\lim_{R\to 0} g_{xx,x} &= \lim_{R\to 0} \frac{\Delta x}{R} \cdot \lim_{R\to 0} h' + \lim_{R\to 0} \frac{\Delta x^3}{R^3} \cdot \lim_{R\to 0} g' + 2 \lim_{R\to 0} \left(\frac{\Delta x}{R} - \frac{\Delta x^3}{R^3} \right) \cdot \lim_{R\to 0} \frac{g}{R} \\ &= \lim_{R\to 0} \frac{\Delta x}{R} \cdot 0 + \lim_{R\to 0} \frac{\Delta x^3}{R^3} \cdot 0 + 2 \lim_{R\to 0} \left(\frac{\Delta x}{R} - \frac{\Delta x^3}{R^3} \right) \cdot 0 \\ &= 0\end{aligned} \quad , \qquad \text{(E-108)}$$

Similarly,

$$\lim_{R\to 0} g_{zz,z} = \lim_{R\to 0} \frac{\Delta z}{R} h' + \lim_{R\to 0} \frac{\Delta z^3}{R^3} g' + 2 \lim_{R\to 0} \left(\frac{\Delta z}{R^2} - \frac{\Delta z^3}{R^4} \right) g = 0 , \qquad \text{(E-109)}$$

$$\lim_{R\to 0} g_{xx,z} = \lim_{R\to 0} \frac{\Delta z}{R} h' + \lim_{R\to 0} \frac{\Delta x^2 \Delta z}{R^3} g' - \lim_{R\to 0} \frac{2\Delta x^2 \Delta z}{R^4} g = 0 , \qquad \text{(E-110)}$$

$$\lim_{R\to 0} g_{zz,x} = \lim_{R\to 0} \frac{\Delta x}{R} h' + \lim_{R\to 0} \frac{\Delta z^2 \Delta x}{R^3} g' - \lim_{R\to 0} \frac{2\Delta z^2 \Delta x}{R^4} g = 0 , \qquad \text{(E-111)}$$

$$\lim_{R\to 0} g_{xz,x} = \lim_{R\to 0} g_{zx,x} = \lim_{R\to 0}\frac{\Delta x^2 \Delta z}{R^3} g' + \lim_{R\to 0}\left(\frac{\Delta z}{R^2} - \frac{2\Delta x^2 \Delta z}{R^4}\right) g = 0\,, \tag{E-112}$$

and

$$\lim_{R\to 0} g_{xz,z} = \lim_{R\to 0} g_{zx,z} = \lim_{R\to 0}\frac{\Delta z^2 \Delta x}{R^3} g' + \lim_{R\to 0}\left(\frac{\Delta x}{R^2} - \frac{2\Delta z^2 \Delta x}{R^4}\right) g = 0\,. \tag{E-113}$$

For the second-order derivatives, it follows that

$$\begin{aligned} \lim_{R\to 0} g_{xx,xx} &= \lim_{R\to 0}\frac{h'}{R} + \lim_{R\to 0}\frac{\Delta x^2}{R^2}\left(h'' - \frac{h'}{R}\right) + \lim_{R\to 0}\frac{2g}{R^2} \\ &\quad + \lim_{R\to 0}\frac{5\Delta x^2}{R^2}\left(\frac{g'}{R} - \frac{2g}{R^2}\right) + \lim_{R\to 0}\frac{\Delta x^4}{R^4}\left(g'' - \frac{g'}{R}\right). \end{aligned} \tag{E-114}$$

By referring to the above equations concerning the limits of the functions *h* and *g* and of their derivatives, one obtains

$$\begin{aligned} \lim_{R\to 0} g_{xx,xx} &= \lim_{R\to 0}\frac{h'}{R} + \lim_{R\to 0}\frac{\Delta x^2}{R^2}\cdot 0 + \lim_{R\to 0}\frac{2g}{R^2} + \lim_{R\to 0}\frac{5\Delta x^2}{R^2}\cdot 0 + \lim_{R\to 0}\frac{\Delta x^4}{R^4}\cdot 0 \\ &= \lim_{R\to 0}\frac{h'}{R} + \lim_{R\to 0}\frac{2g}{R^2} \\ &= \lim_{R\to 0} h'' + \lim_{R\to 0} g'' \\ &= -\frac{3}{16}\frac{1}{\rho_b \omega^2} i\pi a k_{cb}^3 H_1^{(1)}\left(k_{cb}a\right) - \frac{1}{16}\frac{1}{\rho_b \omega^2} i\pi a k_{sb}^3 H_1^{(1)}\left(k_{sb}a\right) \quad , \end{aligned} \tag{E-115}$$

$$\begin{aligned} \lim_{R\to 0} g_{xx,xz} &= \lim_{R\to 0}\frac{\Delta x \Delta z}{R^2}\left(h'' - \frac{h'}{R}\right) \\ &\quad + \lim_{R\to 0}\frac{2\Delta x \Delta z}{R^2}\left(\frac{g'}{R} - \frac{2g}{R^2}\right) + \lim_{R\to 0}\frac{\Delta x^3 \Delta z}{R^4}\left(4\cdot\frac{2g}{R^2} - \frac{5g'}{R} + g''\right) \\ &= 0 \end{aligned} \quad , \tag{E-116}$$

$$\lim_{R\to 0} g_{xx,zx} = \lim_{R\to 0} g_{xx,xz} = 0\,, \tag{E-117}$$

and

$$\begin{aligned}
\lim_{R\to 0} g_{xx,zz} &= \lim_{R\to 0}\frac{h'}{R} + \lim_{R\to 0}\frac{\Delta z^2}{R^2}\left(h'' - \frac{h'}{R}\right) \\
&\quad + \lim_{R\to 0}\frac{\Delta x^2}{R^2}\left(\frac{g'}{R} - \frac{2g}{R^2}\right) + \lim_{R\to 0}\frac{\Delta x^2 \Delta z^2}{R^4}\left(4\cdot\frac{2g}{R^2} - \frac{5g'}{R} + g''\right) \\
&= \lim_{R\to 0}\frac{h'}{R} \\
&= -\frac{1}{16}\frac{1}{\rho_b \omega^2} i\pi a k_{cb}^3 H_1^{(1)}\left(k_{cb}a\right) - \frac{3}{16}\frac{1}{\rho_b \omega^2} i\pi a k_{sb}^3 H_1^{(1)}\left(k_{sb}a\right).
\end{aligned} \tag{E-118}$$

Similarly,

$$\begin{aligned}
\lim_{R\to 0} g_{zz,zz} &= \lim_{R\to 0}\frac{h'}{R} + \lim_{R\to 0}\frac{\Delta z^2}{R^2}\left(h'' - \frac{h'}{R}\right) + \lim_{R\to 0}\frac{2g}{R^2} \\
&\quad + \lim_{R\to 0}\frac{5\Delta z^2}{R^2}\left(\frac{g'}{R} - \frac{2g}{R^2}\right) + \lim_{R\to 0}\frac{\Delta z^4}{R^4}\left(g'' - \frac{g'}{R}\right) \\
&= \lim_{R\to 0}\frac{h'}{R} + \lim_{R\to 0}\frac{2g}{R^2} \\
&= -\frac{3}{16}\frac{1}{\rho_b \omega^2} i\pi a k_{cb}^3 H_1^{(1)}\left(k_{cb}a\right) - \frac{1}{16}\frac{1}{\rho_b \omega^2} i\pi a k_{sb}^3 H_1^{(1)}\left(k_{sb}a\right) \\
&\qquad ,
\end{aligned} \tag{E-119}$$

$$\lim_{R\to 0} g_{zz,xz} = \lim_{R\to 0} g_{zz,zx} = 0\,, \tag{E-120}$$

$$\begin{aligned}
\lim_{R\to 0} g_{zz,xx} &= \lim_{R\to 0}\frac{h'}{R} \\
&= -\frac{1}{16}\frac{1}{\rho_b \omega^2} i\pi a k_{cb}^3 H_1^{(1)}\left(k_{cb}a\right) - \frac{3}{16}\frac{1}{\rho_b \omega^2} i\pi a k_{sb}^3 H_1^{(1)}\left(k_{sb}a\right),
\end{aligned} \tag{E-121}$$

$$\begin{aligned}
\lim_{R\to 0} g_{xz,xx} &= \lim_{R\to 0}\frac{3\Delta x \Delta z}{R^2}\left(\frac{g'}{R} - \frac{2g}{R^2}\right) + \lim_{R\to 0}\frac{\Delta x^3 \Delta z}{R^4}\left(4\cdot\frac{2g}{R^2} - \frac{5g'}{R} + g''\right) \\
&= 0 \qquad ,
\end{aligned} \tag{E-122}$$

$$\begin{aligned}
\lim_{R\to 0} g_{xz,zz} &= \lim_{R\to 0}\frac{3\Delta x \Delta z}{R^2}\left(\frac{g'}{R} - \frac{2g}{R^2}\right) + \lim_{R\to 0}\frac{\Delta z^3 \Delta x}{R^4}\left(4\cdot\frac{2g}{R^2} - \frac{5g'}{R} + g''\right) \\
&= 0 \qquad ,
\end{aligned} \tag{E-123}$$

$$
\begin{aligned}
\lim_{R\to 0} g_{xz,xz} &= \lim_{R\to 0}\left(\frac{g'}{R}-\frac{g}{R^2}\right)+\lim_{R\to 0}\frac{\Delta x^2\Delta z^2}{R^4}\left(4\cdot\frac{2g}{R^2}-\frac{5g'}{R}+g''\right)\\
&=\frac{1}{2}\lim_{R\to 0} g''\\
&=-\frac{1}{16}\frac{1}{\rho_b\omega^2}i\pi a k_{cb}^3 H_1^{(1)}\left(k_{cb}a\right)+\frac{1}{\rho_b\omega^2}\frac{1}{16}i\pi a k_{sb}^3 H_1^{(1)}\left(k_{sb}a\right),
\end{aligned}
\tag{E-124}
$$

$$
\begin{aligned}
\lim_{R\to 0} g_{xz,zx} &= \lim_{R\to 0} g_{xz,xz}\\
&=-\frac{1}{16}\frac{1}{\rho_b\omega^2}i\pi a k_{cb}^3 H_1^{(1)}\left(k_{cb}a\right)+\frac{1}{16}\frac{1}{\rho_b\omega^2}i\pi a k_{sb}^3 H_1^{(1)}\left(k_{sb}a\right),
\end{aligned}
\tag{E-125}
$$

$$
\begin{aligned}
\lim_{R\to 0} g_{zx,zx} &= \lim_{R\to 0} g_{xz,zx}\\
&=-\frac{1}{16}\frac{1}{\rho_b\omega^2}i\pi a k_{cb}^3 H_1^{(1)}\left(k_{cb}a\right)+\frac{1}{16}\frac{1}{\rho_b\omega^2}i\pi a k_{sb}^3 H_1^{(1)}\left(k_{sb}a\right),
\end{aligned}
\tag{E-126}
$$

$$
\begin{aligned}
\lim_{R\to 0} g_{zx,xz} &= \lim_{R\to 0} g_{xz,zx}\\
&=-\frac{1}{16}\frac{1}{\rho_b\omega^2}i\pi a k_{cb}^3 H_1^{(1)}\left(k_{cb}a\right)+\frac{1}{16}\frac{1}{\rho_b\omega^2}i\pi a k_{sb}^3 H_1^{(1)}\left(k_{sb}a\right),
\end{aligned}
\tag{E-127}
$$

$$
\lim_{R\to 0} g_{zx,xx} = \lim_{R\to 0} g_{xz,xx} = 0\,,
\tag{E-128}
$$

and

$$
\lim_{R\to 0} g_{zx,zz} = \lim_{R\to 0} g_{xz,zz} = 0\,.
\tag{E-129}
$$

Therefore, the extended diagonal entries of matrix *A* are given by

$$
\begin{aligned}
a_{kk} &= 1-\omega^2\delta\rho\lim_{R\to 0} g_{xx}\\
&=1+\frac{\delta\rho}{\rho_b}\left[1-\frac{1}{4}i\pi a k_{cb} H_1^{(1)}\left(k_{cb}a\right)-\frac{1}{4}i\pi a k_{sb} H_1^{(1)}\left(k_{sb}a\right)\right],
\end{aligned}
\tag{E-130}
$$

$$
a_{k(k+1)} = -\omega^2\delta\rho\lim_{R\to 0} g_{zx} = 0\,,
\tag{E-131}
$$

$$
a_{k(k+2)} = -\delta\lambda\lim_{R\to 0}\left(g_{xx,x}+g_{zx,z}\right)-2\delta\mu\lim_{R\to 0} g_{xx,x} = 0\,,
\tag{E-132}
$$

$$
a_{k(k+3)} = -\delta\mu\lim_{R\to 0}\left(g_{xx,z}+g_{zx,x}\right) = 0\,,
\tag{E-133}
$$

$$
a_{k(k+4)} = -\delta\lambda\lim_{R\to 0}\left(g_{xx,x}+g_{zx,z}\right)-2\delta\mu\lim_{R\to 0} g_{zx,z} = 0\,,
\tag{E-134}
$$

$$a_{(k+1)k} = -\omega^2 \delta\rho \lim_{R\to 0} g_{xz} = 0\,, \tag{E-135}$$

$$\begin{aligned} a_{(k+1)(k+1)} &= 1 - \omega^2 \delta\rho \lim_{R\to 0} g_{zz} \\ &= 1 + \frac{\delta\rho}{\rho_b}\left[1 - \frac{1}{4} i\pi a k_{cb} H_1^{(1)}(k_{cb}a) - \frac{1}{4} i\pi a k_{sb} H_1^{(1)}(k_{sb}a)\right], \end{aligned} \tag{E-136}$$

$$a_{(k+1)(k+2)} = -\delta\lambda \lim_{R\to 0}\left(g_{xz,x} + g_{zz,z}\right) - 2\delta\mu \lim_{R\to 0} g_{xz,x} = 0\,, \tag{E-137}$$

$$a_{(k+1)(k+3)} = -\delta\mu \lim_{R\to 0}\left(g_{xz,z} + g_{zz,x}\right) = 0\,, \tag{E-138}$$

$$a_{(k+1)(k+4)} = -\delta\lambda \lim_{R\to 0}\left(g_{xz,x} + g_{zz,z}\right) - 2\delta\mu \lim_{R\to 0} g_{zz,z} = 0\,, \tag{E-139}$$

$$a_{(k+2)k} = -\omega^2 \delta\rho \lim_{R\to 0} g_{xx,x} = 0\,, \tag{E-140}$$

$$a_{(k+2)(k+1)} = -\omega^2 \delta\rho \lim_{R\to 0} g_{zx,x} = 0\,, \tag{E-141}$$

$$\begin{aligned} a_{(k+2)(k+2)} &= 1 - \delta\lambda \lim_{R\to 0}\left(g_{xx,xx} + g_{zx,zx}\right) - 2\delta\mu \lim_{R\to 0} g_{xx,xx} \\ &= 1 - \delta\lambda \lim_{R\to 0}\left(g'' + h'' + \frac{1}{2} g''\right) - 2\delta\mu \lim_{R\to 0}\left(g'' + h''\right) \\ &= 1 + \frac{\delta\lambda}{\rho_b \omega^2}\left[\frac{1}{4} i\pi a k_{cb}^3 H_1^{(1)}(k_{cb}a)\right] \\ &\quad + \frac{\delta\mu}{\rho_b \omega^2}\left[\frac{3}{8} i\pi a k_{cb}^3 H_1^{(1)}(k_{cb}a) + \frac{1}{8} i\pi a k_{sb}^3 H_1^{(1)}(k_{sb}a)\right], \end{aligned} \tag{E-142}$$

$$a_{(k+2)(k+3)} = -\delta\mu \lim_{R\to 0}\left(g_{xx,zx} + g_{zx,xx}\right) = 0\,, \tag{E-143}$$

$$\begin{aligned} a_{(k+2)(k+4)} &= -\delta\lambda \lim_{R\to 0}\left(g_{xx,xx} + g_{zx,zx}\right) - 2\delta\mu \lim_{R\to 0} g_{zx,zx} \\ &= -\delta\lambda \lim_{R\to 0}\left(g'' + h'' + \frac{1}{2} g''\right) - 2\delta\mu \lim_{R\to 0}\left(\frac{1}{2} g''\right) \\ &= \frac{\delta\lambda}{\rho_b \omega^2}\left[\frac{1}{4} i\pi a k_{cb}^3 H_1^{(1)}(k_{cb}a)\right] \\ &\quad + \frac{\delta\mu}{\rho_b \omega^2}\left[\frac{1}{8} i\pi a k_{cb}^3 H_1^{(1)}(k_{cb}a) - \frac{1}{8} i\pi a k_{sb}^3 H_1^{(1)}(k_{sb}a)\right], \end{aligned} \tag{E-144}$$

$$a_{(k+3)k} = -\omega^2 \delta\rho \lim_{R\to 0}\left(g_{xx,z} + g_{xz,x}\right) = 0\,, \tag{E-145}$$

$$a_{(k+3)(k+1)} = -\omega^2 \delta\rho \lim_{R\to 0}\left(g_{zx,z} + g_{zz,x}\right) = 0\,, \tag{E-146}$$

$$\begin{aligned} a_{(k+3)(k+2)} &= -\delta\lambda \lim_{R\to 0}\left(g_{xx,xz} + g_{zx,zz} + g_{xz,xx} + g_{zz,zx}\right) \\ &\quad - 2\delta\mu \lim_{R\to 0}\left(g_{xx,xz} + g_{xz,xx}\right) \\ &= 0 \end{aligned}\,, \tag{E-147}$$

$$\begin{aligned} a_{(k+3)(k+3)} &= 1 - \delta\mu \lim_{R\to 0}\left(g_{xx,zz} + g_{zx,xz} + g_{zz,xx} + g_{xz,zx}\right) \\ &= 1 - \delta\mu \lim_{R\to 0}\left(2h'' + g''\right) \\ &= 1 + \frac{\delta\mu}{\rho_b \omega^2}\left[\frac{1}{4} i\pi a k_{cb}^3 H_1^{(1)}\left(k_{cb}a\right) + \frac{1}{4} i\pi a k_{sb}^3 H_1^{(1)}\left(k_{sb}a\right)\right] \end{aligned}, \tag{E-148}$$

$$\begin{aligned} a_{(k+3)(k+4)} &= -\delta\lambda \lim_{R\to 0}\left(g_{xx,xz} + g_{zx,zz} + g_{xz,xx} + g_{zz,zx}\right) - 2\delta\mu \lim_{R\to 0} g_{zx,zz} \\ &= 0 \end{aligned}\,, \tag{E-149}$$

$$a_{(k+4)k} = -\omega^2 \delta\rho \lim_{R\to 0} g_{xz,z} = 0\,, \tag{E-150}$$

$$a_{(k+4)(k+1)} = -\omega^2 \delta\rho \lim_{R\to 0} g_{zz,z} = 0\,, \tag{E-151}$$

$$\begin{aligned} a_{(k+4)(k+2)} &= -\delta\lambda \lim_{R\to 0}\left(g_{zz,zz} + g_{xz,xz}\right) - 2\delta\mu \lim_{R\to 0} g_{xz,xz} \\ &= -\delta\lambda \lim_{R\to 0}\left(g'' + h'' + \frac{1}{2} g''\right) - 2\delta\mu \lim_{R\to 0}\left(\frac{1}{2} g''\right) \\ &= \frac{\delta\lambda}{\rho_b \omega^2}\left[\frac{1}{4} i\pi a k_{cb}^3 H_1^{(1)}\left(k_{cb}a\right)\right] \\ &\quad + \frac{\delta\mu}{\rho_b \omega^2}\left[\frac{1}{8} i\pi a k_{cb}^3 H_1^{(1)}\left(k_{cb}a\right) - \frac{1}{8} i\pi a k_{sb}^3 H_1^{(1)}\left(k_{sb}a\right)\right] \end{aligned}, \tag{E-152}$$

$$a_{(k+4)(k+3)} = -\delta\mu \lim_{R\to 0}\left(g_{xz,zz} + g_{zz,xz}\right) = 0\,, \tag{E-153}$$

and

$$
\begin{aligned}
a_{(k+4)(k+4)} &= 1 - \delta\lambda \lim_{R\to 0}\left(g_{zz,zz} + g_{xz,xz}\right) - 2\delta\mu \lim_{R\to 0} g_{zz,zz} \\
&= 1 - \delta\lambda \lim_{R\to 0}\left(g'' + h'' + \frac{1}{2} g''\right) - 2\delta\mu \lim_{R\to 0}\left(g'' + h''\right) \\
&= 1 + \frac{\delta\lambda}{\rho_b \omega^2}\left[\frac{1}{4} i\pi a k_{cb}^3 H_1^{(1)}\left(k_{cb} a\right)\right] \\
&\quad + \frac{\delta\mu}{\rho_b \omega^2}\left[\frac{3}{8} i\pi a k_{cb}^3 H_1^{(1)}\left(k_{cb} a\right) + \frac{1}{8} i\pi a k_{sb}^3 H_1^{(1)}\left(k_{sb} a\right)\right],
\end{aligned}
\qquad \text{(E-154)}
$$

where k=1, 6, 11, 16,…5N-4.

Appendix F: Expressions for the Entries of the Matrices E_j in Chapter 3

Second-order derivatives of Hankel functions are first calculated to obtain explicit expressions for stress. It is known that

$$\overline{H}_{n,r}^{(m)}(kr) = k\overline{H}_{n-1}^{(m)}(kr) - \frac{n}{r}\overline{H}_{n}^{(m)}(kr), \tag{F-1}$$

$$\overline{H}_{n,r}^{(m)}(kr) = \frac{n}{r}\overline{H}_{n}^{(m)}(kr) - k\overline{H}_{n+1}^{(m)}(kr), \tag{F-2}$$

$$\overline{H}_{n,r}^{(m)}(kr) = \frac{k}{2}\left[\overline{H}_{n-1}^{(m)}(kr) - \overline{H}_{n+1}^{(m)}(kr)\right], \tag{F-3}$$

and

$$n\overline{H}_{n}^{(m)}(kr) = \frac{k}{2}\left[\overline{H}_{n-1}^{(m)}(kr) + \overline{H}_{n+1}^{(m)}(kr)\right], \tag{F-4}$$

where the superscript *m* is used to describe the type of Hankel function. One then obtains

$$\begin{aligned} \overline{H}_{n,rr}^{(m)}(kr) &= \frac{k}{2}\left[\overline{H}_{n-1,r}^{(m)}(kr) - \overline{H}_{n+1,r}^{(m)}(kr)\right] \\ &= \frac{n^2}{r^2}\overline{H}_{n}^{(m)}(kr) - \frac{1}{r}\overline{H}_{n,r}^{(m)}(kr) - k^2\overline{H}_{n}^{(m)}(kr). \end{aligned} \tag{F-5}$$

The following relationship exists among Lamé constants λ and μ, rock density ρ and its compressional velocity v_c and shear velocity v_s:

$$\lambda = \rho v_c^2 - 2\mu, \tag{F-6}$$

and

$$\mu = \rho v_s^2. \tag{F-7}$$

To simplify the expressions of the displacement and stress, the radial component of the compressional wavenumber of layer j is defined as

$$kp_j = \sqrt{k_{cj}^2 - k^2}\ ,\ \mathrm{Im}\{kp_j\} > 0\,, \tag{F-8}$$

where

$$k_{cj} = \frac{\omega}{v_{cj}} \tag{F-9}$$

is the compressional wavenumber.

For an arbitrary layer j, one multiplies both sides of equation (F-6) by k_{cj}^2, and then substitutes equations (F-8) and (F-9) into the resulting equation, to obtain

$$\begin{aligned} \lambda k_{cj}^2 &= \rho v_{sj}^2 k_{sj}^2 - 2\mu\left(k_{pj}^2 + k^2\right) \\ &= \mu k_{sj}^2 - 2\mu\left(k_{pj}^2 + k^2\right) \qquad . \end{aligned} \tag{F-10}$$

For the same layer,

$$v_{cj} k_{cj} = \omega = v_{sj} k_{sj}\,, \tag{F-11}$$

where v_{sj} and k_{sj} are the shear velocity and wavenumber, respectively.

Substitution of equations (F-7) and (F-11) into equation (F-10) yields

$$\begin{aligned} \lambda k_{cj}^2 &= \rho v_{sj}^2 k_{sj}^2 - 2\mu\left(k_{pj}^2 + k^2\right) \\ &= \mu k_{sj}^2 - 2\mu\left(k_{pj}^2 + k^2\right) \qquad . \end{aligned} \tag{F-12}$$

By multiplying by -1 and subtracting the term $-2\mu k_{pj}^2$ from both sides of equation (F-12), one obtains,

$$\begin{aligned} &-\lambda k_{cj}^2 - 2\mu k_{pj}^2 \\ &= -\mu k_{sj}^2 + 2\mu\left(k_{pj}^2 + k^2\right) - 2\mu k_{pj}^2 \\ &= 2\mu\left(k^2 - \frac{1}{2}k_{sj}^2\right) \\ &= 2\mu\Omega_j\,, \end{aligned} \tag{F-13}$$

where

$$\Omega_j = k^2 - \frac{1}{2}k_{sj}^2 . \tag{F-14}$$

By substituting the potential solutions equations (3.13) through (3.14) into the displacement and stress relations given by equations (3.26) through (3.31), it follows that

$$\begin{aligned}
u &= c_{P_j-}e^{ikp_j(r_j-r)}\overline{H}^{(2)}_{n,r}(kp_jr) + c_{P_j+}e^{ikp_j(r-r_{j-1})}\overline{H}^{(1)}_{n,r}(kp_jr) \\
&+ \frac{n}{r}\left[c_{SH_j-}e^{iks_j(r_j-r)}\overline{H}^{(2)}_{n}(ks_jr) + c_{SH_j+}e^{iks_j(r-r_{j-1})}\overline{H}^{(1)}_{n}(ks_jr)\right], \\
&+ ik\left[c_{SV_j-}e^{iks_j(r_j-r)}\overline{H}^{(2)}_{n,r}(ks_jr) + c_{SV_j+}e^{iks_j(r-r_{j-1})}\overline{H}^{(1)}_{n,r}(ks_jr)\right]
\end{aligned} \tag{F-15}$$

$$\begin{aligned}
v &= -\frac{n}{r}\left[c_{P_j-}e^{ikp_j(r_j-r)}\overline{H}^{(2)}_{n}(kp_jr) + c_{P_j+}e^{ikp_j(r-r_{j-1})}\overline{H}^{(1)}_{n}(kp_jr)\right] \\
&- c_{SH_j-}e^{iks_j(r_j-r)}\overline{H}^{(2)}_{n,r}(ks_jr) - c_{SH_j+}e^{iks_j(r-r_{j-1})}\overline{H}^{(1)}_{n,r}(ks_jr) \\
&- \frac{ink}{r}\left[c_{SV_j-}e^{iks_j(r_j-r)}\overline{H}^{(2)}_{n}(ks_jr) + c_{SV_j+}e^{iks_j(r-r_{j-1})}\overline{H}^{(1)}_{n}(ks_jr)\right],
\end{aligned} \tag{F-16}$$

$$\begin{aligned}
w &= ik\left[c_{P_j-}e^{ikp_j(r_j-r)}\overline{H}^{(2)}_{n,r}(kp_jr) + c_{P_j+}e^{ikp_j(r-r_{j-1})}\overline{H}^{(1)}_{n,r}(kp_jr)\right] \\
&+ ks_j^2\left[c_{SV_j-}e^{iks_j(r_j-r)}\overline{H}^{(2)}_{n}(ks_jr) + c_{SV_j+}e^{iks_j(r-r_{j-1})}\overline{H}^{(1)}_{n}(ks_jr)\right] ,
\end{aligned} \tag{F-17}$$

$$\begin{aligned}
\sigma_{rr} &= c_{P_j+}2\mu\left[\Omega_j\overline{H}^{(1)}_{n}(kp_jr) + \frac{1}{r}\left(\frac{n^2}{r}\overline{H}^{(1)}_{n}(kp_jr) - \overline{H}^{(1)}_{n,r}(kp_jr)\right)\right]e^{ikp_j(r-r_{j-1})} \\
&+ c_{SH_j+}\frac{2\mu n}{r}\left[\overline{H}^{(1)}_{n,r}(ks_jr) - \frac{1}{r}\overline{H}^{(1)}_{n}(ks_jr)\right]e^{iks_j(r-r_{j-1})} \\
&+ c_{SV_j+}2ik\mu\left[-ks_j^2\overline{H}^{(1)}_{n}(ks_jr) + \frac{1}{r}\left(\frac{n^2}{r}\overline{H}^{(1)}_{n}(ks_jr) - \overline{H}^{(1)}_{n,r}(ks_jr)\right)\right]e^{iks_j(r-r_{j-1})} \\
&+ c_{P_j-}2\mu\left[\Omega_j\overline{H}^{(2)}_{n}(kp_jr) + \frac{1}{r}\left(\frac{n^2}{r}\overline{H}^{(2)}_{n}(kp_jr) - \overline{H}^{(2)}_{n,r}(kp_jr)\right)\right]e^{ikp_j(r_j-r)} \\
&+ c_{SH_j-}\frac{2\mu n}{r}\left[\overline{H}^{(2)}_{n,r}(ks_jr) - \frac{1}{r}\overline{H}^{(2)}_{n}(ks_jr)\right]e^{iks_j(r_j-r)} \\
&+ c_{SV_j-}2ik\mu\left[-ks_j^2\overline{H}^{(2)}_{n}(ks_jr) + \frac{1}{r}\left(\frac{n^2}{r}\overline{H}^{(2)}_{n}(ks_jr) - \overline{H}^{(2)}_{n,r}(ks_jr)\right)\right]e^{iks_j(r_j-r)} ,
\end{aligned} \tag{F-18}$$

$$\begin{aligned}
\sigma_{r\theta} &= c_{P_j+}\frac{2\mu n}{r}\left[\frac{1}{r}\overline{H}_{n}^{(1)}\left(kp_j r\right)-\overline{H}_{n,r}^{(1)}\left(kp_j r\right)\right]e^{ikp_j\left(r-r_{j-1}\right)}\\
&+c_{SH_j+}\mu\left[\frac{2}{r}\left(\overline{H}_{n,r}^{(1)}\left(ks_j r\right)-\frac{1}{r}\overline{H}_{n}^{(1)}\left(ks_j r\right)\right)+ks_j^2\,\overline{H}_{n}^{(1)}\left(ks_j r\right)\right]e^{iks_j\left(r-r_{j-1}\right)}\\
&+c_{SV_j+}\frac{2ik\mu n}{r}\left[\frac{1}{r}\overline{H}_{n}^{(1)}\left(kp_j r\right)-\overline{H}_{n,r}^{(1)}\left(kp_j r\right)\right]e^{iks_j\left(r-r_{j-1}\right)}\\
&+c_{P_j-}\frac{2\mu n}{r}\left[\frac{1}{r}\overline{H}_{n}^{(2)}\left(kp_j r\right)-\overline{H}_{n,r}^{(2)}\left(kp_j r\right)\right]e^{ikp_j\left(r_j-r\right)}\\
&+c_{SH_j-}\mu\left[\frac{2}{r}\left(\overline{H}_{n,r}^{(2)}\left(ks_j r\right)-\frac{1}{r}\overline{H}_{n}^{(2)}\left(ks_j r\right)\right)+ks_j^2\,\overline{H}_{n}^{(2)}\left(ks_j r\right)\right]e^{iks_j\left(r_j-r\right)}\\
&+c_{SV_j-}\frac{2ik\mu n}{r}\left[\frac{1}{r}\overline{H}_{n}^{(2)}\left(kp_j r\right)-\overline{H}_{n,r}^{(2)}\left(kp_j r\right)\right]e^{iks_j\left(r_j-r\right)}
\end{aligned}\quad, \qquad \text{(F-19)}$$

and

$$\begin{aligned}
\sigma_{rz} &= c_{P_j+}2ik\mu\overline{H}_{n,r}^{(1)}\left(kp_j r\right)e^{ikp_j\left(r-r_{j-1}\right)}\\
&+c_{SH_j+}\frac{ik\mu n}{r}\overline{H}_{n}^{(1)}\left(ks_j r\right)e^{iks_j\left(r-r_{j-1}\right)}\\
&+c_{SV_j+}\left(-2\right)\mu\Omega_j\overline{H}_{n,r}^{(1)}\left(ks_j r\right)e^{iks_j\left(r-r_{j-1}\right)}\\
&+c_{P_j-}2ik\mu\overline{H}_{n,r}^{(2)}\left(kp_j r\right)e^{ikp_j\left(r_j-r\right)}\\
&+c_{SH_j-}\frac{ik\mu n}{r}\overline{H}_{n}^{(2)}\left(ks_j r\right)e^{iks_j\left(r_j-r\right)}\\
&+c_{SV_j-}\left(-2\right)\mu\Omega_j\overline{H}_{n,r}^{(2)}\left(ks_j r\right)e^{iks_j\left(r_j-r\right)}
\end{aligned}\quad. \qquad \text{(F-20)}$$

In order to simplify the expressions in equations (F-15) through (F-20), the following functions are defined:

$$F_1\left(kr\right)=\overline{H}_{n,r}^{(1)}\left(kr\right)=k\overline{H}_{n-1}^{(1)}\left(kr\right)-\frac{n}{r}\overline{H}_{n}^{(1)}\left(kr\right), \qquad \text{(F-21)}$$

$$F_2\left(kr\right)=F_1\left(kr\right)-\frac{1}{r}\overline{H}_{n}^{(1)}\left(kr\right), \qquad \text{(F-22)}$$

$$F_3(kr) = F_1(kr) - \frac{n^2}{r}\overline{H}_n^{(1)}(kr), \tag{F-23}$$

$$G_1(kr) = \overline{H}_{n,r}^{(2)}(kr) = k\overline{H}_{n-1}^{(2)}(kr) - \frac{n}{r}\overline{H}_n^{(2)}(kr), \tag{F-24}$$

$$G_2(kr) = G_1(kr) - \frac{1}{r}\overline{H}_n^{(1)}(kr), \tag{F-25}$$

and

$$G_3(kr) = G_1(kr) - \frac{n^2}{r}\overline{H}_n^{(1)}(kr). \tag{F-26}$$

By comparing equations (F-15) through (F-20) to their matrix form given by equation (3.32) and by making use of the functions defined by equations (F-21) through (F-26), the entries of matrix $\boldsymbol{E_j}$ (j=2, 3, …N-1) can then be written as:

$$e_{11} = G_1(kp_j r)e^{ikp_j(r_j - r)} \ , \tag{F-27}$$

$$e_{14} = F_1(kp_j r)e^{ikp_j(r - r_{j-1})}, \tag{F-28}$$

$$e_{12} = \frac{n}{r}\overline{H}_n^{(2)}(ks_j r)e^{iks_j(r_j - r)}, \tag{F-29}$$

$$e_{15} = \frac{n}{r}\overline{H}_n^{(1)}(ks_j r)e^{iks_j(r - r_{j-1})}, \tag{F-30}$$

$$e_{13} = ikG_1(ks_j r)e^{iks_j(r_j - r)}, \tag{F-31}$$

$$e_{16} = ikF_1(ks_j r)e^{iks_j(r - r_{j-1})}, \tag{F-32}$$

$$e_{21} = -\frac{n}{r}\overline{H}_n^{(2)}(kp_j r)e^{ikp_j(r_j - r)}, \tag{F-33}$$

$$e_{24} = -\frac{n}{r}\overline{H}_n^{(1)}(kp_j r)e^{ikp_j(r - r_{j-1})}, \tag{F-34}$$

$$e_{22} = -G_1(ks_j r)e^{iks_j(r_j - r)}, \tag{F-35}$$

$$e_{25} = -F_1\left(ks_j r\right)e^{iks_j\left(r-r_{j-1}\right)}, \tag{F-36}$$

$$e_{23} = -\frac{ink}{r}\overline{H}_n^{(2)}\left(ks_j r\right)e^{iks_j\left(r_j-r\right)}, \tag{F-37}$$

$$e_{26} = -\frac{ink}{r}\overline{H}_n^{(1)}\left(ks_j r\right)e^{iks_j\left(r-r_{j-1}\right)}, \tag{F-38}$$

$$e_{31} = ik\overline{H}_n^{(2)}\left(kp_j r\right)e^{ikp_j\left(r_j-r\right)}, \tag{F-39}$$

$$e_{34} = ik\overline{H}_n^{(1)}\left(kp_j r\right)e^{ikp_j\left(r-r_{j-1}\right)}, \tag{F-40}$$

$$e_{32} = 0, \tag{F-41}$$

$$e_{35} = 0, \tag{F-42}$$

$$e_{33} = ks_j^2\overline{H}_n^{(2)}\left(ks_j r\right)e^{iks_j\left(r_j-r\right)}, \tag{F-43}$$

$$e_{36} = ks_j^2\overline{H}_n^{(1)}\left(ks_j r\right)e^{iks_j\left(r-r_{j-1}\right)}, \tag{F-44}$$

$$e_{41} = 2\mu_j\left[\Omega_j\overline{H}_n^{(2)}\left(kp_j r\right)-\frac{1}{r}G_1\left(kp_j r\right)\right]e^{ikp_j\left(r_j-r\right)}, \tag{F-45}$$

$$e_{44} = 2\mu_j\left[\Omega_j\overline{H}_n^{(1)}\left(kp_j r\right)-\frac{1}{r}F_1\left(kp_j r\right)\right]e^{ikp_j\left(r-r_{j-1}\right)}, \tag{F-46}$$

$$e_{42} = \frac{2n}{r}\mu_j G_2\left(ks_j r\right)e^{iks_j\left(r_j-r\right)}, \tag{F-47}$$

$$e_{45} = \frac{2n}{r}\mu_j F_2\left(ks_j r\right)e^{iks_j\left(r-r_{j-1}\right)}, \tag{F-48}$$

$$e_{43} = -2ik\mu_j\left[ks_j^2\overline{H}_n^{(2)}\left(ks_j r\right)+\frac{1}{r}G_3\left(ks_j r\right)\right]e^{iks_j\left(r_j-r\right)}, \tag{F-49}$$

$$e_{46} = -2ik\mu_j\left[ks_j^2\overline{H}_n^{(1)}\left(ks_j r\right)+\frac{1}{r}F_3\left(ks_j r\right)\right]e^{iks_j\left(r-r_{j-1}\right)}, \tag{F-50}$$

$$e_{51} = -\frac{2n}{r}\mu_j G_2\left(kp_j r\right)e^{ikp_j\left(r_j-r\right)}, \tag{F-51}$$

$$e_{54} = -\frac{2n}{r}\mu_j F_2\left(kp_j r\right)e^{ikp_j\left(r-r_{j-1}\right)}, \tag{F-52}$$

$$e_{52} = \mu_j\left[ks_j^2\overline{H}_n^{(2)}\left(ks_j r\right)+\frac{2}{r}G_3\left(ks_j r\right)\right]e^{iks_j\left(r_j-r\right)}, \tag{F-53}$$

$$e_{55} = \mu_j\left[ks_j^2\overline{H}_n^{(1)}\left(ks_j r\right)+\frac{2}{r}F_3\left(ks_j r\right)\right]e^{iks_j\left(r-r_{j-1}\right)}, \tag{F-54}$$

$$e_{53} = -\frac{2ikn}{r}\mu_j G_2\left(ks_j r\right)e^{iks_j\left(r_j-r\right)}, \tag{F-55}$$

$$e_{56} = -\frac{2ikn}{r}\mu_j F_2\left(ks_j r\right)e^{iks_j\left(r-r_{j-1}\right)}, \tag{F-56}$$

$$e_{61} = 2ik\mu_j G_1\left(kp_j r\right)e^{ikp_j\left(r_j-r\right)}, \tag{F-57}$$

$$e_{64} = 2ik\mu_j F_1\left(kp_j r\right)e^{ikp_j\left(r-r_{j-1}\right)}, \tag{F-58}$$

$$e_{62} = \frac{ikn}{r}\mu_j\overline{H}_n^{(2)}\left(ks_j r\right)e^{iks_j\left(r_j-r\right)}, \tag{F-59}$$

$$e_{65} = \frac{ikn}{r}\mu_j\overline{H}_n^{(1)}\left(ks_j r\right)e^{iks_j\left(r-r_{j-1}\right)}, \tag{F-60}$$

$$e_{63} = -2\mu_j\Omega_j G_1\left(ks_j r\right)e^{iks_j\left(r_j-r\right)}, \tag{F-61}$$

and

$$e_{66} = -2\mu_j\Omega_j F_1\left(ks_j r\right)e^{iks_j\left(r-r_{j-1}\right)}, \tag{F-62}$$

where $\Omega_j = k^2 - \frac{1}{2}k_{\beta j}^2$, and $k_{\beta j}$ is the shear wavenumber of layer j.

For the outermost layer (j = N), which only supports outward-directed waves, the entries of the first three columns of matrix $\boldsymbol{E_j}$ become zero, while those of the remaining three columns remain unchanged.

For j = 1 in the borehole fluid, the entries of matrix $\boldsymbol{E_j}$ read as

$$e_{11} = F_1^{(2)}\left(kp_f r\right)e^{ikp_f\left(r_1 - r\right)}, \tag{F-63}$$

$$e_{12} = F_1^{(1)}\left(kp_f r\right)e^{ikp_f r}, \tag{F-64}$$

$$e_{21} = -\lambda_f k_f^2 \overline{H}_n^{(2)}\left(kp_f r\right)e^{ikp_j\left(r_j - r\right)}, \tag{F-65}$$

and

$$e_{22} = -\lambda_f k_f^2 \overline{H}_n^{(1)}\left(kp_f r\right)e^{ikp_j r}. \tag{F-66}$$

Appendix G: Formulation of the Gauss-Newton Nonlinear Inversion

The estimation of $\mathbf{m}$ is undertaken from the measured data by minimizing the quadratic cost function, $C(\mathbf{m})$ defined by Torres-Verdín and Habashy (1994), namely,

$$2C(\mathbf{m}) = \left[\left\| \mathbf{W}_d \cdot \left[\mathbf{d}(\mathbf{m}) - \mathbf{d}^{obs} \right] \right\|^2 - \chi^2 \right] + \lambda \left\| \mathbf{W}_m \cdot (\mathbf{m} - \mathbf{m}_R) \right\|^2, \tag{G-1}$$

Various parameters involved in (G-1) are described in Chapter 5.

To obtain a stationary point, $\mathbf{m},$ where the quadratic cost function attains a minimum, a Gauss-Newton nonlinear fixed-point iteration scheme (Gill et al., 1981) is employed. Let $\mathbf{m}^k$ be a pivoting vector where k is the iteration count. The first three terms of the Taylor series expansion of $C(\mathbf{m})$ about the pivoting point $\mathbf{m}^k$ are given by

$$\begin{aligned} C(\mathbf{m}) &= C(\mathbf{m}^k) + \nabla^T C(\mathbf{m}^k) \cdot (\mathbf{m} - \mathbf{m}^k) \\ &+ \frac{1}{2} (\mathbf{m} - \mathbf{m}^k)^T \cdot \nabla \nabla C(\mathbf{m}^k) \cdot (\mathbf{m} - \mathbf{m}^k), \end{aligned} \tag{G-2}$$

where the superscript T denotes transpose, the operator ∇ is defined as

$$\nabla = \left[\frac{\partial}{\partial x_1}, \frac{\partial}{\partial x_2}, \ldots, \frac{\partial}{\partial x_j}, \ldots, \frac{\partial}{\partial x_{3N}} \right]^T, \tag{G-3}$$

and the matrix $\nabla \nabla C(\mathbf{m})$ denotes the Hessian of the cost function. It then follows that

$$\nabla C(\mathbf{m}) = \mathbf{J}^T(\mathbf{m}) \cdot \mathbf{W}_d^T \cdot \mathbf{W}_d \cdot [\mathbf{d}(\mathbf{m}) - \mathbf{d}^{obs}] + \lambda \mathbf{W}_m^T \cdot \mathbf{W}_m \cdot (\mathbf{m} - \mathbf{m}_R), \tag{G-4}$$

where $\mathbf{J}(\mathbf{m})$ is the Jacobian matrix of $C(\mathbf{m})$ of size $2M \times 3N,$ which can be written as

$$\mathbf{J}(\mathbf{m}) = \begin{bmatrix} \partial d_1 / \partial m_1 & \ldots & \partial d_1 / \partial m_l & \ldots & \partial d_1 / \partial m_{3N} \\ \vdots & & \vdots & \ddots & \vdots \\ \partial d_j / \partial m_1 & \ldots & \partial d_j / \partial m_l & \ldots & \partial d_j / \partial m_{3N} \\ \vdots & & \vdots & \ddots & \vdots \\ \partial d_{2M} / \partial m_1 & \ldots & \partial d_{2M} / \partial m_l & \ldots & \partial d_{2M} / \partial m_{3N} \end{bmatrix}. \tag{G-5}$$

Here, the integers M and N are the number of traces of the normalized spectra and the number of radial layers for the invaded formation model, respectively.

A first-order forward difference (Fréchet derivative) formula is used to approximate the entries of the Jacobian matrix, i.e.,

$$\frac{\partial d_j}{\partial m_l} \approx \frac{d_j(m_l + \Delta m_l) - d_j(m_l)}{\Delta m_l}, \tag{G-6}$$

where Δm_l is chosen as small as possible without compromising the intrinsic accuracy of the forward modeling codes (approximately 1%). The entries of the Jacobian matrix are subsequently updated as the values of m_l change and the iterations progress in their way toward the extremum of the cost function. As implied by equation (G-6), this approach requires two forward modeling computations per unknown. To accelerate the computation of the Jacobian matrix, one makes use of the fact that the Jacobian matrix could be updated using the values taken by the same matrix at previous iterations. This is achieved with the Broyden's rank-one update formula (Gill et al., 1981), i.e.,

$$\mathbf{J}(\mathbf{m}^{k+1}) \approx \mathbf{J}(\mathbf{m}^k) + [\Delta \mathbf{d}(\mathbf{m}^k) - \mathbf{J}(\mathbf{m}^k) \cdot \Delta \mathbf{m}^k] \cdot \frac{[\Delta \mathbf{m}^k]^T}{[\Delta \mathbf{m}^k]^T \cdot [\Delta \mathbf{m}^k]}, \tag{G-7}$$

where

$$\Delta \mathbf{d}(\mathbf{m}^k) = \mathbf{d}(\mathbf{m}^{k+1}) - \mathbf{d}(\mathbf{m}^k) \text{ and } \Delta(\mathbf{m}^k) = \mathbf{m}^{k+1} - \mathbf{m}^k. \tag{G-8}$$

In the above equations, it is assumed that $\mathbf{d}(\mathbf{m}^k)$ changes in linear fashion with respect to $\mathbf{m}^k$ along the step direction $\Delta \mathbf{m}^k$. Often, this remains a good approximation provided that $\mathbf{m}^k$ is close to the extremum of the least-squared cost function. Subsequent to the computation of the Jacobian matrix, Broyden's rank-one update formula is used through a few iterations. If a fast convergence toward the minimum is not observed, then the Jacobian matrix is reset by performing the numerical simulations required to compute its entries. Such a procedure proved to be highly efficient in solving the inversion problems described in Chapter 5.

In the Gauss-Newton iterative scheme, one discards the second-order derivatives of the cost function about the pivot point, $\mathbf{m}^k$. Consequently, the approximate representation of the Hessian becomes

$$\nabla\nabla C(\mathbf{m}) \cong \mathbf{J}^T(\mathbf{m})\cdot \mathbf{W}_d^T \cdot \mathbf{W}_d \cdot \mathbf{J}(\mathbf{m}) + \lambda\, \mathbf{W}_m^T \cdot \mathbf{W}_m . \qquad \text{(G-9)}$$

By reordering equation (C-2) one obtains

$$\Phi(\mathbf{m}-\mathbf{m}^k) = C(\mathbf{m}) - C(\mathbf{m}^k) = \nabla^T C(\mathbf{m}^k)\cdot(\mathbf{m}-\mathbf{m}^k)$$

$$+\frac{1}{2}(\mathbf{m}-\mathbf{m}^k)^T \cdot \nabla\nabla C(\mathbf{m}^k)\cdot(\mathbf{m}-\mathbf{m}^k), \qquad \text{(G-10)}$$

where Φ is a quadratic function. This latter function exhibits a stationary point at $(\mathbf{m}-\mathbf{m}^k)$ if the gradient vector of Φ vanishes at $(\mathbf{m}-\mathbf{m}^k)$. Let

$$\nabla\Phi(\mathbf{m}-\mathbf{m}^k) = \nabla\nabla C(\mathbf{m}^k)\cdot(\mathbf{m}-\mathbf{m}^k) + \nabla C(\mathbf{m}^k) = 0 , \qquad \text{(G-11)}$$

whereupon

$$\nabla C(\mathbf{m}^k) = \mathbf{J}^T(\mathbf{m}^k)\cdot \mathbf{W}_d^T \cdot \mathbf{W}_d \cdot [\mathbf{d}(\mathbf{m}^k) - \mathbf{d}^{obs}] + \lambda\, \mathbf{W}_m^T \cdot \mathbf{W}_m \cdot (\mathbf{m}^k - \mathbf{m}_R), \qquad \text{(G-12)}$$

and

$$\nabla\nabla C(\mathbf{m}^k) = \mathbf{J}^T(\mathbf{m}^k)\cdot \mathbf{W}_d^T \cdot \mathbf{W}_d \cdot \mathbf{J}(\mathbf{m}^k) + \lambda\, \mathbf{W}_m^T \cdot \mathbf{W}_m . \qquad \text{(G-13)}$$

By substituting equations (C-12) and (C-13) into equation (C-11) and by rearranging terms, a final expression is obtained to compute the next iteration point. At a given iteration, $\mathbf{m} = \mathbf{m}^{k+1}$, one has

$$\mathbf{m}^{k+1} = \left[\mathbf{J}^T(\mathbf{m}^k)\cdot \mathbf{W}_d^T \cdot \mathbf{W}_d \cdot \mathbf{J}(\mathbf{m}^k) + \lambda\, \mathbf{W}_m^T \cdot \mathbf{W}_m\right]^{-1}$$

$$\cdot\left\{\mathbf{J}^T(\mathbf{m}^k)\cdot \mathbf{W}_d^T \cdot \mathbf{W}_d \cdot \left[\mathbf{d}(\mathbf{m}^k) - \mathbf{d}^{obs} + \mathbf{J}(\mathbf{m}^k)\cdot \mathbf{m}^k\right] + \lambda \mathbf{W}_m^T \cdot \mathbf{W}_m \cdot \mathbf{m}_R\right\}, \qquad \text{(G-14)}$$

subject to the physical hard bounds

$$l_i \leq m_i^{k+1} \leq u_i , \tag{G-15}$$

where $i = 1, 2, ..., N$.

Bibliography

Aki, K., and Richards, P. G, 1980, Quantitative Seismology: W. H. Freeman Co., San Francisco.

Ayme-Bellegarda, E. J., and Habashy, T. M., 1992, On multi-dimensional ultrasonic scattering in an inhomogeneous elastic background: J. Acoustic Soc., Am., 91, 3104-3115.

Baghai-Wadji, A. R., 1999, 2D and 3D models for the cross-talk modeling in acoustic devices: a fast-MoM approach: IEEE Ultrason. Sym., Lake Tahoe, Nevada.

Baker, C. T. H., 1977, The Numerical Treatment of Integral Equations, 358-360: Clarendon Press, Oxford, England.

Baker, L. J., and Winbow, G. A., 1988, Multipole P-wave logging in formations altered by drilling: Geophysics, 53, 1207-1218.

Ben-Menahem, A., and Gibson, Jr., R. L., Scattering of elastic waves by localized anisotropic inclusions, J. Acoust. Soc. Am., 87, 2300-2309, 1990.

Ben-Menahem, A., and Singh, S. J., 1981, Seismic Waves and Sources: Dover Publications, Inc, New York.

Biot, M. A., 1956a, Theory of propagation of elastic waves in a fluid saturated porous solid I. Low-frequency range: J. Acoust. Soc. Am, 28, 168-178.

Biot, M. A., 1956b, Theory of propagation of elastic waves in a fluid saturated porous solid II. Higher frequency range: J. Acoust. Soc. Am., 28, 179-191.

Bouchon, M., and Aki, K., 1977, Discrete wavenumber presentation of seismic-source wavefields: Null. Seis. Soc. Am., 67, 259-277.

Chen, X., 1993, A systematic and efficient method of computing normal modes for multilayered half-space: Geophys. J. Internat., 115, 391-409.

Chen, X., Quan, Y., and Harris, J. M., 1996, Seismogram synthesis for radially layered media using the generalized reflection/transmission coefficients method: Theory and applications to acoustic logging: Geophysics, 61, 1150-1159.

Cheng, C. H., 1989, Full waveform Inversion of P waves for Vs and Qp: J. of Geophys. Res., 94, 15619-15625.

Cheng, C. H., and Toksöz, M. N., 1981, Elastic wave propagation in a fluid-filled borehole and synthetic acoustic logs: Geophysics, 46, 1042-1053.

Cheng, C. H., Wilkens, and Meredith, J. A., 1986, Modeling of full waveform acoustic logs in soft marine sediments: 27th Trans. SPWLA Ann. Logging Symp., Paper LL, Houston, Texas.

Cheng, N., 1994, Borehole wave propagation in isotropic and anisotropic media: three-dimensional finite difference approaches: PhD Thesis, MIT.

Cheng, N., Cheng, C. H., and Toksöz, M. N., 1995, Borehole wave propagation in three dimensions: J. of Acoust. Soc. Am., 97, 3383-3393.

Chew, W. C., and Liu, Q. H., 1994, Inversion of induction tool measurements using the distorted Born iterative method and CG-FFHT: IEEE Trans. Geosci. Remote Sensing, 878-884.

Constable, S. C., Parker, R. L., and Constable, C. G., 1987, Occam's inversion: A practical algorithm for generating smooth models from electromagnetic sounding data: Geophysics, 52, 289-299.

Domenico, S. N., 1976, Effect of brine-gas mixture on velocity in an unconsolidated sand reservoir: Geophysics, 41, 882-894.

Dunkin, J. W., 1965, Computation of modal solutions in layered, elastic media at high frequencies: Bull. Seis. Soc. Am., 55, 335-358.

Dutta, N. C., and Ode, H., 1979a, Attenuation and dispersion of compressional waves in fluid-filled rocks with partial gas saturation White model: Part I-Biot theory: Geophysics, 44, 1777-1788.

Dutta, N. C., and Ode, H., 1979b, Attenuation and dispersion of compressional waves in fluid-filled rocks with partial gas saturation, White model: Part II-Results: Geophysics, 44, 1789-1805.

Frazer, L. N., and Sun, X., 1998, New objective functions for waveform inversion: Geophysics, 63, 213-222.

Frazer, L. N., Sun, X., and Wilkens, R. H., 1997, Inversion of sonic waveforms with unknown source and receiver functions: Geophys. J. Int., 129, 579-586.

Gao, G., Fang, S., and Torres-Verdín, C., 2003, A new approximation for 3D electromagnetic scattering in the presence of anisotropic conductive media: Three-Dimensional Electromagnetics Workshop No. 3 (3DEM-3), Adelaide, Australia, February 20-21.

Gao, G., Torres-Verdín, C., and Fang, S., 2003, Fast 3D modeling of borehole induction data in dipping and anisotropic formations using a novel approximation technique: submitted for publication, Petrophysics.

Gassmann, F., 1951, Uber die Elastizitat porijser medien: Vierteljahrschr. Naturforsch. Ges.. Zurich, 96, l-23.

Geertsma, J., and Smit, D. C., 1961, Some aspects of elastic wave propagation in fluid-saturated porous solids: Geophysics, 26, 169-181.

George, B. K., Torres-Verdín, C., Delshad, M., Sigal, R., Zouioueche, F., Anderson, B., 2003, A case study integrating the physics of mud-filtrate invasion with the physics of induction logging: assessment of in-situ hydrocarbon saturation in the presence of deep invasion and highly saline connate water: Presented at the 44th Ann. SPWLA Conf., paper K, Galveston, Texas.

Gill, P. E., Murray, W., and Wright, M. H., 1981, Practical optimization: Academic Press, London.

Gregory, A. R., 1976, Fluid saturation effects on dynamic elastic properties of sedimentary rocks: Geophysics, 41, 895-921.

Habashy, T. M., and Mittra, R., 1987, On some inverse problems in electromagnetics: Electromagn. Waves Appl., 1, 25-28.

Habashy, T. M., Torres-Verdín, C., and Kostek, S., 1994, A New Nonlinear Approximation for Elastic Wave Scattering: Schlumberger-Doll Research, preprint.

Harrington, R. F., 1968, Field Computation by Moment Methods: MacMillan, New York, NY.

Hohmann G. W. 1975, Three-dimensional induced polarization and electromagnetic modeling: Geophysics, 40, 309-324.

Hohmann, G. W., 1971, Electromagnetic scattering by conductors in the earth near a line source of current: Geophysics, 36, 101-131.

Hohmann, G. W., 1983, Three-dimensional EM modeling: Geophys. Surv., 6, 27-53.

Hornby, B. E., 1993, Tomographic reconstruction of near-borehole slowness using refracted borehole sonic arrivals: Geophysics, 58, 1726-1738.

Huang, X., 2003, Effects of tool positions on borehole acoustic measurements: A stretched grid finite-difference approach: Ph.D. Thesis, MIT.

Hyde, E. M., 2002, Fast, High-Order Methods for Scattering by Inhomogeneous Media: Ph.D. Dissertation, California Institute of Technology.

Kennett, B. L. N., 1983, Seismic wave propagation in stratified media: Cambridge Univ. Press, Cambridge, London, New York, New Rochelle, and Melbourne Sydney.

Kimball, C. V., Lewicki, P., Wijeyesekera, N. I., 1995, Error analysis of maximum likelihood estimates from one or more dispersive waves: IEEE Trans. on Signal Processing, 43, 2928-2936.

Kimball, C.V., and Marzetta, T. L., 1986, Semblance processing of borehole acoustic array data: Geophysics, 49, 274-281.

Kong, J. A., 1990, Electromagnetic Wave Theory: John Wiley, New York.

Kurkjian, A. L., and Chang, S. K., 1983, Geometric decay of the headwaves excited by a point force in a fluid-filled borehole: Presented at the 53rd Ann. Internat. Mtg. and Expos., Soc. Explor. Geophys., Las Vegas, Nevada.

Kurkjian, A. L., and Chang, S. K., 1986, Acoustic multipole sources in fluid-filled boreholes: Geophysics, 51, 148-163.

Lane, H. S., 1993, Numerical simulation of mud filtrate invasion and dissipation: Presented at SPWLA 34th Ann. Symp., Paper D, Calgary, Alberta, Canada.

Lee, K. H., and Kim, H. J., 2003, Source-independent full waveform inversion of seismic data: Geophysics online, Published electronically on May 20, 2003.

Liu, Q. H., and Sinha, B. K., 2000, Multipole acoustic waveforms in fluid-filled boreholes in biaxially stressed formations: a finite-difference method: Geophysics, 65, 190-201.

Lu, C. C., and Liu, Q. H., 1995, A three-dimensional dyadic Green's function for elastic waves in multilayer cylindrical structures: J. Acoust. Soc. Am., 98, 2825-2835.

Luco, J. E., and Apsel, R. J., 1983, On the Green’s function for a layered half-space, Part I: Bull. Seis. Soc. Am., 73, 909-929.

Moroney, D. T., and Cullen, P. J., 1998, A fast integral equation approach to acoustic scattering from three-dimensional objects using a natural basis set: J. Acoust. Soc. Am., 103, 2354-2364.

Murphy. W. F. III, 1982a. Effects of microstructure and pore fluids on the acoustic properties of granular sedimentary materials: Ph.D. thesis, Stanford University.

Nieto-Vesperinas, M., 1991, Scattering and diffraction in physical optics: John Wiley, New York.

Paillet, F. L., and Cheng, C. H., 1991, Acoustic Waves in Boreholes: CRC Press, Boca Raton, Florida.

Pao, Y. H., and Varatharajulu, V., 1976, Huygens’ principle, radiation conditions, and integral formulas for the scattering of elastic waves: J. Acoustic Soc., Am., 59, 1361-1371.

Pearson, C. E., 1990, Handbook of Applied Mathematics: Van Nostrand, New York.

Pereira, A., Tadeu, A., and António, J., 2002, Influence of the cross-section geometry of a cylindrical solid submerged in an acoustic medium on wave propagation: Wave Motion, 36, 23–39.

Pike, R., Sabatier, P., 2002, Scattering and Inverse Scattering in Pure and Applied Science: Academic Press, San Diego, California.

Pratt, R. G., 1990, Inverse theory applied to multi-source cross-hole tomography, Part II: elastic wave-equation method: Geophys. Prosp., 38, 311-330.

Pratt, R. G., 1999a, Seismic waveform inversion in frequency domain, Part 1: Theory and verification in physical scale model: Geophysics, 64, 888-901.

Pratt, R. G., 1999b, Seismic waveform inversion in frequency domain, Part 2: Fault delineation in sediments using crosshole data: Geophysics, 64, 902-914.

Rao, S. M., and Sridhara, B. S., 1992, Acoustic scattering from arbitrarily shaped multiple bodies in half-space: Method of moments solution: J. Acoust. Soc. Am., 91, 652-657.

Roever, W., Rosenbaum, J., and Vining, T., 1974, Acoustic waves from an impulsive source in a fluid-filled borehole: J. Acoust. Soc. Am., 55, 1144-1157.

Salazar, J. M., Torres-Verdín, C., and Sigal, R., 2003, Facies and flow unit indetification in a tight-gas hydrocarbon field: Presented at the 3rd annual Formation Evaluation Conference at the University of Texas at Austin, Austin, Texas.

Schmitt, D. P., 1988, Shear wave logging in elastic formations: J. Acoust. Soc. of Am., 84, 2215-2229.

Sen, M. K., and Stoffa, P. L., 1991, Nonlinear one-dimensional seismic waveform inversion using simulated annealing: Geophysics, 56, 1624-1638.

Sheng, J., and Schuster, G. T., 2000, Finite-frequency resolution limits of traveltime tomography for smoothly varying velocity models: Presented at 70th Ann. Internat. Mtg., Soc. Expl. Geophys., Expanded Abstracts, 2134-2137.

Shi, Y., and Shirahatti, U. S., 1996, The use of the method of moments with finite difference operator in acoustics: J. Acoust. Soc. Am., 99, 2667-2673

Smith, T. M., Sondergeld, C. H., and Rai, C. S., 2003, Gassmann fluid substitutions: A tutorial: Geophysics, 68, 430-440.

Stephen, R. A., Cardo-Casas, F., and Cheng, C. H., Finite-difference synthetic acoustic logs: Geophysics, 50, 1588-1609.

Tang, X. M., and Cheng, C. H., 1988, Wave propagation in a fluid-filled fracture - an experimental study: Geophys. Res. Lett., 15, 1463-1466.

Tang, X. M., and Cheng, C. H., 1993, Borehole Stoneley wave propagation cross permeable structures: Geophys. Prospecting, 41, 165-187.

Tang, X. M., and Cheng, C. H., 1993, Effects of a logging tool on the Stoneley waves in elastic and porous boreholes: The Log Analyst, 46-56, Sept.-Oct..

Tang, X. M., and Cheng, C. H., 1996, Fast inversion of formation permeability from Stoneley wave logs using a simplified Biot-Rosenbaum model: Geophysics, 61, 639-645.

Tang, X. M., Cheng, C. H., and Toksöz, M. N., 1991, Dynamic permeability and borehole Stoneley waves: A simplified Biot-Rosenbaum model: J. Acoust. Soc. Am., 90, 1632-1646.

Tang, X. M., Dubinsky, V., Wang, T., Bolshakov, A., and Patterson, D., 2002, Shear-velocity measurement in the logging-while-drilling environment: modeling and field evaluations: Petrophysics, 44, 79-90.

Toksöz, M. N., Wilkens, R. H., and Cheng, C. H., 1985, Shear wave velocity and attenuation in ocean bottom sediments from acoustic log waveforms: Geophys. Res. Lett., 12, 37-40.

Toksoz. M. N., Cheng, C. H., and Timur, A., 1976, Velocities of seismic waves in porous rocks: Geophysics, 41, 621-645.

Tongtaow, C., 1982, Wave propagation along a cylindrical borehole in a transversely isotropic medium: Ph.D. dissertation, Colorado School of Mines.

Torres-Verdín, C., and Habashy, T. M., 1994, Rapid 2.5-dimensional forward modeling and inversion via a new nonlinear scattering approximation: Radio Science, 1051-1079.

Torres-Verdín, C., and Habashy, T. M., 1995, A two-step linear inversion of two-dimensional electrical conductivity: IEEE Trans. On Geoscience and Remote sensing, 43, 405-415.

Torres-Verdín, C., and Habashy, T.M., 1993, Cross-well electromagnetic tomography: Expanded Abstract, 3rd International Congress of the Brazilian Geophysical Society.

Torres-Verdín, C., and Habashy, T.M., 2001, Rapid numerical simulation of axisymmetric single-well induction data using the extended Born approximation: Radio Sci., 36, 1287-1306.

Torres-Verdín, C., Druskin, V. L., Fang, S., Knizhnerman, L. A., and Malinverno, A., 2000, A dual-grid nonlinear inversion technique with applications to the interpretation of DC resistivity data: Geophysics, 65, 1733-1745.

Tsang, L., and Rader, D., 1979, Numerical evaluation of transient acoustic waveforms due to a point source in a fluid-filled borehole: Geophysics, 44, 1706-1720.

Tubman, K. M., Cheng, C. H., and Toksöz, M. N., 1984, Synthetic full waveform acoustic logs in cased boreholes: Geophysics, 49, 1051-1059.

Tygel, M., and Hubral, P., 1987, Transient waves in layered media: Amsterdam, Elsevier.

Varela, O. J., 2003, Stochastic Inversion of Pre-Stack Seismic Data to Improve Forecasts of Reservoir Production: Ph.D. dissertation, The University of Texas at Austin.

Walls, J., and Carr, M., 2001, The use of fluid substitution modeling for correction of mud filtrate invasion in sandstone reservoirs: Presented at the 71st Ann. Internat. Mtg. And Expos., Soc. Explor. Geophys., San Antonio, Texas.

Watson, G. N., 1980, A Treatise on the Theory of Bessel Functions, 2nd Edition: Cambridge University Press, Cambridge.

White, J. E., 1967, The hula log-a proposed acoustic tool: Presented at the 8th SPWLA Conf., Paper I, Denver, Colorado.

Winbow, G., 1980, How to separate compressional and shear arrivals in a sonic log: Presented at the 50th Ann. Internat. Mtg. And Expos., Soc. Explor. Geophys., Houston, Texas.

Winbow, G., and Rice, J. A., 1984, Theoretical performance of multipole sonic logging tools: Presented at the 54th Ann. Internat. Mtg. and Expos., Soc. Explor. Geophys., Atlanta, Georgia.

Wood, A. B., 1941, A textbook of sound: G. Bell and Sons, London.

Wu, J., Torres-Verdín, C., Sepehrnoori, K., and Delshad, M., 2001, Numerical simulation of mud filtrate invasion in deviated wells: Paper SPE 71739, SPE Ann. Tech. Conf. and Exhib., New Orleans, Louisiana.

Xu, X. M., and Liu, Q. H., 2001, Fast spectral-domain method for acoustic scattering problems: IEEE Trans. Ultrason. Ferroelectr. Freq. Control. 48, 522-529.

Yoon, K. H., and McMechan, G. A., 1992, 3-D finite-difference modeling of elastic waves in borehole environments: Geophysics, 57, 793-804.

Zhdanov M. S., and Fang S., 1996, Quasi-linear approximation in 3-D electromagnetic modeling: Geophysics, 61, 646-665.

Zhou, C., Schuster, G. T., Hassanzadeh, S., and Harris, J. M, 1997, Elastic wave equation traveltime and wavefield inversion of crosswell data: Geophysics, 62, 853-868.

Vita

Shihong Chi was born in the village of Big Chimney, Hui Nan County, Ji Lin Province, China, on May 5th, 1970, the son of Shan-ping Chi and Shu-lan Zhang. In 1994, he received his B.S. degree in Geophysics from the University of Science and Technology of China in He Fei, An Hui; in 1997 his M.S. degree in Exploration Geophysics from the University of Petroleum, East China in Dong Ying, Shan Dong; and in 1999 his M. S. degree in Petroleum Engineering from the University of Texas at Austin. He worked with Schlumberger during the summer of 2000 and with Baker Atlas/Inteq during the summer of 2001.

In December 1999, he married Aichou Lin from Wen Ling, Zhe Jiang, China. And they have a 2-year-old son, Isaac Lin.

Permanent address:
Da Yan Tong,
Hui Nan County,
Ji Lin Province, 135122
China

This dissertation was typed by the author.